Full Field Swept Source Optical Coherence Tomography

James Fergusson

Cardiff University School of Optometry and Vision Sciences

A thesis submitted for the degree of doctor of philosophy

January 2013

Summary

Optical Coherence Tomography (OCT) is a non-invasive volumetric imaging technique that offers micron scale resolution over several millimetres of depth penetration in tissue. The aim of the project was to develop Full Field Swept Source OCT (FFSSOCT), charting the specifications of the system throughout and drawing comparisons with available Fourier domain OCT (FDOCT) systems. A super luminescent diode (SLD) light source was tuned to different optical frequencies using an acousto-optical tunable filter. The successive optical frequencies were distributed across the sample in parallel and the sequential interference spectra were recorded with a high speed digital camera. Using a 5mW optical source at 850nm, 70dB sensitivity was ultimately achieved in a single five second acquisition, improving the original performance by 5dB and increasing acquisition and processing time significantly. *Ex vivo* retinal images of rat and tree shrew were recorded with multiple layers visible. All software was custom written in Labview, improving the user interface and processing time over the existing Matlab code.

To enhance the performance of the system, the camera was subsequently upgraded from 15 to 45% quantum efficiency and from 250k to 1.3M pixels. The light source was also upgraded to 20mW. The software was improved with spectral processing and dispersion compensation. 85dB sensitivity was ultimately achieved. Further *ex vivo* retinal images were taken, showing comparative image quality to those of the same retinal samples recorded with FDOCT. Further attempts to increase the system performance were limited by internal reflections and interfering surfaces within the FFSSOCT design leading to saturation of the digital camera. *In vivo* imaging was attempted using software based phase jitter compensation. Improvement could be seen with simple reflecting structures.

Acknowledgements

I would like to acknowledge the support and guidance received from my supervisors Professor Wolfgang Drexler, Dr Boris Považay and Professor John Wild during the different stages of the project.

I would also like to thank Dr. Bernd Hofer for sharing his knowledge of Labview programming and data processing and Nick White for numerous conversations on all things OCT.

My friends and family should also be thanked for their support during the project.

I would also like to thank the BBSRC for funding this PhD project.

Table of Contents

Declaration....ii
Summary....iii
Acknowledgements....iv
List of Tables....viii
List of Figures and Illustrations....ix
List of Abbreviations....xiv
List of Equation Nomenclature....xvi

Chapter One: Introduction to Optical Coherence Tomography (OCT)....1
1.1 Optical Coherence Tomography....2
1.1.1 Optical principles for OCT....4
1.2 Theory of Time Domain Optical Coherence Tomography (TDOCT)....8
1.3 Fourier Domain Optical Coherence Tomography (FDOCT)....11
1.4 Theory of Fourier Domain Optical Coherence Tomography....14
1.5 Swept Source Optical Coherence Tomography (SSOCT)....17
1.6 Full Field Swept Source Optical Coherence Tomography (FFSSOCT)....18
1.7 Comparison of the different types of OCT....20
1.8 Advantages and disadvantages of OCT compared to other multi-dimensional imaging techniques....21
1.9 Aim of the research....24

Chapter Two: Creating an FFSSOCT system....25
2.1 Operational Logistics....26
2.2 Labview programming language....26
2.2.1 Justification for Labview....26
2.2.2 Labview format....27
2.3 Extending Swept Source OCT to Full Field Swept Source OCT....28
2.4 Original hardware....28
2.4.1 Crosstalk....32
2.5 Software....34
2.5.1 Frequency Stepper....35
2.5.2 FFSSOCT real time B-scan viewer....36
2.5.3 FFSSOCT acquisition software....37
2.6 Specifications....39
2.6.1 Acquisition speed....39
2.6.2 Signal to noise ratio....39
2.6.3 Image resolution....40
2.6.4 Optical power....41
2.7 Acquired images....41
2.8 Summary....42

Chapter Three: Improving the FFSSOCT system....43
3.1 Improvement aims....44
3.2 Hardware improvements....44
3.3 Software improvements....45
3.4 Using a multimode fibre and spinning diffuser....47
3.5 Images acquired with the multimode fibre and diffuser....50
3.6 Retinal images....52

3.7 Volumetric imaging with FFSSOCT 55
3.8 Upgrading the camera 57
3.9 Retinal images 61
3.10 Illumination arm redesign 61
3.11 Retinal imaging with improved sensitivity 62
3.12 Rat retinal imaging 65
3.13 Improved Software 67
3.13.1 Acquisition software 67
3.13.2 Processing software 69
3.14 Summary 72

Chapter Four: FFSSOCT Data Processing 74
4.1 Improvement aims 75
4.2 Introduction to OCT data processing 75
4.3 Spectral subtraction and shaping 76
4.4 Spectral shaping 80
4.5 Background subtraction 82
4.6 Resampling 87
4.6.1 Constructing a resampling function 88
4.6.2 Measurement of the FFSSOCT resampling function 91
4.6.3 Generation of the FFSSOCT resampling function 94
4.7 Zero padding 101
4.8 Fourier transform and file saving 105
4.9 Post processing 107
4.10 Dispersion correction 107
4.11 Summary 108

Chapter Five: Analysis of FFSSOCT data 110
5.1 Improvement aims 111
5.2 Introduction to FFSSOCT data analysis 111
5.3 Depth range 111
5.4 Resolution and sampling 114
5.4.1 Lateral resolution 114
5.4.2 Lateral sampling 117
5.4.3 Axial resolution 118
5.4.4 Axial Sampling 119
5.5 Signal to noise ratio (SNR) 119
5.5.1 Problems with measuring real SNR 121
5.6 Sensitivity fall-off 123
5.6.1 Theory of OCT sensitivity fall-off 124
5.6.2 Sensitivity fall-off in FFSSOCT 130
5.6.3 Measurement of the sensitivity fall-off of the FFSSOCT instrument 132
5.7 Summary 137

Chapter Six: FFSSOCT in comparison to FDOCT 138
6.1 Comparing FFSSOCT to FDOCT 139
6.2 Retinal imaging comparison 142
6.3 Mirror sample comparison 145
6.4 *In vivo* imaging 152
6.5 Summary 152

Chapter Seven: Conclusions 153
7.1 Aim and accomplishments 154
7.2 Advantages and disadvantages of using a FFSS approach to OCT 154
7.3 Applications of FFSSOCT 156
7.4 Future work 156

References 157

Appendix A: Labview Diagrams 164

List of Tables

Table 1-1: A comparison of the different types of OCT operating at a central wavelength of ~800nm. 21

Table 2-1: The speed limiting factors in the current FFSSOCT design. 39

Table 3-1: Hardware improvements made to the FFSSOCT design. 45

Table 3-2: List of the software improvements compiled during the FFSSOCT project. 46

Table 6-1: Comparison of FFSSOCT and FDOCT system parameters 141

List of Figures and Illustrations

Figure 1-1: A time domain OCT system. 3

Figure 1-2: The beam path of a time domain OCT system. 3

Figure 1-3: Coherence length comparison....4

Figure 1-4: Comparison of a low numerical aperture (NA) verses a high NA. 6

Figure 1-5: The relative absorbance properties of various tissue components as a function of wavelength. 7

Figure 1-6: The beam path and energy division of a simple OCT system. 8

Figure 1-7: The spectral correlation interferogram for single and multiple reflectors. 11

Figure 1-8: Schematic of an FDOCT design. 12

Figure 1-9: Signal from an FDOCT instrument. 16

Figure 1-10: Schematic of a Swept Source OCT design. 17

Figure 1-11: Different techniques for ocular imaging. 23

Figure 2-1: The original FFSSOCT design. 30

Figure 2-2: The modified microscope used for FFSSOCT. 30

Figure 2-3: The effect of the mode mixer. 32

Figure 2-4: An OCT tomogram montage of a coin acquired with the FFSSOCT system. .41

Figure 3-1: The modified illumination arm. 48

Figure 3-2: Sensitivity of the FFSSOCT system after redesigning the illumination arm. ..49

Figure 3-3: 3D topographical projections of the foot and the eye of a wasp. 50

Figure 3-4: Images of a lettuce leaf taken at different depths from a tomographic volume. 51

Figure 3-5: Bright field image of lettuce cells. 52

Figure 3-6: A 2D B-scan of an *ex vivo* tree shrew retina. 53

Figure 3-7: Identification of the visible retinal layers of an *ex vivo* tree shrew FFSSOCT image. 53

Figure 3-8: A false colour 2D B-scan of an *ex vivo* tree shrew retina. 55

Figure 3-9: Volumetric image of an *ex vivo* tree shrew retina. 56

Figure 3-10: En face fly-through of an *ex vivo* tree shrew retina. 57

Figure 3-11: Detector quantum efficiency comparison. 59

Figure 3-12: Linear vs Linlog® camera response. 60

Figure 3-13: *Ex vivo* tree shrew retinal B-scan imaged with the new detector. 61

Figure 3-14: *Ex vivo* tree shrew retinal B-scan acquired with the improved SNR. 62

Figure 3-15: Spatially averaged *ex vivo* tree shrew retinal B-scan. 64

Figure 3-16: Four B-scans of an *ex vivo* tree shrew retina, each comprising of 10 spatially averaged frames. 64

Figure 3-17: Four en face scans of *ex vivo* tree shrew retina, each comprising of 5 spatially averaged frames. 65

Figure 3-18: Four B-scan images of *ex vivo* rat retina. 66

Figure 3-19: Six en face *ex vivo* rat retina scans at different depths. 66

Figure 3-20: The user interface panel of the FFSSOCT acquisition software. 68

Figure 3-21: The user interface panel of the FFSSOCT processing software. 71

Figure 4-1: Flow chart showing the processing steps required to transform the FFSSOCT spectral data into TD data. 76

Figure 4-2: A-line data from a mirror with no processing applied. 77

Figure 4-3: A-line data from a mirror after Fourier transform with no processing applied. 78

Figure 4-4: Spectral data from a mirror with a 5th order polynomial fit. 78

Figure 4-5: Spectral waveform from a mirror after removing the low frequency components. 79

Figure 4-6: Fourier transform of the spectral waveform after removing the low frequency components. 79

Figure 4-7: Spectral waveform data from a mirror multiplied by a Gaussian filter. 80

Figure 4-8: Fourier transform of the spectral waveform data multiplied by a Gaussian filter. 81

Figure 4-9: Comparison of the effect of Gaussian shaping. 81

Figure 4-10: *Ex vivo* tree shrew retinal image showing pseudo-fixed pattern background noise. 83

Figure 4-11: An A-line from a tree shrew retinal image at lateral position 250. 83

Figure 4-12: The short-term fluctuation in intensity across the fixed pattern noise at axial position 44.....85

Figure 4-13: *Ex vivo* tree shrew retina with the horizontal noise pattern suppressed by Method 2.....86

Figure 4-14: The effect of chirping on an OCT spectral waveform.....90

Figure 4-15: The effect of resampling a chirped spectral waveform. 90

Figure 4-16: Uncorrected FFSSOCT data showing the reflectivity of a mirror at different depth points.....91

Figure 4-17: Uncorrected unwrapped phase data from a mirror at different depth positions.....92

Figure 4-18: Flow diagram of the phase extraction process.....93

Figure 4-19: Uncorrected FFSSOCT phase data with the linear phase component removed. 94

Figure 4-20: Uncorrected FFSSOCT phase data with the highly unstable phase traces removed. 95

Figure 4-21: The relationship between the input frequency and the output wavelength of the Broadsweeper 96

Figure 4-22: The averaged non-linear phase data. 97

Figure 4-23: FFSSOCT A-scans from a mirror, interpolated with the resampling function.....98

Figure 4-24: Unwrapped phase data from the resampled FFSSOCT data of a mirror.....98

Figure 4-25: The resampled spectral waveform data showing regular periodicity. 99

Figure 4-26: Fourier transform of the resampled spectral waveform data.....100

Figure 4-27: Comparison of the effect of Gaussian shaping and resampling. 100

Figure 4-28: Fourier transform of a noiseless sine wave with a frequency of 50.525Hz..102

Figure 4-29: Fourier transform of a noiseless sine wave with a frequency of 50.525Hz that has been zero padded once. 102

Figure 4-30: Fourier transform of two summed noiseless sine waves with frequencies of 5Hz and 6.425Hz.....103

Figure 4-31: Fourier transform of two summed noiseless sine waves with frequencies of 5Hz and 6.425Hz.....103

Figure 4-32: FFSSOCT spectral waveform from a mirror with zero padding applied. 104

Figure 4-33: Fourier transform of the FFSSOCT spectral waveform with zero padding applied. 105

Figure 4-34: Fourier transform of the FFSSOCT mirror data with all the pre-Fourier transform processing applied. 106

Figure 4-35: FFSSOCT mirror data with the 'absolute' function applied. 107

Figure 5-1: USAF 1951 target imaged by FFSSOCT. 115

Figure 5-2: USAF target imaged by a single wavelength (850nm). 116

Figure 5-3: Four sample spectra generated by a Fourier transform of a noisy sine wave signal. 120

Figure 5-4: An A-line of FFSSOCT data taken from an image of a mirror. 121

Figure 5-5: An A-line of FFSSOCT data with the amplitude cropped. 123

Figure 5-6: Sampling a 16hz waveform with FDOCT and FFSSOCT. 125

Figure 5-7: The real part of the Fourier transform of the sampled data shown in Figure 5-6. 126

Figure 5-8: Sampling a 159Hz waveform with FDOCT and FFSSOCT. 127

Figure 5-9: The reconstructed waveform from the data sampled by FDOCT and FFSSOCT. 128

Figure 5-10: The FFT of the data sampled by FDOCT and FFSSOCT. 128

Figure 5-11: The sensitivity decrease of OCT. 129

Figure 5-12: The theoretical sensitivity decrease of FFSSOCT and FDOCT due to spectral sampling. 131

Figure 5-13: The theoretical and measured fall-off functions of FFSSOCT. 133

Figure 5-14: The spectral interferogram, phase and iFFT data for three axial positions. . 135

Figure 6-1: Schematic of the FDOCT instrument. 140

Figure 6-2: *Ex vivo* tree shrew retina imaged by FFSSOCT (top) and FDOCT (bottom). 142

Figure 6-3: *Ex vivo* tree shrew retina imaged with FFSSOCT. 143

Figure 6-4: *Ex vivo* tree shrew retina imaged with FDOCT. 144

Figure 6-5: Spectral waveform of a mirror recorded with FFSSOCT. 145

Figure 6-6: Spectral waveform of a mirror recorded with FDOCT. 146

Figure 6-7: The phase signal generated from the FFSSOCT spectral waveform. 147

Figure 6-8: Cropped section of the phase signal generated from the FDOCT spectral waveform. 147

Figure 6-9: Fourier transform of the FFSSOCT spectral waveform. 149

Figure 6-10: Fourier transform of the FDOCT spectral waveform. 149

Figure 6-11: Section of the background noise taken from the FFSSOCT mirror signal... 151

Figure 6-12: Section of the background noise taken from the FDOCT mirror signal..... 151

Figure A-1: The first frame of the frequency sweeper control Labview VI..... 164

Figure A-2: The second frame of the frequency sweeper control Labview VI. 164

Figure A-3: The third frame of the frequency sweeper control Labview VI. 165

Figure A-4: The Labview VI for the real time 2D imager. 166

Figure A-5: FFSSOCT acquisition software. 167

Figure A-6: The first part of the Labview VI for processing the acquired data 168

Figure A-7: The second part of the Labview VI for processing the acquired data. 169

Figure A-8: The final version of the acquisition software (v2.1) for the FFSSOCT instrument. 170

Figure A-9: The processing software used to transform the stack of frequency domain data into a 3D OCT tomogram. 171

List of Abbreviations

Abbreviation	Definition
2D	Two-dimensional
3D	Three-dimensional
AOTF	Acousto-optic tuning filter
APC	Automatic power control
ASE	Amplified spontaneous emission
AVI	Audio visual interleave
BS	Beam splitter
CCD	Charge coupled device
CMOS	Complimentary metal-oxide semiconductor
CPU	Central processing unit
dB	Decibel
DC	Direct current
DoF	Depth of field
FC/APC	Fibre connector/angled physical contact
FDOCT	Fourier domain OCT
FFSSOCT	Full field swept source OCT
FFT	Fast Fourier transform
FPGA	Field-programmable gate array
FPS	Frames per second
FWHM	Full width at half maximum
IFFT	Inverse fast Fourier transform
IR	Infrared
LED	Light emitting diode
LUT	Look-up table
MIT	Massachusetts Institute of Technology
MMF	Multimode fibre
MRI	Magnetic resonance imaging
NA	Numerical aperture
ND	Neutral density
OCT	Optical coherence tomography
PCI	Peripheral component interconnect
PET	Positron emission tomography
PNG	Portable network graphics
QE	Quantum efficiency
RAID	Redundant array of independent disks
RAM	Random-access memory
RM	Reference mirror
SD	Standard deviation
SEM	Scanning electron microscopy
SLD	Super luminescent diode
SMF	Single mode fibre
SNR	Signal to noise ratio
SRAM	Static RAM
SSOCT	Swept source OCT
TCP/IP	Transmission control protocol/internet protocol
TDOCT	Time domain OCT
TIFF	Tagged image file format
UBM	Ultrasound biomicroscopy
UI	User interface

Abbreviation	Definition
USAF	United States Air Force
VI	Virtual instrument
VISA	Virtual instrument software architecture

List of Equation Nomenclature

Symbol	Definition	Unit
z(r)	Reference arm distance	meter
z(s)	Sample arm distance	meter
υ(r)	Velocity of reference arm	meters per second
z	Axial distance	meter
c	Speed of light	meters per second
n	Refractive index	dimensionless
Δλ	Bandwidth	meter
L_c	Coherence length	meter
δz	Axial resolution	meter
λ_0	Central wavelength	meter
f	Focal length	meter
D	Beam diameter	meter
Δ*x*	Lateral resolution	meter
λ	Wavelength	meter
k	Wavenumber/spatial frequency	reciprocal meter
ω	Angular frequency	radians per second
s/S	Wave amplitude	dimensionless
ΔL	Optical path difference	meter
E	Electric field strength	Volts per meter
r/R	Reflectivity	dimensionless ratio
R_S	Reflectivity of sample	dimensionless ratio
R_R	Reflectivity of reference target	dimensionless ratio
ρ	Responsivity	Amperes per Watt
E_S	Electric field strength from sample arm	Volts per meter
E_R	Electric field strength from reference arm	Volts per meter
I_D	Photocurrent	Ampere
γ(z)	Coherence function	meter
P_{vox}	Power deposited on a voxel	Watt
R_{vox}	Reflectivity of a voxel	dimensionless ratio
Δt	Time period	second
e	Electronic charge	Coulomb
A	Amplitude	dimensionless
m	Integer	dimensionless
d	distance	meter
N_S	Number of pixels	dimensionless
d_{norm}	Normalised distance	dimensionless

Chapter One: Introduction to Optical Coherence Tomography (OCT)

1.1 Optical Coherence Tomography

Optical coherence tomography (OCT) is a relatively new imaging technique that has the ability to create three-dimensional (3D) images with a high axial and lateral resolution (close to 1μm). It has gained popularity due to its combination of non-invasive image acquisition, high resolution and depth penetration compared to other imaging techniques such as MRI, ultrasound and confocal microscopy. The principle of imaging via the interference of backscattered light was first demonstrated by a group from Massachusetts Institute of Technology (MIT) led by Huang, who recorded the first *ex vivo* images of biological tissue (retina) using OCT in 1991[1,2]. The images they produced had a depth resolution of ~15μm, 10 times the resolving power of ultrasound and a depth penetration of ~2mm, 6 times the penetration of confocal microscopy. Following these publications, interest in OCT began to accumulate and in 1993, the first *in vivo* images of a human retina were produced by Swanson[2-4].

At the simplest level, an optical coherence device is a Michelson-Morley interferometer. The illuminating light is split by a semi-silvered prism (beam splitter) with half of the light going to the sample (sample arm) and the other half towards a movable mirror (reference arm). The backscattered light from the sample is interfered with the light from the reference arm and when the two path lengths are the same, the relative phase difference of the light is zero and constructive interference occurs. This is detected as a maximum signal by a photodiode and occurs at the 'zero delay' point - there is no delay between the two beams. When the two beams have a relative phase difference that is not equal to zero, less or no signal may be recorded. Thus, the components of the backscattered light of interest appear as maximum signal intensities and can easily be isolated from the rest of the background light. As there can be multiple reflecting surfaces in the structure that is being investigated, the reference is arm is moved along the optical path (shortening and lengthening the reference arm path length with respect to the sample arm) creating a maximum signal where the path lengths are the same. Thus, the internal structure of the sample can be determined (A-scan). The illumination spot can then can moved, point by point (raster scanning) along the sample, building up a two-dimensional (2D) cross section (tomogram or B-scan) and then an entire 3D volume. 3D images contain voxels, 3D

resolution elements, rather than pixels (2D resolution elements). This form of OCT is known as time domain (TDOCT) and is the simplest form of OCT.

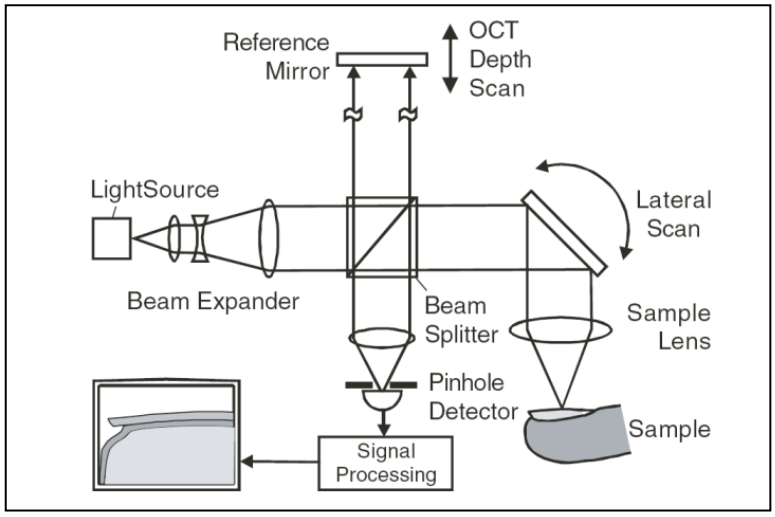

Figure 1-1: A time domain OCT system.

Adapted from *OCT:Technology and Applications*, Drexler and Fujimoto (2008)[3].

Figure 1-1 shows the schematic of a TDOCT system. Galvonometic mirrors allow for rapid raster scanning of the beam over the sample. The reference mirror can be rapidly moved by using a motor or a piezoelectric crystal, one that contracts/expands in the presence of an electric field. The pinhole detector gates some of the out of focus light in order to reduce the background noise.

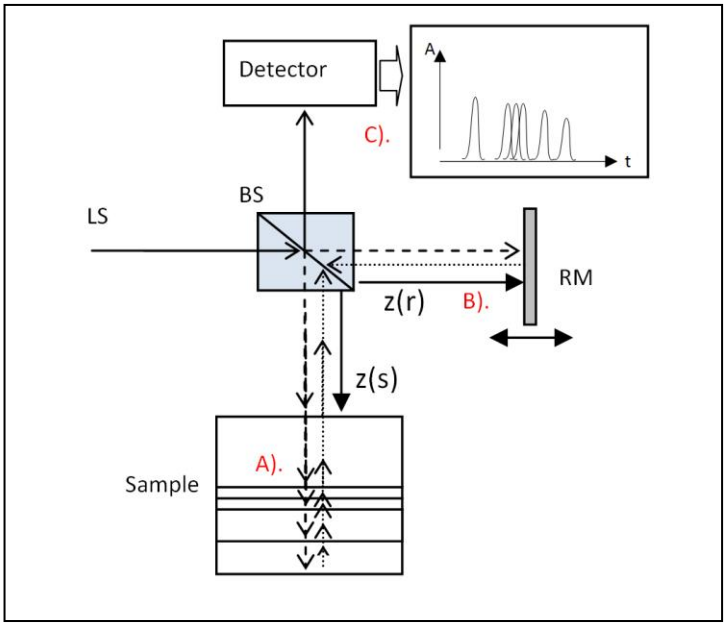

Figure 1-2: The beam path of a time domain OCT system.

LS is the light source. BS is the beamsplitter. RM is the reference mirror. Adapted from *OCT:Technology and Applications*, Drexler and Fujimoto (2008)[3]

As Figure 1-2 shows, each of the different layers in the sample (A), located at different depths z(s), reflect some of the light back to the beam splitter (BS). Each reflected beam has an associated phase delay dependent on its depth but remains spatially coherent. The reference mirror (RM) is moved with speed *v(r)* (B). When the lengths z(r) and z(s) are the same, a peak appears on the interferogram (C). The distance between the peaks is dependent on the speed of the reference mirror however; they will always appear to scale so long as *v(r)* remains constant.

1.1.1 Optical principles for OCT

The choice of light source for use in OCT is important as it ultimately determines both the signal power and resolution of the system. A laser light source is a popular choice for performing OCT they can have high output power that can be easily coupled into an optical fibre, facilitating transport of the light and reducing the complexity of the optical design of the instrument. Another defining characteristic of a laser is its extremely long coherence length, an entirely unwanted property for OCT. The coherence length is a measure of how long (spatially) the light remains in phase.

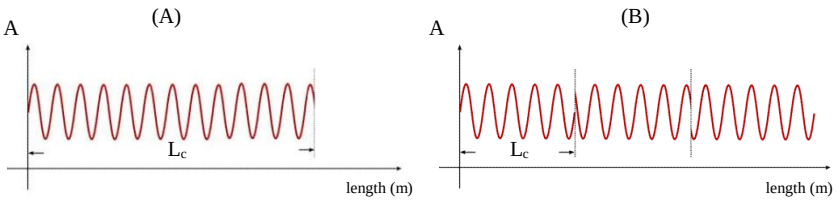

$$L_c = \frac{c}{n\Delta\lambda} \qquad \text{Eqn. 1}$$

Figure 1-3: Coherence length comparison.

(A) An example of a long coherence length (L_c) beam. The coherence length is many times the wavelength. (B) An example of a short coherence length. (C) The equation for coherence length (L_c) where *n* is refractive index and $\Delta\lambda$ is the bandwidth of the light source[3].

As described, OCT relies on the phase of the sample and reference beams being the same in order to create an image. When the coherence length is longer than a single wavelength, it is possible for the two beams to be completely in phase at more than one point (the zero delay plus any multiple of the light source wavelength over two). It, therefore, becomes impossible to know the exact position of the scattering surface in the sample. As the coherence length becomes longer, the number of in phase positions becomes greater and the accuracy of the system quickly diminishes.

To overcome this problem, light sources with large bandwidths are used, thus decreasing the coherence length proportionally according to Equation 1 (Figure 1-3). Such sources include femto-second pulsed lasers[5-9], white light super luminescent diodes (SLDs), amplified spontaneous emission (ASE) sources and halogen lamp white light sources. Although white light lamps have extremely large bandwidths (>1000nm), coupling the light into an optical fibre is inefficient compared to a laser light source. In OCT, sensitivity levels are stated as the ratio of the maximum signal to the background noise (signal to noise ratio – SNR) in decibels (dB). White light sources are preferred to laser sources for full field OCT as they also have very low spatial coherence, a property that reduces the unwanted spatial interference in the images[10-12].

The equation linking the resolution to the bandwidth of the light source has been widely referenced[13] and has been defined as:

$$\delta z = l_c = \frac{2log_e(2)}{\pi}\frac{{\lambda_0}^2}{\Delta\lambda} \qquad \text{Eqn. 2}$$

Here, l_c is now the coherence length of the detected light (after interference) and is equal to the resolution of the system. δz is the resolution and λ_0 is the central wavelength of the light source. This equation is true for all types of OCT. This equation does not include any optical properties of the OCT system such as the focussing lenses etc; the resolution is an explicit function of the light source. Thus, δz is referred to as the axial or depth resolution. The lateral resolution is determined by the optics of the system (as with a regular microscope) but the lenses also affect the depth of field of the focussed beam. This imposes a depth limit on the distance at which the detected signal intensity can be maintained.

From Figure 1-4, it can be seen that there arises a trade off between the transverse resolution and axial range, the higher the transverse resolution, the smaller the axial scanning range. Deciding which is best for a particular system depends on its application.

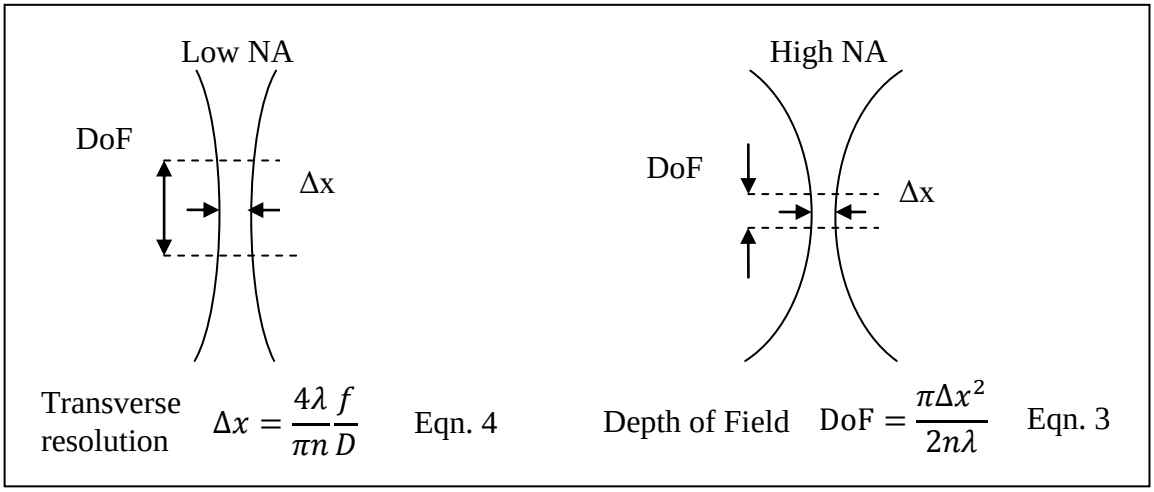

Figure 1-4: Comparison of a low numerical aperture (NA) verses a high NA.

The inverse relationship between the depth of field (DoF) and the transverse resolution (Δx) is shown[3]. f is the focal length and D is the diameter of the aperture of the focussing lens. *n* is the refractive index of the probed material.

Another important property of the light source is the central wavelength. The attenuation of electromagnetic radiation can be extremely variable depending on the molecular arrangement of the investigated medium. For example, light scattering from the tissue dominates the attenuation at the shorter wavelengths of the visible spectrum whereas longer wavelengths are more attenuated by absorption by the water in the tissue[14]. The greater the attenuation, the shorter the distance that light will penetrate into a sample before back scattered light can no longer be detected. This distance is known as the penetration depth.

As the red arrow in Figure 1-5 indicates, there is a natural absorbance low point at around 1000-1300nm where the melanin absorbance declines and the water absorbance starts to increase. The extension of OCT into these longer wavelengths in an attempt to gain penetration depth at the expense of resolution is a recent development, hindered by the relatively underdeveloped broad bandwidth laser technology at these wavelengths compared to light sources operating in the 800nm range. OCT instruments operating at 1050nm and 1300m show this enhanced penetration depth by acquiring signal from deeper parts of the retina that are not detected with 800nm OCT machines[15-18].

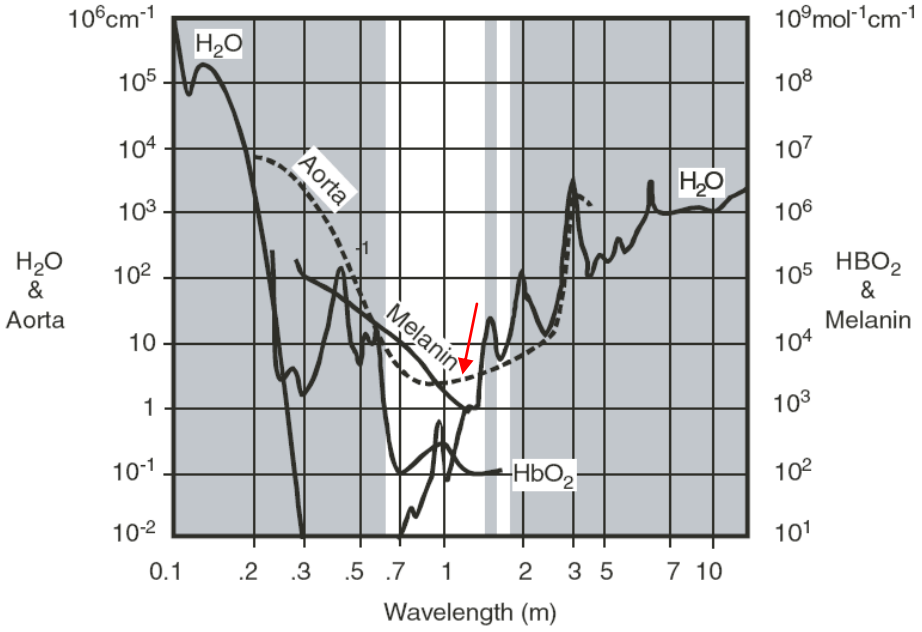

Figure 1-5: The relative absorbance properties of various tissue components as a function of wavelength.

HbO_2 and H_2O represent the absorption due to oxyhaemoglobin and water respectively. Adapted from *OCT:Technology and Applications,* Drexler and Fujimoto (2008)[3].

In terms of the specifications of TDOCT, there is a trade off between the speed of imaging and the SNR that can be obtained, i.e. the faster the sample is scanned, the smaller is the amount of light that can be collected. Around 70dB of signal is required to image weakly scattering biological tissue such as the retina[3]. Time domain OCT systems have been shown to exceed 100dB of SNR but the maximum speed at which they can operate is limited to around 2-4 B-scans per second purely due to the mechanical nature of the lateral and axial scanning aspects of the system[5,19].

The signal processing for TDOCT is relatively straight forward. A simple program loop (written in Matlab or Labview etc) controls the scanning of the reference mirror, records and saves the data and then sets the galvanometers to the next scanning point before repeating the process. The individual data points can then be constructed into an image as a single B-scan in the same program. Creating a volume scan with TDOCT is possible[10,20] but the acquisition time is generally far too long for any object that is not absolutely stationary. The acquired data can be 'post-processed'; a term describing any number of transformations performed on the data such as noise reduction or back ground subtraction. Post-processing helps to increase the quality of the obtained images but it can take some

time depending on the nature of the processing, for example Fourier based transformations are computationally intensive.

1.2 Theory of Time Domain Optical Coherence Tomography (TDOCT)

As well as obtaining a reflected signal, two other signals occur as a result of the properties of interferometry[3].These signals are always present and can degrade the quality of the system if they are not properly dealt with. These signals can be described mathematically by a combination of the spatial and temporal frequency of the light. To calculate these extra terms, the incoming light is described in terms of its wave number $k = \frac{2\pi}{\lambda}$ (spatial frequency), angular frequency $\omega = 2\pi v$ (temporal frequency) wave amplitude *s* (a function of k and ω) and wavefunction $e^{i(kz-\omega t)}$ where z is distance and t is time:

$$E_i = s(k,\omega)e^{i(kz-\omega t)} \qquad \text{Eqn. 5}$$

The subscript i (E_i) represents the incident power whereas the i in the exponential represents the square root of negative 1. Figure 1-6 shows the various equations for the incident and reflected beams.

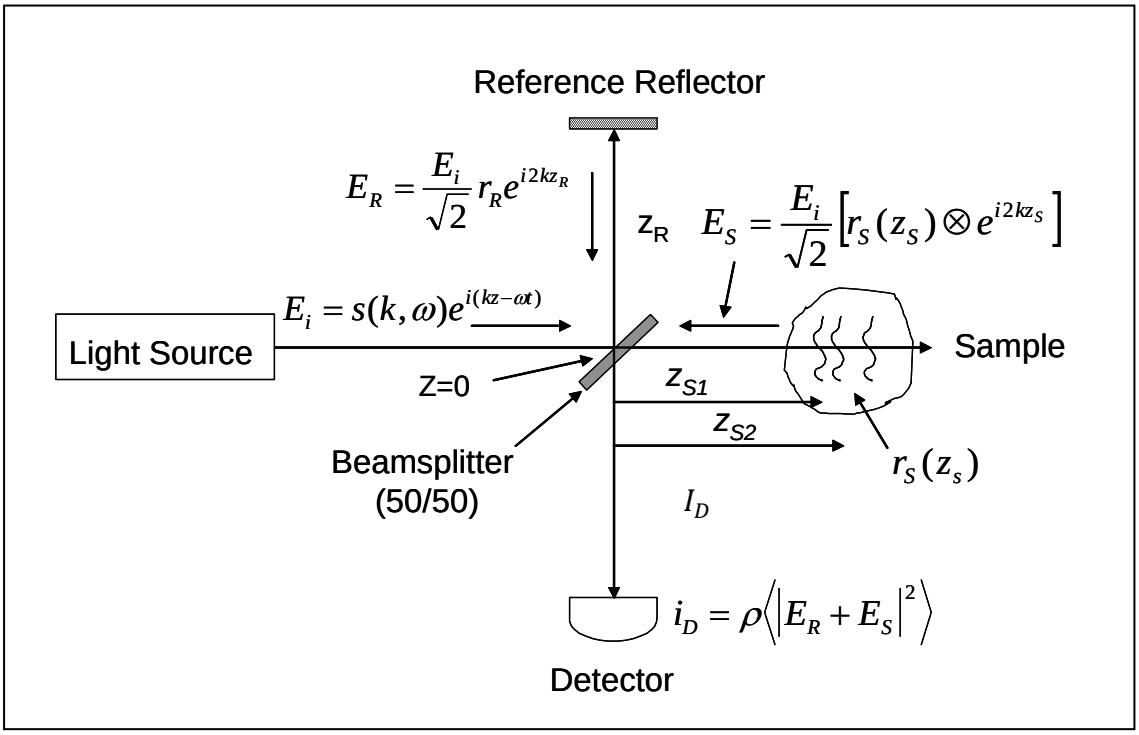

Figure 1-6: The beam path and energy division of a simple OCT system.
Adapted from *OCT:Technology and Applications*, Drexler and Fujimoto (2008)[3].

E_i is divided by the beam splitter into two beams each with an amplitude of $\frac{E_i}{\sqrt{2}}$ (the $\sqrt{2}$ denominator appears due to the square law of power division), some reflection constant r and the wavefunction e^{i2k} with the additional 2 in the power exponent coming from the round trip distance from the beam splitter and back. Ideally, the reference reflector should be a perfect mirror and have an r_R value as close to 1 as possible. The sample arm has a more complicated reflectivity function due to the multiple reflections occurring at different values of z_S. The electric field reflectivity profile is depth dependent resulting in the reflectivity variable being a function of the sample depth z_S. This function is as follows:

$$r_s(z_s) = \sum_{n=1}^{N} r_{Sn}\delta(z_S - z_{Sn}) \qquad \text{Eqn. 6}$$

The sum total of the delta functions results in r_{Sn} (the sample reflectivity) only when the depth z_S (the depth of interest) matches z_{Sn} (some depth in the sample). $r_s(z_s)$ encodes all the depth information about the sample and recovering it from the other information is the primary objective of OCT. In order to decode the reflectivity information $r_s(z_s)$, it is necessary to perform the convolution $\left[r_s(z_s) \otimes e^{i2kz_s}\right]$, multiplying the wave function by each reflection from the sample giving the returning electric field as $\mathrm{E_S} = \frac{\mathrm{E_i}}{\sqrt{2}} \sum_{\mathrm{n=1}}^{\mathrm{N}} \mathrm{r_{Sn}} \mathrm{e}^{\mathrm{i2kz_{Sn}}}$. The detected photocurrent ($I_D(k, w)$ – Figure 1-6) is expressed as a time averaged square law addition of the two returning electric fields, E_S and E_R. The square modulus of the two electric fields can be expressed via the multiplication of its complex conjugate by itself:

$$I_D(k, w) = \frac{\rho}{2}\langle |E_R + E_S|^2 \rangle = \frac{\rho}{2}\langle (E_R + E_S)(E_R + E_S)^* \rangle \qquad \text{Eqn. 7}$$

In Equation 7, ρ represents the response of the detector (based on its quantum efficiency) and the angled brackets indicate the time averaging performed by the detector (based on its set exposure time). Inserting the expressions for E_S and E_R and setting the spatial origin (z=0) at the surface of the beam splitter an equation for the detector current is obtained:

$$I_D(k,w) = \frac{\rho}{2}\left\langle \left| \frac{s(k,\omega)}{\sqrt{2}} r_R e^{i(2kz_R - \omega t)} + \frac{s(k,\omega)}{\sqrt{2}} \sum_{n=1}^{N} r_{Sn} e^{i(2kz_{Sn} - \omega t)} \right|^2 \right\rangle \quad \text{Eqn. 8}$$

Expanding the modulus function eliminates the temporal frequency terms ω in the exponentials. This is useful as the wavelengths that OCT operates at, typically 800-1300nm (3.75×10^{14}Hz – 2.31×10^{14}Hz), oscillate far quicker than the response time of any practical detector. Simplifying the exponential terms with Euler's rule leaves the temporally invariant terms:

$$I_D(k,w) = \frac{\rho}{4}[S(k).(R_R + R_{S1} + R_{S2} + \cdots)] \quad \boxed{\text{A}}$$

$$+ \frac{\rho}{2}\left[S(k). \sum_{n=1}^{N} \sqrt{R_R R_{Sn}}(\cos[zk2(z_R - z_{Sn})])\right] \quad \boxed{\text{B}}$$

$$+ \frac{\rho}{2}\left[S(k). \sum_{n \neq m=1}^{N} \sqrt{R_{Sn} R_{Sm}}(\cos[zk2(z_{Sn} - z_{Sm})])\right] \quad \boxed{\text{C}}$$

Eqn. 9

In Equation 9, z_{Sm} is the axial position of another sample reflection with reflectivity R_{Sm}, at a different depth z_{Sn}. The equation for the detector current now has three main components:

A. DC term – A constant current offset proportional to the reflectivity of the reference mirror plus the sum of sample reflectivities. This term does not depend on the distance to either the sample or the reference mirror. The reflected light from the reference arm will dominate this term if the sample reflectivity is low. Typically, the reference arm is attenuated with a neutral density filter to avoid saturating the detection instrument (e.g. CCD camera).

B. Cross correlation – This is the most important term for OCT. It describes the position of the sample reflectivities with respect to the reference mirror for the optical path difference of $(z_R - z_{Sn})$.

C. Auto correlation – This component of the signal describes the interference between axially separated reflectors within the sample $(z_{Sn} - z_{Sm})$. This term creates

artefacts in the image that can be reduced by correct selection of the reference reflectivity.

Plotting this function for a single sample reflector (R_{S1}) with a reflectivity of 0.1 at position z_{S1} gives an impression of the type of results seen with TDOCT.

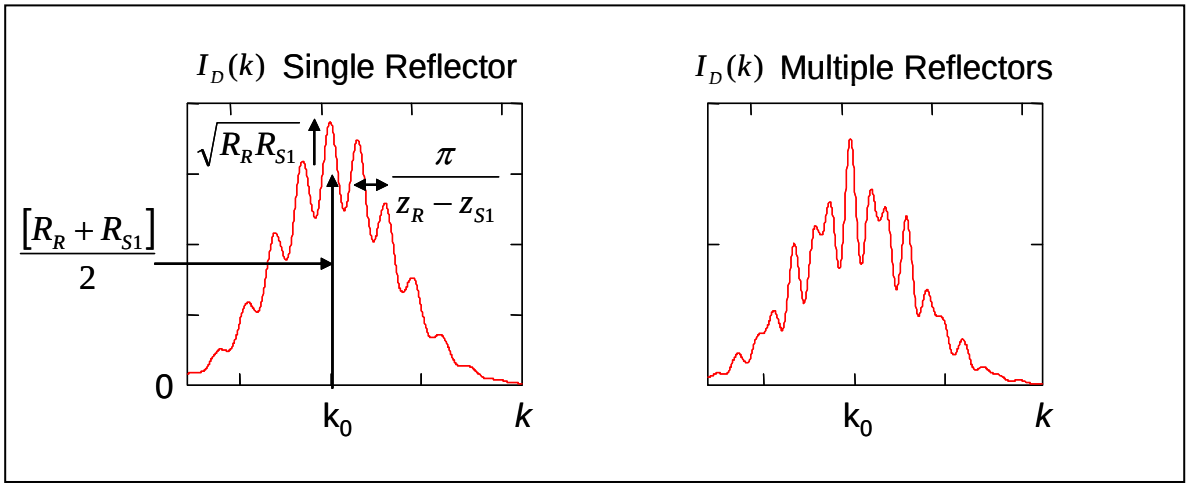

Figure 1-7: The spectral correlation interferogram for single and multiple reflectors. Auto-correlations terms are introduced into multiple reflector interferogram due to interference between multiple sample boundaries. Adapted from *OCT:Technology and Applications*, Drexler and Fujimoto (2008)[3].

The oscillations in the wave number spectrum (Figure 1-7) reveal the position of the reflecting surface by their periodicity $\frac{\pi}{z_R - z_{S1}}$ and the reflectivity of the sample by their amplitude $\sqrt{R_R R_{S1}}$. The oscillations appear on top of the DC offset $\frac{[R_R + R_{S1}]}{2}$. Multiple sample reflectors appear as a superposition of multiple oscillations, each with a different amplitude and modulation periodicity depending on their reflectivity and position in the sample, respectively (Figure 1-7). In addition to these terms, auto correlation terms will appear, typically with a modulation frequency higher than those of the cross correlation terms due to the small distance between reflectors in the sample ($z_{Sn} - z_{Sm}$) compared to the distance between the sample and the reference reflector ($z_R - z_{Sn}$).

1.3 Fourier Domain Optical Coherence Tomography (FDOCT)

The concept of Fourier domain OCT (FDOCT) was outlined by Fercher in 1995[21]. In the literature, OCT that encodes depth information in frequency rather than in time has

multiple pseudonyms such as FDOCT, Spectral OCT, optical frequency domain imaging etc. For this thesis, this technique will be known as FDOCT. FDOCT has the same optical set up as TDOCT but utilises a broad bandwidth light source and a stationary reference reflector to encode the depth information in spectral frequency rather than in time. As described above, the interferometric principle used in TDOCT gives a maximum signal when the path length of the reference reflector and the sample reflector are the same. This is true for any single wavelength where the distance from the beam splitter to the sample reflector is the same as the reference path length plus any multiple of the wavelength over two (the optical path difference is not equal to zero but the beams remain in phase at the detector). If a different wavelength is now used, it would not be detected as a maximum as the extra distance the sample beam must take is no longer a multiple of its wavelength and the interfering beams at the beam splitter are no longer in phase. If this is performed with many wavelengths and a suitable detector, the result is an oscillating frequency spectrum that has the depth position of the sample encoded in it. The different reflector in the sample will create a waveform with a different periodicity overlaid on each other; the greater the optical path difference between the two arms of the spectrometer, the greater the periodicity. The depth information can be extracted from the waveform by applying a Fourier transform, separating the components of the waveform into discrete amplitudes representing the axial reflectivity profile of the sample[21,22].

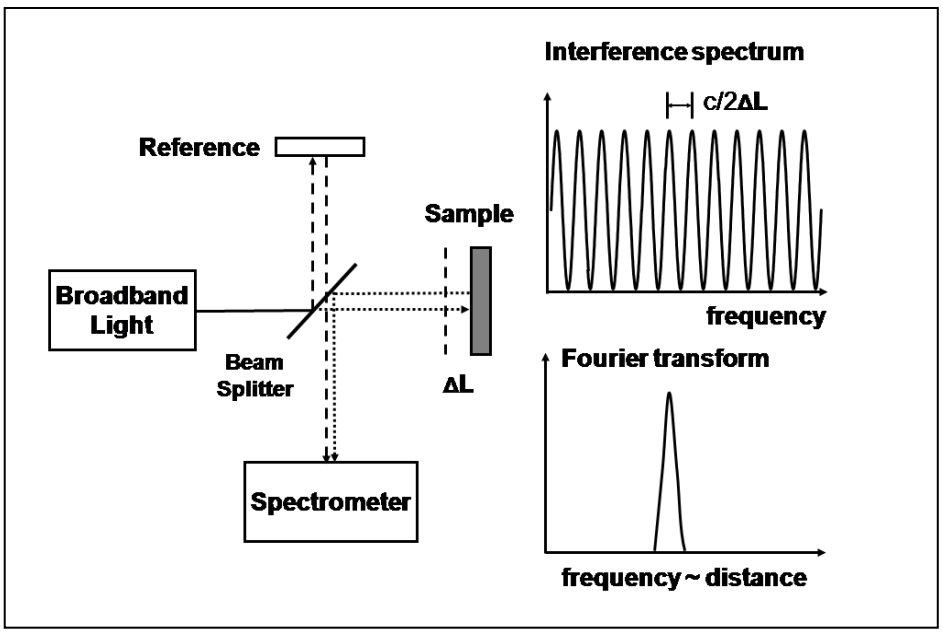

Figure 1-8: Schematic of an FDOCT design.

The spacing of the oscillations in the interference spectrum is inversely proportional to the distance of the sample reflector from the zero delay. Adapted from *OCT:Technology and Applications*, Drexler and Fujimoto (2008)[3]

The standard pinhole detector used in TDOCT is replaced with a spectrometer in FDOCT. This consists of a grating to disperse the broadband light and a line scan camera to read each frequency component. A major advantage of FDOCT over TDOCT is that there is no longer any need to move the reference mirror. This results in a dramatic B-scan speed increase of ~50 times and the ability to produce video rate *in vivo* 2D images[2,5,23,24]. Also, the light sources used need not necessarily be different from TDOCT - the resolution of the system is still determined by the bandwidth of the source as per Equation 2. Generally, ultra short pulse lasers are used as they can provide the power and bandwidth necessary to achieve OCT images approaching 1μm resolution. Despite the increase in speed reducing the integration time of the camera, a signal to noise ratio of >90dB can still be achieved due to the use of a high power laser light source[25,26].

Although the increased speed of FDOCT systems when compared to TDOCT systems has made them a viable option for clinical imaging, FDOCT has several distinct disadvantages that do not hamper TDOCT. The major disadvantages are the presence of mirror terms in the FDOCT images, sensitivity decline with image depth and limited depth of focus. The mirror images appear due to an ambiguity in which side of the zero delay the sample appears on relative to the reference arm. The Fourier domain signal from a sample located at z appears identical to a signal originating from -z (where z is some arbitrary depth). The result of this is a mirrored version of the sample data in the image, potential obscuring non-mirror data. There are solutions to eliminate the mirror terms, however these typically involve complex optical pathways or additional image processing[27-29]. The second major disadvantage to FDOCT is the sensitivity decay caused by the limited sampling of the Fourier domain signal and the finite coherence length of the light source (described in detail in section 5.6.1). The decay in sensitivity limits the useable depth range of the FDOCT instrument and any FDOCT instrument must be carefully designed in order to limit the rate of sensitivity decay[26]. The third major disadvantage to FDOCT is the limited depth of focus. As all the data from an A-line is collected in a single spectral image, each point within the depth profile of the sample must remain in focus during the image acquisition. To maintain this illumination, the NA of the objective lenses must be kept low (Equation 4, Figure 1-4), resulting in a limited transverse resolution of the system. A TDOCT system does not suffer this drawback as the sample stage can be moved axially

through the depth of focus of a very high NA objective (or dynamic focussing can be employed), giving superior lateral resolution compared to an FDOCT system[30,31].

Other drawbacks with FDOCT compared to TDOCT include the image post processing times. Whereas TDOCT data needs only to be aligned to create a 2D image, FDOCT data must first be Fourier transformed. As performing Fourier transforms is a processor intensive tasks for a computer, it can take some time to display an image. FDOCT has benefited greatly from the rapid increase in computer performance over the last ten years. With current technology it is possible to process a 512x512x1024 pixel image in a few minutes using a standard desktop computer. Moving the processing onto a graphics processing unit (on a graphics card) can improve the processing rate significantly due to the number of processors located on the card, making near video rate 3D imaging a reality[32]. The dispersion effects of the optics in the system also degrade the FDOCT image. As each frequency in the broadband spectrum contributes to rebuilding the time domain data, if the spectral power is skewed by dispersion, the encoded data will be skewed accordingly. This problem can be compensated for with achromatic lenses and mirrors but, as the bandwidths of the lasers become larger, in order to obtain better resolution, dispersion becomes a major problem.

Although the reference mirror no longer needs to be moved, the focal point of the sample beam must still be raster scanned, limiting the absolute imaging speed. However, the amount of optical power that can be safely put into the eye, limits the shortest possible frame acquisition time, capping the maximum possible acquisition speed and sensitivity.

1.4 Theory of Fourier Domain Optical Coherence Tomography

The mathematics of FDOCT is understandably quite similar to Equation 9 for TDOCT. The only extra factors in the equation come from the Fourier transform properties of the cosinusoidal components namely, $\frac{1}{2}[\delta(z+z_0)+\delta(z-z_0)] \overset{F}{\leftrightarrow} \cos kz_0$ and convolution transforms $x(z) \otimes y(z) \overset{F}{\leftrightarrow} X(k)Y(k)$. Equation 9 may now be written as:

$$I_D(z) = \frac{\rho}{4}[\gamma(z).(R_R + R_{S1} + R_{S2} + \cdots)] + \frac{\rho}{4}\left[\gamma(z) \otimes \sum_{n=1}^{N} \sqrt{R_R R_{Sn}}(\delta(z \pm 2(z_R - z_{Sn})))\right] + \frac{\rho}{4}\left[\gamma(z) \otimes \sum_{n \neq m=1}^{N} \sqrt{R_{Sn} R_{Sm}}(\delta(z \pm 2(z_{Sn} - z_{Sm})))\right] \quad \text{Eqn. 10}$$

The power spectral density $S(k)$ from the TDOCT Equation 9 has been replaced by the corresponding real space coherence function $\gamma(z)$. The two functions Fourier transform pairs. The full width half maximum (FWHM) of the coherence function equalling the coherence length, l_c, of the light source. Three terms representing the DC, cross correlation and auto correlation components appear with the cross correlation term containing the important reflectivity profile $\sqrt{R_S(z_S)}$. Although access to this term is hampered by the convolution operator, carrying out the convolution is straight forward thanks to the shifting properties of the delta functions giving:

$$I_D(z) = \frac{\rho}{4}[\gamma(z).(R_R + R_{S1} + R_{S2} + \cdots)] + \frac{\rho}{4}\sum_{n=1}^{N} \sqrt{R_R R_{Sn}}\left[\gamma[2(z_R - z_{Sn})] + \gamma[-2(z_R - z_{Sn})]\right] + \frac{\rho}{4}\sum_{n \neq m=1}^{N} \sqrt{R_{Sn} R_{Sm}}\left[\gamma[2(z_{Sn} - z_{Sm})] + \gamma[-2(z_{Sn} - z_{Sm})]\right] \quad \text{Eqn. 11}$$

Both the cross and the auto correlation terms thus have a positive and a negative component (arising from the result of the Fourier transform). Each component appears either side of the zero delay (position z_R) with identical magnitude. The negative term is usually referred to as the complex conjugate artefact and can be completely ignored as long as the two terms do not overlap. Other unwanted properties of Equation 11 include the DC term, which can be compensated for in post-processing, by Fourier transforming the data and removing the bottom lines of the image closest to the zero delay. The $\sqrt{R_R}$ term in the cross correlation term will be larger than $\sqrt{R_{Sn}}$ and acts as a linear multiplication of the sample reflectivity. The autocorrelation terms manifest themselves in

the same way as Equation 5 and, hence, the best way to reduce them is to choose the correct reference reflectivity. As with Figure 1-7, the typical image of a sample using FDOCT is shown below, calculated from Equation 11 using two arbitrary sample reflections z_{S1} and z_{S2}.

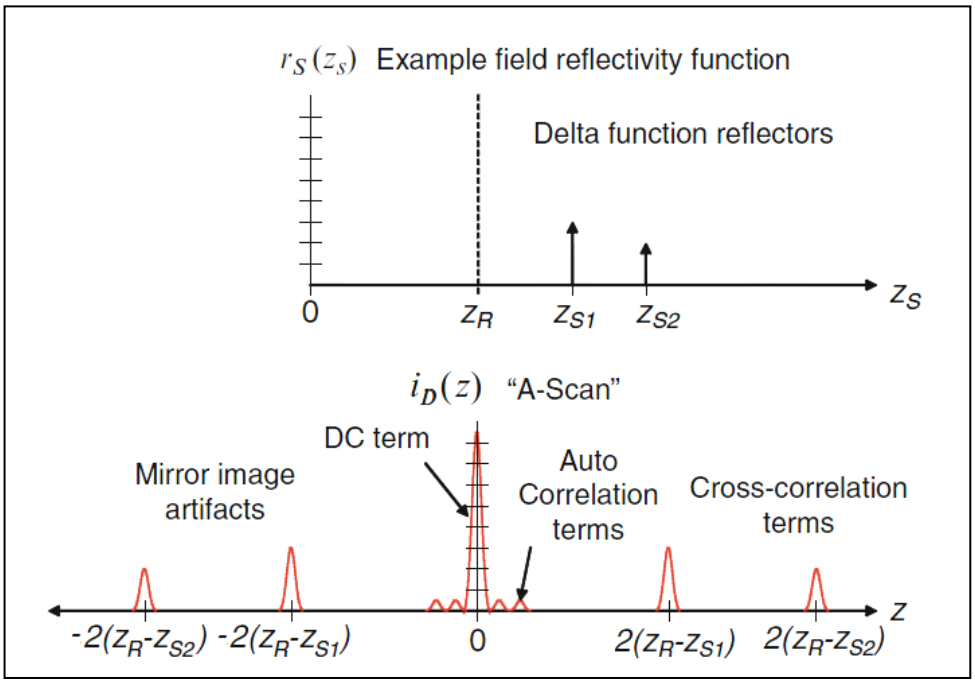

Figure 1-9: Signal from an FDOCT instrument.

Top: The reflectivity function for two delta functions z_{S1} and z_{S2} with the second having a slightly lower amplitude due to the attenuation of the light through the sample. Bottom: The observed outcomes of the Fourier transform. Adapted from *OCT:Technology and Applications*, Drexler and Fujimoto (2008)[3].

As Figure 1-9 shows, each sample reflectivity is offset according to their depth on both sides of the DC constant term. The auto correlation terms and complex conjugate terms can be identified as long as the cross correlation terms remain significantly far from the DC term. The broadening of each of the cross correlation terms is a result of the convolution of the sample delta reflection function with the Gaussian-shaped coherence function of light source $\gamma(z)$. As the FWHM of the $\gamma(z)$ function is the coherence length, l_c, of the light source, each cross correlation term is approximately broadened by this value.

1.5 Swept Source Optical Coherence Tomography (SSOCT)

Swept source OCT (SSOCT) is a variation on the FDOCT design. Whereas FDOCT uses a broadband width light source and a spectrometer, SSOCT uses a narrow bandwidth light source that is frequency swept in time and a standard photo detector[6,16,33-35]. Frequency sweeping is a technique for progressively selecting single frequencies from a spectrum in a specified time. In SSOCT, as the light source is swept, the interference signal is recorded at each optical frequency. Much like FDOCT, each optical frequency will return to the detector with varying power depending on the interference between the reflectivity profile of the sample and the fixed reference mirror. The recorded intensity from each optical frequency encodes the depth information as a function of the sweep time of the light source. The physical depth location can then be determined through the inverse Fourier transform of this function[33].

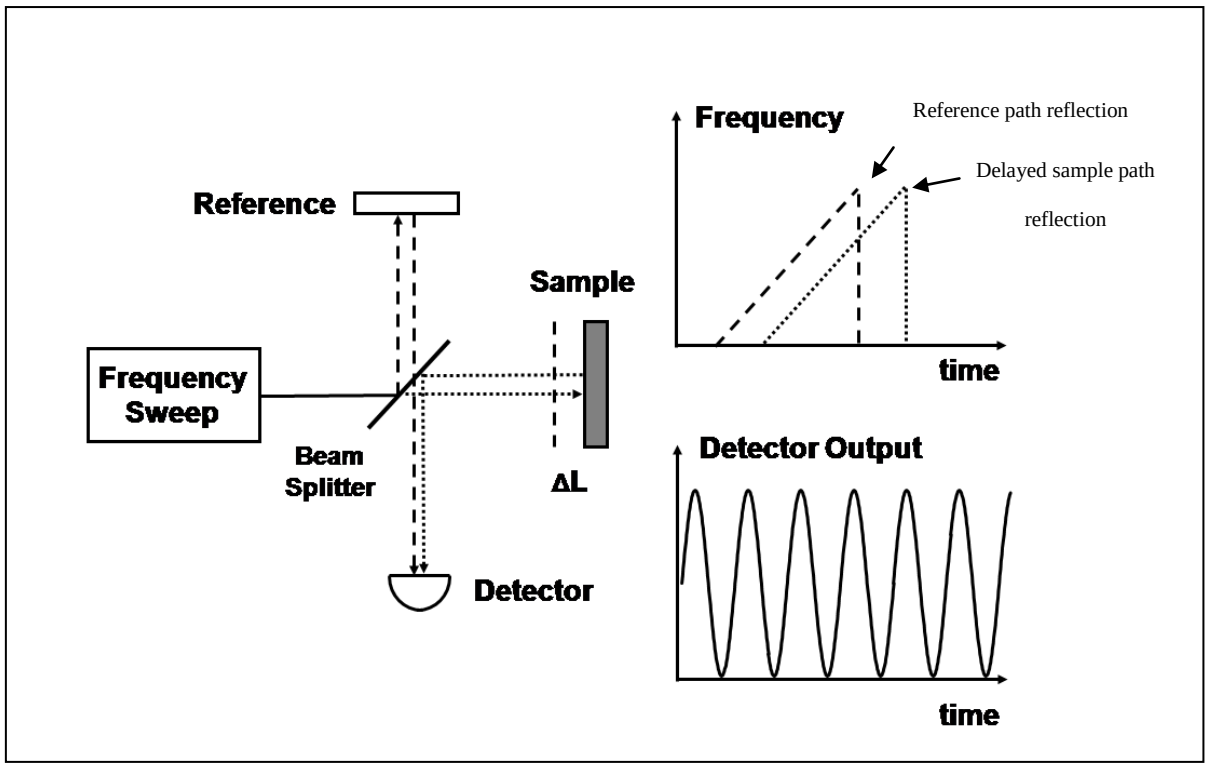

Figure 1-10: Schematic of a Swept Source OCT design.

The time (and hence phase) delay between the reference beam and the delayed $(2\Delta l)$ sample beam creates an oscillating beat frequency at the detector. Adapted from *OCT:Technology and Applications*, Drexler and Fujimoto (2008)[3].

Figure 1-10 shows a basic SSOCT system with the two spectra (from the sample and reference arms) separated by an arbitrary amount of time. The detector output shows how the signal oscillates as a function of the sweep time of the light source. The frequency sweeping aspect of the light source is usually a method of selecting a specific frequency from a spectrum rather than generating only one specific frequency at a time. This can be done in a number of ways, e.g., by employing an acousto-optic filter in the beam path, where the physical oscillation of the crystal creates a diffraction grating effect allowing only a specific narrow wavelength range (termed linewidth) to pass.

This method can select a single frequency very accurately and also enables sweeping through the spectrum at a very precise rate, either set beforehand or triggered by a computer. Another method is to use a rotating multisided mirror that reflects the light from a diffraction grating, progressively illuminating the sample. This system can achieve a higher sweep speed then using an acousto-optic filter, however it is more difficult to control the speed of the sweep accurately when using triggered sweep steps. SSOCT has been shown to achieve comparable SNR to FDOCT[34-37] and faster acquisition speeds[7-9,37-40].

SSOCT is still restricted in comparison to TDOCT by the same disadvantages described in section 1.3 namely, the mirror terms, sensitivity decay and limited depth of focus. Similar techniques used in FDOCT can be used for SSOCT to combat some of these limitations[27,28].

1.6 Full Field Swept Source Optical Coherence Tomography (FFSSOCT)

In terms of resolution performance, FDOCT and SSOCT can achieve similar results[41]. SSOCT does several advantages over FDOCT. As SSOCT only records one frequency at a time, there is no need for spectrometer based detection and a single photo detector can be used. SSOCT can, therefore, adopt a full field approach to imaging, whereby the entire imaging area is illuminated and captured at the same time on a 2D CCD camera. This eliminates the need for the lateral scanning components required for volumetric FDOCT imaging.

Although full field OCT imaging has been well established, it has previously been performed only in the time domain[11,12,20], hence Full Field SSOCT (FFSSOCT) was a completely novel way of performing OCT when it was first performed by the Drexler group. FFSSOCT has no moving components and in terms of speed, is limited only by the electrical technology of the system rather than the inherently slower mechanical scanners. This, however, has only become possible in recent years, as computer and camera technologies have progressed extremely rapidly. The frequency sweeping speed is now no longer as restrictive to FFSSOCT as to SSOCT; sufficient information can now be obtained in a single sweep to construct an entire 3D tomogram.

Another advantage of FFSSOCT is that there is no positional ambiguity between each lateral pixel on a single image as they are all acquired at the same time. The ambiguity in FFSSOCT can appear during the acquisition when small movements in the sample cause intensity changes in the interference pattern and is dubbed 'phase-washout'. It is possible to correct this if the phase of the detected signal is known whereas correcting the lateral position discrepancies in FDOCT pixel alignment can be more difficult.

By using a full field approach as opposed to a scanning spot, the power surface density on the sample for each frequency is a lot lower than in FDOCT. However, as each point on the sample is illuminated at all times during the volume acquisition, the total power can be substantially more than FDOCT. This leads to a direct increase in the sensitivity of the system, particularly when the laser power is increased. There is a power limit in the imaging of biological tissue since there is a point at which it can no longer dissipate enough heat and becomes damaged by the laser light. The focussed beam used in FDOCT systems will damage sensitive tissue, such as the retina, at 2mW of 800nm optical power (at the cornea)[42]. The dissipated beam used in a FFSSOCT system can be at least an order of magnitude higher before tissue damage becomes a concern. There is an additional aspect that should be considered when increasing the power in this diffuse way, the tissue will not be able to dissipate the heat as easily, as each neighbouring cell will be heated as well[17].

The main disadvantages to using FFSSOCT are the same as SSOCT and FDOCT namely the presence of mirror terms, sensitivity decay and limited depth of focus as described in

section 1.3. In addition to these, there are several other limiting factors affecting the potential performance of the technique.

The main drawback to extending the illumination to full field is the large increase in background noise due to interference of the light between pixels. Reflected light from within the sample may be scattered by the sample medium and interfere with light reflected from a different location. This interference results in a speckle-like appearance on the interference image that is termed 'crosstalk'. Crosstalk and phase washout are the two main causes of noise in FFSSOCT and currently limit the applications of the system[43]. The mathematics and results from the acquired data are the same as for FDOCT. The depth scan for each pixel is calculated using a Fourier transform and the result would be identical to Figure 1-9.

A slight disadvantage of recording the data in a full field approach is that there is now no difference in acquisition time between completing a B-scan and completing a C scan as the entire image area is captured. Therefore, the real time 2D depth view of FFSSOCT can only be as quick as FDOCT if the CCD camera is replaced by a much faster linescan camera. Despite FFSSOCT being relatively new compared to FDOCT, early designs have shown that it is capable of volumetric imaging at speeds beyond that of FDOCT whilst retaining the sensitivity advantage that Fourier domain imaging has over conventional TDOCT.

Since commencing the research of the thesis, working FFSSOCT systems have been created by a number of different University groups, most notably that of Prof. Dr. Geroen Huttmann (Institute for Biomedical Optics, University of Lubeck, Germany). His group have developed a system capable of *in vivo* images of the retina[23]. Other groups have developed systems capable of imaging highly reflecting surfaces such as microchips[44,45].

1.7 Comparison of the different types of OCT

Table 1-1 shows a comparison of the properties of the different types of OCT. There are a number of variations of FDOCT and SSOCT but the values shown for the SNR and the acquisition speed represent the maximum that each system can achieve[46].

Type	Axial Resolution	SNR (dB)	Acquisition speed of a 500x500x500 pixel volume (ms)
Time domain OCT	Bandwidth dependent	>100	~2500
Fourier domain OCT	Bandwidth dependent	90-100	~830
Swept Source OCT	Sweep range dependent	>100	~50

Table 1-1: A comparison of the different types of OCT operating at a central wavelength of ~800nm.

Adapted from *Optical Coherence Tomography*, Podoleanu (2012)[46].

For full FFSSOCT to succeed, it must be able to compete with the current generation of systems. Although FFSSOCT will never be able to reach the 2D acquisition speeds of these systems, it should be able to capture 3D datasets at a faster rate than even FDOCT due to its non-reliance on mechanical scanning.

1.8 Advantages and disadvantages of OCT compared to other multi-dimensional imaging techniques

A number of other techniques exist that can also create either 2D depth scans or 3D tomograms of tissue. Each has advantages over the others and each has a specific area in which they are the most useful. The most common ones found in a medical environment are ultrasonography, magnetic resonance imaging (MRI) and confocal microscopy. There are other, more recent, techniques that have not been established in a clinical environment such as digital holography[47]. Other imaging techniques such positron-emission tomography (PET) and fluorescence microscopy are more invasive as they involve some pre-treatment of the sample before imaging.

When comparing the different imaging techniques, there is an apparent trade-off between resolution and imaging depth. The acoustic pulses used in ultrasonography (around 20MHz in the clinical application) have low attenuation in tissue hence large imaging depths can be achieved. However, the resolution is limited to several hundred micrometers[48]. It is possible to increase the resolution to 15-20μm by using higher frequency pulses (100MHz) but the attenuation in tissue increases sharply with higher

frequency pulses and imaging is limited to a few millimetres[3]. Like OCT, ultrasonography is quick and cheap to operate and is widely used in clinical applications that involve imaging of larger objects, such as a foetus in the womb.

MRI can also penetrate much further than OCT into biological media and has the facility for the generation of 3D images[49]. The trade-off is again the resolution; current MRI instruments achieve an axial resolution of approximately 1mm[50]. Although this is several orders of magnitude worse than OCT, MRI instruments a better axial range to resolution ratio, ~10,000 compared to ~5,000 for OCT. MRI machines are also at a disadvantage in terms of their cost and size, they are extremely large, very expensive to purchase and require dedicated rooms and trained personnel to operate. The main clinical use of MRI lies in brain imaging where other techniques are not possible.

Confocal microscopy sacrifices the imaging depth of ultrasonography and MRI in order to greatly increase the resolving power. Extremely high resolution images can be achieved, less than 1µm[51], approaching the resolution limit of what is possible with visible light. While this resolution is beyond that achievable by OCT, the axial range is limited to only a few hundred microns and, therefore, has limited clinical use[52].

Due to the completely non-invasive nature of *in vivo* OCT, it has proved to be a very useful tool in the field of optometry and ophthalmology. Although the penetration depth is limited, it is enough to visualise the retina and subsequent deeper layers of the eye. The high imaging resolution of OCT allows unprecedented levels of detail to be observed aiding diagnosis and early detection of the onset of retinal diseases[15,25,53-56].

A comparative example of what is achievable with OCT, confocal microscopy, ultrasound imaging and MRI is shown in Figure 1-11.

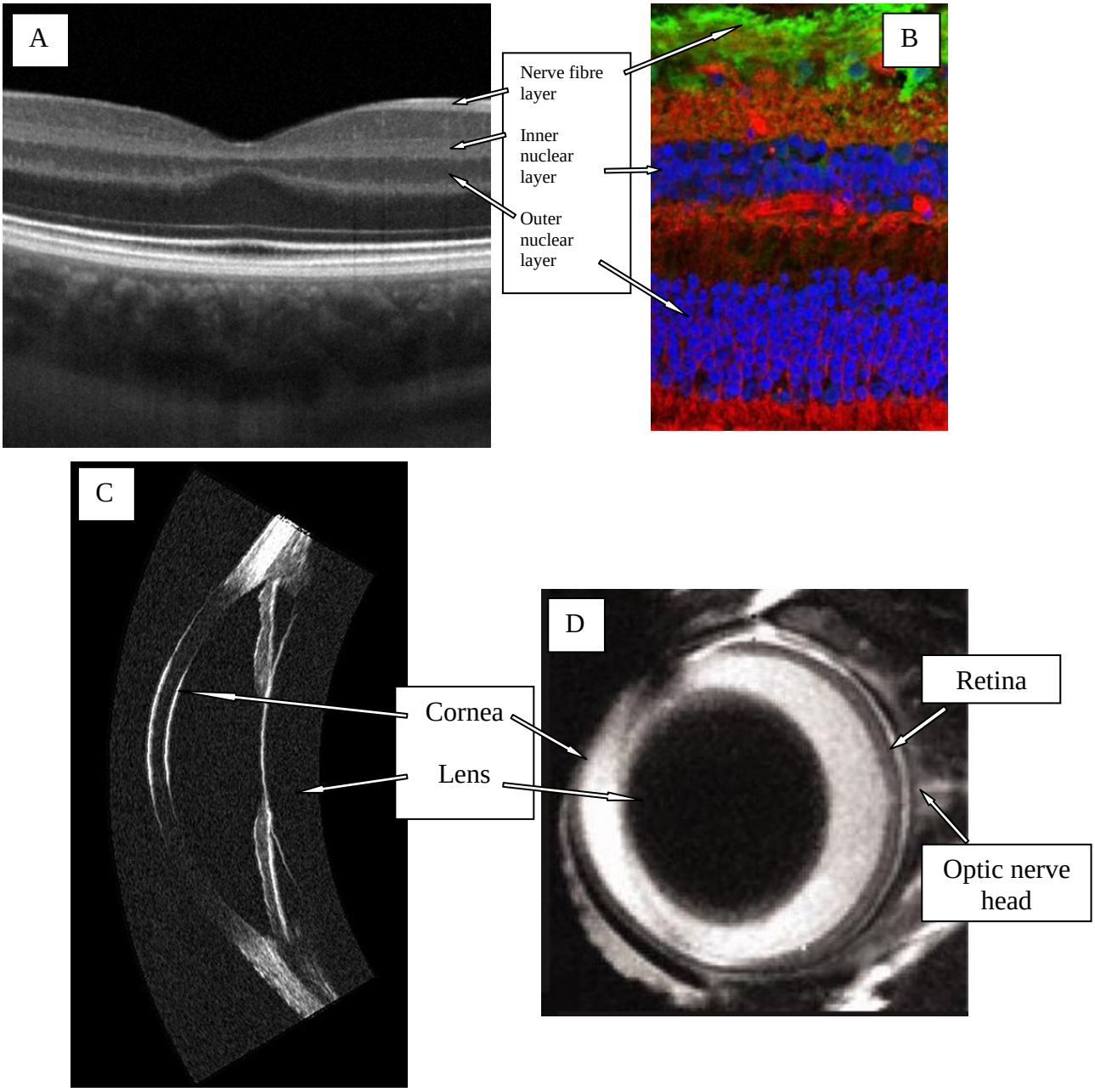

Figure 1-11: Different techniques for ocular imaging.

A comparison of the image quality obtainable with different 3D imaging techniques; (A) 850nm OCT image (3x1mm) of the human retina taken with the Copernicus SD OCT HR (Optopol Technology S.A., Zawiercie, Poland). Adapted from Alonso-Caneiro et al (2011)[58]. (B) Triple stained fluorescent confocal image (150x220µm) of the human retina taken with the E800 (Nikon, Tokyo, Japan). Adapted from Tan, P.E. et al (2012)[51]. (C) 35MHz ultrasound biomicroscopy (UBM) image (60º arc, 6.8mm depth) of human cornea taken with a prototype instrument (Cornell Universtiy, New York, USA). Adapted from Silverman, R.H. (2009)[48]. (D) MRI image of a mouse eye (5x5mm) imaged by a Bruker instrument (Bruker, Billerica, Massachusetts, USA). Adapted from Nuir, E.R et al (2011)[49].

1.9 Aim of the research

The purpose of this research was to improve upon an available initial design for an FFSSOCT imaging device with the intent of discovering if FFSSOCT could be a viable alternative to existing OCT modalities in a clinical environment. The main benefit of using the FFSS approach to OCT is the potential to increase the optical power that can be delivered without incurring retinal damage. The limiting factor in improving the sensitivity of FDCOT systems is the limit to the optical power that can be used. A diffuse full field light distribution allows more optical power to be distributed on the retina leading to an increase in sensitivity. Further benefits include the potential elimination of lateral stack alignment, due to parallel acquisition, and the simple, relatively inexpensive design since no scanning elements is required.

Chapter Two: Creating an FFSSOCT system

2.1 Operational Logistics

To achieve the goal of assessing the viability of FFSSOCT as a potential competitor to established OCT systems, it was necessary to improve both the existing hardware and software. The existing design[57] had achieved modest sensitivity levels using relatively long acquisition times, proving the FFSS approach had the ability to acquire images but not in a comparative way to existing contemporary FDOCT systems[25]. The first step in the research project was to rebuild the existing prototype, allowing the author to familiarise himself with the operating principles of OCT, including the hardware interface and the software, with the aim of generating 3D tomographic images with comparable quality to those produced by the original FFSSOCT design. The process of rebuilding the instrument is described in this Chapter.

2.2 Labview programming language

2.2.1 Justification for Labview

As the FFSS approach to performing OCT was novel, the all required software to capture and process the interferometric data had to be created. The majority of the initial work on the project was to design and write software that would control the major hardware elements i.e. the frequency generator and the camera. Following this, software was developed to process the acquired data in real time in order to provide a continual B-scan view of the sample. Separate software was then created to process the saved interferometric data into stacks of 2D B-scans that could be viewed and analysed. With the capture and processing software written, additional software was then written to perform various analysis functions such as data averaging, phase analysis, resampling, dispersion compensation and more.

Labview (National Instruments Corporation, Texas, USA) was chosen as the main programming language for the project due to its inherent advantages in interfacing with hardware. Labview was designed by the same company as the frame grabber card used in the FFSSOCT design which meant that interfacing with the camera would be straight forward. The other programming language that could have potentially been used was MATLAB. This language benefits from a larger user base than for Labview and has

existed for longer, meaning there would be an inherently greater number of functions and solutions available. However, Labview offered several major advantages over Matlab; as mentioned, hardware interfacing is significantly easier due to its pre-installed device drivers and connection to the framegrabber. In Labview, it is easier to visualise data in real time due to its split window design. This allows the user to make changes to the sample alignment (for example) without the need to stop and rerun the program. Labview could also make use of the quad core CPU of the Lenovo Thinkstation used for the FFSSOCT system whereas version of MATLAB available at the time could not. Also, the 64 bit version of Windows Vista that was used was not fully supported by MATLAB at the time; some of the toolboxes were not compatible with the latest operating system.

As prototype design had been shown to work[57], software did exist to control the instrument; however, as the decision was made to switch the Biomedical Imaging Group to using Labview and as I was unfamiliar with MATLAB at the time, the code was never used. As a result, writing the control code in Labview allowed the author to become familiar with the programming language and enabled him to build the complex analysis programs needed to evaluate the FFSSOCT data output.

2.2.2 Labview format

Labview programs are called VIs (Virtual Instruments) and are separated into two windows on the computer desktop. The first window shows a graphical programming view, where individual programming components, such as functions and arrays, are joined together by virtual wires. Wires can then be branched, sending data to multiple functions or subroutines (called subVIs). The logical flow of the language is determined on whether the current element has required data to run; if so, it will perform its operation. This creates a possible problem with ‘rat race’ scenarios whereby a function may run before or after data has passed though another parallel function resulting in output that maybe different each time the program is run. This can be avoided by running error lines between functions, thereby forcing the order of logical flow. The second window is the user interface (UI) window and allows the user to interact with the program while it is running e.g. change the value of a variable or view the images coming from the camera.

2.3 Extending Swept Source OCT to Full Field Swept Source OCT

The initial design was similar to a traditional scanning SSOCT system, comprising a scanning light source, interferometer and optical detection device. A typical scanning swept source design will comprise of an optical light source that emits a series of narrow linewidth optical frequencies evenly distributed in time[6,16,37]. The emitted light is split into two identical beams, each with a proportion of the original optical power determined by the splitting ratio of the optical beam splitter (typically 90/10 or 80/20). One beam, termed the sample beam, is shaped to fit its purpose by multiple transfer optics; typically focussed for an ex vivo sample or collimated for an eye (where the focussing is achieved by the optics of the eye). Scanning SSOCT systems use galvanometers in the sample arm to scan the light over the sample, building up an image point by point. Being a full field system, there is no need for galvanometers or the transform optics, thereby reducing the complexity and cost of the design. The second beam from the beam splitter, termed the reference beam, is sent to a retro-reflector, returning an identical wavefront to that sent, typically mounted on a translation stage that enables the optical path of the reference arm to be lengthened or shortened. The recombined beam is imaged by a photomultiplier tube and the spectral interferogram containing the depth information of the sample structure is built up by 'sweeping' through the available optical frequencies from the light source.

To achieve full field illumination and hence, achieve FFSSOCT, the above design must be modified in several ways. Whereas the SS approach uses optical fibres to transport the optical signal between the elements of the instrument, the FFSSOCT interferometer is entirely free space as the lateral sample information cannot be transmitted through a fibre. The optomechanical scanning mirrors are removed as the beam is no longer scanned over the sample and the single pixel photodiode detector is replaced by a 2D CCD/CMOS camera to acquire the lateral sample information concurrently.

2.4 Original hardware

The design was housed in a modified microscope body (Axioskop2 MOT plus, Zeiss, Oberkochen, Germany) in order to provide both a rigid platform for the optics, a simple way to manipulate the sample focus and position via the microscope translation stage, and a viewing position via the microscope eyepiece. To perform OCT, a beamsplitter (50:50

splitting ratio) and a reference arm were added to the main body of the microscope by custom made aluminium pieces. The top illumination arm of the microscope was modified to allow extra aluminium pieces to be added in order to mount the light source fibre output and collimating optics. The lower illumination path remained unchanged to allow traditional underside illumination for viewing of the sample through the eyepiece. Optically dense samples were illuminated from above via a flexible LED light with magnetic base to improve stability.

The modified microscope was placed on a small section of optical bench (Thorlabs inc, New Jersey, USA) which in turn was set on top of a vibration dampening unit. The light source and its associated electronic controllers were situated on overhanging shelves attached to structural framework surrounding a Thorlabs (Thorlabs inc, New Jersey, USA) air cushioned optical bench on which the microscope and vibration dampening unit were placed.

The light source used to perform FFSSOCT was a BS 840M (Broadsweeper) tuneable super luminescent diode (SLD) light source (Superlum Diodes ltd, Republic of Ireland). The SLD had a central wavelength of 849.3nm and was capable of generating a 50.8nm bandwidth that could be tuned to output any wavelength within that range.

The schematic of the FFSSOCT instrument and a photograph of the initial FFSSOCT design are shown in Figure 2-1 and Figure 2-2 respectively.

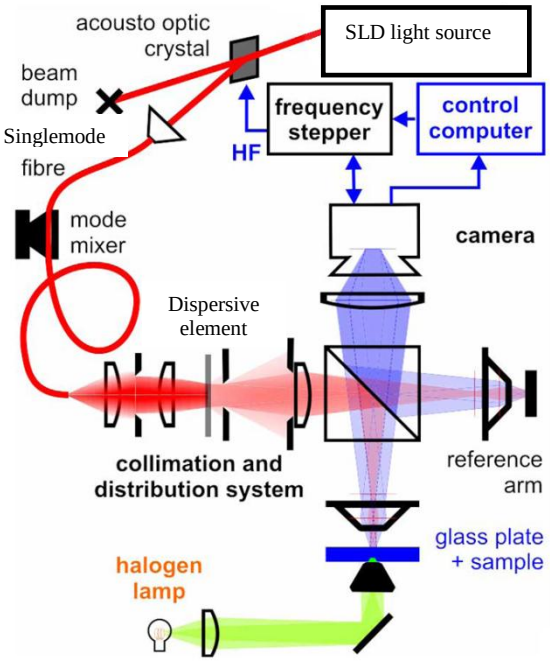

Figure 2-1: The original FFSSOCT design.

The SLD light source, acousto-optic crystal and beam dump are located inside the closed Broadsweeper unit. The collimation system, camera, reference arm and halogen lamp are incorporated in the microscope housing. Adapted from Povazay et al (2006)[57].

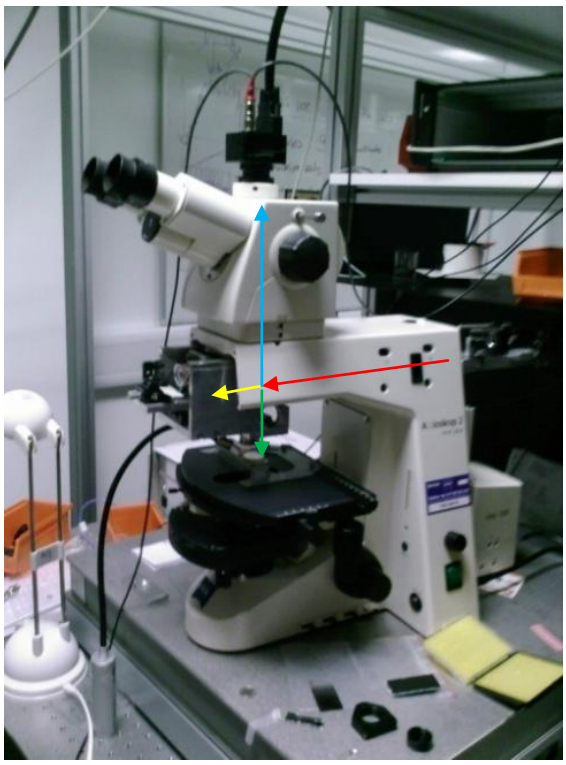

Figure 2-2: The modified microscope used for FFSSOCT.

Red line: illumination path. Green line: sample arm of the interferometer. Yellow line: reference arm. Blue line: recombined beam.

The tuning was accomplished by an acousto-optic tuning filter (AOTF), a piezoelectric crystal that creates a pressure wave diffraction grating effect when an oscillating input voltage is connected to it. By using input voltages of different frequencies, the associated diffraction gratings will vary the coupling of the optical wavelengths passing though the AOTF into the output fibre. The AOTF used in the BS840M has a narrow line width of 0.045nm, an important consideration for OCT applications as this affects the performance of the OCT system. A traditional FDOCT system has a line width that is not determined by the light source but rather by the distribution of the spectral light across of the pixels on the detector and can be more than twice as large as the BS840M[3]. This results in a quicker sensitivity fall-off when compared to the FFSSOCT system (the effect is described in detail in section 5.6). The AOTF crystal responds to MHz frequency voltages generated by an external radio frequency (RF) generator in the range 100.3-107.3MHz (corresponding to 873.6-822.4nm). The maximum tuning rate of the device is 1.1nm per millisecond or (>2000 full sweeps per second). Although only one sweep is required to generate a 3D tomogram, operating at the maximum sweep rate would potentially allow for extremely high acquisition speeds. In addition to the SLD and AOTF, the BS840M employs an automatic power control (APC) device that adjusts the current to the SLD in order to give a stable optical power output (+- 0.15dB across the bandwidth).

The external voltage source was an amplified (from 0.5 to 6.5V) frequency generator that could be preloaded with an array of up to 4096 discrete frequencies. The frequency array was incremented sequentially by an external trigger from the computer. The number of discrete frequencies used in the array is analogous to the number of pixels on the detector in an FDOCT system, i.e. the greater the number of frequencies, the higher the Nyquist sampling limit becomes, resulting in a larger axial probing depth (see section 5.3 for a detailed analysis).

The optical output of the SLD was delivered to the modified illumination arm via a 15m single mode fibre, coupled by a standard FC/APC (fibre connector/angled physical contact) connector to the broadsweeper light source and launched into the microscope through a bare end. An aluminium support was fixed to the microscope illumination arm in order to facilitate mounting and aligning the fibre with the optics within the microscope. A translation mount for the bare fibre end and a 25mm lens designed to collimate the light to

a 10mm diameter were fixed to the aluminium support. The original telescopic lens system in the microscope was retained and used to enlarge the beam diameter in order to fill the back of the objective lenses whilst retaining the collimation. It was also fitted with a dispersive element (20 degrees) in front of the telescopic lenses designed to flatten the Gaussian beam profile and reduce the spatial coherence of the light.

2.4.1 Crosstalk

The 15m coiled single mode fibre was connected to a loudspeaker designed to vibrate the fibre at different frequencies. Designated as a 'mode mixer', the purpose of the vibrations is to micro bend the fibre, destroying the spatial coherence of the SLD light inside. The effect of 'mode mixing' was to reduce the amount of noise in the images caused by the spatial interference of light reflecting from the sample and reaching a neighbouring pixel on the camera[57]. This crosstalk noise is separate from speckle noise[58,59] usually found in OCT images and is unique to full field OCT as the entire area of interest is illuminated by the spatially coherent light of the SLD[43].

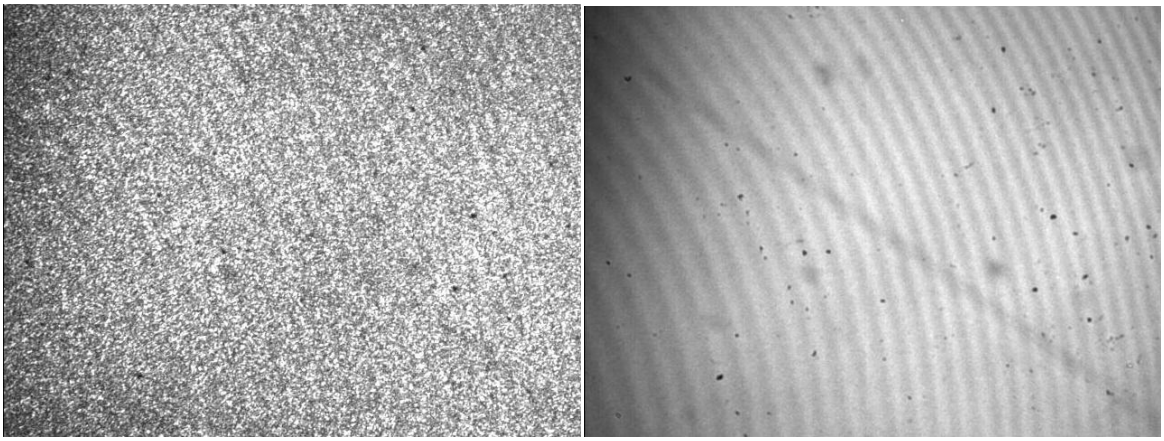

Figure 2-3: The effect of the mode mixer.
Left: mode mixer is off. Right: mode mixer is oscillating at 5 kHz.

Figure 2-3 shows the effect of the mode mixer on an en face image of a mirror, illuminated with a single frequency. The reference arm has been blocked. The large amount of crosstalk is very apparent in the left image, highlighting the extent of the spatial coherence of the light. The right image shows the effect of vibrating the optical fibre at an

audible frequency, approximately 5 kHz was found to be optimum. Operating the system with the mode mixer increases the signal to noise ratio by approximately 10dB. The curved lines present in the images (more apparent in the right image) are interference fringes caused by the interference of the light within the glass cover slide that protects the camera CCD chip. As these lines are products of optical interference, they will change depending upon the frequency of the light. Therefore, as the light source is swept, the lines will appear to move across the image producing a very strong oscillating pattern. Under Fourier transform, this pattern produces several very prominent lines that can drown out a weakly reflecting sample.

The free space beam splitter had a 50:50 splitting ratio. Although other splitting ratios were available and traditional OCT systems use unbalanced ratios of 80:20 or 90:10, the limited optical power available ruled out these options. Both arms of the interferometer contained identical objective lenses in order to minimise the dispersion mismatch. Each lens was a Zeiss 5x planar achromat microscope objective lens (5x, 0.15NA). The sample arm focussed down to the microscope stage with lateral movement control and electronic focus control via dials on the microscope. The reference arm was constructed of two translation stages, an objective lens and a mirror. The first translation stage had the mirror mounted on it, held in a 2 axis kinematic mount for alignment purposes. This was mounted onto the second translation stage along with the objective lens. This design allowed both the mirror to objective lens distance and the objective lens to beamsplitter distance to be adjusted independently, in order to give focus and optical path length control respectively.

Control of the relative length of the two interferometer arms allowed the image position to be manipulated; typically, it is desirable to have it as close to the zero delay as possible. The beams returning from the sample and reference arms recombined in the beamsplitter and were focussed onto the digital camera on top of the microscope. The camera was a 12bit 640HF monochrome CCD (Silicon Imaging, New Jersey, USA) with a resolution of 640x480 pixels. At this resolution, the camera could acquire 250 frames per second, although the pixel readout could have been decreased in order to increase the imaging speed (for example; 640x60 gave 2000fps). However, as the imaging speed was increased, the photon collection time (integration time) per frame was reduced resulting in a decrease in sensitivity.

The data from the camera was brought onboard the computer via a PCIe-1429 framegrabber card (National Instruments Inc, Texas, USA). This gave a data throughput rate (baud rate) of 340MB per second, sufficient for the camera which produced a maximum data output of 115MB/s (640x480 x 250fps x 12-bit). The 1429 card also had an external trigger, used for communication with the frequency stepper.

The computer was a Lenovo D10 (Lenovo, North Carolina, USA), one of the first personal computers to have four processing cores (upgradeable to eight). More cores increases the speed of the image processing as Fourier transform operations can be multi-threaded and sent to be processed on separate cores, leading to a direct linear speed increase proportionate to the number of cores. The computer RAM had been upgraded to 16GB and the storage capacity to 2.2TeraBytes, 1TB in the form of a 4x250GB striped RAID array, 0.2TB for the system requirements (Operating system, etc) and a 1TB drive for the long-term storage of data. The RAID (redundant array of independent disks) drive was in 0 configuration (striped) to achieve the fastest possible read and write speeds but another drive was required to store data since striped RAID drive arrays have a high probability of corruption and data loss. The computer ran Windows Vista 64-bit (Microsoft, Washington, USA) in order to fully utilise the additional RAM (Vista 32-bit will only support a maximum of 3GB).

2.5 Software

The Labview software used for the FFSSOCT system was custom written and learning to write programs and programmatically manipulate the hardware formed the majority of the initial work done for the research. The initial software components of the system that were required to produce the first tomographic images were completed in the following order:

1. A program to control the wavelength output of the SLD light source.
2. A program to generate a real time 2D depth view of the sample. This program incorporates a trigger mechanism to control the RF generator, a window showing the output of the camera and background subtraction to reduce the noise in the image.
3. A program to capture and save a series of interference images to the RAID drive of the computer.

4. A series of programs to convert the acquired interference images into a series of B-scans of the sample and resave them to the RAID drive.

The resulting B-scans were stacked together to form a 3D image in the freeware image processing program ImageJ (Wayne Rasband, National Institutes of Health, USA).

2.5.1 Frequency Stepper

The Frequency Stepper was the name given to the program that controlled the output wavelength of the broadsweeper light source. This program sent TCP/IP (transmission control protocol/internet protocol) commands to the RF generator in the form of an array of hexadecimal commands. After preloading the array into the RF generator, a trigger signal could be sent from within a Labview program to step to the next element in the array, changing the output wavelength of the light source. The data sent comprised the range of frequencies to generate, the amplitude (voltage) of the RF to generate, the number of frequency steps it should generate and the trigger parameters.

The program for controlling the Frequency Stepper had a series of frames stacked in a sequence to allow easier debugging as the entire program fitted on a single screen. The frame progression only occurred when all the operators in the frame have been completed. This program also featured a series of subVIs, another separate program that is called when appropriate, much like a subroutine in a text based programming language. This performed simple operations that were not featured in Labview's main functions palette such as conversion to bit specific hexadecimal.

Figure A-1 shows the first panel for controlling the frequency sweeper. The user controlled variables are highlighted in red. These are linked to the front panel of the Labview VI where the user can select the frequency range, amplitude, sweep time and number of frequency steps for the frequency sweeper. The blue variable represents a menu selection for the user, controlling what type of operation the frequency stepper performs. For example, it could also emit just one frequency or provide the user with information about the last operation that was sent to it.

The green box contains a subVI that checked the variables to ensure they lay within a set range. This was to prevent the user entering values that the frequency sweeper will accept but that might damage the AO crystal such as setting the amplitude too high/low. If any of the values appear out of range, the VI returns a message to the user and stops the program from sending any information to the frequency sweeper. The arrows pointing toward the edge of the box represent data being passed to the next, or any subsequent, frame of the sequence.

The red box in Figure A-2 shows a subVI inside a selection ring. The selection ring was controlled by the selection menu variable and contained various preset hexadecimal commands as well as the subVI. The subVI was required to convert the frequency range, amplitude value and number of steps value into hexadecimal. The arrows pointing away from the frame box represent data coming into the frame from any previous frame.

The red box in Figure A-3 is required to compensate for a glitch in the Labview program. Although the data has already been converted to hexadecimal (by a built-in conversion operator) in the previous frame, Labview does not recognise this as true hexadecimal and the frequency sweeper will not respond to the commands. The array of false hexadecimal values had to be type cast as hexadecimal using the highlighted operator.

The remaining frames of this program were dedicated to sending and receiving the hex data to the frequency sweeper using virtual instrument software architecture (VISA) ead/write commands, a standard way of communicating with external hardware via a TCP/IP connection initiated through Labview.

2.5.2 FFSSOCT real time B-scan viewer

Figure A-4 shows the program for generating a real time 2D depth view of the sample. It was divided into three major parts: acquisition of a set number of images (defined by the user), transformation of a single line from those images into a depth scan and application of some background subtraction. The highlighted sections performed the following tasks: the red sections were responsible for generating trigger pulses that move the frequency stepper to the next frequency. The first entry of the frequency table must be pulsed twice in

order for the frequency stepper to progress hence, the code appears both inside and out of the image acquisition loop. This is due to the internal firmware of the frequency stepper. The blue section took the image from the image capture VI and read off a single line of intensity values at a position defined by the user, concatenating them into a 2D array as the loop repeated. The green section accepted the 2D array of intensity values from the image acquisition loop and performed a spectral power Fourier transform to each vertical line of intensity values, one by one.

The data was passed out of the loop in the form of another 2D array of intensity values. The yellow section passed the data into an intensity graph on the front panel of the VI but also performed background subtraction when activated by the user. First, the background must be captured by removing the sample from the light, and then by toggling a switch on the front panel, storing the background image data in a perpetual loop in the program

The captured background was then subtracted from all subsequent images. There is also a multiplier present to increase the amount of background that is removed. The program also featured various smaller pieces of code for calculating the frame rate of the camera and of the program.

2.5.3 FFSSOCT acquisition software

Figure A-5 shows the program used for saving images to the RAID drive. Again, the two sets of trigger pulse generation were present. The red section shows the code used to generate sequential file names for each image, saved in a user selected folder location. The blue section shows the VI used to save the files.

TIFF (tagged image file format) is a standard image file format that can handle 16bits of information per channel. The file saving was originally done by recording an AVI (audio visual interlace) movie with each image recorded as a frame of the movie. In terms of speed, this was a very effective method of saving a large amount of image data in a short amount of time. However, this process was swapped for the slower design when it became apparent that Labview could only support a maximum of 8-bit AVI file recording and was compressing the 12 bit camera images down, resulting in a loss in image dynamic range.

Figure A-6 shows the program for converting the TIFF interference images into 480 depth scans. However, this program was originally slightly simpler, opening each image in succession, reading the relevant horizontal line from each image then performing the point by point Fourier transform much like the real time viewer displays an image. These steps were then repeated for each line from each of the images to create 480 depth scan images. This method was extremely slow, taking over 130 minutes to process 512 images (15.2 seconds per image) and was due to the repeated reopening of each image file.

An improved version of the program used an interim step before Fourier transforming the spectral data. Each of the image files is only opened once thus dramatically increasing the speed of the process. The red section on Figure A-6 shows how each image was read, line by line into 480 separate spreadsheet files. The loop then repeated, opening the second image and reading each line into the relevant spreadsheet file. The result was that the information for each depth scan was now contained entirely within one file which could be easily processed and resaved. The code for this is contained in a subVI highlighted in blue in Figure A-6 and is shown in Figure A-7.

This processing code was similar to the right hand side of the real time imaging code. The Fourier transforming took place inside the red section of the code, the blue section removed the large DC component term (Equation 9) from the image and the green section transformed the array back into an image, saved it as a PNG (portable network graphics) file and deleted the interim spreadsheet file. This method was far quicker than the previous one (over 20 times quicker) and processed 512 images in 6½ minutes (0.78 seconds per image).

In addition to these four core programs, there was a background subtraction program to reduce the noise in the image and increase the SNR. This program required that a series of ‘blank’ images be recorded, images where the sample was not present. The program simply opened the original image and the background image, subtracted the two and resaved the image.

2.6 Specifications

The specifications of the system are divided into four areas, acquisition speed, signal to noise ratio (SNR), resolution and power.

2.6.1 Acquisition speed

Each hardware component of the system introduced a speed limiting factor preventing it from becoming faster. As one barrier was overcome, by for example upgrading the equipment to a newer faster design, another component would limit the speed. The limiting speed of each component is listed in Table 2-1.

As only one sweep needs to be completed per 3D tomogram, both the frequency stepper and the AO crystal were easily fast enough to support even video rate imaging (Table 2-1). However, the camera could only acquire one 3D dataset every 5 seconds (for 512 images) or every 2.5 seconds (for 256 images) and the frame grabber could only throughput 512 full frames every 0.69 seconds. The limiting speed therefore was the CCD camera.

Component	Limiting speed	Limiting speed (ms)
Camera	125 FPS at 640x480 pixels (256 required per 3D dataset)	8 (2500 for dataset)
Frequency stepper	91 sweeps per second (only 1 needed per 3D dataset)	11
AO crystal in the SLD	2000 complete sweeps per second (only 1 needed per 3D dataset)	0.5
Frame grabber card (PCIe 1429)	340MB/s = 737 full frames per second (256 required per 3D dataset)	1.4 (360 for dataset)

Table 2-1: The speed limiting factors in the current FFSSOCT design.

2.6.2 Signal to noise ratio

Another important parameter of any OCT system is the signal to noise ratio (SNR), a measure of the sensitivity of the system. In the case of FFSSOCT, the main noise factor is the cross talk from the spatial coherence of the light. The theoretical limit of the SNR can be calculated from the equation for the SNR limit of FDOCT, taking into account that the source power is distributed over the entire sample.

$$SNR_{FFSS} = \frac{\rho P_{vox} R_{vox} \Delta t}{2e} \qquad \text{Eqn. 12}$$

Equation 12 is the theoretical limit of the SNR[17] for a given camera integration time, Δt. ρ is the responsivity of the detector (based on the quantum efficiency of the camera) and can be set as 0.15. P_{vox} is the optical power deposited on each sample point and equals the sample illumination power at camera saturation divided by the number of pixels, $\frac{15\mu W}{640x480} = 48.8pW$. R_{vox} is the sample point reflectivity equal to approximately 1 for a mirror. e is electron charge. At a camera rate of 125fps, the system can capture 512 images in 5.2 seconds (Δt =5.2) giving a theoretical SNR limit of 79dB. The actual SNR was measured using a neutral density (ND) filter in the illumination arm and a mirror as the sample to create a known signal power reference with which to compare the noise floor (a complete analysis of the measurement of SNR for the FFSSOCT system can be found in section 5.5). Using this value as a basis for comparison, the SNR of the system was measured as 50.2dB using an ND filter with an attenuation of 16.2dB, giving a system sensitivity of 66.4dB.

2.6.3 Image resolution

The theoretical axial resolution of the system can be calculated from Equation 2 and, using the full bandwidth of 50.8nm, the theoretical resolution is 6.27μm. However, dispersion due to the lenses in the microscope results in a measured resolution that is never as good. The actual resolution can be calculated by examining the point spread function of a boundary step such as a piece of glass. As the step from air to glass should be infinitely small in terms of axial distance, any spread of this step represents a limit to the resolution of the system. If relationship between the axial distance measurement and real space is known, the axial resolution can be found. Using this method, the real axial resolution of the system was 9.6μm. The lateral resolution of 7.8μm was measured using a USAF resolution target. The measurement of axial and lateral resolution is discussed further in section 5.4.

2.6.4 Optical power

The power of the laser at source was 5mW but each optical element of the microscope attenuated this power, so just 127μW actually reached the sample. The system loss before the beam splitter was, therefore, approximately 95%. It was clear that this was a major source of performance loss within the system and should be the first stage for improvement.

2.7 Acquired images

With the specifications detailed in section 2.6, the rebuilt FFSSOCT system could produce images such as the following:

Figure 2-4: An OCT tomogram montage of a coin acquired with the FFSSOCT system. This image was composed of 512 interference images, acquired in 5.2 seconds and has lateral dimensions of 640x480 pixels (970x730μm) and an axial dimension of 128 pixels (260μm).The projection of the volumetric image has been rotated in 40 degree steps, starting from the top left and finishing in the bottom right.

Figure 2-4 is a topographic image of the surface of a 1p coin acquired with the FFSSOCT instrument. The image is shown as a montage of a rotated 3D stack of B-scans, highlighting the raised surface topography of the ‘P’ letter.

2.8 Summary

The objective of the work covered in this Chapter, was to rebuild the existing FFSSOCT system and to write new acquisition and processing software in order to achieve 3D tomographic images of highly scattering samples. The existing FFSSOCT design was rebuilt and software written in Labview to control the broadsweeper light source in order to acquire spectral data. To transform the spectral data into time domain data, software was written to perform this task and to give a real time B-scan view of the sample. The real time B-scan viewing program was rewritten to acquire and save 3D tomographic spectral data at a rate of one tomogram every 5 seconds (640x480x512 pixels), the equivalent of ~50,000 A-lines per second. Software was written to process the spectral data into time domain images, initially taking several hours but reduced to 6.5 minutes after the code was improved and rewritten.

Using the redesigned FFSSOCT system, a sensitivity of 66.4dB was measured with 127µW of optical power on the sample and an image acquisition time of 5 seconds (640x480x512 pixels). Images were acquired of highly reflective samples (mirror and coin), processed in 6.5 minutes and rendered in ImageJ (Figure 2-4).

Chapter Three: Improving the FFSSOCT system

3.1 Improvement aims

Over the course of the research, the initial design described in Chapter 2 was improved with hardware improvements and new software designed to improve various aspects of the system. To realise the goal of imaging weakly scattering tissue (retina) and creating an OCT system with comparable performance to that of other OCT modalities, several key areas were identified that would provide significant performance improvements:

1. Optical power throughput – This was identified as the first area for improvement due to the high throughput loss of the initial design (~95%). From Equation 12, any increase in optical power on the sample should directly result in an increase in the sensitivity of the system.
2. Camera performance – Improving the specifications of the camera should bring an increased sensitivity via; (i) higher detector quantum efficiency (ii) an improved potential acquisition speed and (iii) a higher spatial sampling rate (smaller pixel pitch) which would allow frame averaging, giving a further boost to the SNR.
3. Software improvements – Decreasing the acquisition and processing time by optimising the Labview code would increase the number of images that could be acquired in an imaging session and improve image quality through averaging. Other processing steps such as data resampling and dispersion correction could be incorporated into the processing code to improve the image quality.

In addition to these main areas, many further improvements were made to the FFSSOCT design, incrementally improving the sensitivity and other parameters with each refinement. Sections 3.2 and 3.3 detail the major hardware and software improvements made during the course of the project.

3.2 Hardware improvements

The major novel hardware changes to the FFSSOCT system in detailed in Chapter 3 are listed in Table 3-1.

Each of the hardware upgrades was accompanied by changes in the existing alignment of the optical beam path and modifications to the Labview software. The effect of the implementation of these improvements on the image quality of the FFSSOCT system was

performed by constant measurement of the SNR. Over the same time course, the Labview was continually modified as well, as detailed in the following section.

Hardware	Function	Description
Optical fibre launcher	Deliver optical power into the microscope	SMF was replaced with an MMF and collimator improving optical power into the microscope from 15% to 95%
Spinning diffuser	Destroy SLD spatial coherence	Mode mixer was replaced with a spinning diffuser (required to use MMF). SNR unaffected
Illumination arm	Couple SLD into the microscope	2 adjustable mirrors added to the illumination arm. Allows for precise optical alignment, optical power on sample increased by 5%
Camera serial link	Change base settings of camera	The camera serial link via the 1429 PCI card was enabled giving access to control over the image acquisition parameters. Acquisition rate increased from 125 to 250fps
Photon focus camera	Capture images	SI camera replaced with photon focus camera. QE increased from 15 to 45%. Full well capacity remained the same at ~100k e^{-1}. Pixels increased from 250k to 1.3M. Frames per second increased from 250fps to 500fps
Optical booster	Increase optical power	Additional optical booster module, increases SLD optical power from 5 to 20mW
Illumination optics	Transfer light through the system	Original microscope optics removed and replaced with separate lenses. Increases optical power on the sample by 5%

Table 3-1: Hardware improvements made to the FFSSOCT design.

3.3 Software improvements

Many of the programs created were continually improved over the duration of the research, both with incremental steps and major revisions to accommodate new hardware. Table 3-2 lists the creation and major revisions of the programs used to control the FFSSOCT instrument and process its output, detailing why each change was performed and what effect it had.

Program name	Function	Description
Frequency Stepper	Sends a table of frequency steps to the RF frequency generator	Required to control the Wavelength output of the SLD
B-scan viewer	Repeatedly acquires images from the camera and processes the data into a B-scan	First iteration of the FFSSOCT acquisition software
3D tomogram acquisition	Acquires and saves images from the camera	Images are acquired and streamed to an AVI file
Tomogram processing 1	Rewrites the saved data into individual B-scans	Opens each file saved by '3D tomogram acquisition' and reorganises the spectral data into separate B-scans.
Tomogram processing 2	Transforms the B-scan data into time domain images	Uses FFT power spectrum
3D tomogram acquisition 1.1		Saves data on a file by file basis as multiple TIFF files
Tomogram processing 1.1		Reduces the number of times each spectral data file is opened.
B-scan viewer 1.1		System for active background subtraction added
Tomogram processing 2.0	Processes spectral data into time domain images	Combines 'tomogram processing 1 & 2' in order to decrease the overall processing time
3D tomogram acquisition 1.2		Uses a queue system to reduce 'down time' during the acquisition
3D tomogram acquisition 1.3		Uses binary file streaming to decrease save time
B-scan viewer 2.0		Combines 'B-scan viewer 1.1' with '3D tomogram acquisition 1.3' to enable tomogram acquisition whilst viewing B-scans acquired in real time
B-scan viewer 2.1		System for averaging sequential images added
Tomogram processing 2.1		Removes interim file save to decrease processing time
Phase analysis	Extracts phase	Attempts to extract and correct phase instabilities on a per image basis
Data resampling	Interpolates each a-scan to remove signal chirp	Increases SNR by removing spectral chirp
Dispersion compensation	Removes the artefacts caused by the dispersion mismatch	Increases SNR by numerically compensating for the wavelength dependent velocity delay due to the refractive index mismatch in the interferometer
Tomogram processing 3.0		Combines 'tomogram processing 2.1', 'data resampling' and 'dispersion compensation'
Tomogram processing 3.1		Implements averaging of multiple 3D tomograms

Table 3-2: List of the software improvements compiled during the FFSSOCT project.

The implementation and development is listed in chronological. Minor revisions to the established programs have been omitted.

Although many more programs were written when developing the FFSSOCT system, the listed programs were the most used and the majority of the results were acquired using them. Other programs written include those for testing hardware, running simulations, analysing and preparing images and general computation.

The final versions of the acquisition and processing software are detailed at the end of the Chapter.

3.4 Using a multimode fibre and spinning diffuser

The first hardware modification was to change the 15m single mode delivery fibre to a multimode fibre (MMF) with an FC/APC launcher. It was found that launching through the bare end of the single made fibre was a cause of significant power loss; approximately 1mW was being lost between the SLD and the microscope. Using a multimode fibre with FC/APC launchers, the optical losses were reduced to less than 0.5mW. Additionally, as collimating the exposed single mode fibre with a 25mm single lens resulted in further optical power losses, using an appropriate FPC/AC collimator ensured greater optical throughput. The collimator (CFC-11X-B, Thorlabs inc, New Jersey, USA) was chosen to operate at 800nm with a focal length of 11.0mm, giving a 2.1mm diameter beam. Replacing the singlemode fibre with a shorter multimode fibre meant that the ‘mode mixer’ was no longer effective at reducing the crosstalk. Using an optical diffuser in the beam path, the collimated beam was diffused at different angles, resulting in a change in the spatial coherence of the light. By then rotating the diffuser, the spatial coherence was also changed, effectively destroying the crosstalk. This remained valid as long as the exposure time of the camera was long enough to ensure that the changing spatial coherence pattern of the light was averaged to the point of homogeneity across the field of view. The required rotation speed was approximately 6000 revolutions per minute for an exposure time of 4ms, or two fifths of a rotation per frame.

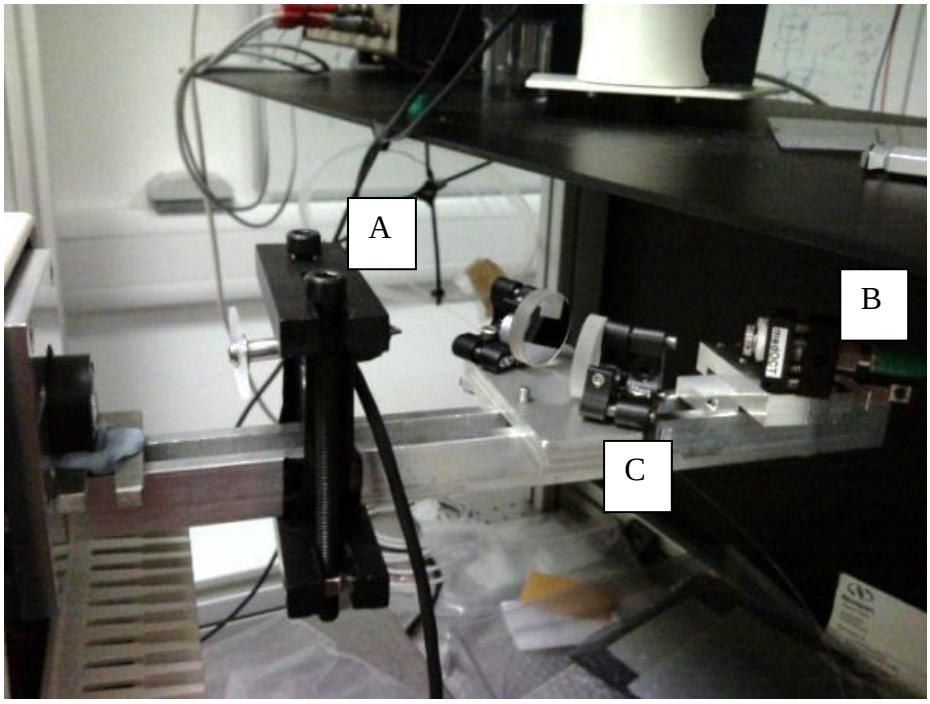

Figure 3-1: The modified illumination arm.

A) The spinning diffuser. B) Fibre collimator. C) Steering optics; these were added at a later date. The spinning diffuser was eventually attached to a suspended arm in order to reduce mechanical vibrations within the system.

After replacing the single mode fibre with the multimode fibre and collimator, the optical power on the sample increased from 127µW to 720µW. From Equation 12, this improvement in optical power on the sample should result in a theoretical maximum SNR increase of 15.1dB. From Figure 3-2, the peak SNR close to the zero delay of the system had increased from 66dB to 75dB. Up to this point in the project, the camera operated at its maximum speed of 125fps, however the increase in the optical power returning from the reference arm was now enough to saturate the camera. To measure the SNR, the optical power was attenuated after the spinning diffuser by an ND6 (17.5% transmittance) neutral density filter and the resulting 15dB attenuation was added to the calculated SNR value. To image samples with low reflectivity, the ND filter was used in the reference arm in order to illuminate the sample with as much of the available power as possible.

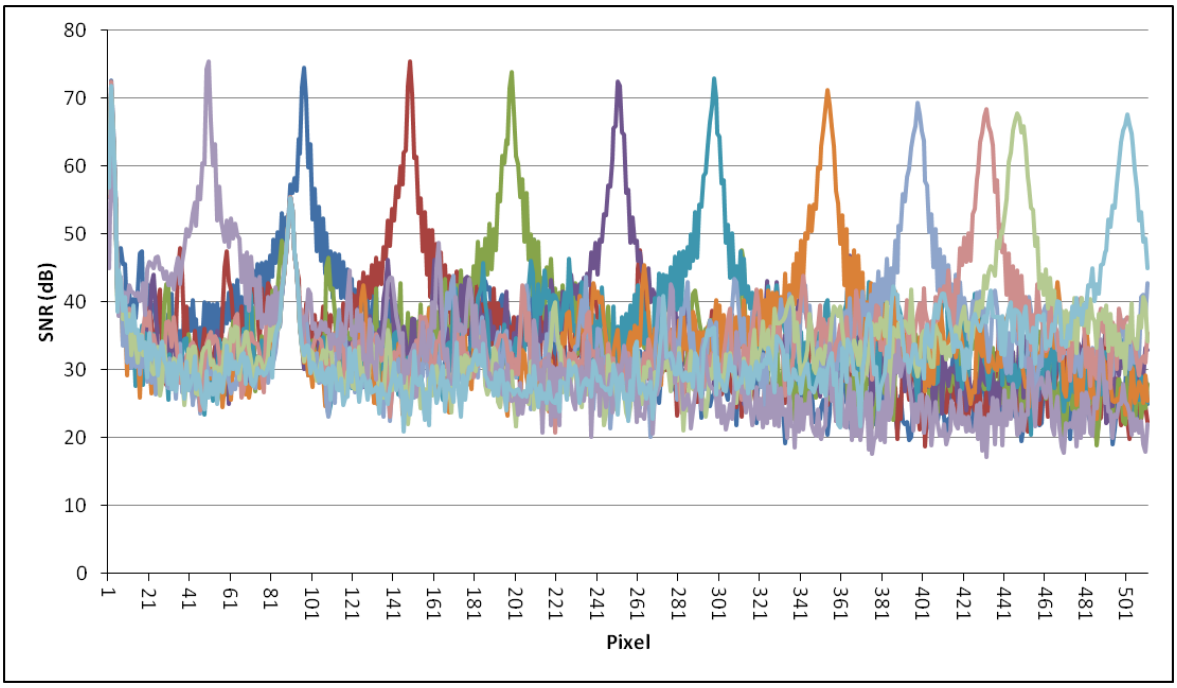

Figure 3-2: Sensitivity of the FFSSOCT system after redesigning the illumination arm. The datasets were volumes of 640x480x512 pixels acquired in 2 seconds per volume.

It was discovered that the SI-640HF M camera was capable of a higher frame rate without sacrificing the frame integration time. This was achieved by switching the camera from 'continuous snapshot' mode to 'live video' mode using serial commands sent through the NI 1429 PCI card. The increase in speed was achieved via the two-cell SRAM (static RAM) pixel architecture onboard the camera that enabled the current frame to be acquired whilst the previous frame was being readout. In this mode, the camera acquisition would no longer be triggered; however as the camera was acting as the master clock (controlling the timing of the entire instrument) in the FFSSOCT design, it was not necessary to have this feature. Initially, the serial commands were sent through a separate program. It was later discovered that Labview could store and send the commands, enabling the camera acquisition parameters to be changed from the main 'B-scan viewer' program. By using the serial commands, the exposure time of the camera could also be changed potentially allowing for very long frame integration times in order to increase the sensitivity of the system. The ND filter in the reference arm was used to prevent saturation of the camera when imaging with long exposure times.

3.5 Images acquired with the multimode fibre and diffuser

The increased sensitivity of the system meant that it was possible to move from highly reflective metallic samples to less reflective biological material, the aim being to acquire images with depth information. The first biological samples chosen had optically dense surfaces in order to create large amounts of surface scattering. Images were captured of wasp eye and foot (Figure 3-3) and plant leaves.

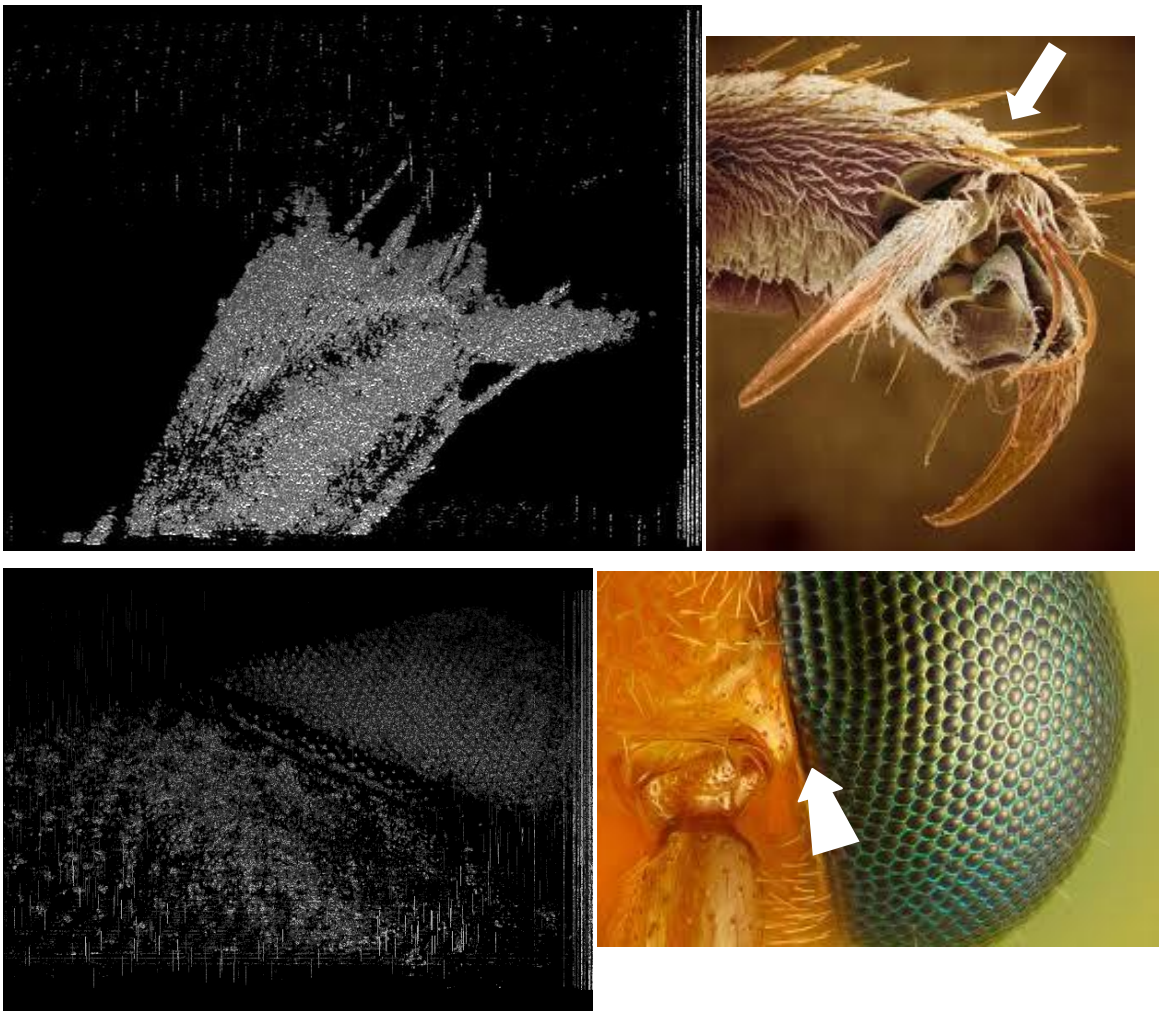

Figure 3-3: 3D topographical projections of the foot and the eye of a wasp.

The wasp's foot (top left) and eye (bottom left) are compared to images from scanning electron microscopy (top right - adapted from The Science Photo Library (2010)[60]) and a 40x bright field microscope (bottom right - adapted from Krebs, C. (2010)[61]). White arrows indicate OCT imaging direction. The volumes were constructed from 512 B-scans each with 640x480 lateral pixels (970x730µm) and 256 axial pixels (520µm) acquired in 5 seconds. Both volumes have been tilted 30 degrees using ImageJ to enhance the perspective.

The basic structure of the wasp anatomy, seen in Figure 3-3, is easily recognisable when compared to the scanning electron microscopy (SEM) and microscopy images[60,61]. The claws and hairs on the wasp hand and the mosaic of the compound eye structure can be seen in the FFSSOCT images.

Having successfully acquired tomographic images of highly scattering samples, images were then acquired of less scattering samples. Less scattering samples should enable more information to be imaged at layers beneath the surface as more optical power penetrates into the sample. Images were captured of lettuce leaves (Figure 3-4) and onions; biological matter that has a highly layered structure and low reflectivity that should enable light scattered from layers deep within the sample to be detected.

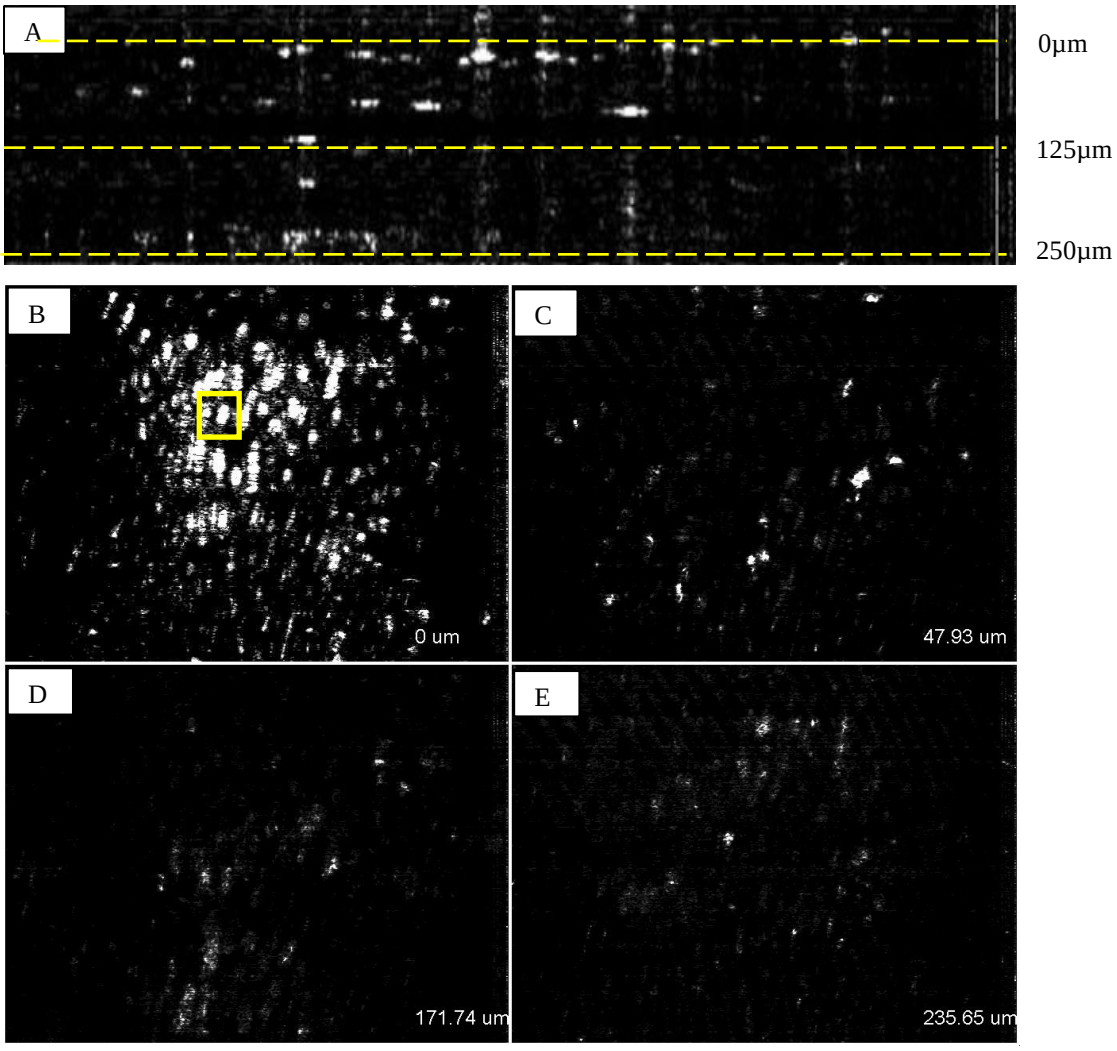

Figure 3-4: Images of a lettuce leaf taken at different depths from a tomographic volume. A single B-scan (A) taken from the volume (vertical pixel 180) shows the depth information, the image dimensions are 640x128 pixels (970x260µm). The enface images (B, C, D, E) are 640x480 pixels (970x730µm). The tomographic volume was acquired in 1 second. Each lettuce cell (yellow box, B) is approximately 20x30µm in size.

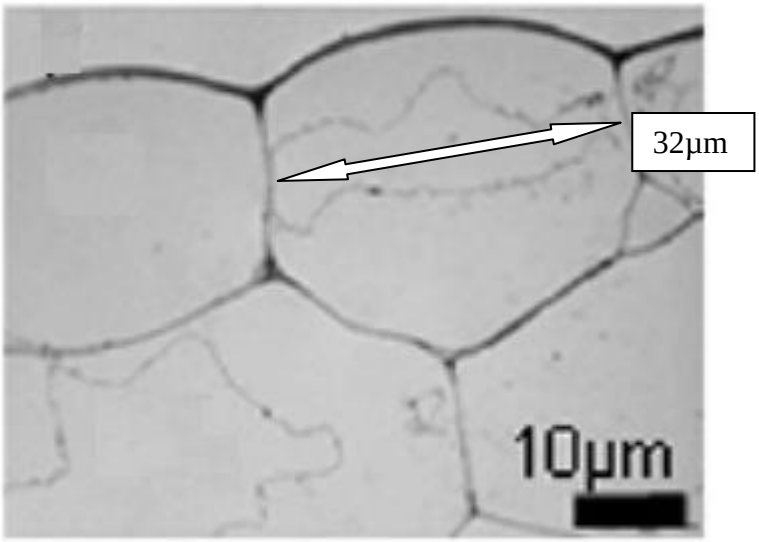

Figure 3-5: Bright field image of lettuce cells.
Adapted from *Modification of Cell Wall Properties* Wagstaff (2010)[62].

The lettuce leaf cells are clearly visible in Figure 3-4 with an approximate size of 20-30µm which is in good agreement with the cell size as measured by microscopy (Figure 3-5)[62]. The rectangular cellular structure of the lettuce, which is larger than the wavelength of the FFSSOCT system, resulted in highly direction dependent Mie scattering[63] of the incident beam. As the structure of the lettuce leaf is almost completely homogeneous, with a very regular distribution of large rectangular cells, the FFSSOCT images show only the bright reflections of the planar surfaces of the cells. When imaging retinal tissue, the size of the cellular structure is typically close to the wavelength of the OCT imaging system. On this scale, Rayleigh scattering occurs, and the incident beam is scattered with less directionality by the tissue resulting in greater visibility of the retinal structure. A drawback of the increase in scattering is the increase in image speckle and crosstalk caused by the interference of scattered beams (section 2.4.1).

3.6 Retinal images

As the minimum sensitivity required for retinal imaging is approximately 70dB[3], it was felt that the FFSSOCT system could now acquire images of retinal tissue. The retinal samples were stored in refrigerated preservation fluid (phosphate buffered saline) until required. The first *ex vivo* retinal image was that from a tree shrew. The optics of the tree shrew eye were previously removed. To image the sample, it was placed in a hollow

moulded putty mount and filled with the preserving storage liquid to the brim of the retinal cup. A cover slip was placed across the top of the retinal cup, ensuring no air bubbles were trapped in the liquid. By tilting the retina, the cover slip reflected the OCT beam and reduced the amount of unwanted light returning to the system; without the cover slip, the reflection from the surface of the preservation liquid would saturate the FFSSOCT system.

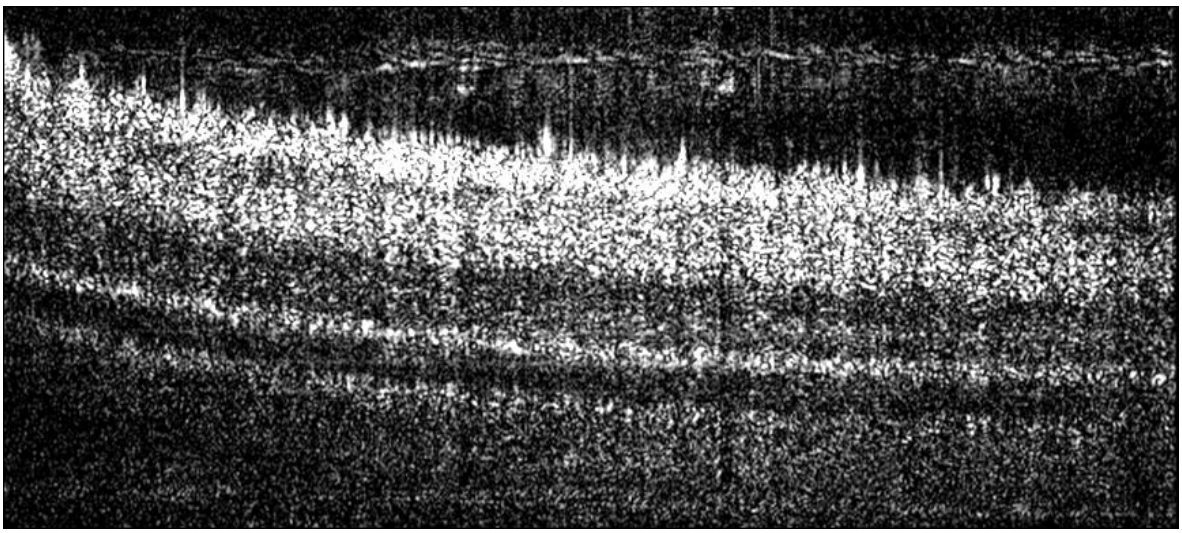

Figure 3-6: A 2D B-scan of an *ex vivo* tree shrew retina.

The image was constructed from an average of 10 B-scans. Each B-scan was 640x512 pixels acquired in 4 seconds. The final image is 640x278 pixels (970x500µm).

Figure 3-6 shows the first *in vitro* retinal image acquired using FFSSOCT[64]. The visible retinal layers are identified in Figure 3-7.

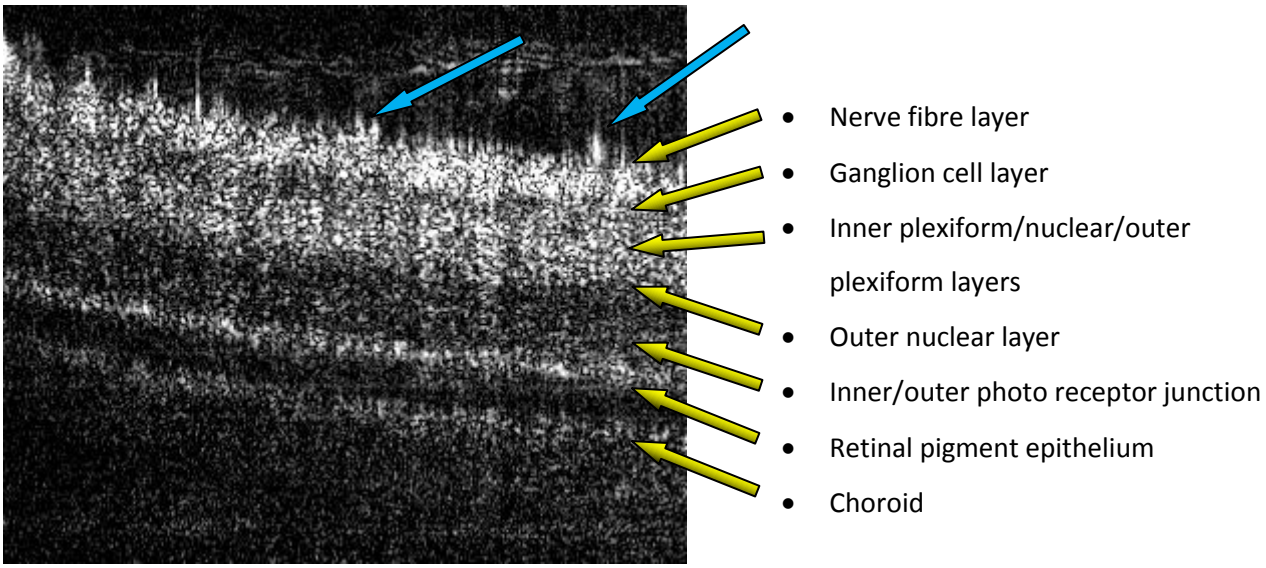

Figure 3-7: Identification of the visible retinal layers of an *ex vivo* tree shrew FFSSOCT image.

The FFSSOCT image has been cropped to 340x278 pixels (515x500µm). The blue arrows indicate retinal debris.

In addition to the layered structure of the retina (Figure 3-6), there were some other image features present that gave an indication of the image producing quality of the FFSSOCT system in its current state. The limitations of the wavelength dependent depth penetration could be seen by the ability to visualise the top of the choroid. This degree of penetration is typical for an OCT system operating at 800nm, whereas longer wavelength systems can image deeper into the tissue[17]. Several image artefacts were also present in Figure 3-6; the horizontal lines at the top and bottom of the image were remnants of the background subtraction (detailed in section 4.5). Additionally, the nerve fibre layer appeared to have multiple artefacts adjacent to it (blue arrows, Figure 3-7). The origin of these is likely to be a combination of loose tissue resulting from the age of the sample and mismatched dispersion between the arms of the interferometer. The dispersion mismatch (explained in section 4.10) was due to a combination of the preservation liquid and the ND filter in the reference arm. Images acquired towards the end of the project were of fresh retinal samples and had dispersion compensation applied to them resulting in less blurring. Fibre based OCT systems may have additional image blurring, similar to that seen in Figure 3-6, which arises due to a mismatch in the polarisation of the two interferometer arms. This may also be the case for FFSSOCT though a polarisation mismatch is usually the result of the presence of a polarisation inducing material e.g. crystalline structure (such as cornea[65]) in one or both of the interferometer arms.

Additional image quality can be obtained by increasing the number of averaged images. The B-scan viewer program was therefore modified to include B-scan averaging (Table 3-2) enabling sequential B-scans to be processed, averaged and saved without the need for stopping the acquisition program and processing the individual images separately. Saving multiple successive tomograms was a slow process, taking over a minute to acquire and save the 10 volume average shown in Figure 3-6 and several hours to process them. By averaging 10 single B-scans in less than a minute, a high quality image could be quickly acquired. In addition to the improved image quality, any problems with the alignment of the FFSSOCT system or the quality of the sample could be quickly identified without the need to process multiple tomograms, reducing the time the system was not being used. Also, the effect of the long-term changes in the background subtraction (detailed in section 4.5) was reduced when using this imaging technique. The background subtraction file is stored by the program via user input when no sample is present and subsequently

subtracted from each image of the sample. An example of the result of image averaging is shown in Figure 3-8.

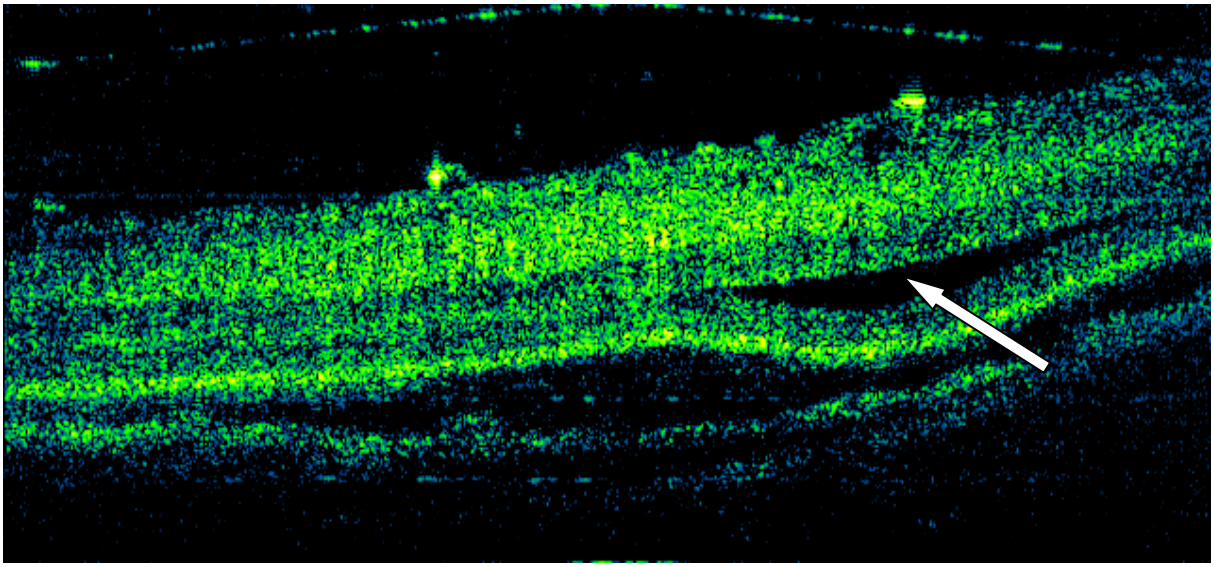

Figure 3-8: A false colour 2D B-scan of an *ex vivo* tree shrew retina.
The retina has detached and liquid has formed above the RPE (white arrow). The image was constructed from 10 averaged B-scans, acquired and processed in 20 seconds. The image size is 640x256 pixels (970x500μm).

When compared to Figure 3-6, it can be seen that the background subtraction in Figure 3-8 has been more effective and results in a clearer image. Also, the blurring on the surface of the nerve fibre layer has been reduced and the overall dynamic range of the image has been increased due to the decreased background noise level. The line at the top of the image originates from the cover slip on the retinal cup. Some light is reflected off dirt or smudges on the cover slip resulting in a small amount of signal detected by the system. The cover slip is not straight as it is partly beyond the imaging range of the system resulting in the phenomenon of image reflection in the axial direction.

3.7 Volumetric imaging with FFSSOCT

By increasing the frame exposure time and adjusting the reference arm power, it was possible to acquire 3D tomographic images of *ex vivo* tree shrew retina in a single volumetric data acquisition.

Different features of the retina can be seen in Figure 3-9, the nerve fibre bundles that run across the surface of the nerve fibre layer can be seen in the en face image (Figure 3-9 E) and some of the large blood vessels can be seen in Figure 3-9 D (red arrow). The poor quality of the retinal sample is made apparent by the presence of with large tears in the surface of the retina (Figure 3-9 E - yellow arrow) and many small floating pieces of tissue obscuring the retina below (Figure 3-9 E - blue arrow). These pieces of floating retina debris attenuate the optical power reaching the tissue below causing shadows to appear in the B-scan view (Figure 3-9 B - blue arrow).

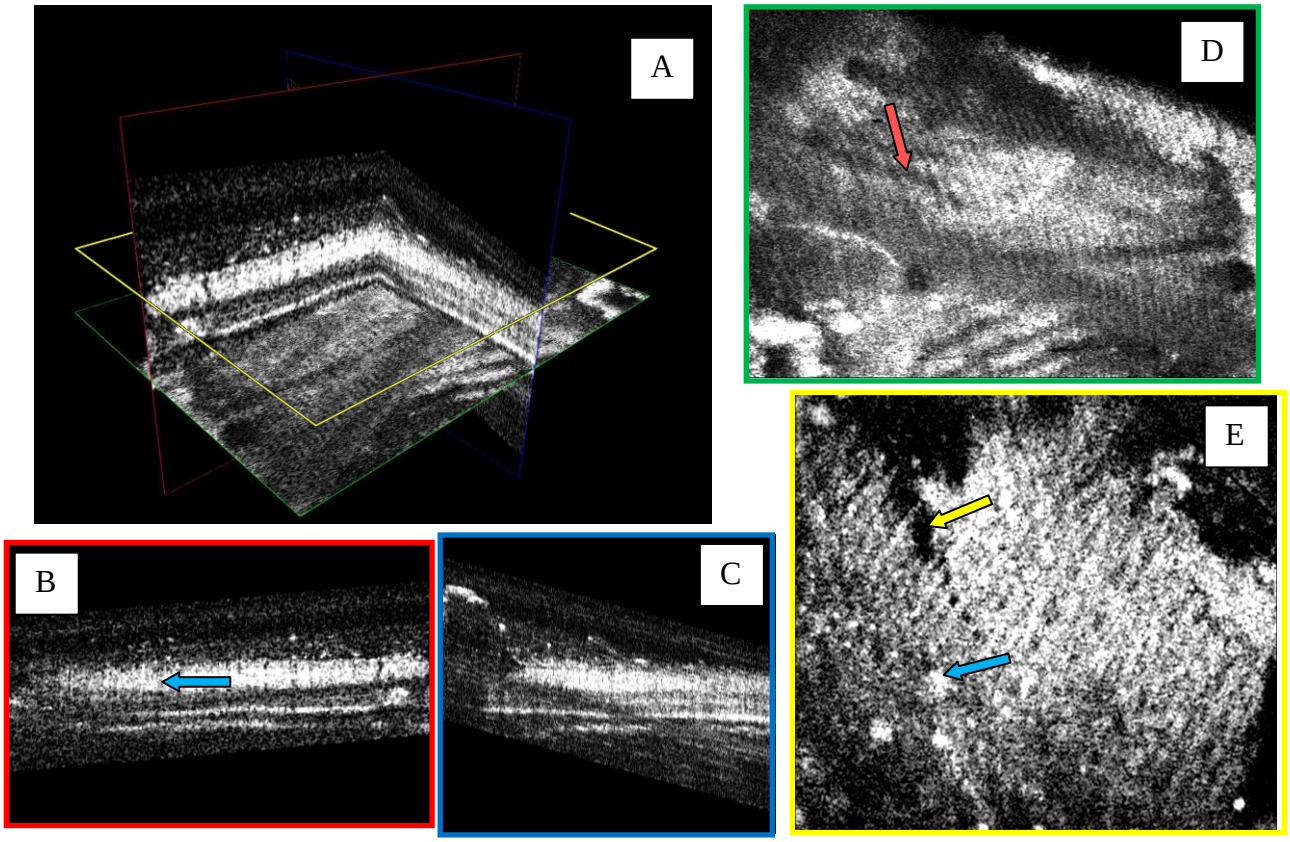

Figure 3-9: Volumetric image of an *ex vivo* tree shrew retina.

The three dimensional image has been registered in ImageJ and cut away in orthogonal planes using Volocity software (PerkinElmer, inc. Massachusetts, USA). The image has 640x480 lateral pixels (970x730µm) and 256 axial pixels (460µm), recorded in 8 seconds. B&C show orthogonal B-scans (640x256 pixels; 970x460µm) of the 3D volume (A). Vertical shadowing caused by debris on the retinal surface has been highlighted in B (blue arrow). D&E show en face images (640x480 pixels; 970x730µm) of the 3D volume at different depths. D is an en face image from the top of the choroid with a blood vessel highlighted (red arrow). E is an en face image from the nerve fibre layer with a retinal tear (yellow arrow) and surface debris highlighted (blue arrow).

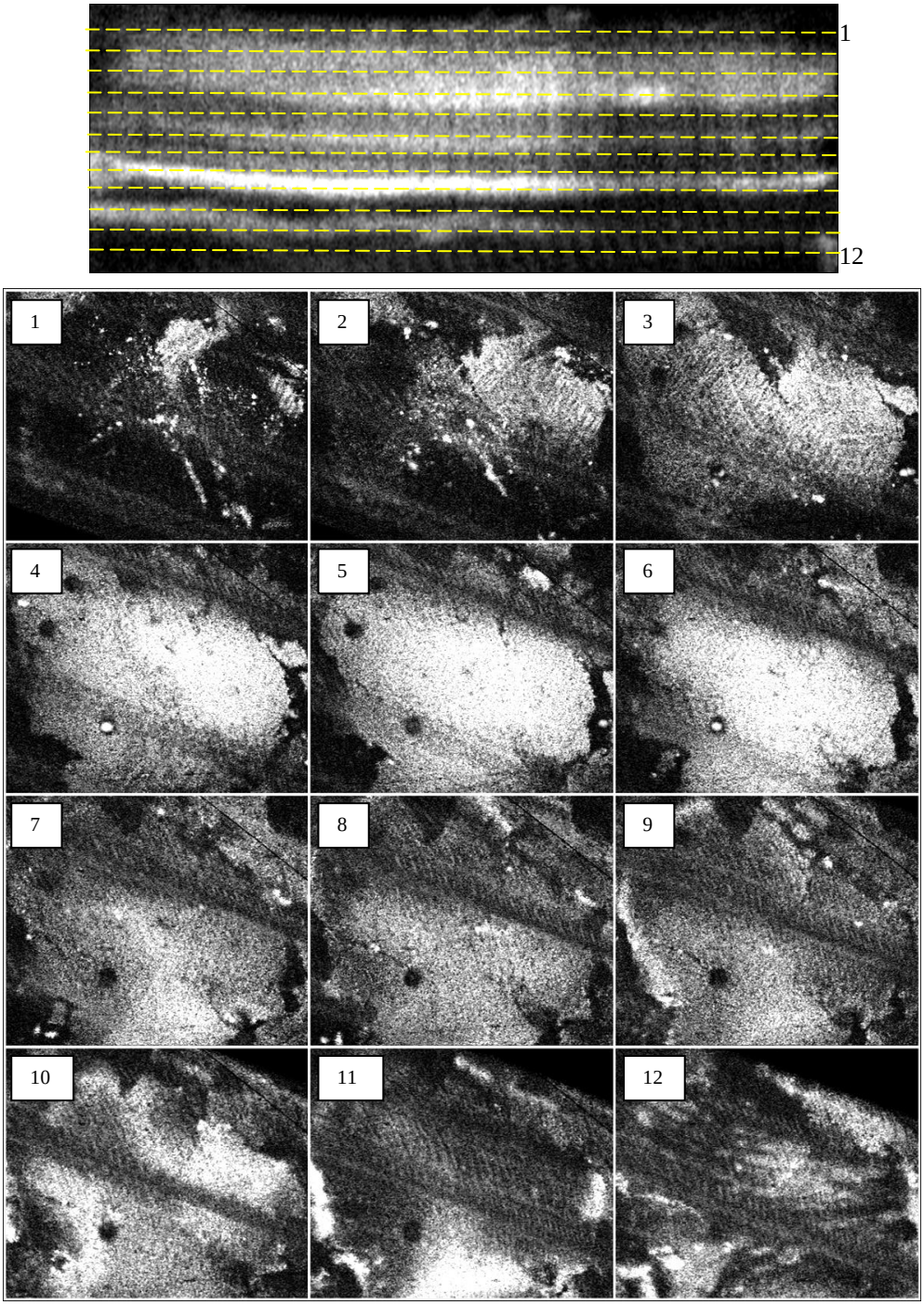

Figure 3-10: En face fly-through of an *ex vivo* tree shrew retina.

The tomographic volume is 640x480 lateral pixels (970x730µm) and 256 axial pixels (460µm), acquired in 8 seconds. The B-scan (top) is 640x256 pixels (970x460µm) and is comprised of an average of 5 consecutive spatially separated B-scans taken from the volume. The en face images (640x480 pixels; 970x730µm) were resliced from sequential depth points (every 40µm axially) within the tomographic volume.

With more optical power available, it became possible to decrease the integration time of the camera and acquire volumetric images at faster speeds with the aim of attempting to achieve *in vivo* imaging with FFSSOCT. To take advantage of this, an MV1-D1312I-160-CL (Photonfocus, Lachen, Switzerland) 1.4 Mega pixel CMOS camera was installed. The maximum acquisition speed of this new camera was 108 frames per second corresponding to 151 Mega pixels per second, approximately twice as many pixels per second as the previous camera. However, to take advantage of the increased speed, the full imaging resolution of the camera needed to be windowed. As the lateral resolution of the objective lens was ~5μm and the optical imaging window was 1x1mm, 2.5 times over sampling could be achieved using only 504x500 pixels. By windowing the acquisition area of the camera to 504x500 pixels, the acquisition speed could be increased to a maximum of 500 frames per second. The 504 pixel window was chosen as the CMOS detector chip would not support an arbitrary amount pixel read out in each row.

The camera provided several additional benefits as well as an increase in acquisition speed One major additional benefit of the camera was a near three-fold increase in the quantum efficiency (QE) of the CMOS detector chip at 850nm (Figure 3-11). Any improvement in QE could be directly translated into an increase in the theoretical maximum SNR (Equation 12) as more photons are detected. Other benefits of the camera include a cover glass free sensor and onboard Linlog® technology.

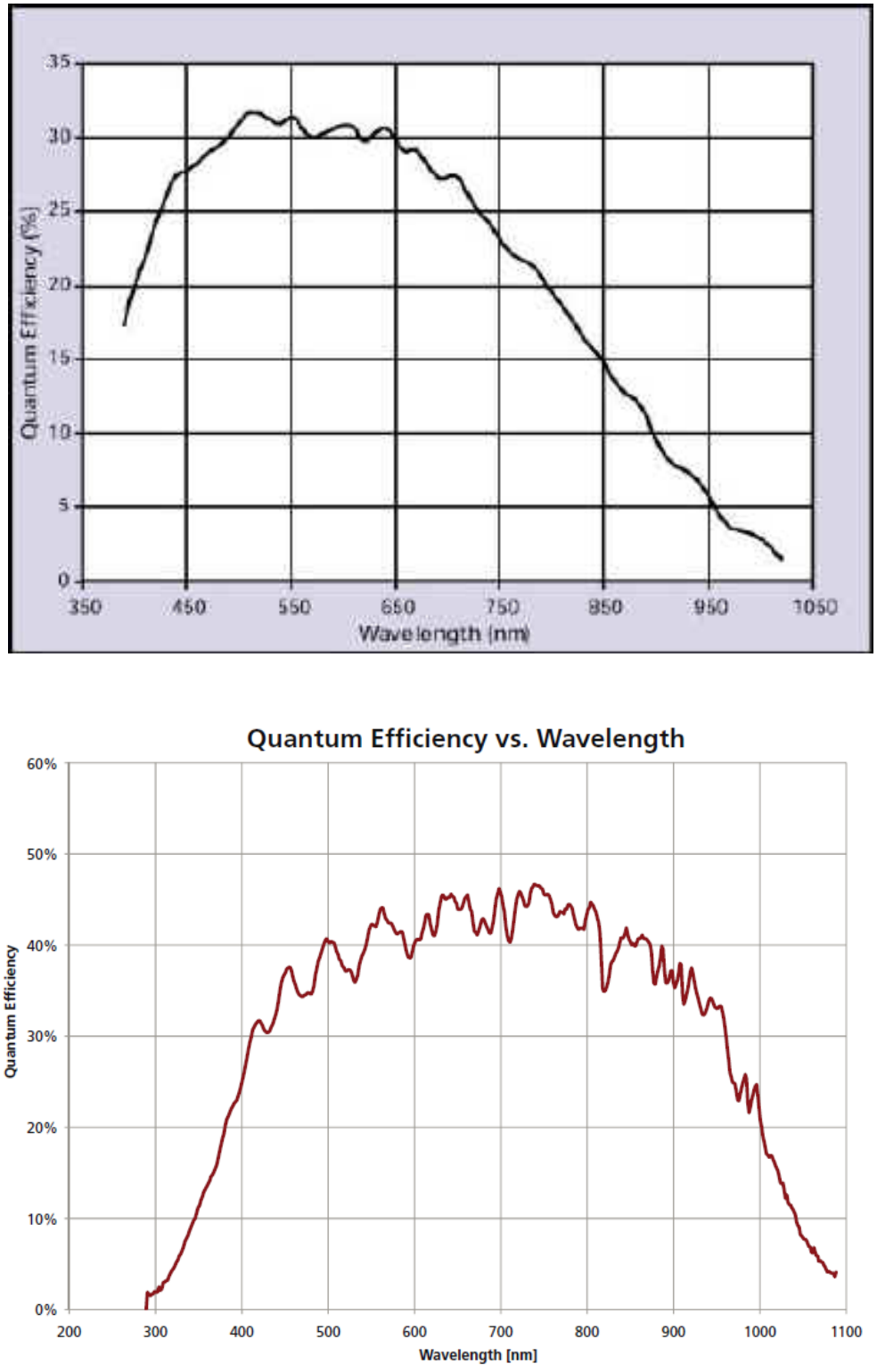

Figure 3-11: Detector quantum efficiency comparison.

Top – The QE curve of the original Silicon Imaging camera showing ~15% QE at 850nm (source: SI640M manual). Bottom – The QE curve of the photon focus camera showing >40% QE at 850nm (source: Photon Focus MV1-D1312I-160-CL manual).

As shown in section 2.4.1 (Figure 2-3), the sensor cover glass on the Silicon Imaging camera created an interference pattern across the image close to the zero delay, creating image artefacts and obscuring structural details of the sample. Without the cover glass, the interference images could be positioned close to the zero delay without obstruction.

LinLog® technology is unique to Photonfocus cameras. It allows onboard response curve changes effectively doubling the dynamic range of the camera. It was believed that this could increase the potential maximum optical power that could be applied to the camera without decreasing the intensity sampling. This was to be achieved by applying an inverse logarithmic gain curve to the camera, decreasing the sampling bins in the darker end of the dynamic range and increasing the optical intensities that could be acquired without saturating the camera.

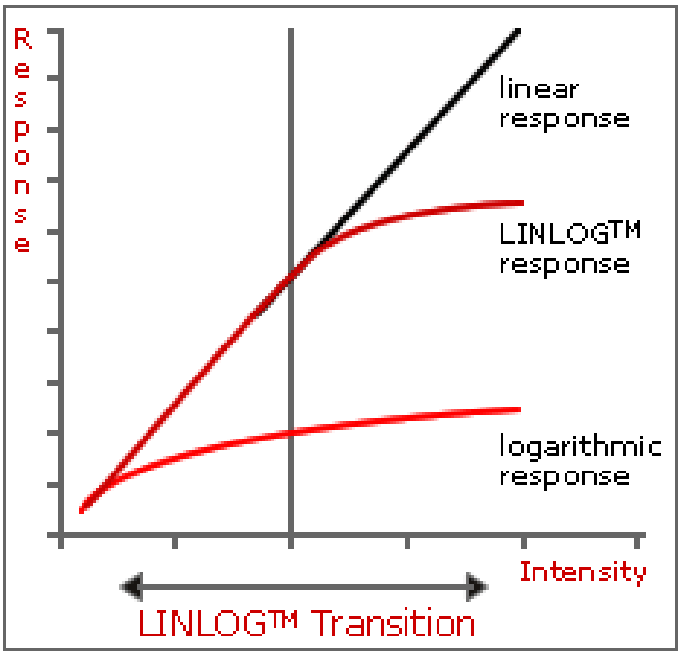

Figure 3-12: Linear vs Linlog® camera response.
Source: Photon focus MV1-D1312I-160-CL manual.

However, as Figure 3-12 shows, the Linlog® response only operates in the high intensity region of the response curve. While the effect would be to increase the dynamic range of the camera, there would be a reduction in the sampling frequency of the high intensities. As this is where the sample information is located in the FFSSOCT spectrum, it was decided that the Linlog® technology would not be appropriate.

3.9 Retinal images

Ex vivo tree shrew retinas were prepared in same way as in section 3.6.

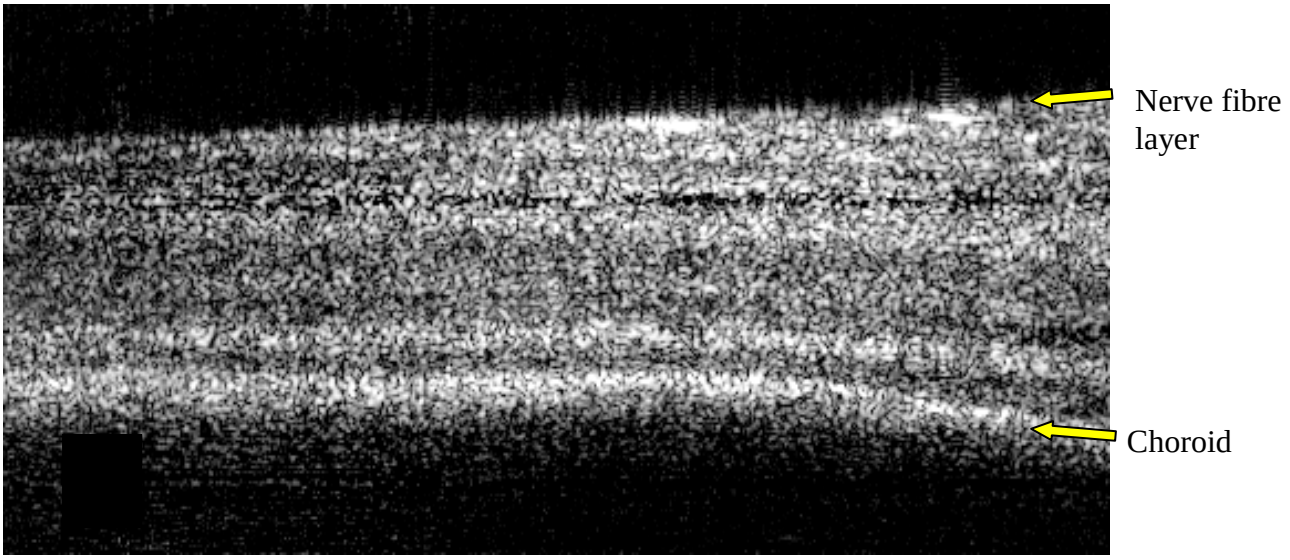

Figure 3-13: *Ex vivo* tree shrew retinal B-scan imaged with the new detector.

One 504x216 (685x390μm) pixel tree shrew retinal B-scan from a stack of 500 recorded in 2 seconds. The choroidal layer is clearly visible below the RPE. The image was averaged 5 times temporally.

The increase sensitivity provided by the increased QE of the photon focus camera can be seen in Figure 3-13 as an increase in the contrast of the acquired image. Compared to Figure 3-6, Figure 3-13 shows less background noise and higher contrast between the layers. Although the size of the camera pixels are reduced by ~20%, the relative size of the speckle and crosstalk in Figure 3-13 remains constant compared to Figure 3-6. This is to be expected as the size of the speckle depends upon the light source and not upon the sampling rate of the camera.

3.10 Illumination arm redesign

To attempt to reduce some of the optical losses within the system, the focussing optics built into the microscope were removed and replaced with individual lenses. The original lenses were designed to focus light from a halogen lamp, transforming the omnidirectional output into an even illumination on the sample. When using a collimated input beam, the original complex system of lenses was not needed and two simple biconvex lenses (20mm

and 25mm) were used in their place. The optical power on the sample was increased from 720µW to 1.2mW, a 66% increase that should provide another 4.5dB to the maximum theoretical SNR. The SNR was measured at 79dB close to the zero delay.

3.11 Retinal imaging with improved sensitivity

Further images of the sample shown in Figure 3-13 were acquired. The increase in optical power made it possible to acquire high contrast retinal images without the need to average multiple images. The single image quality (Figure 3-14) was such as to be able to identify the individual layers of the retina. The image quality and acquisition speed of the system was comparable to that of clinical OCT systems (Topcon 3D OCT Mark 2, Topcon Europe Medical B.V., The Netherlands) at the time, acquiring 500^3 voxel datasets in less than 5 seconds.

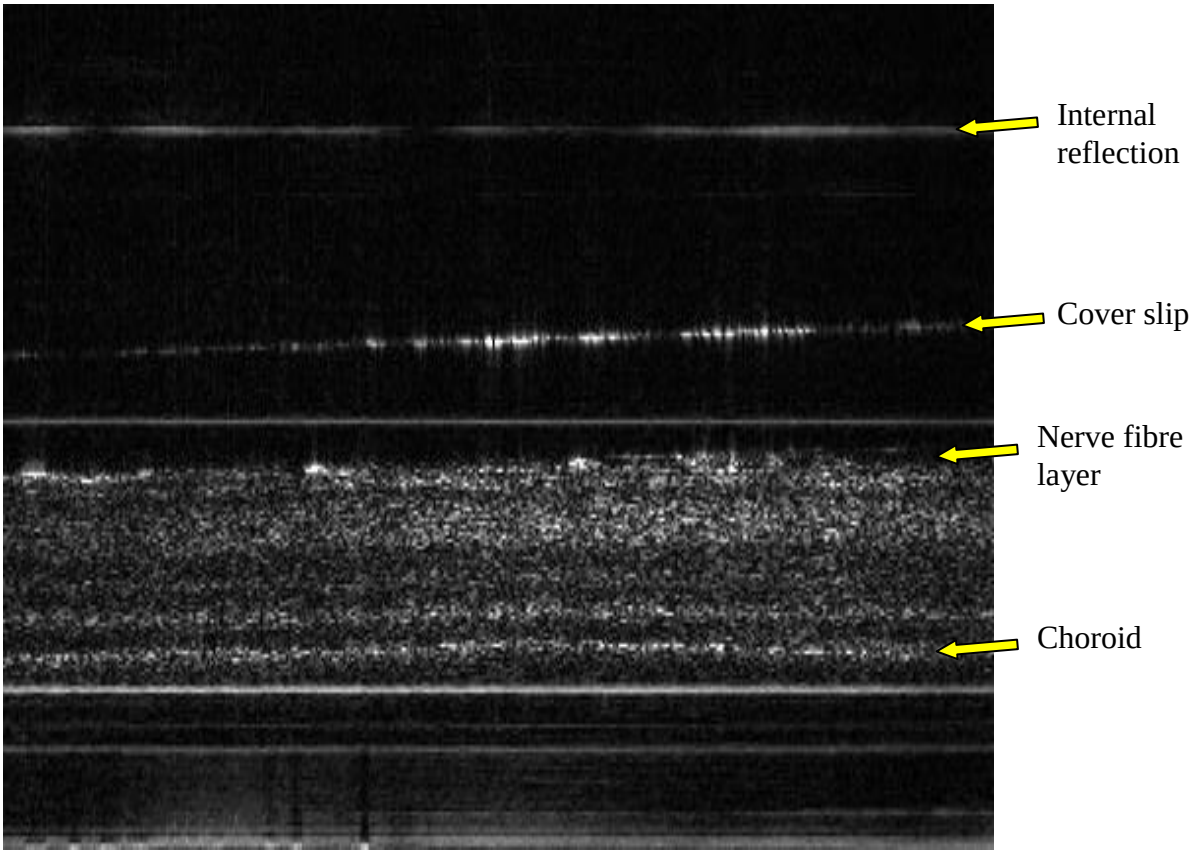

Figure 3-14: *Ex vivo* tree shrew retinal B-scan acquired with the improved SNR.

Image dimensions are 504x242 pixels (685x870µm) acquired in 4 seconds. The image has not had background subtraction applied to it.

As the horizontal background line created by the protective cover glass of the Silicon Imaging camera is no longer present, the remaining horizontal lines can be attributed to reflecting surfaces within the FFSSOCT microscope. With each increase of optical power through the system, the horizontal lines became more pronounced and this presented a significant problem when trying to increase the sensitivity of the system. As a consequence, a maximum amount of optical power can be put into the system before the camera is saturated by the reflection from the surfaces within the system. The amount of reflection can be reduced by using anti-reflection coatings and tilting the objective lenses but due to the very low reflectivity of the retina, the input optical power will always need to be high.

The image quality can be improved by spatial averaging, a commonly applied technique in OCT imaging. This has the dual effect of reducing the image noise (both shot and phase noise – section 4.5) thereby increasing the SNR and averaging out the crosstalk and speckle, increasing overall contrast and layer visibility. The disadvantage is the potential decrease in spatial resolution if the number of pixels averaged exceeds the spatial sampling. Spatial averaging can be performed either by averaging together sequential B-scans or by applying a filter to a single B-scan. Mean, median or mode filters can be used by applying them to a moving square (or rectangle) of pixels. A mean filter will give the most accurate intensity reproduction whereas either median or mode filters will remove outlying pixels (with relatively high or low intensity) from the image.

Despite reducing the spatial resolution, Figure 3-15 demonstrates superior clarity and layer visibility when compared to Figure 3-14. A Labview script was written to perform a rolling 10 frame mean average across of all the images in a tomographic stack.

The spatial averaging was also applied to en face images (Figure 3-17) to reduce the effect of the speckle. However, due to the axial undersampling (see section 5.4.4), averaging 10 frames had a greater detrimental effect on the image resolution. Averaging 5 frames appeared to give the best comprise between resolution and speckle reduction for the FFSSOCT system.

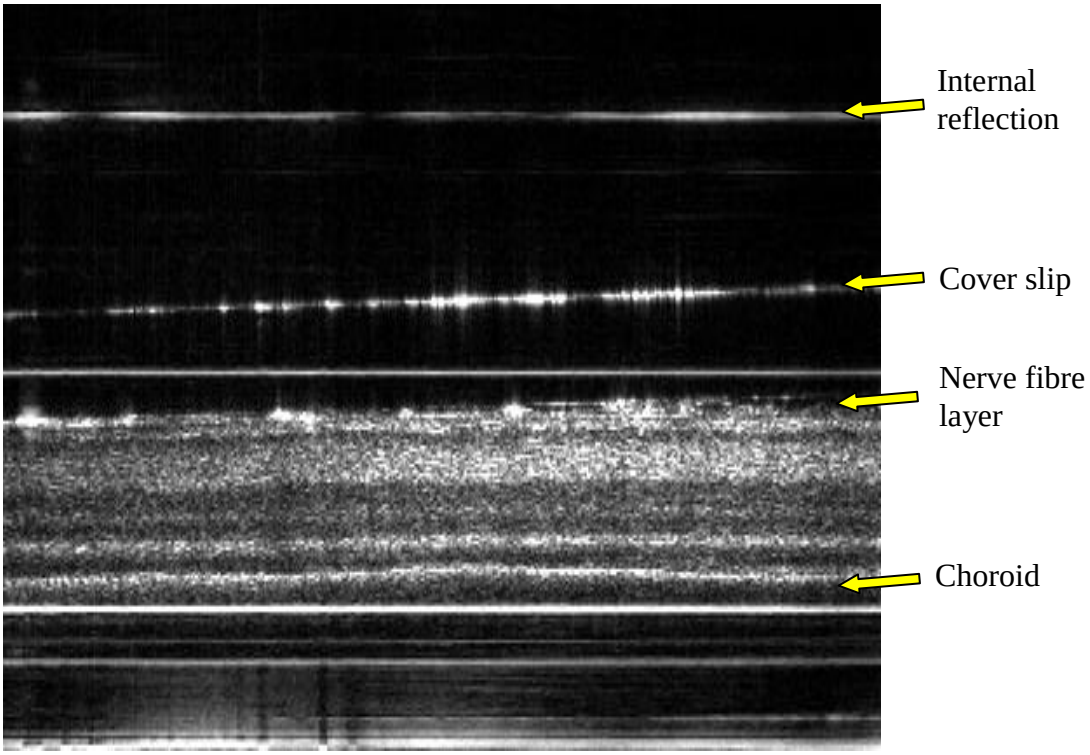

Figure 3-15: Spatially averaged *ex vivo* tree shrew retinal B-scan.

Image dimensions are 504x242 pixels (685x870µm), acquired in 4 seconds. The image is a composite average of 10 sequential frames from a single tomographic image performed in ImageJ. The image has not had background subtraction applied to it and was not zero padded.

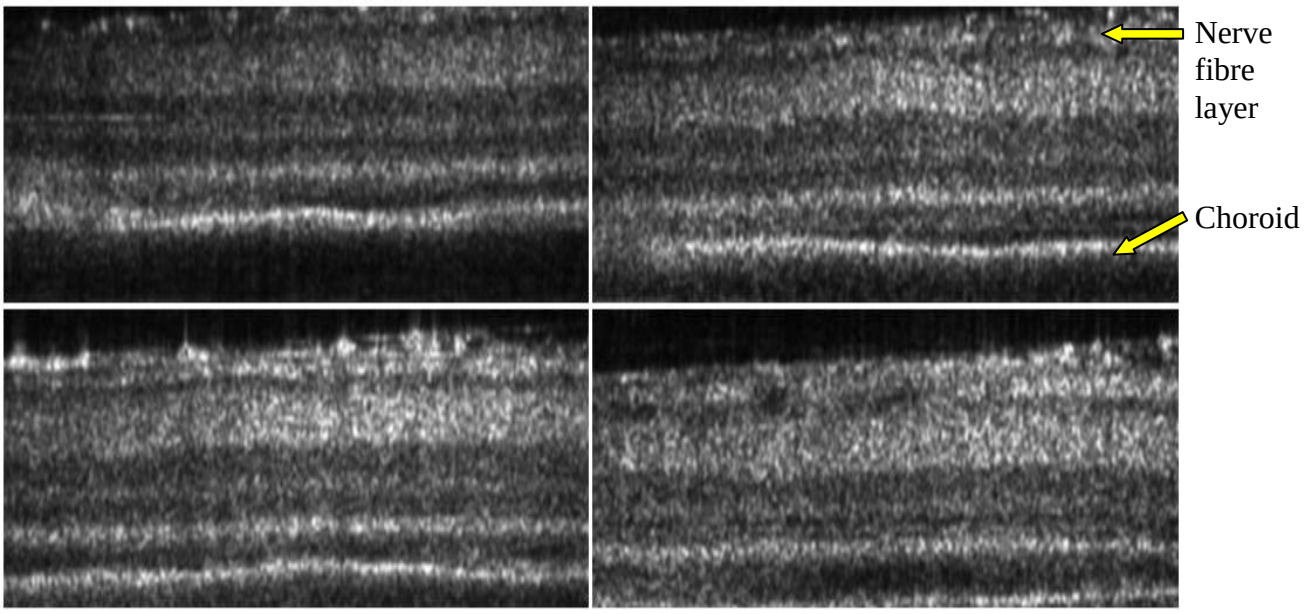

Figure 3-16: Four B-scans of an *ex vivo* tree shrew retina, each comprising of 10 spatially averaged frames.

The 504x500 lateral pixel (685x680µm), 512 axial pixel (870µm) tomogram was acquired in 4 seconds. Each image is comprised of an average of 10 sequential frames from the stack of B-scans at equally spaced positions (every 100 frames), each cropped to 504 lateral pixels (685µm) by 144 axial pixels (520µm) to remove the horizontal background lines.

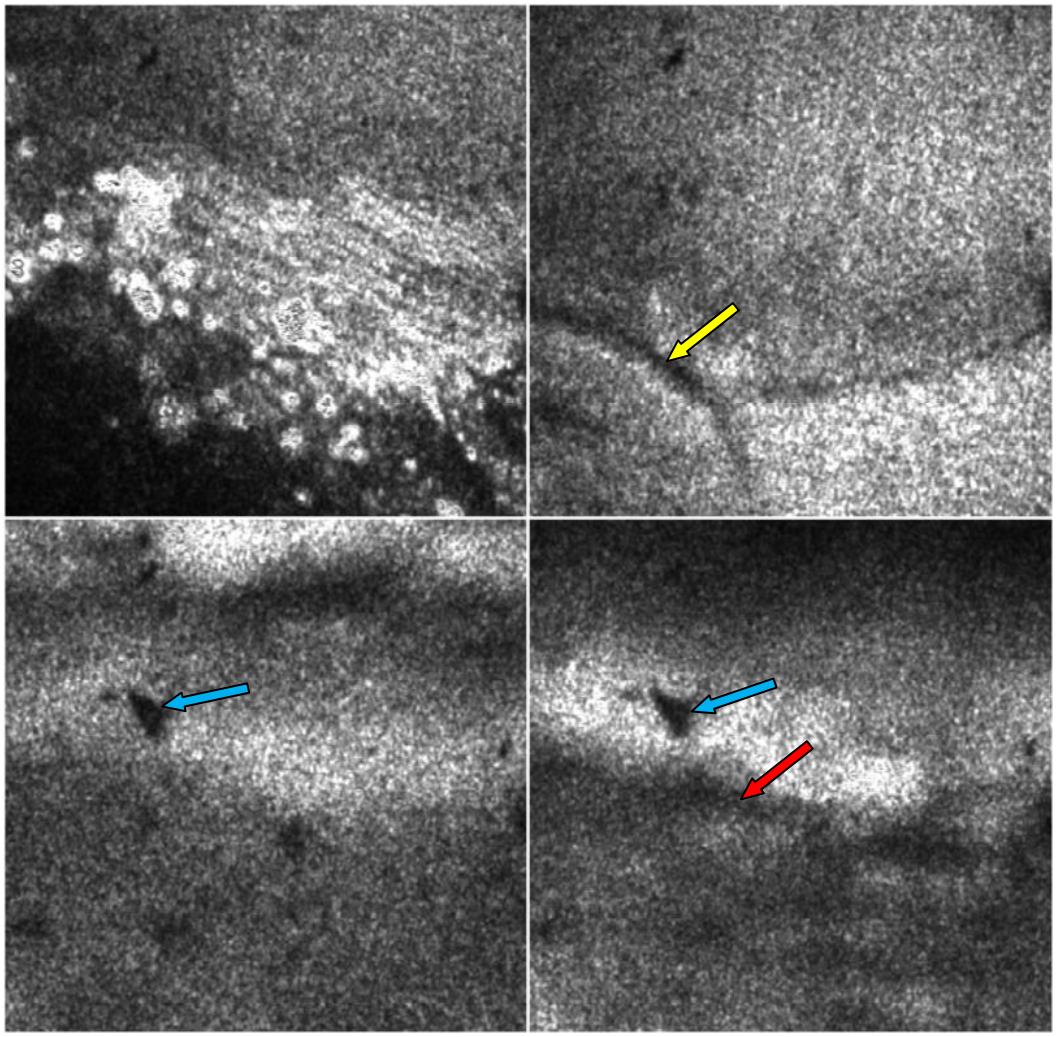

Figure 3-17: Four en face scans of *ex vivo* tree shrew retina, each comprising of 5 spatially averaged frames.

The 504x500 lateral pixel (685x680µm), 512 axial pixel (870µm) tomogram has been resliced in the en face direction. The four en face images were taken at equal depth points from the resliced stack of en face images (every 100µm). The top right image shows some vasculature just underneath the nerve fibre layer (yellow arrow). Larger vasculature can be seen within the choroid in the bottom right image (red arrow). Shadows of debris tissue suspended above the nerve fibre layer can be seen in the bottom two en face images (blue arrows).

3.12 Rat retinal imaging

Rat retina has a different morphology to tree shrew retina[66], there are fewer layers between the nerve fibre layer and the RPE and the choroidal layers below the RPE have more pronounced blood vessels. A rat retina was imaged with the same set up as the tree shrew retina to test if the FFSSOCT system could image the blood vessels within the choroid.

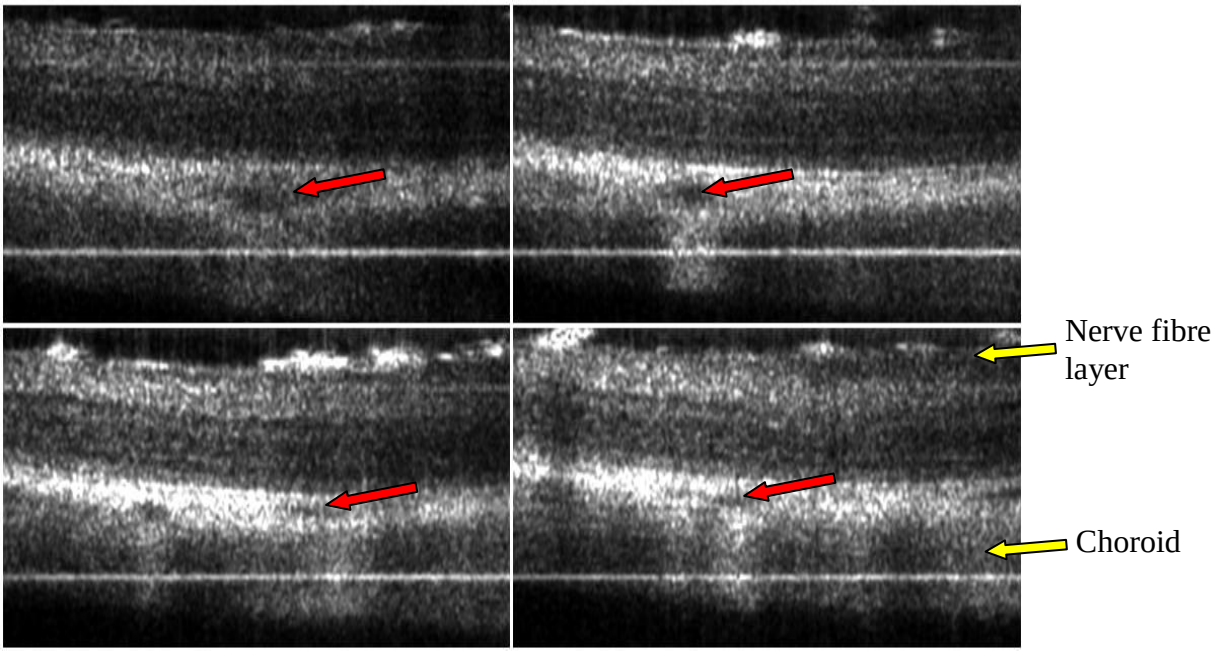

Figure 3-18: Four B-scan images of *ex vivo* rat retina.

Four B-scans (504x191 pixels, 685x324µm) from a stack of 500 (the B–scans shown are 100 images apart). The entire stack was recorded in 4 seconds. The larger relative size of the vasculature in the choroid as compare to the tree shrew retina (Figure 3-16) can be seen as dark holes in all four images (red arrows).

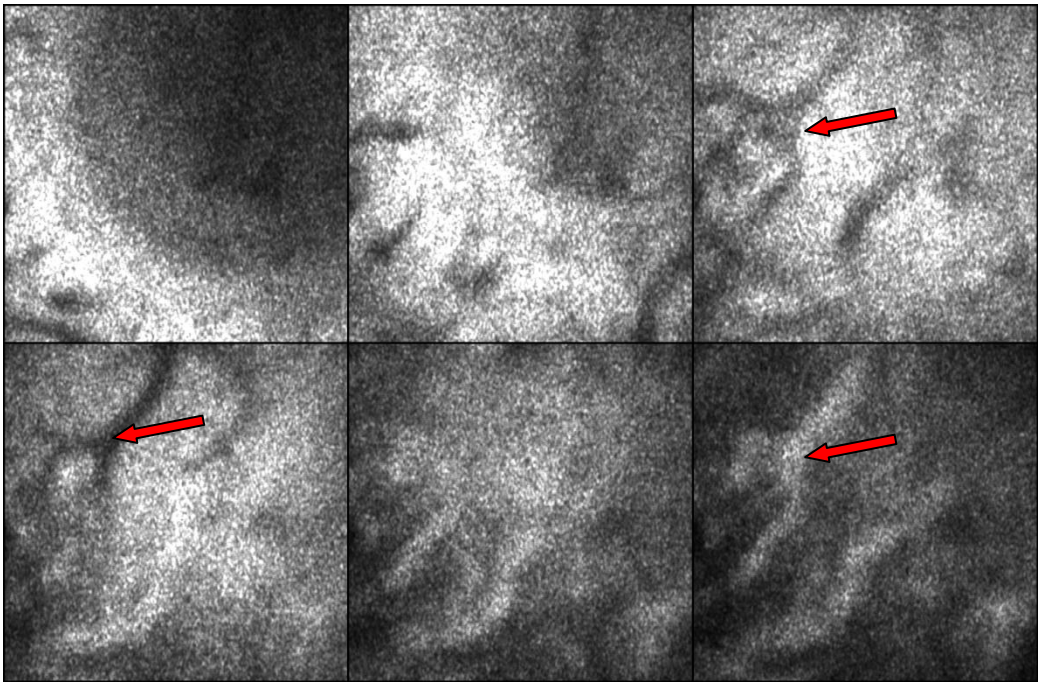

Figure 3-19: Six en face *ex vivo* rat retina scans at different depths.

The images were constructed by reslicing the image stack used to produce the B-scans shown in Figure 3-18. The images show a fly-through (top left to bottom right) of the vessels in the choroid (red arrows) at equal depth intervals (10µm, starting at a depth of 200µm). The tomogram was recorded in 4 seconds; each image is 504x500 pixels (685x670µm).

3.13 Improved Software

The following sections detail the final versions of the acquisition (v2.1) and processing software (v3.1) written for the project and listed in Table 3-2.

3.13.1 Acquisition software

The main components of the acquisition program (Figure A-8 and Figure 3-20) were:

Red – The frame grabber loop of the acquisition process. The loop iterated x number of times where x is the number of specified frequency steps. During the loop, a line of pixels from each acquired frame was read out from the camera and then the frequency generator was triggered, changing the output of the light source to the next frequency. The loop repeated until the specified number of frequency steps has been collected and the data was passed out of the loop as a 2D array of 16 bit numbers. The frame acquisition time was also recorded in each loop. The user interface (UI – Figure 3-20) showed the entire image collected by the camera at each frequency, allowing for direct visualisation of the sample, aiding location and alignment of the target imaging area.

Yellow (block diagram only) – The data from the camera was processed into time domain data. The processing algorithm was a basic version of the full processing used on the FFSSOCT data (detailed in Chapter 4). Dispersion correction, resampling and spectral shaping were omitted.

Blue – 2D sample averaging and background subtraction. This subroutine averaged together sequential B-scans to reduce noise in the image and increase the sensitivity of the FFSSOCT system. Background subtraction used multiple averaged B-scans of the background signal, acquired by blocking the sample arm, to reduce the pseudo-fixed pattern noise in the subsequent B-scans of the sample. The user controlled both of the averaging processes, choosing the number of averages in both cases and turning them on and off independently via controls on the UI (blue box - Figure 3-20).

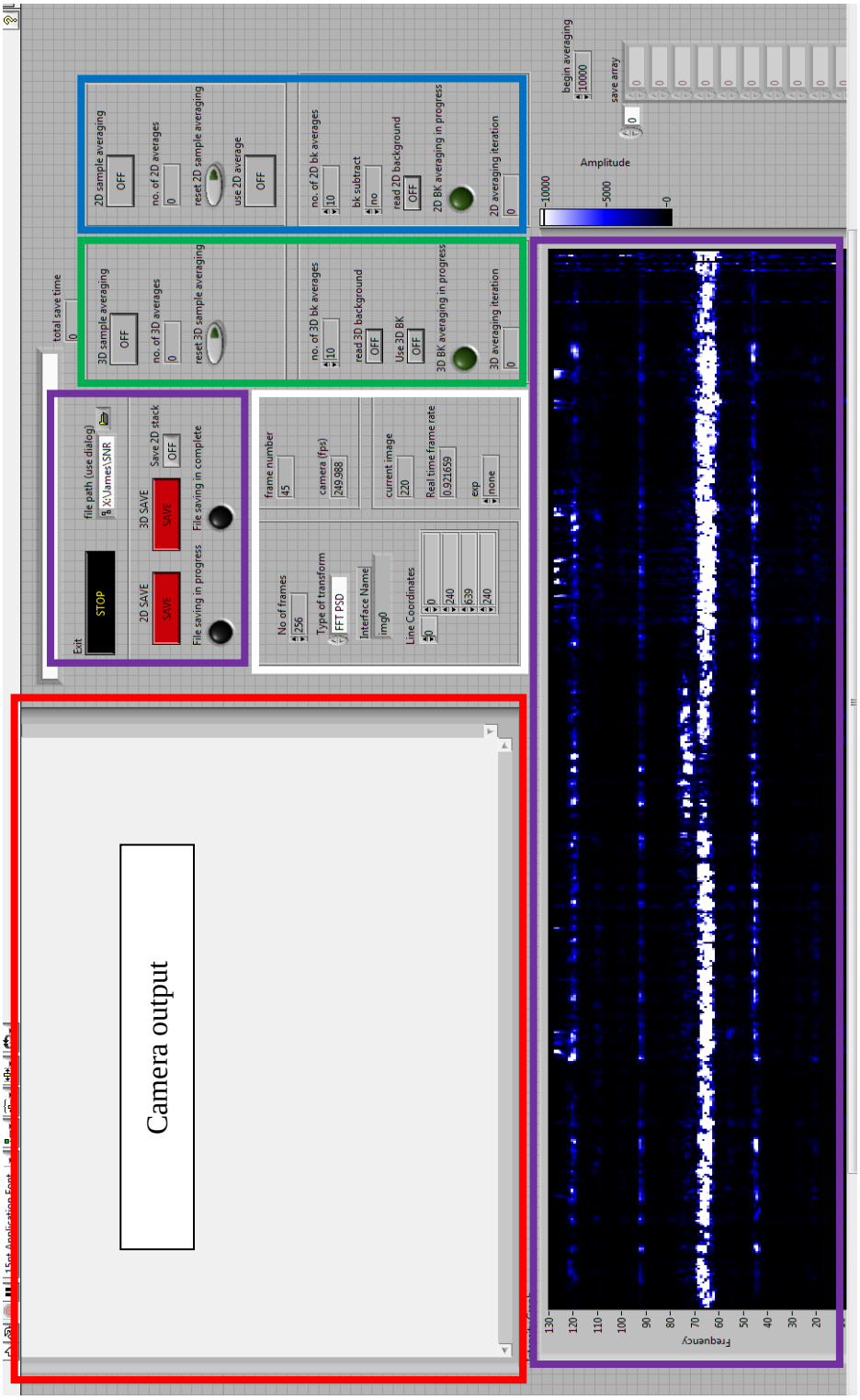

Figure 3-20: The user interface panel of the FFSSOCT acquisition software.
The highlighted areas relate to those shown in Figure A-8 and are explained on pages 67-69.

Green – 3D sample averaging and background subtraction. This was identical to the 2D averaging except that is was applied to the entire 3D tomogram. It significantly reduced the system performance as it requires up to 2GB of free RAM to temporarily store the spectral data during averaging.

Purple – Data saving and image display. A B-scan of the image is shown on the UI (Figure 3-20). The acquired data could be saved either as a single B-scan exactly as is seen on the UI, a single B-scan in the spectral domain (no processing applied) or a 3D stack of spectral domain images.

White (UI panel only) – The acquisition parameters were set here and details of the acquisition speed could be monitored. In addition to setting the number of frequency steps to be acquired, the line of output pixels from the camera could be selected. The acquisition speed of the camera could be viewed as well as the actual acquisition time of the B-scan/tomogram.

3.13.2 Processing software

A comprehensive analysis of the processing techniques used for FFSSOCT is found in Chapter 4. The main components of the FFSSOCT processing algorithm (Figure A-9 and Figure 3-21) are:

Red – Input parameters for the processing. Each step of the processing was optional, allowing the spectral data to be examined in different ways and comparisons between the effect of different processing techniques to be explored. The UI had toggle buttons to enable/disable each processing element though these could not be changed once the processing algorithm has started.

Blue – sequential B-scan averager. Sequential B-scan averaging is a technique to improve the image quality by reducing noise and speckle at the cost of reduced lateral resolution (section 5.4.1). The algorithm separated the 3D data stack, still in its spectral form, into separate B-scans, iteratively averaging together any number of B-scans (set from the UI) into a single B-scan.

Brown – Dispersion correction (see section 4.10 for a detailed description). Due to the identical objective lenses in the two interferometer arms of the FFSSOCT system, dispersion correction was not as essential as for other scanning OCT systems that have complex transfer optics in the sample arm. Though available, it was not used on the majority of images taken. This section of the code was adapted from another Labview program written by Bernd Hofer (BioMedical Imaging Group, Cardiff School of Optometry and Vision Sciences, Cardiff, Wales).

Green – Resampling. An interpolating function designed to remove the non-linear spectral output of the broadsweeper, to reduce the signal chirp and to sharpen the TD signal (section 4.6). The resampling subroutine used a pre-generated set of interpolation values obtained from another program (not shown).

Yellow – Background subtraction. A polynomial fit was used to remove the high amplitude low frequency background signal from the spectral waveform on an A-line by A-line basis. By experimentation, a 5^{th} order polynomial was found to produce the best results.

Purple – Fourier transform. The spectral data was transformed into the TD by an inverse fast Fourier transform (iFFT). In addition, the data was zero padded (section 4.7) once before transform and the ‘absolute’ function was applied to the data after transform to remove the complex imaginary component of the data. The duplicate signal was then deleted from the data.

Light blue – Image rescaling and saving. The TD B-scan data was rescaled by a logarithmic function to reduce the dynamic range, promoting contrast in the low intensities of the image. The scaled data was then resized into a 16bit format and saved as a PNG (portable network graphics) image file.

The processing loop repeated until each B-scan had been processed, generating an individual image file for each B-scan. The sequence of images could then be loaded into an image processing application for further image processing or rendering.

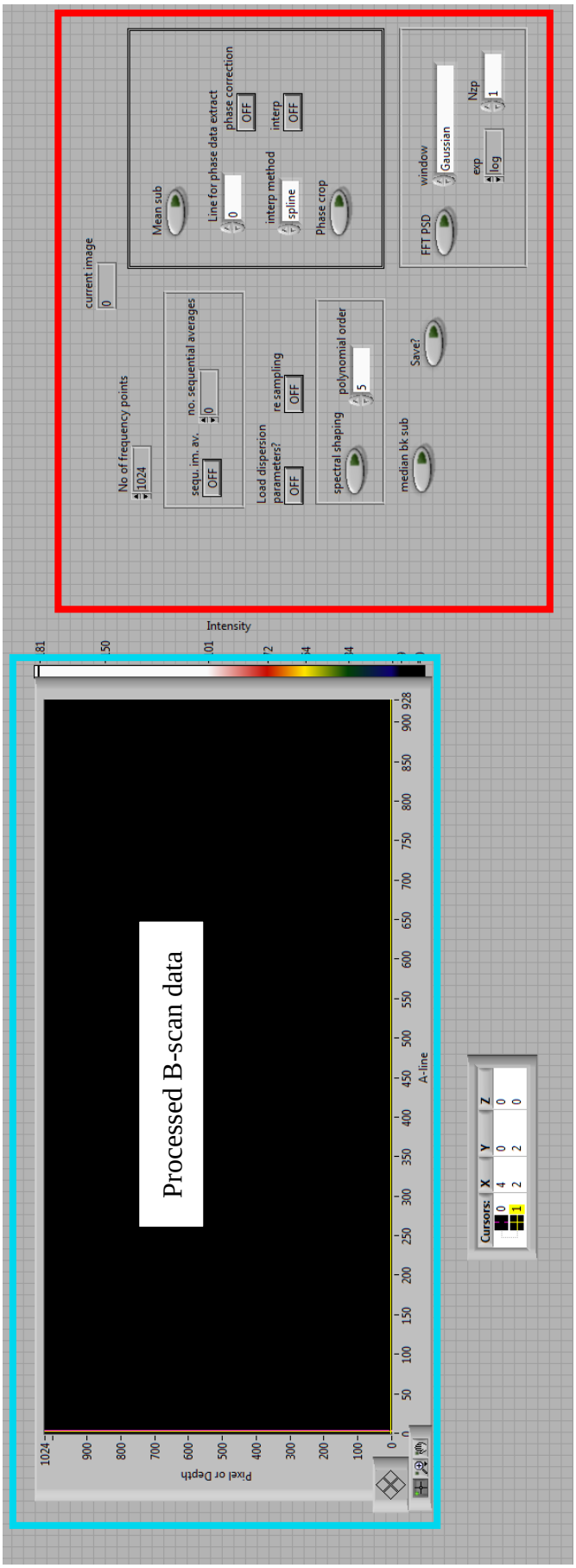

Figure 3-21: The user interface panel of the FFSSOCT processing software.

The program has some initialisation parameters that cannot be modified once the program has begun processing images. The highlighted areas correspond to those in Figure A-9 and are explained on pages 69-70.

3.14 Summary

The main focus of the work presented in Chapter 3 is the improvement of the hardware and software design of the FFSSOCT with the aim of achieving tomographic images of *ex vivo* retinal tissue. The improvements to the FFSSOCT hardware concentrated primarily on increasing the optical signal detected from the sample. This was achieved by increasing the optical power deposited on the sample by redesigning the optical delivery pathway between the broadsweeper and the microscope, reducing the optical loss through the microscope using redesigned optics and increasing the overall optical power by using a booster module. The total improvement in the optical power deposited on the sample was approximately 40 fold (127µW to 5mW). An increase in the detected signal from the sample was achieved by using a different camera with a ~3 times higher quantum efficiency. The result of these improvements was an increase in the system SNR of approximately 20dB.

The FFSSOCT software was continually upgraded over the course of the project, incorporating different features designed to improve both the acquisition and the processing of images. By averaging the images as they were captured by the acquisition software, the sensitivity of the system could be improved without the need for the time-consuming task of processing multiple images.

Initially, topographical images of strongly scattering biological tissue were acquired without the need for image averaging. As the sensitivity of the system was gradually improved over the course of the project, tomographic images of strongly scattering biological matter were acquired and, eventually, images of weakly scattering retinal tissue were acquired.

Ultimately, the improved FFSSOCT system was able to capture images of *ex vivo* rat and tree shrew retina with enough clarity to resolve multiple layers of retinal structure and vasculature up to several hundred microns below the retinal surface.

Further attempts to improve the imaging capabilities of the FFSSOCT system were restricted by the limitations of the hardware; (i) back reflections from within the system

limited the maximum amount of the optical power that could be used and (ii) the limited rotation speed of the spinning diffuser prevented any attempts to increase the acquisition speed significantly.

Chapter Four: FFSSOCT Data Processing

4.1 Improvement aims

The aim of the improvements described in this Chapter was to transform the spectral data from the FFSSOCT to TD data by a similar process to Fourier domain and swept source OCT modalities. At the heart of the process, would be the FFT that would separate the different frequencies in the recorded spectral waveform into a TD image. However, there were several additional stages to the processing of the spectral data, before and after the FFT, which were both necessary and designed to improve the quality of the output image.

The remainder of this Chapter is dedicated to describing the processing steps outlined in Figure 4-1, highlighting the similarities and differences between the FFSSOCT and FDOCT/SSOCT data processing. Each step of the processing will be accompanied with an A-line from an example dataset of a mirror collected during the final stages of the project, giving a clear visualisation of the effect of each step.

4.2 Introduction to OCT data processing

The software required to process the images was written in Labview during the project and is unique to the FFSSOCT instrument (section 3.13). The tomographic spectral data was separated into B-scans and then processed on an A-line by A-line basis (Figure 4-1).

The A-line was taken from the centre of a 504 pixel B-scan located at the centre of the tomogram (B-scan 250 of 500). Each tomogram had 1024 frequency steps and each was recorded in 4 seconds with the mirror axially located at pixel 100 (approximately one fifth of the total axial range of 512). As with the SNR measurements, an ND filter was used to reduce the optical intensity on the camera to avoid saturation.

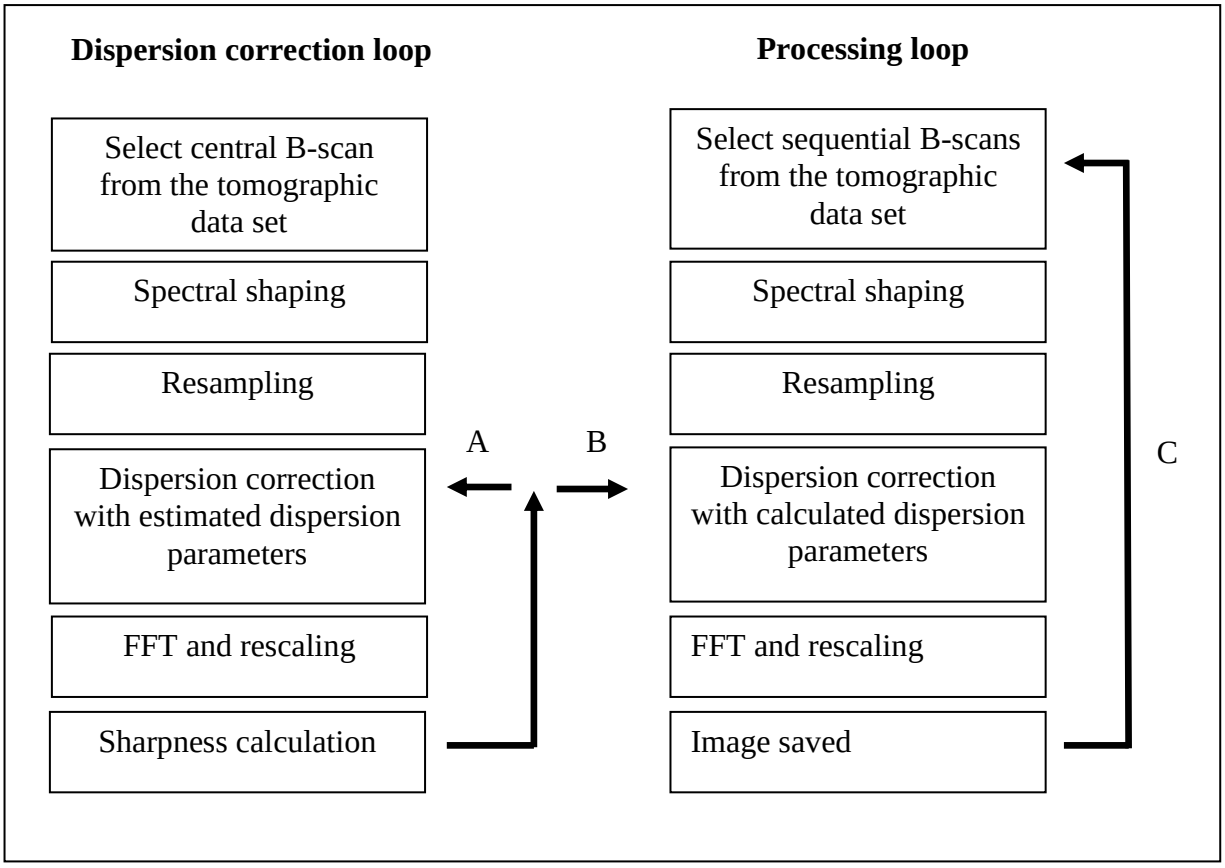

Figure 4-1: Flow chart showing the processing steps required to transform the FFSSOCT spectral data into TD data.

The dispersion correction loop is run first, iteratively calculating the optimum dispersion parameters (loop A). The processing loop begins after the optimum dispersion parameters have been found, passing them through path B and ends when each of the B-scans has been processed and saved (loop C).

4.3 Spectral subtraction and shaping

The first processing step performed was to segregate the data using nested loops; the first to separate the 3D array into 2D B-scans and the second to separate the B-scans into individual A-lines. When all the A-lines from the B-scans had been processed, each B-scan was saved on the hard drive of the pc inside the first loop and the memory allocated to the A-lines was released for the next B-scan. This ensures that the entire tomogram was not stored in the pc memory at once, avoiding any critical errors by over filling the memory on the pc.

Inside the second nested loop, each A-line was transformed from the frequency domain into the TD. The process began by removing the zero frequency from the spectral waveform. This frequency was the result of the constant offset from zero, known as the DC offset, on which the spectral waveform containing the sample information appears. From Figure 4-2, this offset was approximately 2300 and therefore the peak to peak amplitude (around 0) of the detected frequency was 4600 resulting in a TD amplitude of 2300 at 0 axial depth (Figure 4-3). Removal of this high amplitude peak at 0 was important as it dwarfed the signal from the mirror (amplitude ~500), reducing the dynamic range of the final image after it was compressed during saving.

As well as the DC offset, there was a low frequency component in the spectral waveform that needed to be removed; it can be seen in Figure 4-2 as an undulation in the high intensities and in Figure 4-3 as a slight broadening of the DC peak at pixel 0. These frequency components were the combined result of the spectral properties of the optical path through the FFSSOCT system and the spectral response of the camera. There may also be a contribution from the broadsweeper light source despite its automatic power control feedback system.

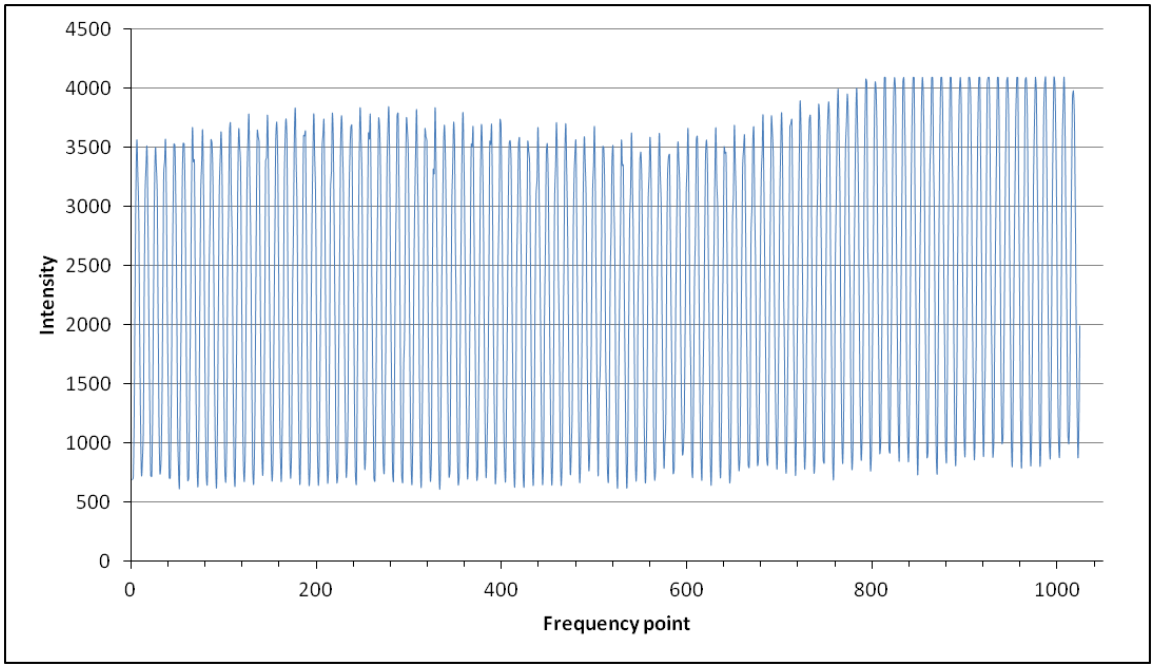

Figure 4-2: A-line data from a mirror with no processing applied.
The higher intensity values at frequencies above 800 are cropped by the saturation limit of the camera (4096).

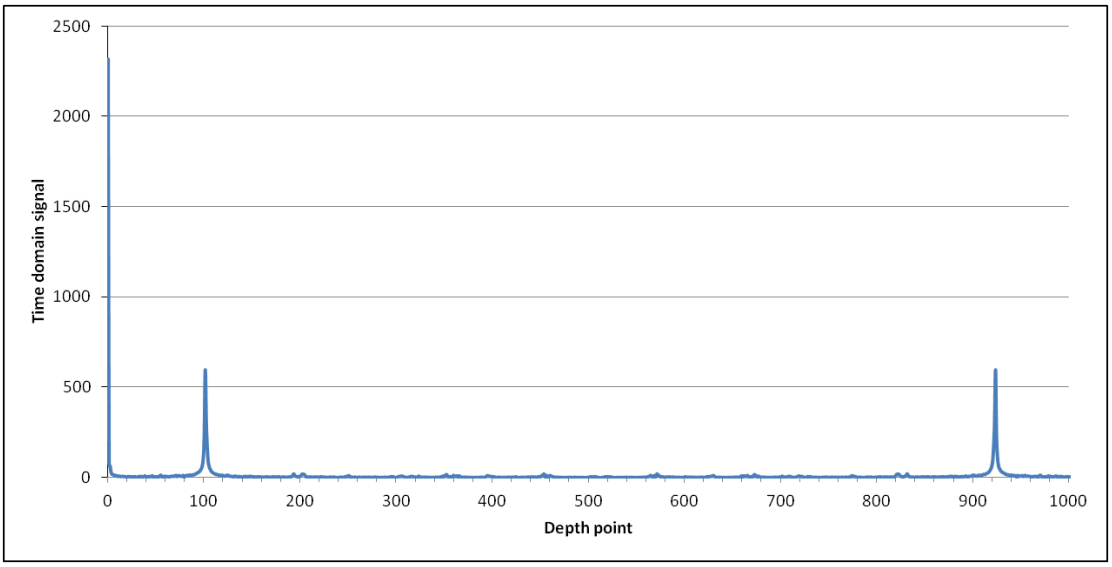

Figure 4-3: A-line data from a mirror after Fourier transform with no processing applied. The dual signal peaks (at 100 and 924) are the result of the Fourier transform process. The axial depth information is mirrored around the centre pixel (512).

To remove the unwanted low frequency component from the spectral waveform, a 5th order polynomial function was used. The polynomial function is an algorithm in Labview that computes the best fit to a 1D array of data points. A 5th order polynomial was chosen as it provided the best fit to the data and was the most effective at reducing the DC offset in the A-line. The 5th order polynomial was fit to the data (Figure 4-4) and then subtracted from the original spectral waveform (Figure 4-5), effectively removing the DC component (Figure 4-6).

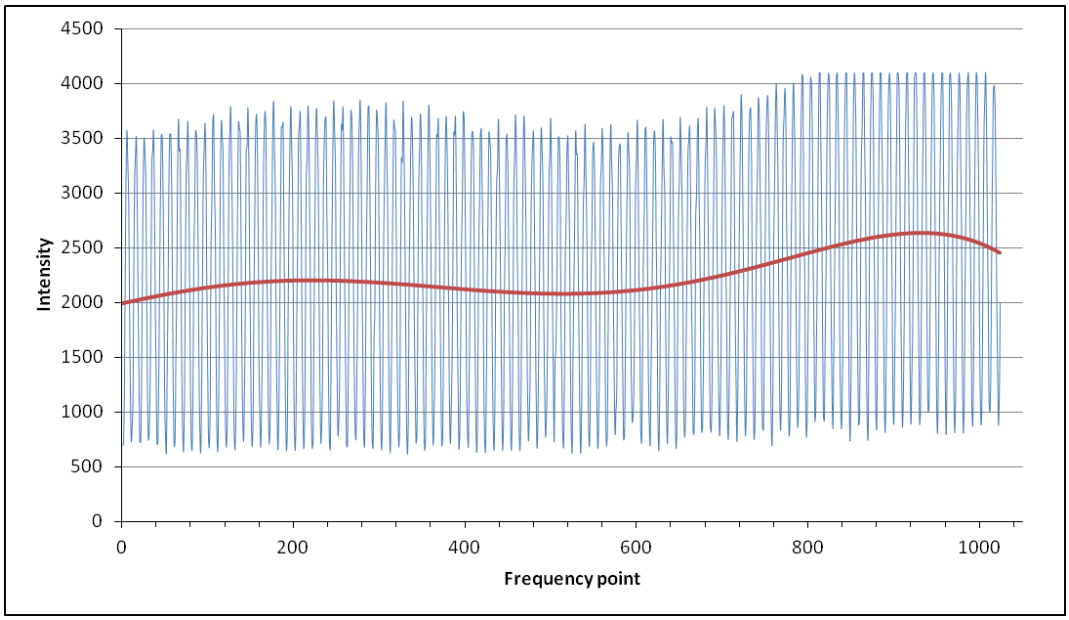

Figure 4-4: Spectral data from a mirror with a 5th order polynomial fit.

Traditional frequency domain systems use an average spectral waveform (from a sum of the spectral waveforms within a B-scan) to remove the low frequency signal, however this was found to be less effective than using a polynomial fit due to the high variation between spectral waveforms (see section 4.5 on background subtraction).

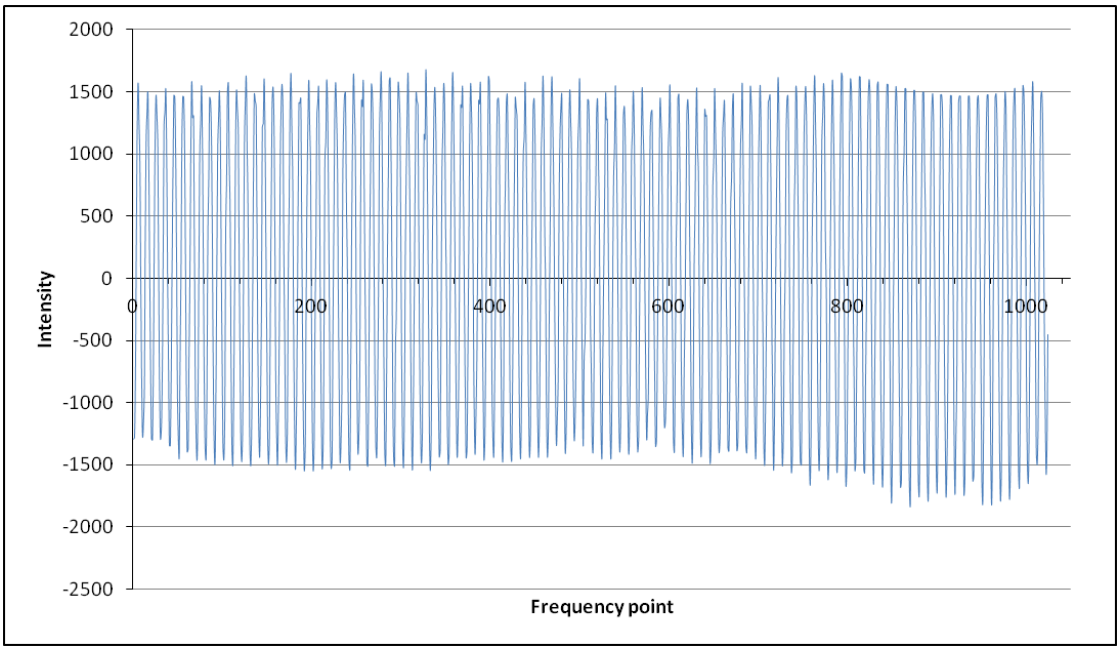

Figure 4-5: Spectral waveform from a mirror after removing the low frequency components.

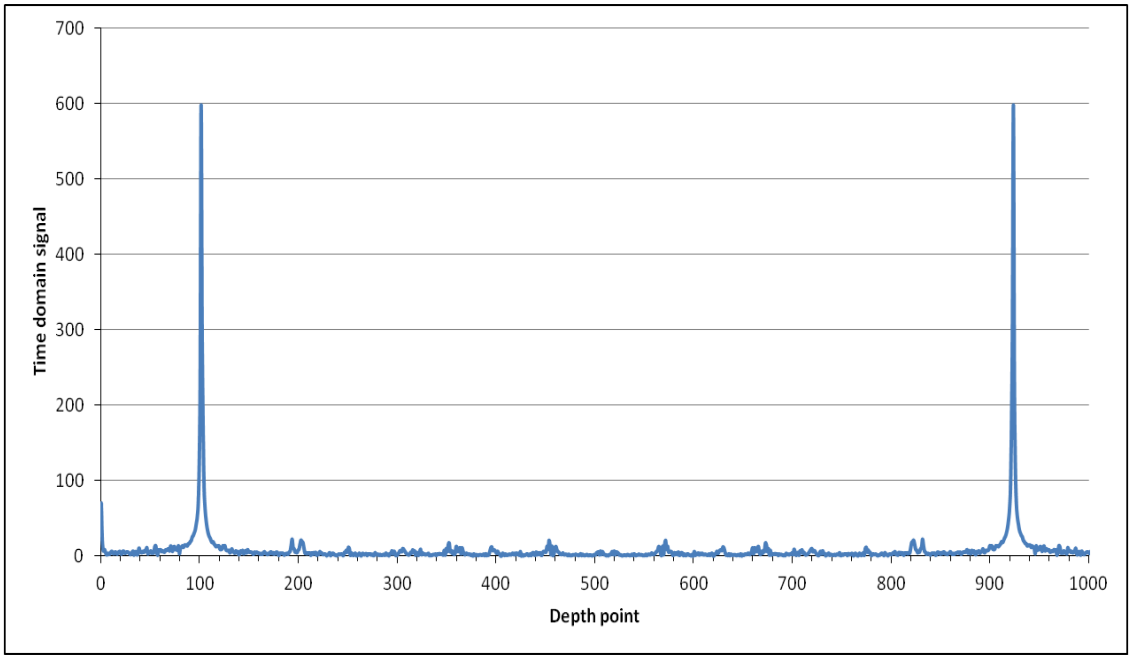

Figure 4-6: Fourier transform of the spectral waveform after removing the low frequency components.

The residual DC offset at depth point 0 can be cropped from the final processed image.

4.4 Spectral shaping

Spectral shaping is used to counteract the negative effects of applying a Fourier transform to a finite (discrete) dataset. The sharp decrease in signal intensity at the boundaries of the frequency acquisition window (0 and 1024) can result in an increased time domain peak width and side lobes around the signal (spectral leakage). This effect can be combated by applying a shaping window to the data that reduces the amplitude of the spectral waveform at the boundaries. A Gaussian filter was used to achieve this with a standard deviation of 0.3, which was found to give effective reduction of the side lobes[52]. Other filters can be used to achieve the same effect such as the Hann or Hamming windows[67]. Each windowing function produces slightly different effects, though all are designed to reduce the amount of spectral leakage.

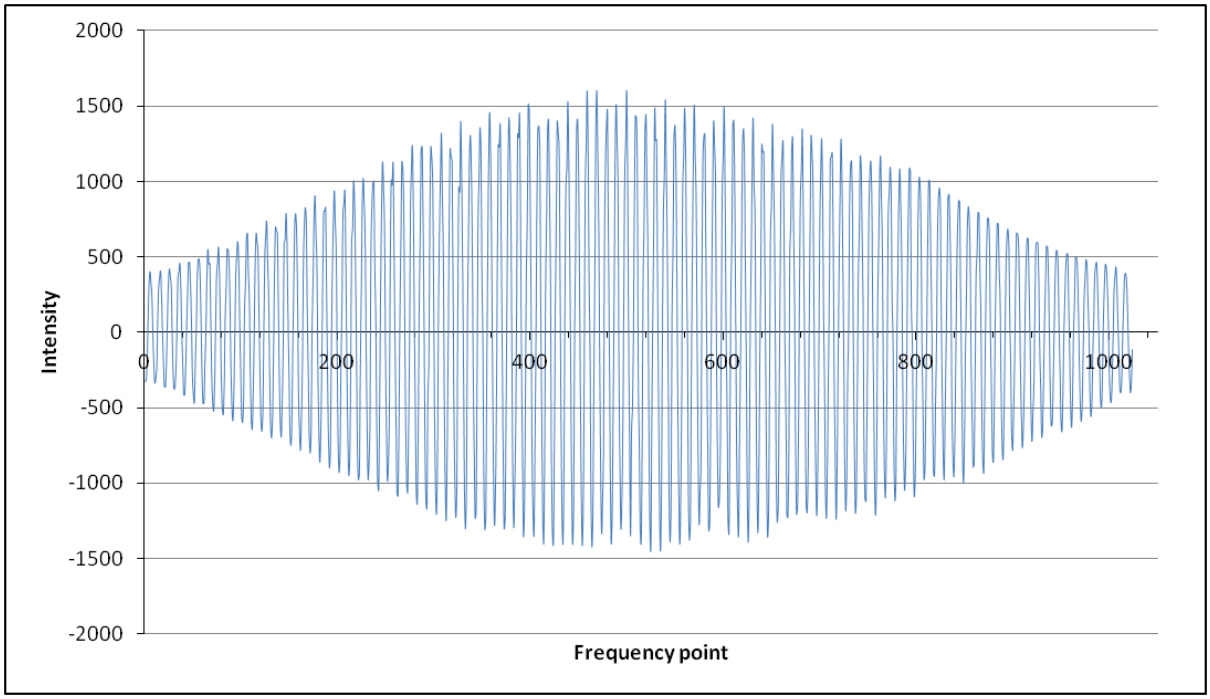

Figure 4-7: Spectral waveform data from a mirror multiplied by a Gaussian filter.

By reducing the intensity of the spectral waveform, the amplitude of the TD signal is also decreased (Figure 4-8). As the interferogram for the mirror has substantially higher amplitude then the noise components, seen in Figure 4-8 as ripples across the time domain image), the filtering has a greater effect on the signal amplitude than the noise. However, as the SNR is a ratio of signal to noise, the sensitivity of the system is not affected. In

addition to the reduction in signal amplitude, the axial width of any peak is reduced, increasing the fidelity of any measured peak position.

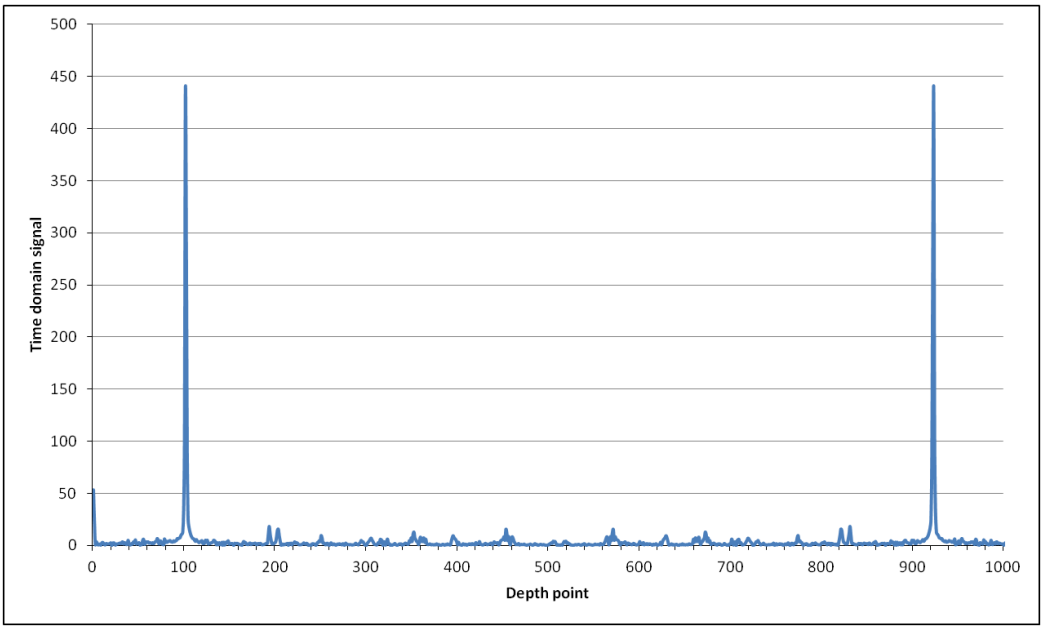

Figure 4-8: Fourier transform of the spectral waveform data multiplied by a Gaussian filter. The Gaussian had a standard deviation of 0.3.

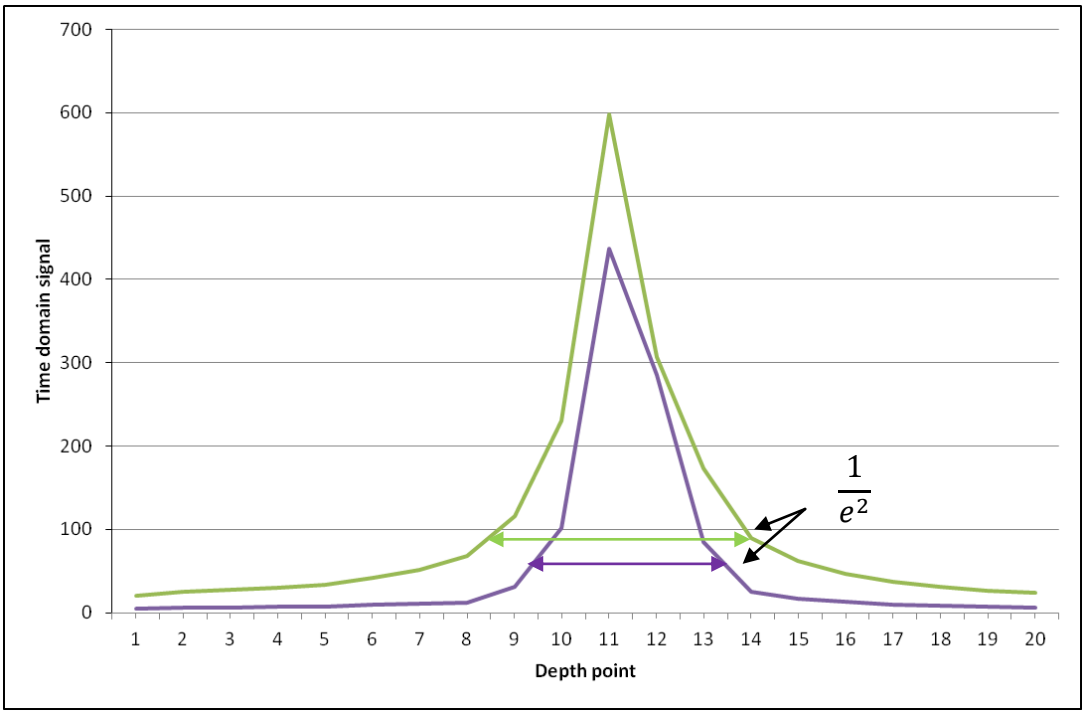

Figure 4-9: Comparison of the effect of Gaussian shaping.

The signal peak was taken from point 100 (Figure 4-8). The effect of the Gaussian filtering (purple) can be seen as a reduction in the signal amplitude and in the axial width. The reduction in the SNR (12%) is relatively less than that of the axial spread (23% reduction at $1/e^2$).

4.5 Background subtraction

Background subtraction is an important step in the processing of any frequency domain OCT image. Any photons recorded by the camera when no sample is present are transformed into a background signal in the output TD image. The background signal is comprised of two parts, static (or fixed pattern) signals that do not change between A-lines and dynamic noise that varies each time a camera pixel is read out. The main contributor to the dynamic noise in FDOCT is shot noise, the statistical variance of the arrival of photons on the detector. Due to its random nature, it cannot be reduced with background subtraction but does respond very well to image averaging, either in time by long exposures or recording multiple images or by spatial averaging (using sequential B-scans).

The static signals are caused by any photons from the light source that reach the detector but do not originate from the sample. The majority of these recorded photons come from the reference arm signal, creating a high amplitude, low frequency waveform in the frequency domain and a high amplitude signal around the zero delay in the TD image. Stray photons will also reach the detector from any reflecting surfaces within the system, also creating a signal around the zero delay of the TD image. Any constant change between the recorded intensities of different wavelengths between each recorded spectral waveform on the detector will cause static lines to appear across every B-scan. This may be caused by dust or particles in the spectrometer (FDOCT), chromatic aberrations in the optics (full field OCT), the fixed pixel readout response of the camera (FDOCT and FFOCT) or the spectral shape of the light source (described above). For FFSSOCT, the static lines shown in (Figure 4-10) originate from the microscope objective lenses.

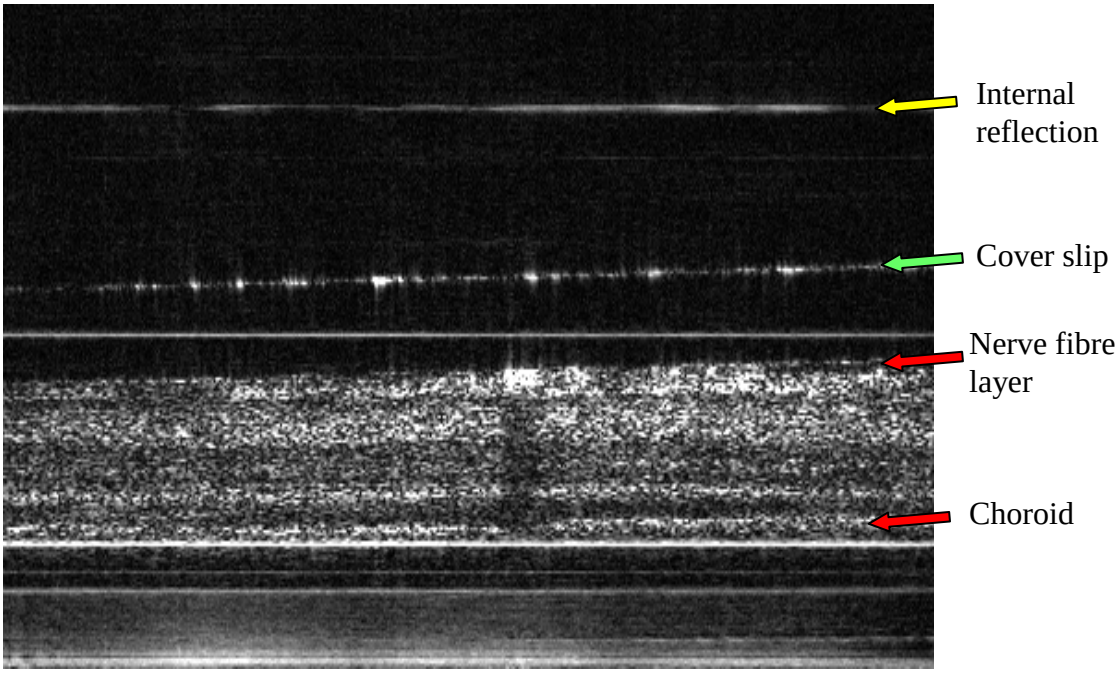

Figure 4-10: *Ex vivo* tree shrew retinal image showing pseudo-fixed pattern background noise.

Tree shrew B-scan number 325 taken from a stack of 512 images. The image is 504x244 pixels (685x870µm) and was recorded in 4.1 seconds. Horizontal lines corresponding to background noise are located at 27, 34, 44, 121 and 205 pixels from the bottom of the image. The data has not been zero padded.

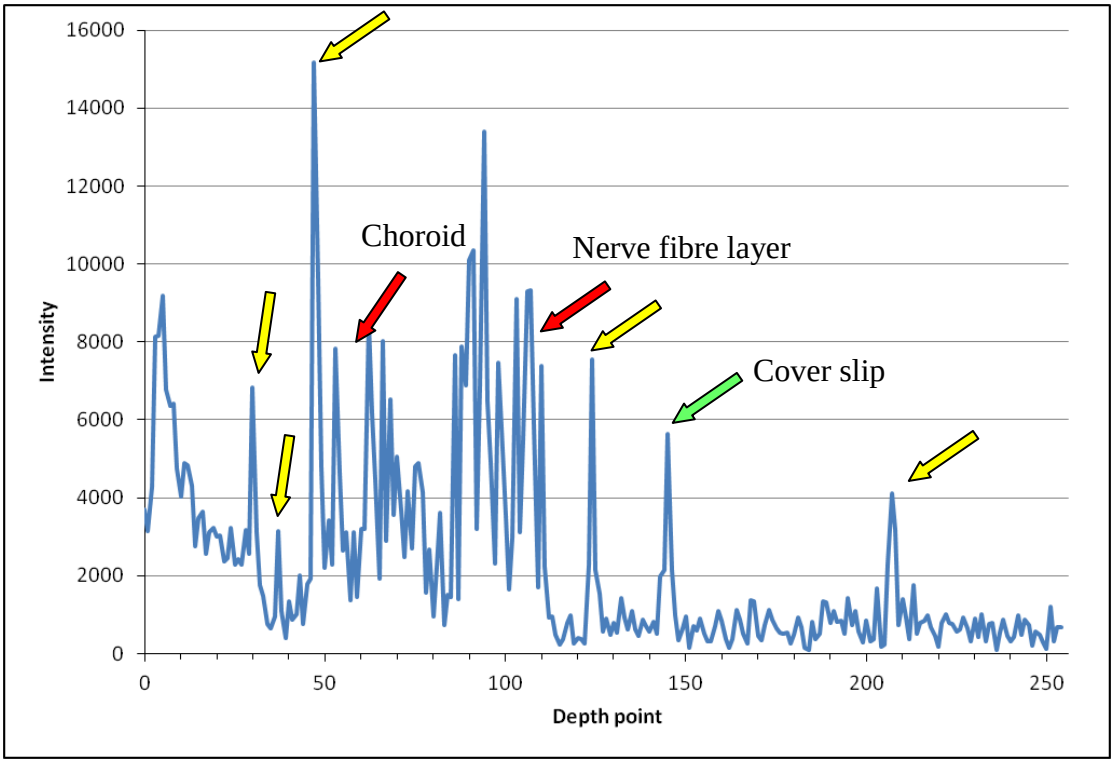

Figure 4-11: An A-line from a tree shrew retinal image at lateral position 250.

Taken from Figure 4-10, the relative intensities of the fixed pattern noise (pixels 27, 34,44,121 and 205 – yellow arrows) and the image data (pixels 50 to 110 – red arrows) can be seen.

The static noise pattern can be removed in a number of ways. The simplest and most computationally undemanding way is to record the background noise with no sample present and subtract the result from the images of the sample acquired thereafter. This method (Method 1) may be done as the image is recorded in order to reduce the required dynamic range of the file type and therefore, the required storage needed to save it. The disadvantage of using this approach is that it may be affected by long-term changes in the intensity of the static noise pattern caused by temperature fluctuations or by any adjustment of the optics within the system. Alternatively, a long-term background subtraction can be achieved by creating a background image on a per B-scan basis by averaging all the spectral waveforms together, effectively averaging away the signal from the sample whilst leaving the static noise pattern (Method 2). The resulting 'noise spectral waveform' can then be subtracted from each spectral waveform within the B-scan and the process repeated for each B-scan in the tomogram.

A possible hardware solution to this problem would be to use a balanced detection system, whereby the reference signal is acquired separately from the signal resulting from the interference of the reference and sample arms. The reference signal represents the background information from the system and can be numerically subtracted from the signal with the sample information encoded in it[68]. This requires multiple cameras and precise optical alignment but can be achieved in full field imaging systems[69].

Unfortunately, the images recorded with the FFSSOCT system had a significant amount of fluctuation between A-lines and B-scans that makes the task of background subtraction more challenging. The background horizontal lines (Figure 4-10) have a pseudo-fixed pattern noise characteristic, their position within the image remains constant between A-lines, B-scans and tomograms but their intensity fluctuates on both a long and a short-term basis.

The root cause of the long-term fluctuation in the intensity of the horizontal lines is not clear. The timescale for the fluctuations was on the order of minutes suggesting a temperature-induced effect although the scale of the intensity change is much larger then would be expected for this to be true. Short-term fluctuation in the fixed pattern noise intensity are due to a combination of unavoidable noise terms, such as shot noise, and

noise terms inherent to FFSSCOT, the random intensity per A-line caused by the spinning diffuser and phase noise.

It can be seen in Figure 4-12, the noise intensity fluctuations have high and low frequency components and an overall intensity variation on the order of 2000 around a background level of ~12,000. If background subtraction Method 2 was applied on the data in Figure 4-11, the resulting image would still have the highly varying horizontal signal with an intensity variation of 2000 (albeit with lower background intensity level) obscuring the sample data. Figure 4-13 shows the effect of applying background subtraction Method 2 to the tree shrew B-scan from Figure 4-10. The horizontal pattern noise has been reduced but the intensity variation in the subtracted background signal has left dark and light patches across the B-scan.

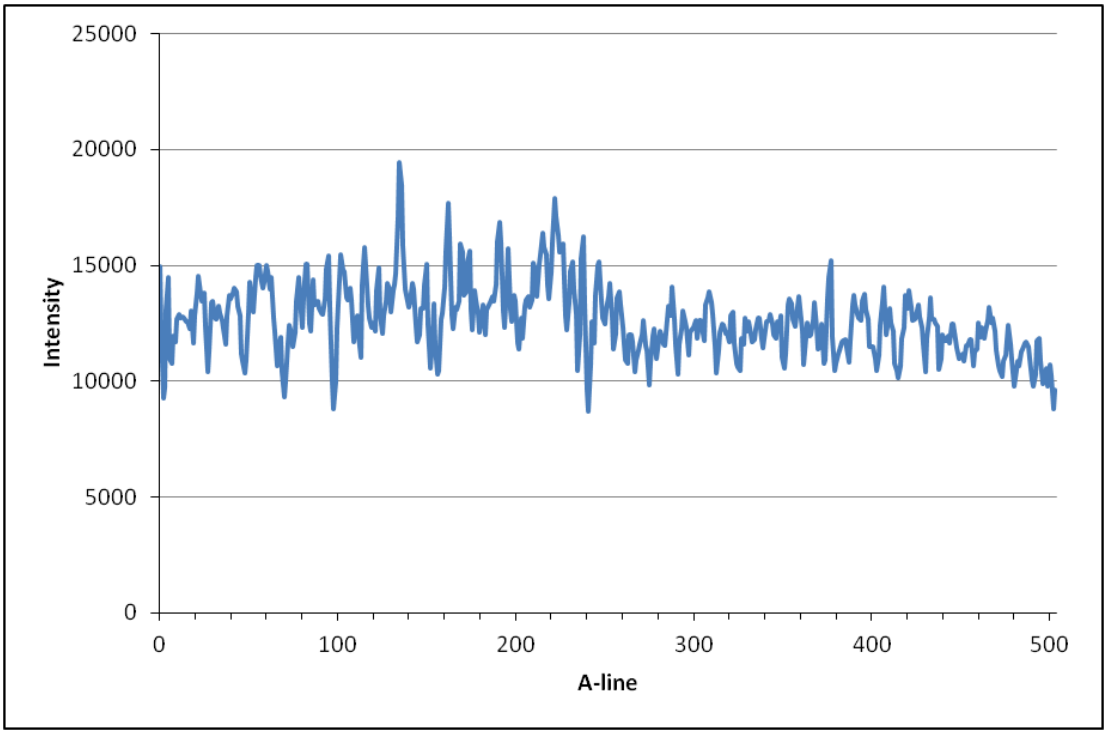

Figure 4-12: The short-term fluctuation in intensity across the fixed pattern noise at axial position 44.

The noise profile from the brightest horizontal line in Figure 4-10.

As discussed above, the shot noise is small compared to the signal and the majority of noise in the images originates from the system diffuser and phase noise. The fluctuating system noise terms are significantly larger than the shot noise and scale linearly with the

intensity of the light source. This creates a significant problem when using a higher power optical source, the associated noise fluctuations of the pseudo-fixed pattern noise become greater and removing them becomes more difficult. Shot noise also scales with intensity but not linearly, it scales as the square root of the power on the detector.

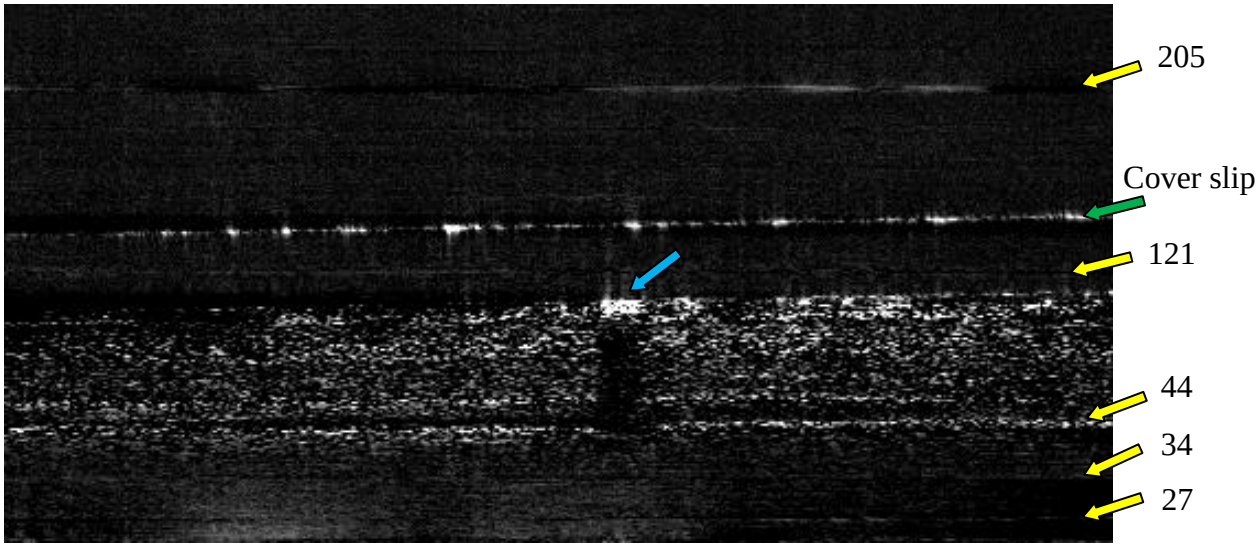

Figure 4-13: *Ex vivo* tree shrew retina with the horizontal noise pattern suppressed by Method 2.

Ex vivo tree shrew B-scan number 325 taken from a stack of 512 images (Figure 4-10). The image is 504x244 pixels (685x870μm) and was recorded in 4.1 seconds. The horizontal lines corresponding to background noise have been reduced leaving dark lines (locations at 27, 34, 44, 121 and 205 pixels from the bottom of the image – yellow arrows). The data has not been zero padded. A dense piece of retinal debris on the nerve fibre layer has cast a shadow down the image (blue arrow).

The background subtraction problem then becomes clear: the large short-term fluctuations in the fixed pattern noise caused by the system render background subtraction Method 2 unusable and the long-term variation in the fixed pattern noise makes the use of background subtraction Method 1 difficult. Ultimately, the background subtraction was performed by recording a separate image and subtracting it during the image processing as per Method 1. Initially, as the fixed pattern noise had higher amplitude than the sample signal (Figure 4-11) and as the background image was recorded separately, the working dynamic range of the system was reduced. This was resolved by including the background subtraction in the acquisition software loop, saving each image with the stored background data already subtracted from it (section 3.13.1).

While the detrimental effect of these noise lines can be limited by background subtraction, their underlying cause is not so easily overcome and represents a significant problem when trying to improve the sensitivity of the FFSSOCT system. The horizontal noise pattern is a result of interference between any reflecting surfaces in either of the interferometer arms within the axial range of the light source. Therefore, when increasing the optical power to the system, the amount of reflected power from these surfaces also increases, resulting in a direct increase in the intensity of the fixed pattern noise. One possible solution to this problem would be to remove the objective lens from the reference arm and use a beamsplitter with an unbalanced splitting ratio, sending more of the optical power to the reference arm. This would eliminate any stray light from the reference arm and reduce the signal reflecting from the objective lens in the sample arm however it was not implemented in the design.

4.6 Resampling

In order for the phase of the detected signal in the spectral interferogram to be linear in wavenumber, the frequency recorded at each time point (sequential frame) must also be linearly distributed. However, there are several factors that affect the distribution of the optical frequencies within the tomogram acquisition time, resulting in a non-linear distribution and requiring a resampling of the signal before the data is Fourier transformed. The following section describes how the data was measured and corrected by resampling for the FFSSOCT instrument.

The first factor affecting the optical frequency distribution is present in all FDOCT techniques and arises as a result of the non-linear sampling in k-space ($k = \frac{2\pi}{\lambda}$) of the spectral waveform[3,70]. The form of the non-linearity is a second order polynomial and is dependent upon the bandwidth and central wavelength of the OCT instrument. The effect on a recoded spectral interferogram is to chirp it, resulting in a change in the periodicity of the spectral waveform (from a single axial point). As discussed in section 1.2, each incident optical wavelength will experience an amount of constructive or destructive interference based upon the optical path difference of the sample and reference arms. As the wavelength changes, the phase difference changes and the interference changes resulting in the detected spectral waveform. However, the phase change is not linear and

this gives rise to the observed chirping effect. If left uncorrected, the chirping in the spectral waveform results in a broadened signal in the TD. The chirping can be corrected by applying a resampling function to the spectral interferogram data. By interpolating the spectral interferogram with the resampling function, the chirping is eliminated out and the TD signal becomes narrower.

In addition to the chirping caused by the non-linear frequency space, there may be other properties of the instrument design that have a similar effect. The grating used in FDOCT has a non-linear angle response with wavelength that also results in a chirping of the spectral interferogram signal. FFSSOCT does not use a grating to separate different wavelengths, but uses the AOTF within the SLD source driven by the external RF frequency generator to produce different wavelengths in time. It is possible that the RF generater was not delivering a linear series of frequencies to the Broadsweeper light source which would also result is a non-linear phase function. This could be checked by recording the RF output with a digital oscilloscope and transferring the data to a pc for analysis.

While it is impossible to say for certain if the RF generator had a non-linear output, the resampling function can be derived in the traditional way regardless. As the chirping function present in FDOCT is difficult to theoretically derive, there are well established methods of obtaining the resampling function from empirically measured data. The same methods can be applied to the data obtained by the FFSSOCT instrument and a resampling file can therefore be created.

4.6.1 Constructing a resampling function

A resampling function for FFSSOCT can be constructed by examining the phase of a strong signal i.e. a mirror in the sample arm. A single spectral interferogram frequency sampled evenly in time should have an unwrapped phase function that increases linearly with optical frequency. However, as the frequency of the FFSSOCT waveform is not constant, it follows that the phase of the signal is now non-linear. By rescaling and fitting a curve to the non-linear phase function, the inverse resampling function necessary to straighten the phase function and de-chirp the waveform can be obtained.

Due to the effects of linear interpolation, the resampled data has reduced amplitude compared to the original data. The result is a loss of almost 10% in the amplitude of the Fourier transformed signal (a perfect signal would have an amplitude of 1). By using a spline based interpolation, the loss can be reduced to 3% but the computation time is significantly increased (>2 times).

As shown in the simulated data (Figure 4-14), the chirping function (exaggerated) has a curved phase function and a broad Fourier transform function related to the number of different frequencies present in the spectral waveform. The resampling function can be constructed from the phase function by rescaling the data between 0 and 1024 (equal to the number of sampling points) and using an interpolating algorithm on the original spectral waveform. The algorithm actually uses the resampling function as the x axis spacing of the spectral waveform data and a straight line (0-1024) as the interpolating points. The result is an un-chirped spectral waveform and a narrow Fourier domain signal (Figure 4-15).

There is a small amount of imperfection in the interpolated signal due to the use of linear interpolation and the non-linear sampling of the chirped signal (the low frequency on the left (left-hand image - Figure 4-14) has more samples per waveform period). In practice, the amount of chirping affecting the spectral interferogram of an OCT tomogram is typically much smaller then that shown in Figure 4-14 and the loss of signal amplitude associated with interpolating the signal is negligible.

As the chirping is a function of only the non-linear sampling in k-space, it follows that it is possible to apply a single resampling correction to any spectral interferogram acquired regardless of its depth profile. Therefore, it is possible to generate the resampling function for any OCT system from a single image of a mirror at any arbitrary depth. However, it is preferable to acquire multiple images at different depths in order to average out some of the noise. This is particularly important for FFSSOCT where instability in the signal phase is the largest source of noise.

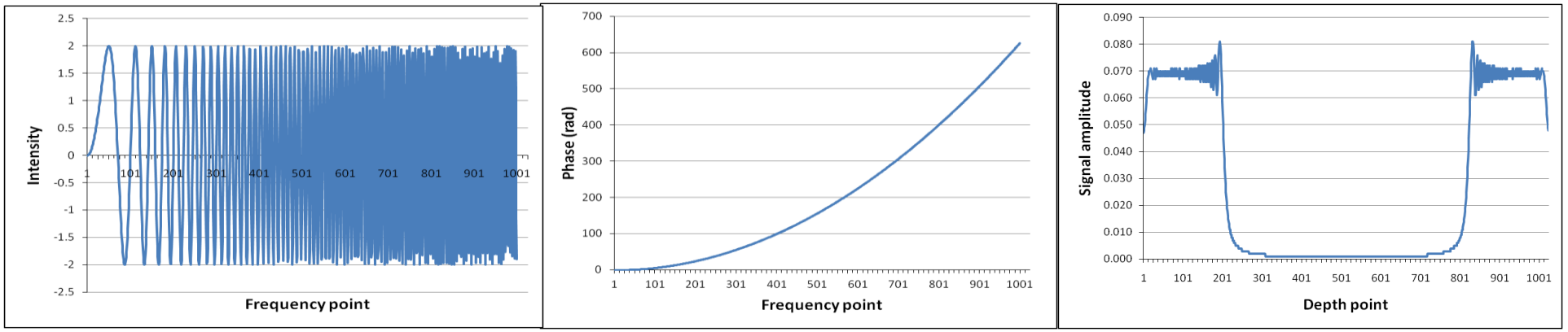

Figure 4-14: The effect of chirping on an OCT spectral waveform.

Generated data showing a chirped spectral waveform (left), its corresponding unwrapped phase (middle) and its Fourier transform (right). The data was created by using a sine function on exponentially increasing time data. As expected, the phase data is exponentially increasing and the Fourier transformed data shows reduced amplitude, blurred over many adjacent points.

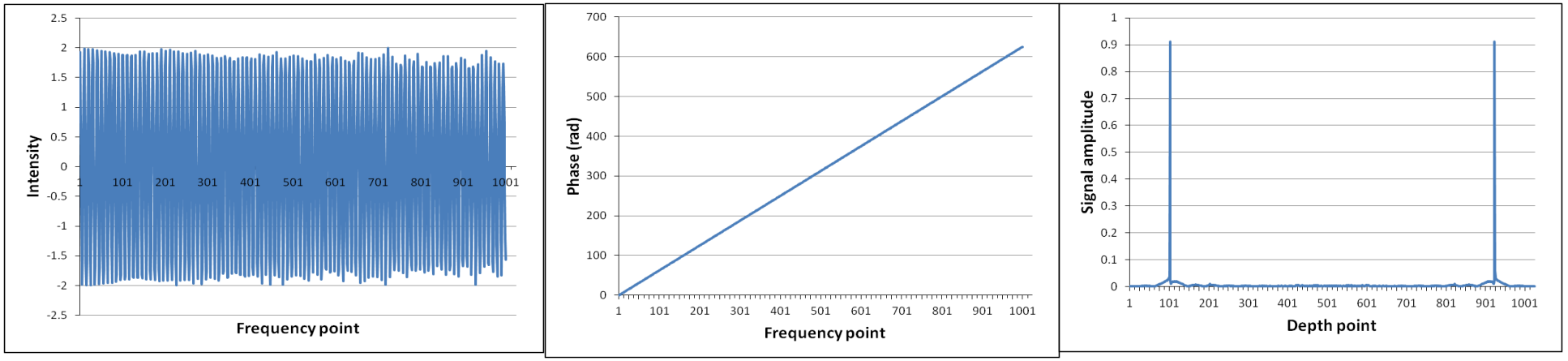

Figure 4-15: The effect of resampling a chirped spectral waveform.

The waveform (left) has been resampled using the unwrapped phase data from Figure 4-14. The resulting waveform is no longer chirped, the phase is linear (middle) and the Fourier transform (right) is narrow with very little amplitude in the points adjacent to the peaks.

4.6.2 Measurement of the FFSSOCT resampling function

Figure 4-16 shows A-line data acquired from different images of a mirror acquired at sequential depth points. In each case, the A-line shown is an average of a single B-scan (512 A-lines) in order to remove some of the noise present in the images that may affect a single A-line. Such noise sources may include sample artefacts, such as dust or poor averaging of the spinning diffuser, over the image acquisition time. Although averaging multiple A-lines together will reduce the overall amplitude of the post-iFFT signal (as a result of the uneven distribution of power across the sample) the phase data will not be affected. The data was checked before averaging to ensure there was no axial difference across the B-scan as this would affect the phase data between the individual spectral waveforms. Additionally, due to the parallel nature of the frame acquisition, any signal fluctuation introduced by phase instabilities will affect every pixel of the frame equally and averaging will have no effect on the phase induced sensitivity drop off of the signal.

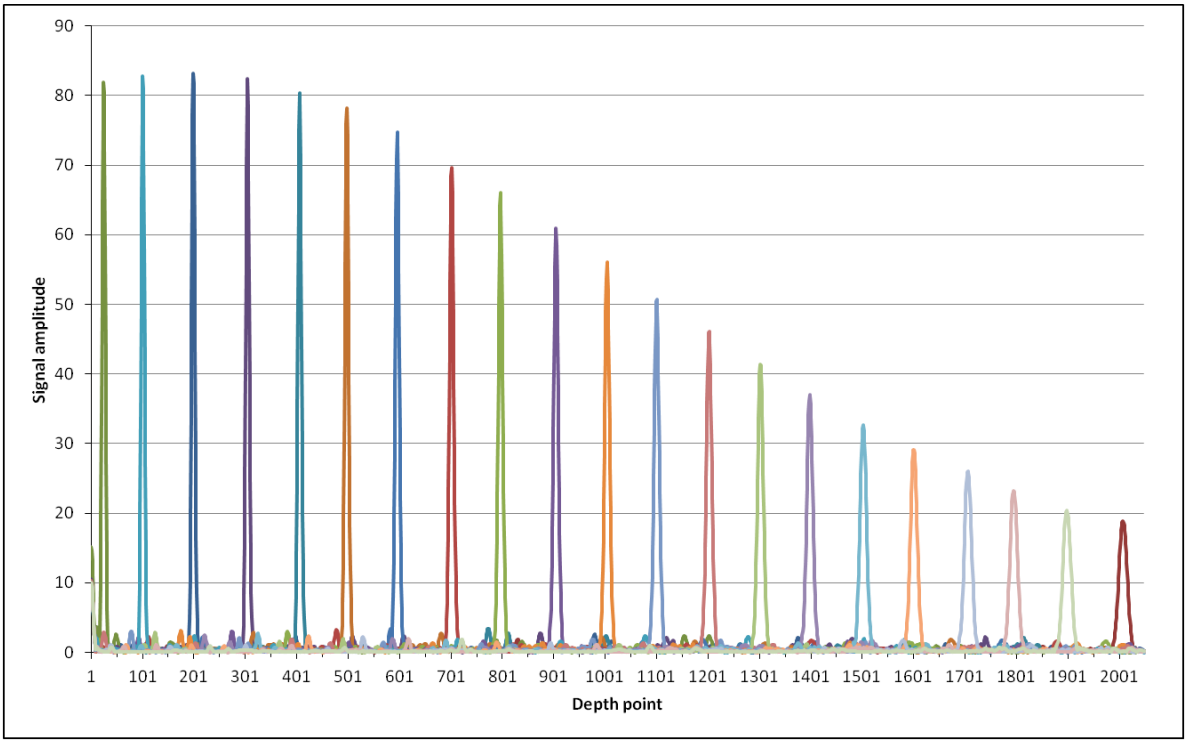

Figure 4-16: Uncorrected FFSSOCT data showing the reflectivity of a mirror at different depth points.

Twenty-one images were taken, each with 1024 frames per image and a frame integration time of 4 milliseconds giving a total acquisition time per volumetric dataset of 4.1 seconds. The effect of the non-linear sampling can be seen most prominently in the deepest axial

position, corresponding to the highest frequencies of the spectral interferogram waveform. This is to be expected as the total magnitude of the phase change of a high frequency signal is greater than that of a low frequency (as shown in Figure 4-14: middle). Ideally, the width of each signal peak should be equal to the axial PSF of the FFSSOCT system, i.e. to the axial resolution which defines the absolute minimum width of the signal peak; however due to the non-linear sampling, the first, centre and last axial depth scans have been broadened to 13.6, 19.9 and 33.4µm respectively. As the axial resolution of the system is 6.27µm, it is clear that there will be a significant degradation in image quality if the non-linear sampling remains uncorrected.

From the data used to produce Figure 4-16, the relative phase information was extracted (Figure 4-17) from each of the axial profiles (the exact phase information could not be measured without significant modifications to the FFSSOCT design for example, quadrature phase acquisition[71]).

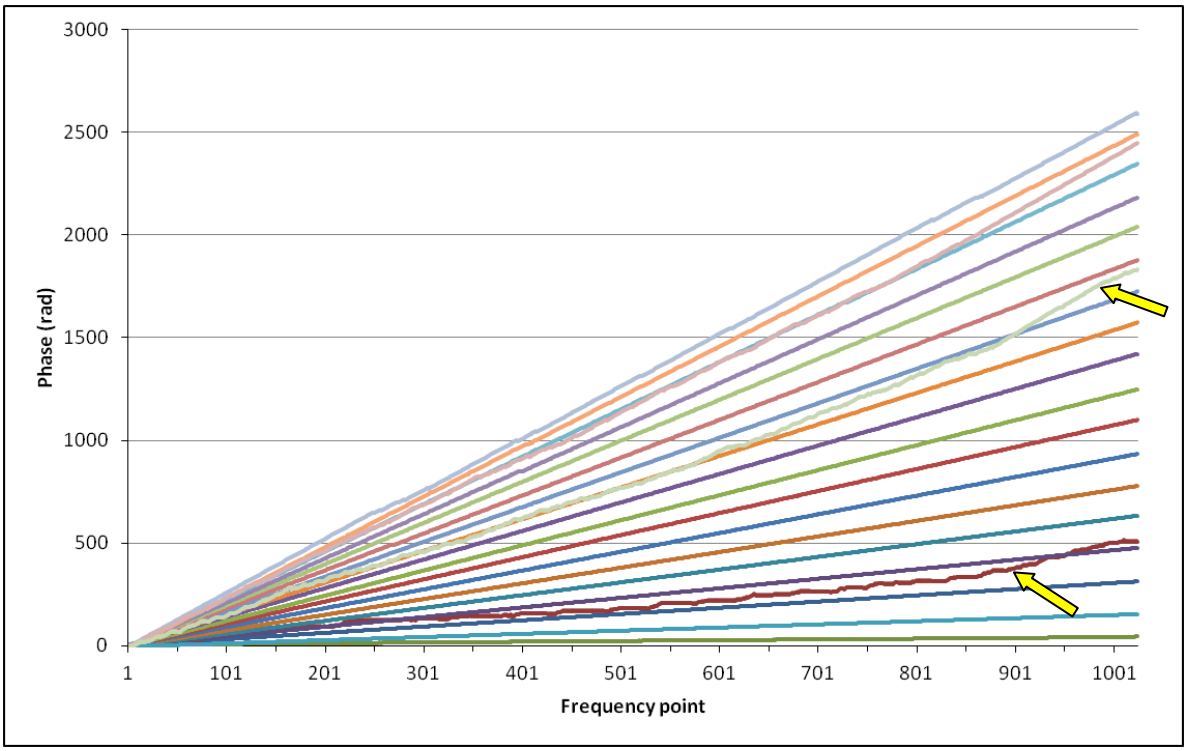

Figure 4-17: Uncorrected unwrapped phase data from a mirror at different depth positions.

The most unstable phase data is highlighted with yellow arrows. The colours of the lines relate to the colours of the depth profile shown in Figure 4-16.

The relative phase information describes the evolution of the phase with the origin at zero radians. To obtain this information a hermitian transform is used to 'reset' the phase of each signal to zero at the same point in the spectral waveform. The exact process for extracting the phase is described in Figure 4-18.

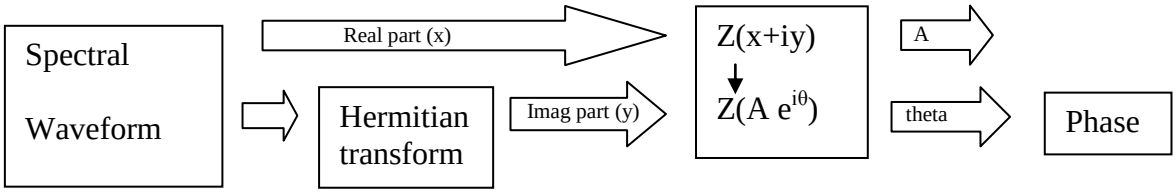

Figure 4-18: Flow diagram of the phase extraction process.

Z represents the complex signal in Cartesian co ordinates x+iy (where x is the real amplitude and y is the imaginary amplitude) and polar co-ordinates $A\ e^{i\theta}$ (where A is the amplitude and θ is the phase).

The real and imaginary components are transformed into polar form by the relationship:

$$Complex\ signal\ (z) = Real\ (x) + \ i\ Imaginary\ (y)$$

Converting x and y from cartesian to polar coordinates gives:

$$Real\ (x) = A\ cos(\theta) \quad \text{and} \quad Imaginary\ (y) = \ A\ sin(\theta)$$

$$\text{Therefore,} \qquad z = \ A\big(cos(\theta) + i\ sin(\theta)\big)$$

$$\text{Which is equal to } z = A\ e^{i\theta} \text{ using Euler's formula}$$

Each phase line of Figure 4-17 represents a different axial scan from Figure 4-16, the steeper the line, the deeper its corresponding axial position. However, the very deepest axial positions cannot be accurately unwrapped and the phase information does not follow the same linearly increasing path as the other axial depth positions (particularly noticeable in the teal and burgundy traces; yellow arrows in Figure 4-17).

Though the phase traces from Figure 4-17 appear straight, the non-linear curve phase is present and can be observed by subtracting a straight line function from the data. Each Phase line has its own straight line function with a minimum set to zero and maximum equal to the maximum of the phase function. The result is shown in Figure 4-19.

The most unstable phase data is now immediately obvious in Figure 4-19. As well as the teal and burgundy phase traces (equal to the two deepest axial positions respectively in

Figure 4-16); other phase traces also show some substantial phase transitions. The phase transitions are a result of the combination of micro vibrations within the system and random signal noise affecting the phase analysis process (Figure 4-18). The effect of micro vibrations will be less noticeable at positions close to the zero delay where the periodicity of the spectral waveform is lower and the sampling is higher. As these traces do not represent the true curvature of the non-linear sampling, they must be removed before the resampling function can be created.

4.6.3 Generation of the FFSSOCT resampling function

By removing the most unstable phase functions from Figure 4-19, the extent of the non-linear sampling on the FFSSOCT signal can be directly observed (Figure 4-20). As the colours of the traces in Figure 4-20 correspond to the axial profile traces in Figure 4-16, it can be seen that the majority of the phase functions removed are from the deeper axial positions where the magnitude of the phase change per pixel, and therefore, potential for error in phase unwrapping, is greatest.

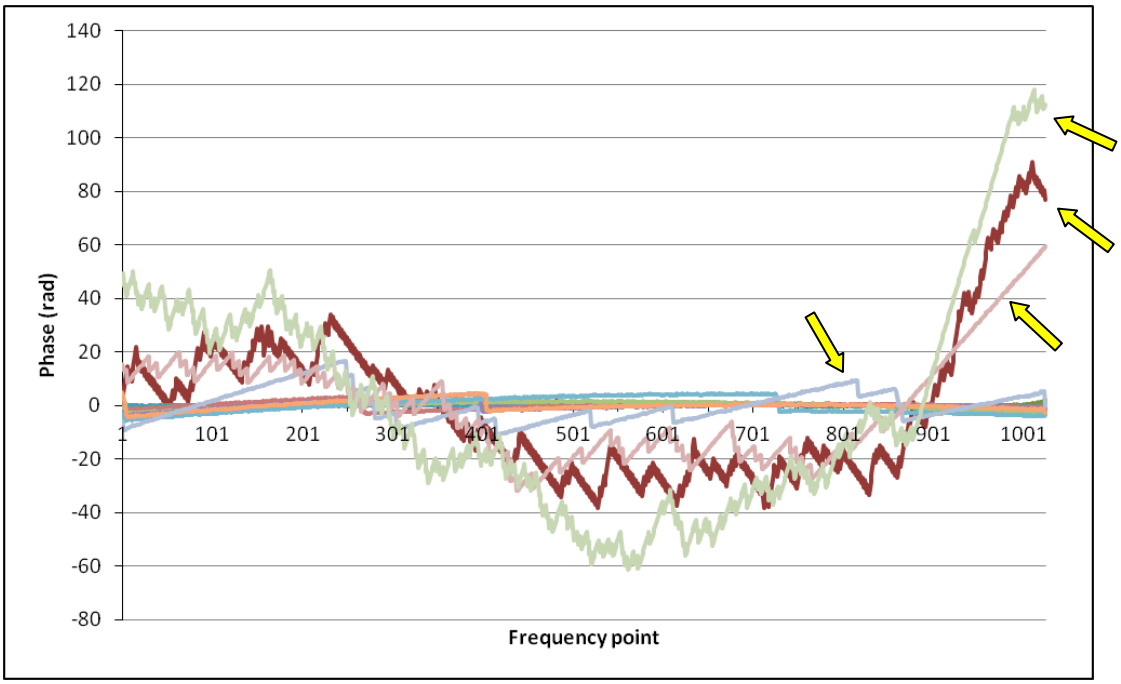

Figure 4-19: Uncorrected FFSSOCT phase data with the linear phase component removed.

The highlighted phase traces have a large amount of phase noise and non-linear signal of interest cannot be extracted from them.

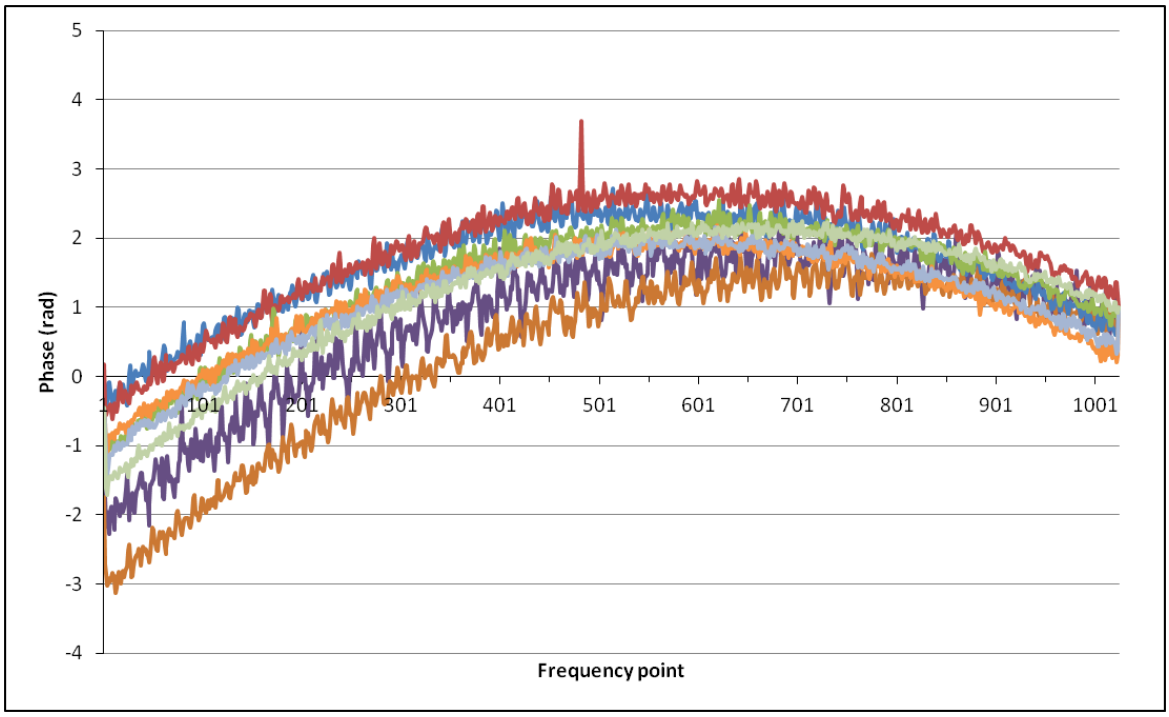

Figure 4-20: Uncorrected FFSSOCT phase data with the highly unstable phase traces removed.

The axial points removed from Figure 4-19 correspond to depth positions 1, 100, 200, 400, 900, 1000, 1300 and 1500-2000 in Figure 4-16 (the line colours have been preserved).

Two aspects of the data shown in Figure 4-20 require some explanation; the variation in the curvature of the different phase functions and the off-centre position of the curve. Although it is not possible to measure the cause of the variations (as the FFSSOCT system is incapable of directly measuring the phase of the signal), an explanation can be hypothesised. The curvature variation could be attributed to an error in the data processing due to the high phase values at the first point of the phase array (Figure 4-20).

Examining the phase data in Figure 4-20, the centre of curvature occurs around the middle of the phase function and if the linearly increasing part of the function were to be removed, the resulting curve would be symmetric around the centre point. It would also be expected that the FFSSOCT phase data would show the same symmetry around the central data point. The decentring of the curve may be attributed to the contribution of the frequency generator which may have also sent a non-linear output to the acousto-optic tuning filter in the SLD light source. This could be measured using a digital oscilloscope however this measurement was not performed. The relationship between the input RF and the output

wavelength of the Broadsweeper is shown in Figure 4-21, there appears to be very little non-linearity between the two that indicates that the chirping of the spectral waveform is not caused by this.

It should also be noted that some of the phase traces in Figure 4-20 appear to have more noise than the others, particularly the purple and orange traces (relating to depths 300 and 500 respectively, Figure 4-16). Unlike the phase functions that were removed from Figure 4-19 on account of the depth related phase instability, these two traces occur close to the zero delay and should have the least amount of phase noise. One possible explanation is that the recorded axial profile of the mirror overlaps with some of the fixed pattern noise caused by internal reflecting surfaces within the FFSSOCT system resulting in an additional waveform on the spectral interferogram. This would manifest as an additional phase function on top of the one derived from the mirror, albeit much smaller due to the smaller amplitude of the waveform, and would manifest as additional phase noise.

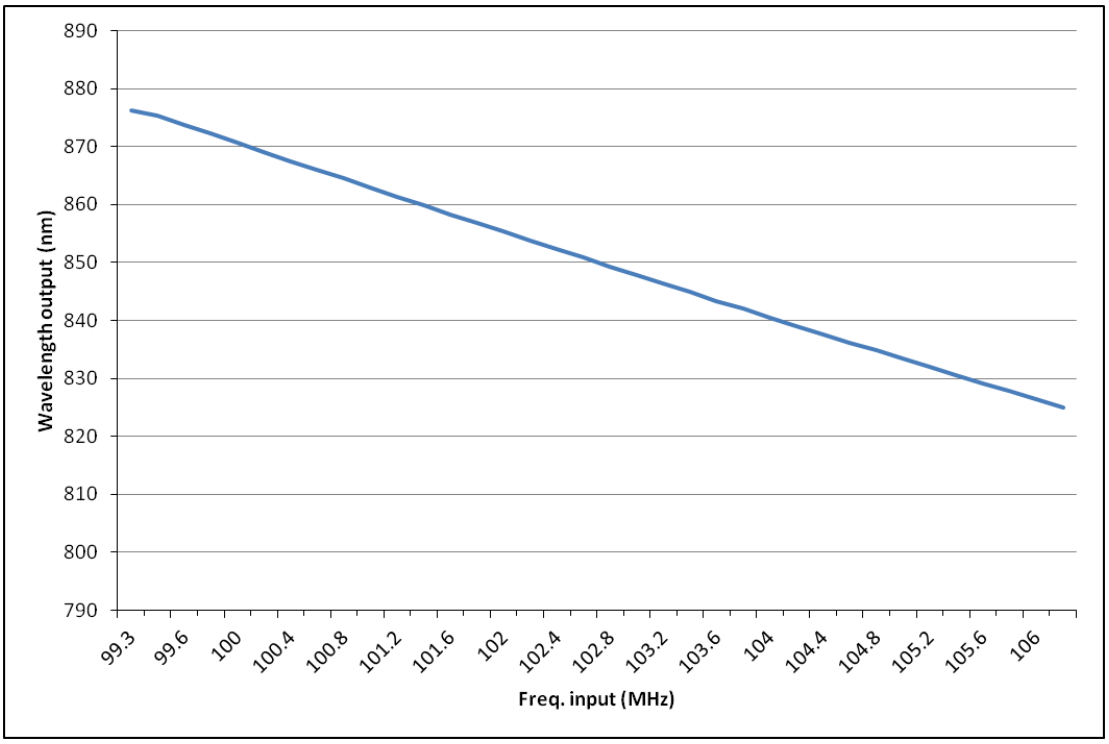

Figure 4-21: The relationship between the input frequency and the output wavelength of the Broadsweeper

The relationship is almost linear; it has a curve that deviates from a linear output by ~0.1%

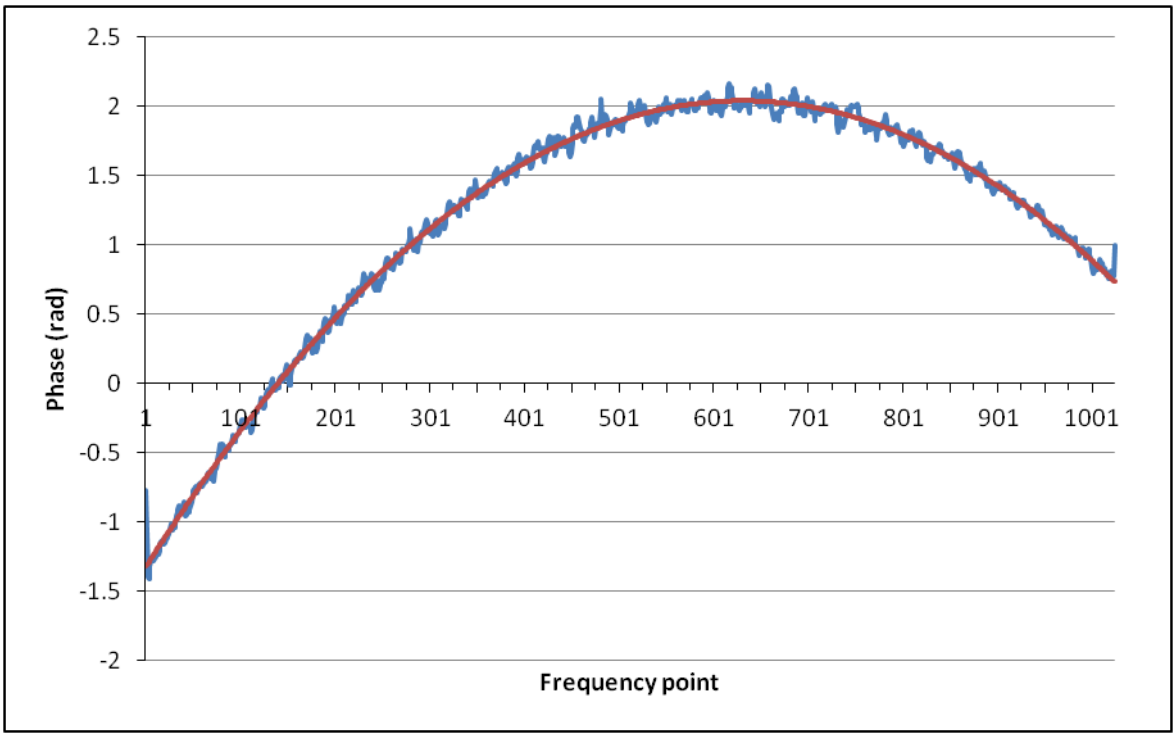

Figure 4-22: The averaged non-linear phase data.

The red line is a second order best fit polynomial. This polynomial can then be used as the resampling function for the original data.

To remove the residual phase noise from the averaged phase function (Figure 4-22) a second order polynomial was fitted to the data. The final step in creating the resampling function was to rescale the amplitude of phase function shown to equal the number of sampling points. This ensured that the overall size of the resampled spectral interferogram remained constant and the position of the post-iFFT signal peaks did not change.

By interpolating the averaged A-line data, shown in Figure 4-16, with the calculated resampling function (Figure 4-22), it can be seen that the spectral broadening of the signal peaks was greatly reduced (Figure 4-23).

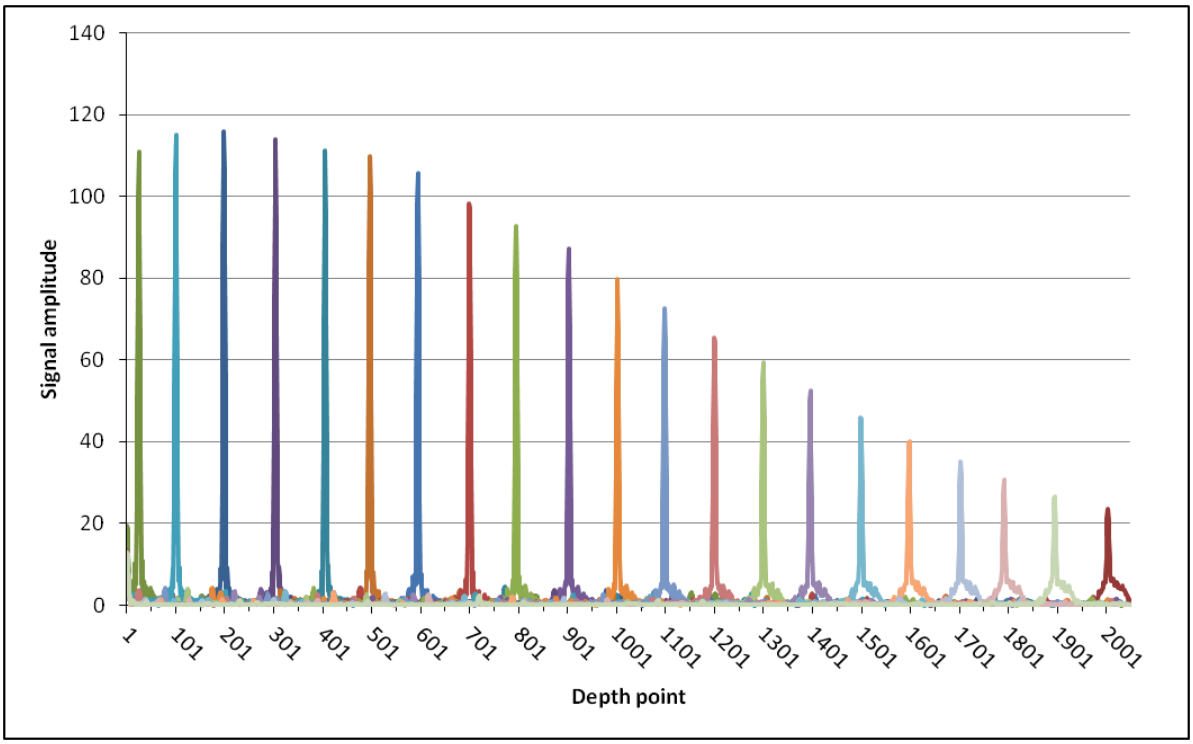

Figure 4-23: FFSSOCT A-scans from a mirror, interpolated with the resampling function. The A-scans shown relate to the non-resampled data shown in Figure 4-16.

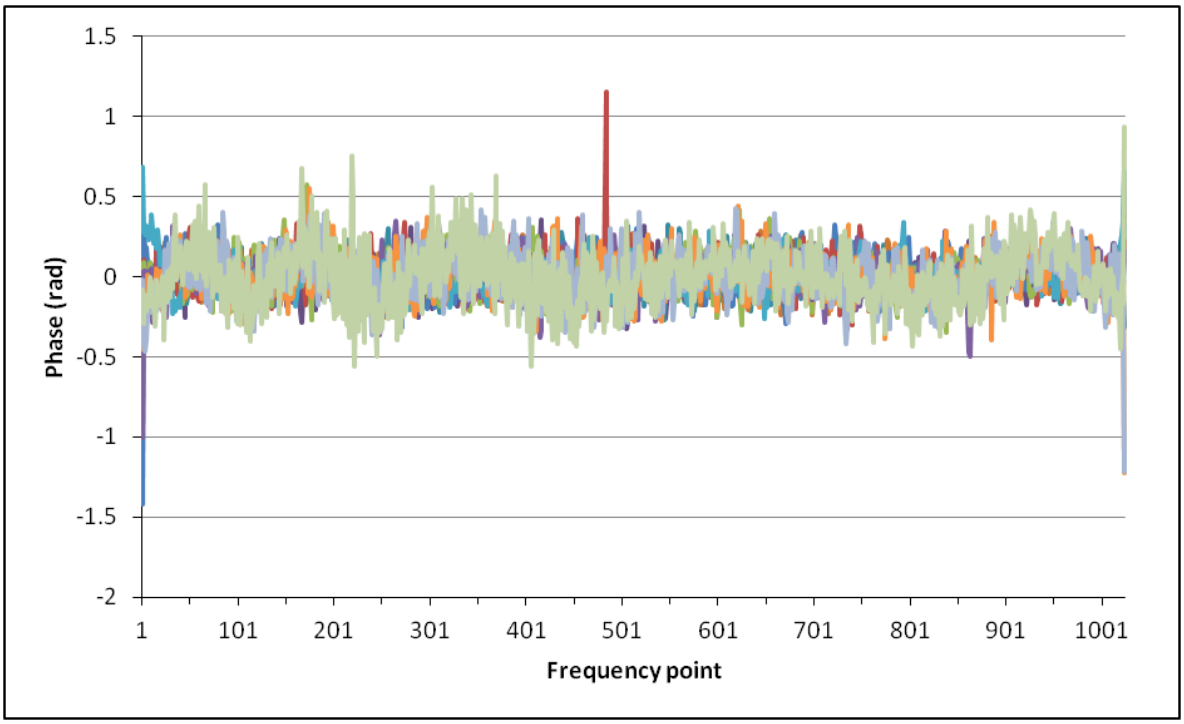

Figure 4-24: Unwrapped phase data from the resampled FFSSOCT data of a mirror. As in Figure 4-20, the highly unstable phase lines have been removed.

By applying the resampling function, the first, centre and final axial depth peaks now have a FWHM of 10.8µm. By examining the phase data of the resampled spectral waveform (Figure 4-24), it can be seen that the curvature in Figure 4-20 has disappeared and only the phase noise remains. This is an important measurement to make repeatedly over the lifetime of any FDOCT instrument as the chirp in the spectral waveform may change, requiring the resampling function to be remeasured.

Figure 4-25 and Figure 4-26 show the effect of applying the FFSSOCT resampling function to the data A-line shown in Figure 4-7.

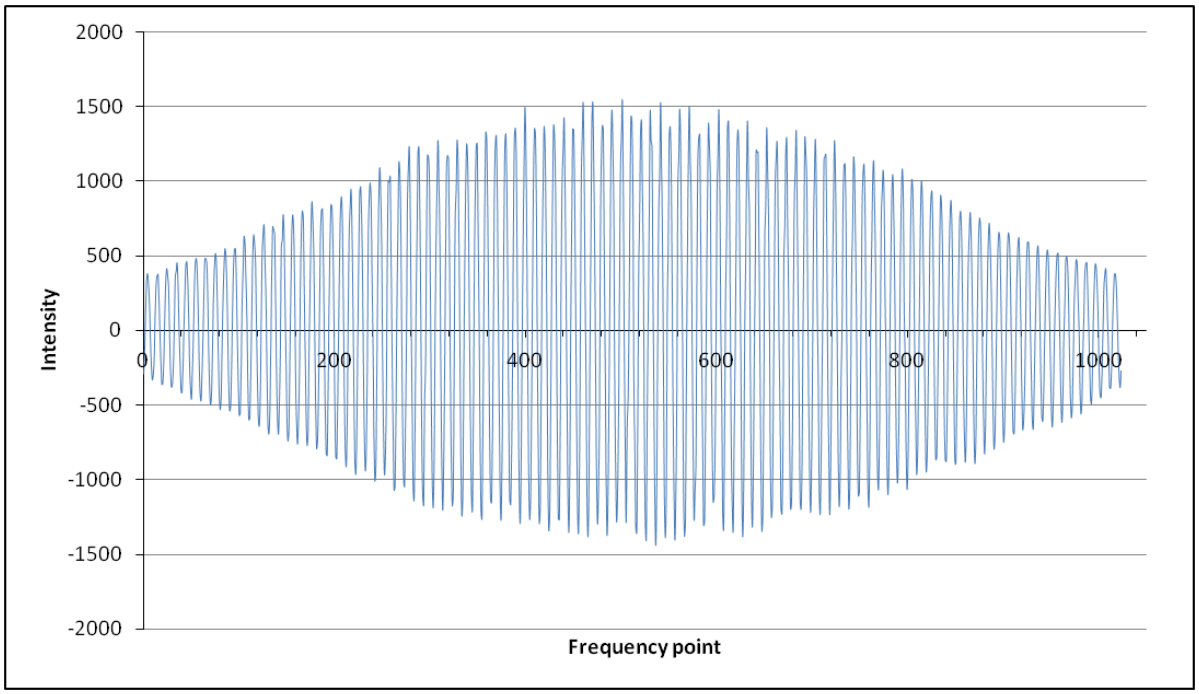

Figure 4-25: The resampled spectral waveform data showing regular periodicity. The data is a continuation from Figure 4-7.

By resampling the spectral waveform data, the broadening of the time domain peak (Figure 4-26) has been reduced and its amplitude has been increased (compared to Figure 4-8) as the spectral energy has been redistributed into fewer pixels.

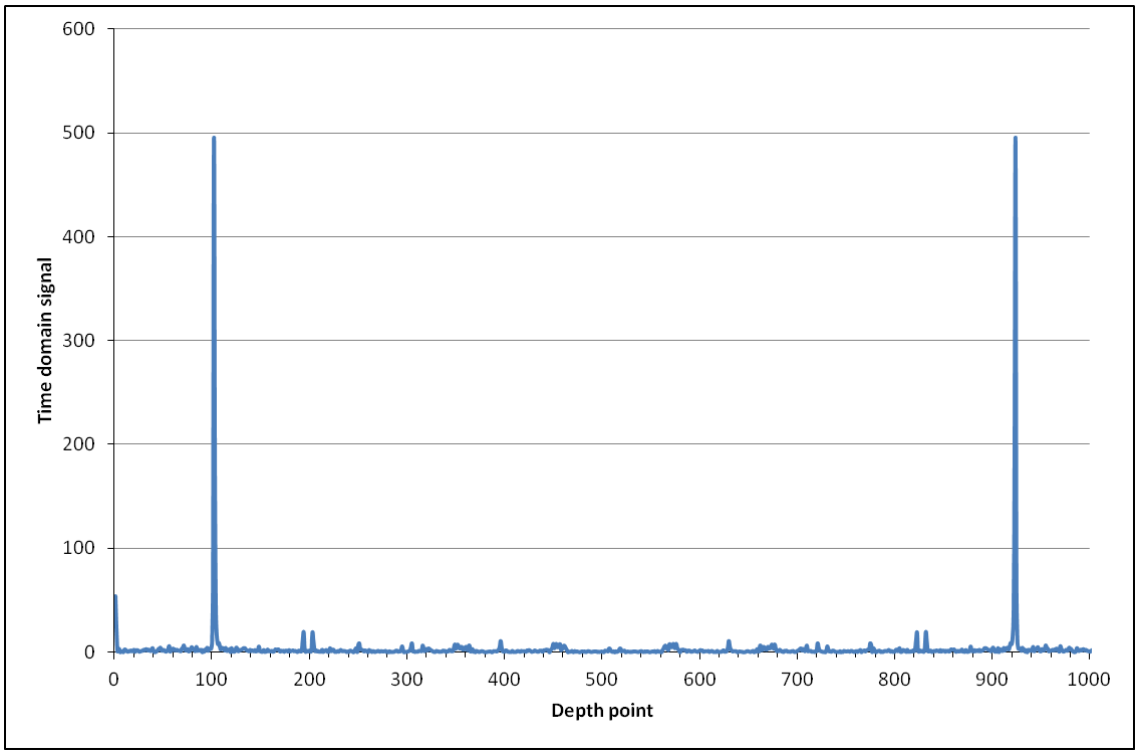

Figure 4-26: Fourier transform of the resampled spectral waveform data.

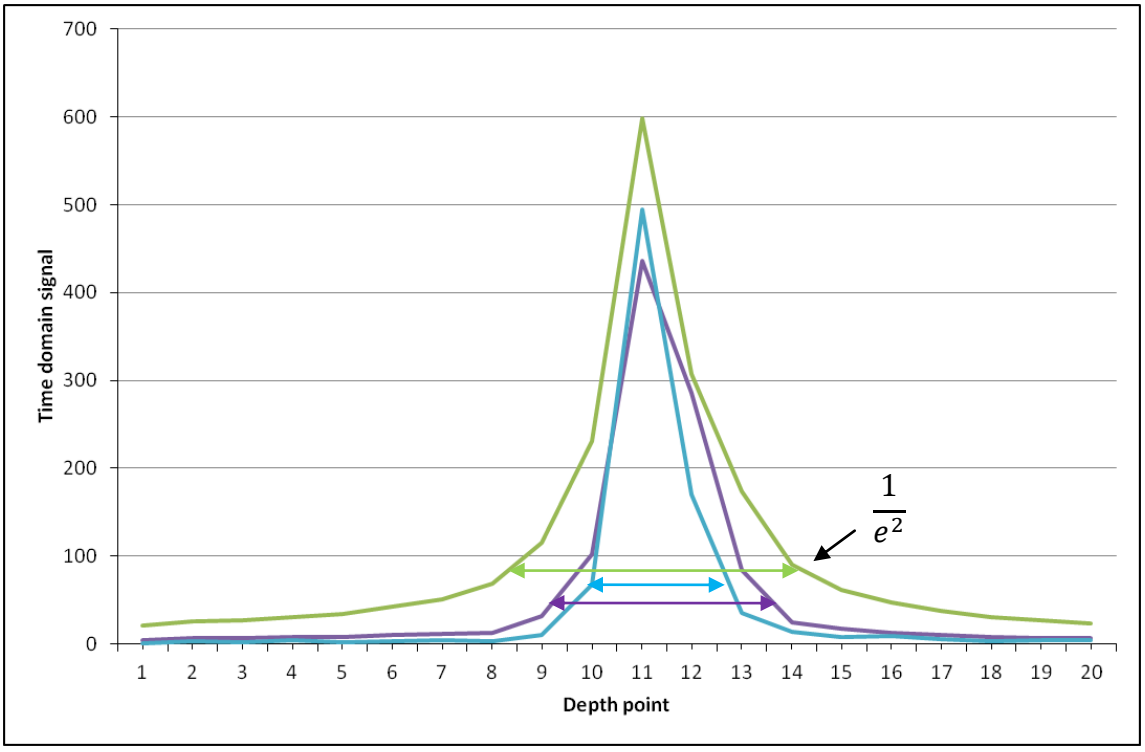

Figure 4-27: Comparison of the effect of Gaussian shaping and resampling.

A comparison of the effect of applying Gaussian shaping (standard deviation = 0.3) (purple) and both resampling and Gaussian shaping (blue) to the spectral data (green). The resampled data shows a decrease in the 1/e^2 width of 25% compared to the Gaussian shaped data.

Figure 4-27 shows a comparison between the unsampled and resampled data as well as the effect of the Gaussian spectral shaping (standard deviation = 0.3). The unsampled data, despite having a higher amplitude, has a significantly larger FWHM than the resampled data (>40%) and higher noise amplitude in the surrounding axial pixels.

4.7 Zero padding

Zero padding is the name given to the act of added zeros onto the end of a frequency spectrum prior to Fourier transform. The number of zeros added is equal to the number of frequency points in the original spectrum and has the effect of interpolating the Fourier transformed image, effectively doubling its length. Zero padding is performed for two reasons; (i) to increase the number of axial samples in the TD image and (ii) to increase the positional accuracy of the time domain signal. The axial sampling (as described in section 5.4.4) for the FFSSOCT system is critically undersampled, zero padding can increase the sampling simply by adding more sampling points in the TD image. As the number of frequencies that can be recorded in a 1024 point spectrum is far greater than 512 (the number of post iFFT axial points), the positional accuracy of the TD signal can be ambiguous. If the detected frequency falls between two axial pixels, the amplitude is split between the two creating an uncertainty in the measurement (Figure 4-28). Zero padding will reduce the uncertainty by increasing the number of sampling points (Figure 4-29). If the signal consists of two peaks separated only by a small distance, without zero padding, the two signals will merge into a single detected peak (Figure 4-30). This is the critical Nyquist criterion that must be fulfilled; the axial sampling must be greater than twice the axial resolution. Applying a single zero padding operation to the data in Figure 4-30 reveals the existence of a second sample peak (Figure 4-31).

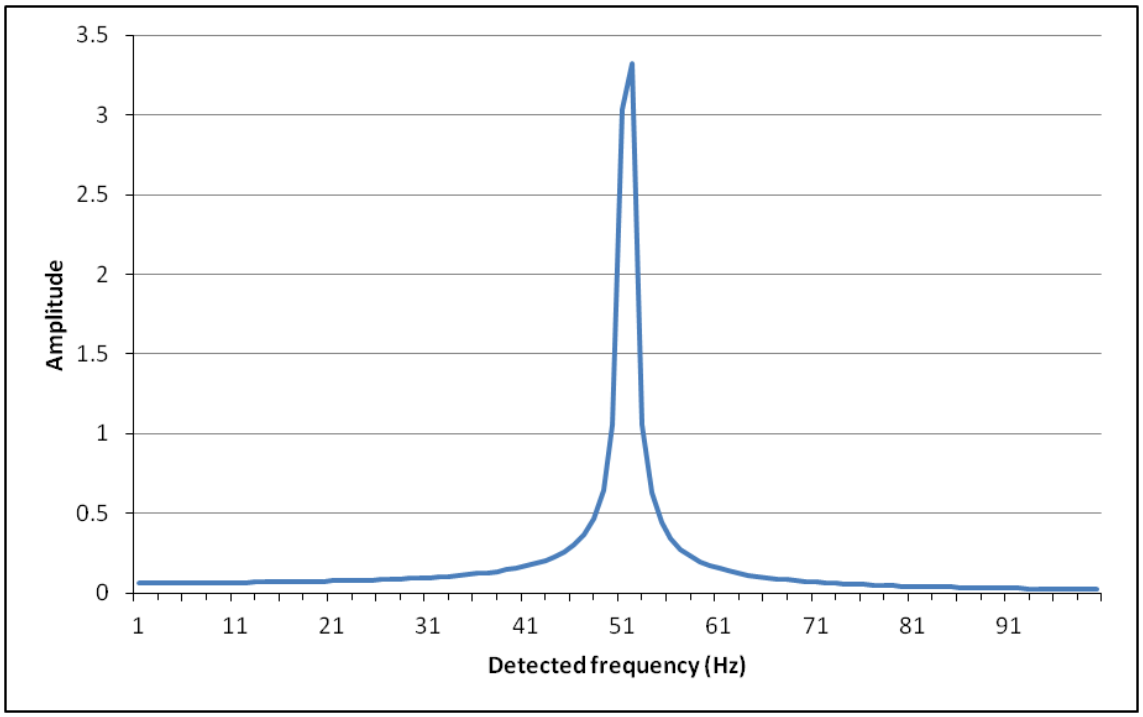

Figure 4-28: Fourier transform of a noiseless sine wave with a frequency of 50.525Hz.

The sine wave had 1024 sample points per second and an amplitude of 10. The limited resolution in the detected frequencies results in a split of the spectral power between neighbouring pixels (50 and 51Hz) and the detected amplitude has been subsequently reduced by ~34% (from 5 to 3.325).

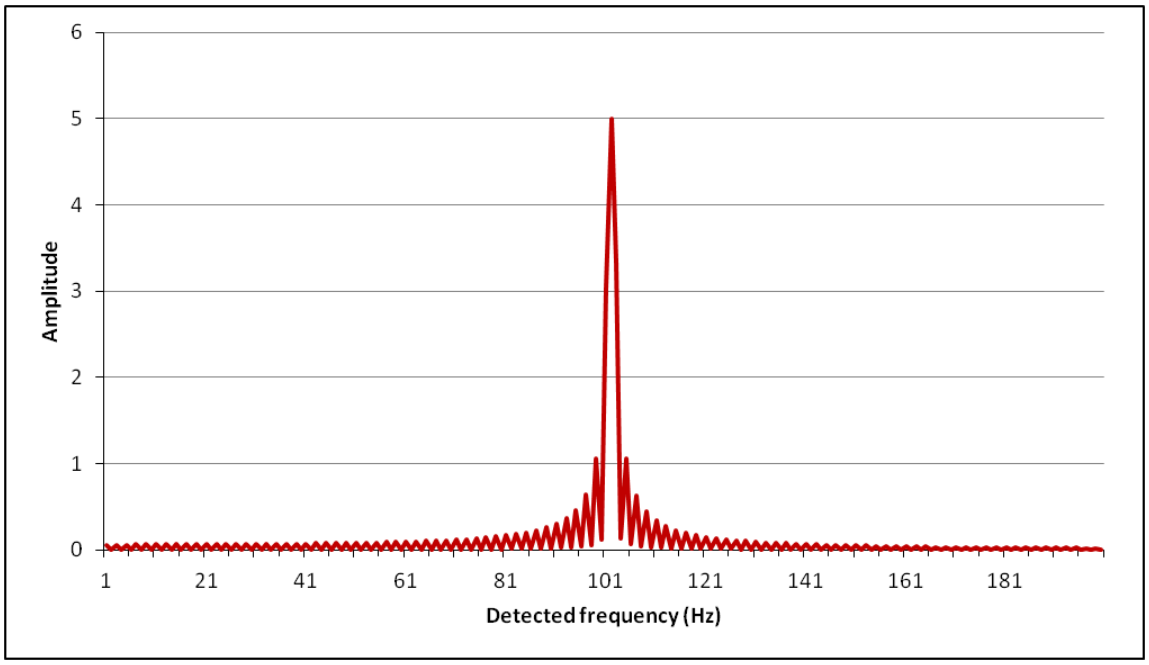

Figure 4-29: Fourier transform of a noiseless sine wave with a frequency of 50.525Hz that has been zero padded once.

The sine wave had 1024 sample points per second and an amplitude of 10. The sine wave has been zero padded once. The increased resolution in the detected frequencies has reduced the splitting of the spectral power and the amplitude has only decreased by ~0.1% (5 to 4.994). The detected frequency is 101Hz/2 = 50.5Hz.

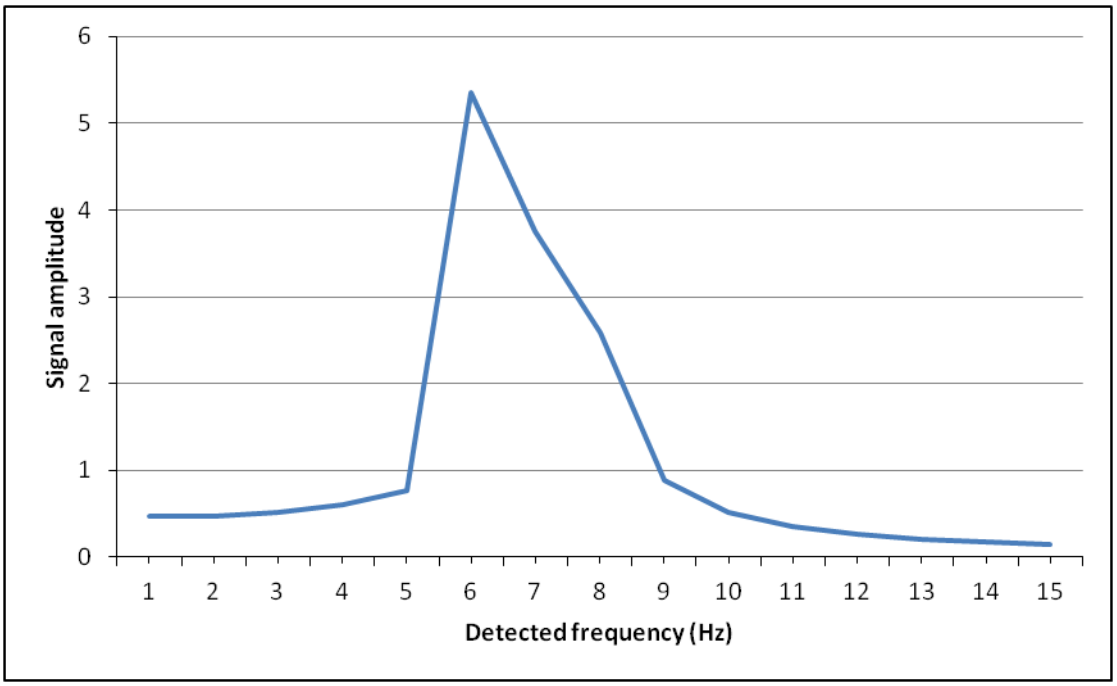

Figure 4-30: Fourier transform of two summed noiseless sine waves with frequencies of 5Hz and 6.425Hz.

The two sine waves had 1024 sample points per second and amplitudes of 10. The two detected frequency peaks cannot be resolved from one another.

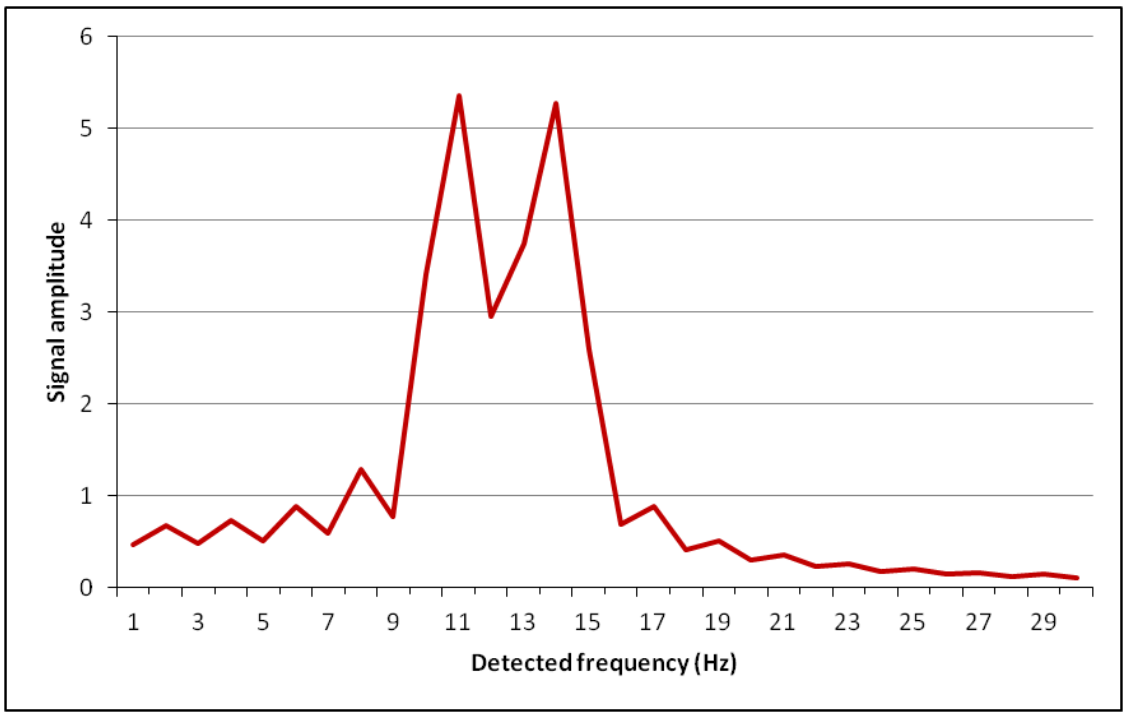

Figure 4-31: Fourier transform of two summed noiseless sine waves with frequencies of 5Hz and 6.425Hz.

The two sine waves had 1024 samples points per second and amplitudes of 10. The summed waveform has been zero padded once. The two detected frequency peaks are now resolvable. The detected peaks have measured frequencies of 5Hz and 6.5Hz respectively.

The number of zero padding operations that should be performed is decided by the axial resolution of the system. While a perfect system would need multiple zero padding operations to give it the required fidelity in its axial position measurements, the FFSSOCT has a limited axial resolution that is already greater than the distance between axial pixels in the A-scan; the theoretical axial resolution is 6.3µm and the axial spacing is 3.6µm (see section 5.4.4 for a detailed explanation of the axial sampling). However, as the axial spacing is not twice the axial resolution, neighbouring image features cannot be adequately discerned (the system is undersampling – Figure 4-30); therefore, the spectral waveform should be zero padded once in order to double the axial range and increase the axial sampling. Figure 4-32 and Figure 4-33 show the effects of zero padding the mirror A-line data from Figure 4-25.

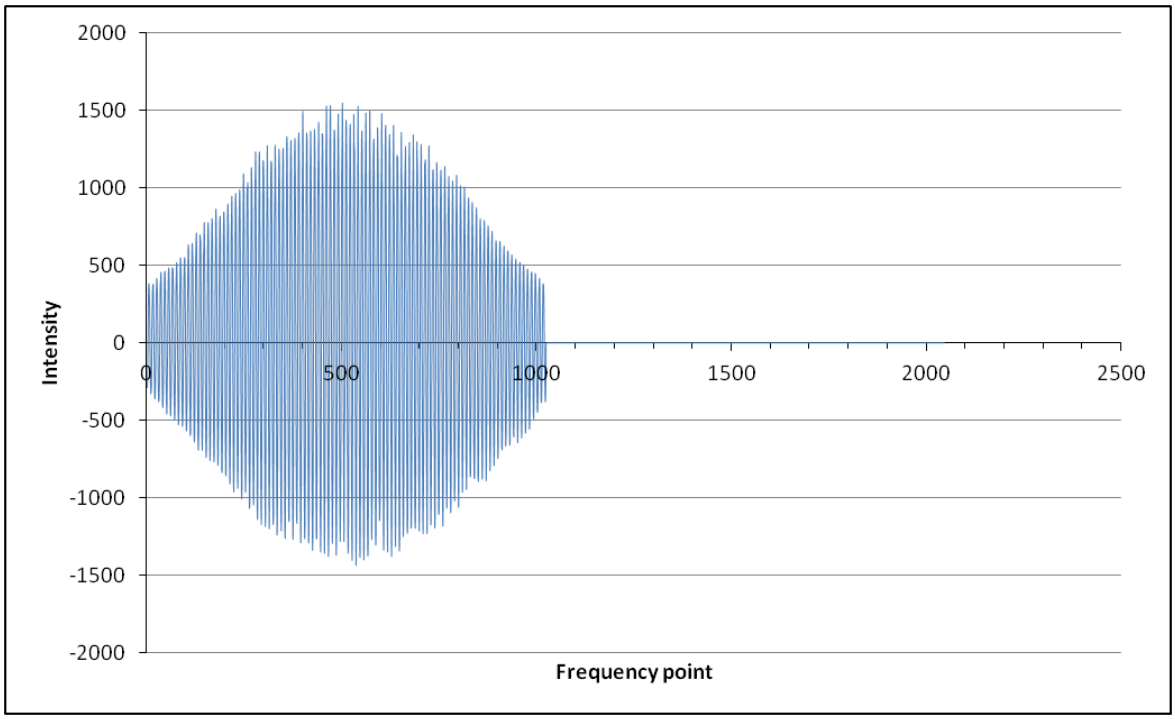

Figure 4-32: FFSSOCT spectral waveform from a mirror with zero padding applied. An array of zeros added is equal in length to the length of the spectral waveform (1024) has been applied after the waveform.

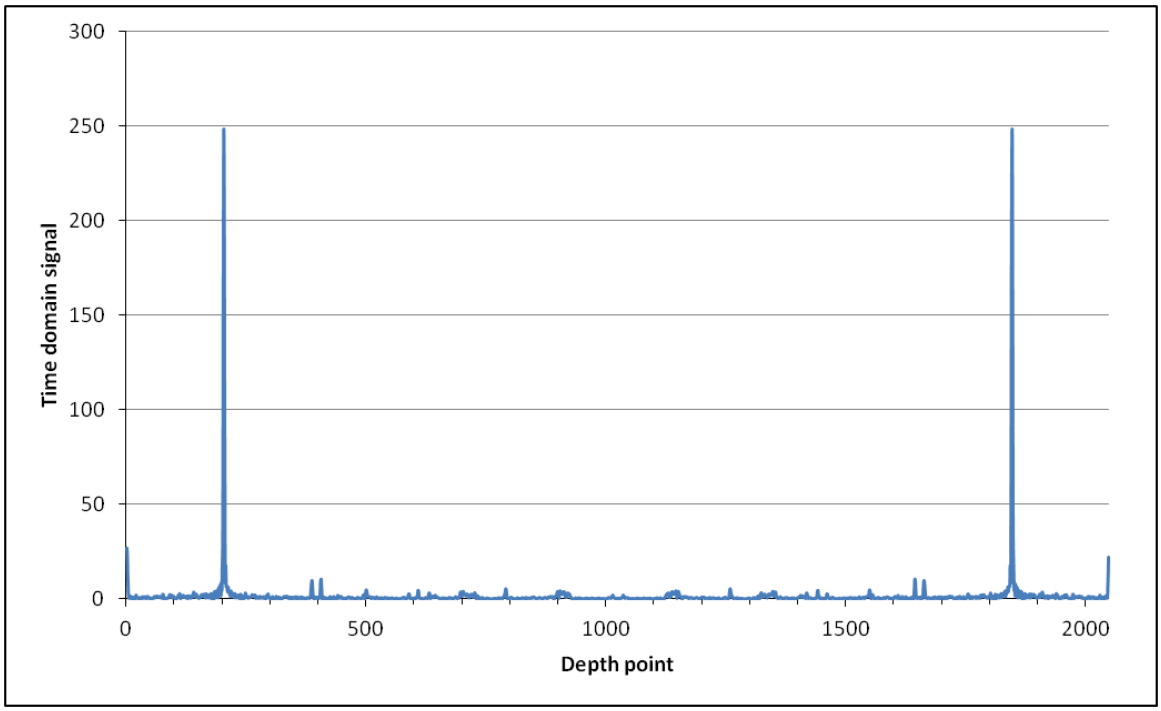

Figure 4-33: Fourier transform of the FFSSOCT spectral waveform with zero padding applied.

Zero padding reduces the amplitude of every depth point by two (except the DC component).

The Fourier transform of the zero padded spectral data (Figure 4-33) shows that the time domain signal now has double the number of axial depth points and half the amplitude of the non-zero padded data (Figure 4-26). Though the number of axial depth points has doubled, the recorded axial distance has not changed since it is defined by the number of frequency steps used when the image is recorded and therefore, only the axial sampling changes. The reduction in amplitude affects all signals within the A-line, and therefore there is no detrimental effect on the sensitivity of the system.

4.8 Fourier transform and file saving

The final steps of the FFSSOCT data processing are to remove the imaginary parts of the post Fourier transform signal (Figure 4-34), rescale the data and save it as an image file. The iFFT accepts and returns complex domain signals in the form $S = x+iy$ where x is the real part, and y is the complex part of the signal *S*. To remove the complex part but retain its amplitude, the Labview 'absolute' function was applied to the data (Figure 4-35). This

function applies the following formula to the complex signal and returns a signal with purely real amplitudes:

$$Abs(S) = \sqrt{(real(S)^2 + Imaginary(S)^2)} \quad \text{Eqn. 13}$$

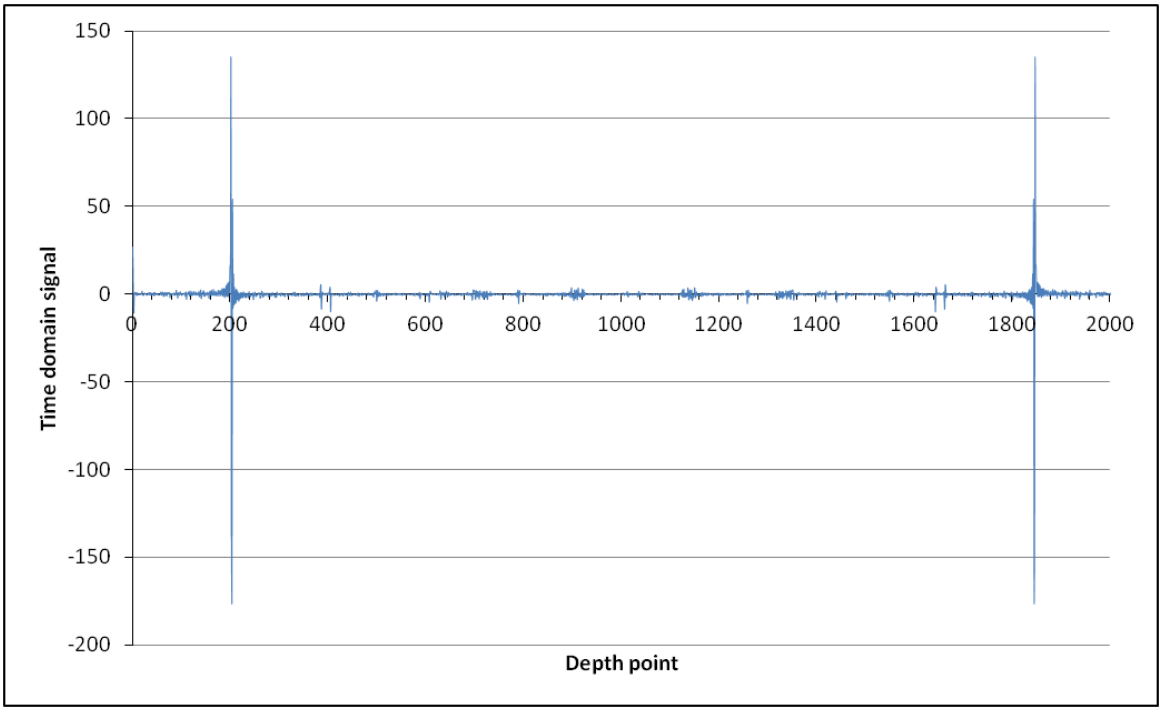

Figure 4-34: Fourier transform of the FFSSOCT mirror data with all the pre-Fourier transform processing applied.

The output of the iFFT is complex and cannot be represented as purely real signal intensities, hence some negative signals.

To reduce the required dynamic range of the output file type, a non-linear rescaling function was applied to the data. A log function was used to reduce the high signal amplitudes and provide a greater image dynamic range for the low intensity signal from a weakly scattering sample. Lastly, the TD data was rescaled into a 16 bit range (0 – 65,535) and saved as a PNG (portable network graphics) image, a lossless compression format.

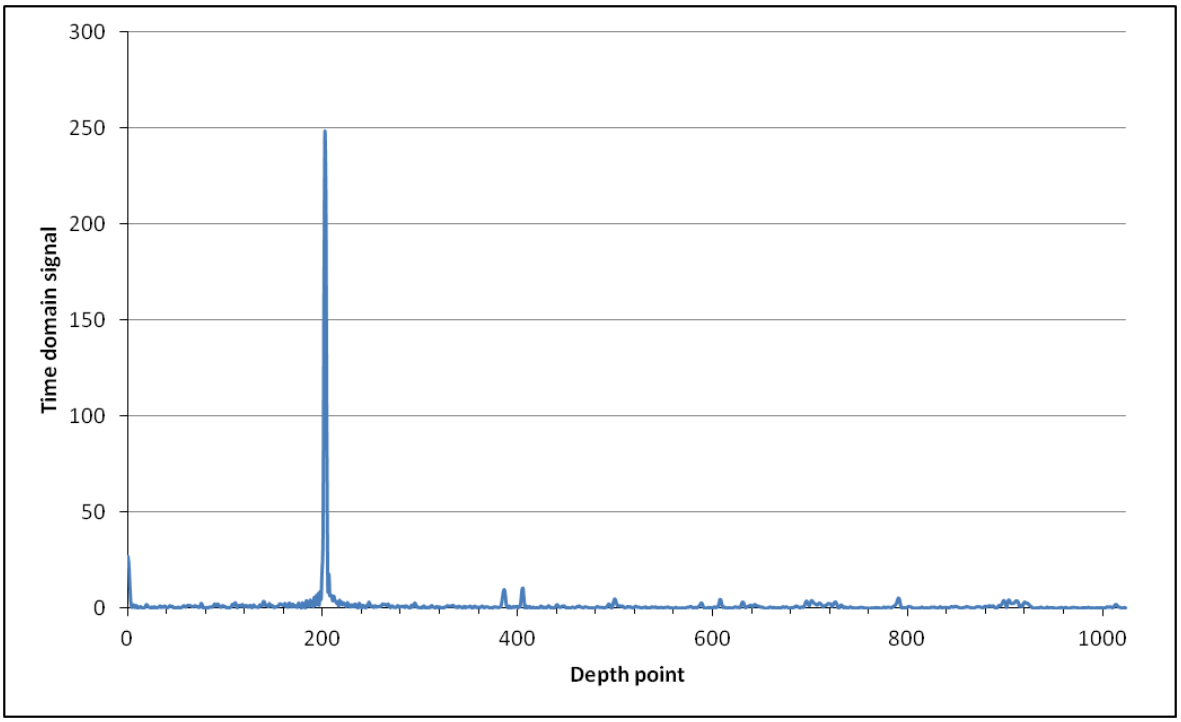

Figure 4-35: FFSSOCT mirror data with the 'absolute' function applied.

The real and imaginary parts of the complex signal have been combined and the signal data is now purely real.

4.9 Post processing

After being processed in Labview, the PNG images were loaded into the freeware image processing program ImageJ. This software could be used to manipulate the images in various ways; contrast improvement, frame averaging, stack registration, shearing, look-up table (LUT) application and 3D presentation. Shearing was used to remove any unwanted tilt from the images resulting from a slanted sample. To preserve the dimensions of the tomogram, shearing and registration was restricted to rotation and translation only. The 3D visualisation in ImageJ is limited to single axis rotation from a static view point making it difficult to effectively visualise the tomographic data.

4.10 Dispersion correction

Dispersion correction is a numerical technique for counteracting the effect of the dispersion mismatch between the two arms of the interferometer. Any optical element with the interferometer has a dispersive effect on the different wavelengths of the optical

source; the relative velocity of each wavelength is reduced by a different amount depending upon the refractive index of the optical material. When one interferometer arm has dispersive material in it and the other does not, the net effect is that each wavelength has a different optical path length, resulting in a non-linear phase relationship between wavelengths and generating chirp in the spectral waveform. This can be numerically addressed by multiplying the signal with an artificial complex phase signal with a real amplitude of one and an opposite phase (θ) non-linearity to the dispersed signal[72-74]. Alternatively, the dispersion mismatch can be reduced by inserting optical material into the interferometer to balance the dispersion in both arms.

As the FFSSOCT system has matched objective lenses in both interferometer arms, there is no dispersion mismatch between them. However, when the system was used to image a weakly reflecting sample, an ND filter was used to reduce the optical power in the reference arm (as described in section 3.4). The presence of this filter may have introduced a small amount of dispersion that could be corrected for by using the numerical dispersion described.

4.11 Summary

This Chapter describes the different techniques to turn the spectral data recorded by the FFSSOCT into TD images. The similarities and differences between the processing techniques used for the FFSSOCT system and those used to process spectral data from a traditional Fourier domain OCT system are also explored. Each technique was designed to improve or enhance the output image and the effect of each technique was demonstrated on a spectral A-line recorded by the FFSSOCT system. The spectral shaping and resampling steps improved the axial resolution by ~40%.

The problem of background subtraction is also explored in this Chapter. The back reflections from within the FFSSOCT system caused horizontal lines to appear across the image. These lines can be described as pseudo fixed pattern noise due to the combination of random noise from the phase instabilities within the system and the uneven distribution of light across the sample on top of the static signal from the back reflections. Removal of this noise by traditional methods was insufficient and was only adequately achieved by

recording multiple images of the background signal. However, this still resulted in the presence of lateral lines of low intensity across the final image, reducing the sensitivity of the system in these regions.

Chapter Five: Analysis of FFSSOCT data

5.1 Improvement aims

The aim of the work described in this Chapter was to evaluate the different operating specifications of the FFSSOCT instrument. It was necessary to investigate each of the various parameters to discover the limits of the system's performance in order to accurately compare it with other OCT systems.

5.2 Introduction to FFSSOCT data analysis

Each operating parameter was acquired using a different technique. The depth range was derived from the properties of the OCT design. The axial and lateral resolution was measured by analysing processed data captured with the FFSSOCT system. The sensitivity fall-off was investigated by analysing the spectral output of the FFSSOCT system. The results of the analysis were used to compare the FFSSOCT system to an FDOCT in Chapter 6.

5.3 Depth range

The depth range of a frequency based OCT system is limited by its spectral resolution, a higher spectral resolution resulting in a greater imaging depth range. The spectral resolution defines the highest detectable frequency of the interference spectrum which is related to the TD signal by inverse Fourier transform. Therefore, as the detected frequency increases, the TD signal is resolved at greater distances from the zero delay.

For FDOCT, the spectral resolution is defined by a combination of the bandwidth of the light source, pixels on the camera and geometry of the spectrometer design[75]. Whilst the bandwidth is also important for defining the depth range of FFSSOCT, the parallel acquisition means that the 'pixels' of FDOCT become samples in time (as described in section 1.6). This is beneficial as it allows for any number of samples to be taken, and hence, the spectral resolution of FFSSOCT can be very high and therefore, the depth range can be very long. Coupled with the greater potential roll-off performance of the swept source design (section 5.6), FFSSOCT could potentially generate very large images with good sensitivity at large imaging depths. The trade-off is the tomogram acquisition time, which has to be increased in order to keep the same frame integration time. Alternatively,

the frame integration time could be reduced, however, this would result in a proportional reduction in the sensitivity.

Using the knowledge that the highest resolvable frequency determines the maximum detectable depth, the depth range of an OCT system can be empirically derived from first principles as follows. The highest resolvable frequency occurs at the Nyquist limit[76], the limit where the maximum and minimum points of the sine wave lie on adjacent sampling points. For an FDOCT system, this would be on adjacent pixels and for FFSSOCT, this would be adjacent time points.

In order to create a spectral waveform with a periodicity equal to the Nyquist sampling limit, the wavelength of light detected at one pixel (λ_1) must create complete constructive interference whilst the wavelength detected at the following pixel (λ_2) must create fully destructive interference. Therefore, λ_1 must arrive at the detector completely in phase with the reference arm signal and λ_2, completely out of phase with reference arm signal. The shortest distance (d) at which this occurs is when an object sits in the sample arm of the interferometer at a distance from the zero delay equal to an integer number m of λ_1 and $m-1$ of λ_2 with an additional half a wavelength of λ_2. The addition of half a wavelength of λ_2 ensures that λ_2 will be out of phase at the detector.

$$m\lambda_1 = (m-1)\lambda_2 + \frac{1}{2}\lambda_2 \qquad \text{Eqn. 14}$$

Re-arranging this Equation 14 to solve for m:

$$m = \frac{\frac{1}{2}\lambda_2}{\lambda_2 - \lambda_1} \qquad \text{Eqn. 15}$$

[This equation assumes that $\lambda_2 > \lambda_1$]

The distance d is now simply the integer number m multiplied by the wavelength λ_1. As the distance calculated does not take into account the reflection of the OCT signal, it is twice as large as the real depth range and must be halved to give the correct value. Re-arranging Equation 15 to calculate d gives:

$$d = \frac{\lambda_1 \lambda_2}{4(\lambda_2 - \lambda_1)} \quad \text{Eqn. 16}$$

As λ_1 and λ_2 are arbitrary wavelengths representing neighbouring time points during the acquisition sweep, the difference between them is exactly equal to the spectral resolution of the spectrometer. Therefore, λ_1 -λ_2 can be equated to the bandwidth of the light source ($\Delta\lambda$) divided by the number of pixels on the spectrometer for FDOCT or frequency samples for FFSSOCT (N_s). Substituting this into Equation 16 gives:

$$d = \frac{\lambda_1 \lambda_2 N_s}{4\Delta\lambda} \quad \text{Eqn. 17}$$

Typically, the spectral resolution is very high and therefore $\lambda_1 \approx \lambda_2$. As a result, the centre wavelength of the light source (λ_0) can be used in order to calculate *d*:

$$d = \frac{{\lambda_0}^2 N_s}{4\Delta\lambda} \quad \text{Eqn. 18}$$

For FDOCT, calculating the number of pixels (N_s) can be difficult as the distribution of frequencies has no reference point in the spectrometer. In FDOCT, the exact frequency distribution is not required in order to generate a tomogram; therefore typically the spectral distribution is unknown. Given a spectral bandwidth and FWHM of the light source, it would be possible to calculate (N_s); however, factors such as the non-linear distribution of frequencies (See section 4.6) and spectral intensity response of the camera can introduce errors into this calculation.

For FFSSOCT, calculating (N_s) is straightforward as the bandwidth of the light source is set by the radio frequency generator and the power is kept constant by feedback circuits within the light source. The small amount of geometry correction required to re-linearise the spectral distribution of frequencies has a negligible effect on the derived depth range compared to the measured one.

It should be noted that in addition to the parameters of Equation 18, other factors such as the coherence length and linewdith of the light source and the sensitivity roll off limit the maximum axial distance that an OCT device can operate at (section 5.6).

5.4 Resolution and sampling

5.4.1 Lateral resolution

The lateral resolution of any microscope system is determined by the focussing optics. The FFSSOCT design used a 5x microscope objective lens from Zeiss. Since the optical beam fills the back plane of the objective, the resolution of the system is theoretically diffraction limited and the standard equations for calculating the FWHM lateral resolution (Δx) can be used:

$$\Delta x = \frac{0.61\lambda}{NA} \qquad \text{Eqn. 19}$$

This equation can be used despite the Gaussian intensity profile of the light because the beam actually over filled the back plane of the objective, producing an approximately planar intensity distribution on the lens. The equation to calculate the minimum theoretical resolution (Equation 19) is based on the numerical aperture (NA) of the objective lens, 0.15NA giving a minimum resolution of 4.7µm.

To accurately measure the true lateral resolution of the FFSSOCT system, a standard resolution target (USAF 1951) was imaged:

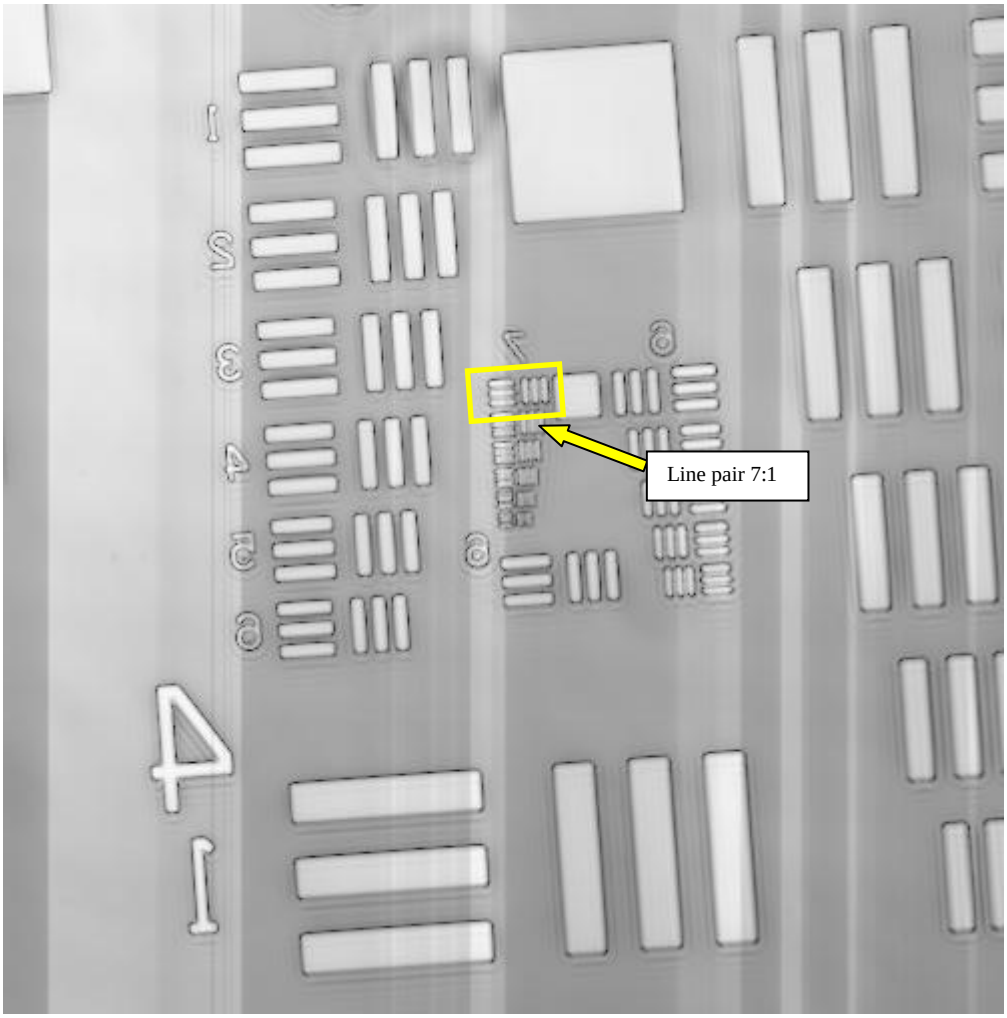

Figure 5-1: USAF 1951 target imaged by FFSSOCT.

The tomogram was resliced into the en face direction giving an image with lateral dimensions of 504x500 pixel (685x680µm). the image was acquired with the Photon Focus camera.

The lateral resolution was obtained from the USAF target by determining the smallest line pair at which the lines are just distinguishable. From Figure 5-1, line pair: group 7, element 1 is just resolvable which corresponds to 128 line pairs per millimetre giving a measured lateral resolution of 7.8µm.

To test if there were any chromatic problems with using multiple wavelengths to construct the image, the USAF 1951 target was imaged a second time with a single wavelength only.

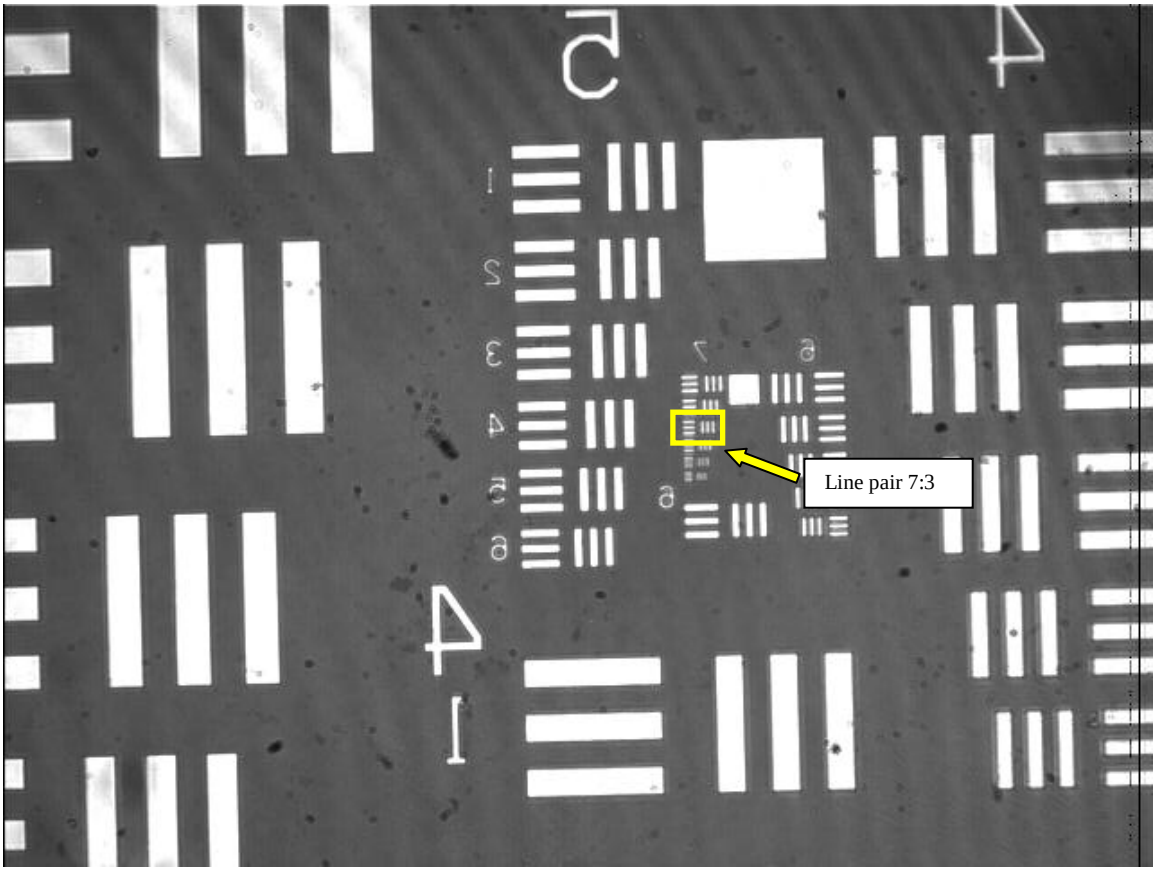

Figure 5-2: USAF target imaged by a single wavelength (850nm).

The image was acquired directly from the camera without sweeping through the optical spectrum. The 640x480 pixel (970x730µm) image was acquired with the Silicon Imaging 640HF M camera.

Figure 5-2 was acquired as a traditional bright field microscopy image using a single wavelength in order to measure the resolution without acquiring a full FFSSOCT interferogram. Line pair 7:3 (161 line pairs per mm = 6.2µm) is still resolvable in Figure 5-2 indicating that the FFSSOCT acquisition process has a detrimental effect on the achievable lateral resolution of the system. The reduction in the measured resolution was due to the change in focal length experienced by each wavelength across the bandwidth of the light source. As the broadsweeper sweeps through each wavelength, the acquired image shifts due to the amount of refraction experienced by each wavelength through the objective lens. The shift in the image position over the acquisition period causes part of the interferogram spectrum to be recorded by adjacent pixels, blurring the recorded data with a resultant reduction in the lateral resolution.

5.4.2 Lateral sampling

Sampling is an important factor in all types of digital imaging. Sampling in OCT refers to the number of detection elements that are dedicated to a specific size region. The size of the region is dictated by the resolution of the system; the sampling size must exceed this value in order to avoid losing information. Nyquist theory states that the sampling rate must be twice the highest frequency signal in order for that signal to be resolved. In the case of OCT, the Nyquist limit is twice the resolution of the system, both laterally and axially. If the sampling rate does not reach this criteria, information from the sample maybe be lost.

The lateral sampling for FFSSOCT is set by the size and number of pixels on the detector and the transfer optics that project the image onto the camera chip. The transfer optics inside the microscope housing remained the same during the study but the camera was changed which resulted in a change in the lateral scaling. The initial camera used (Silicon Imaging 640HF M) had a pixel pitch (size including gaps between pixels) of 9.9µm, this was changed to a Photon Focus (MV1-D1312I-160-CL-12) with a pixel pitch of 8µm which resulted in an increase of the lateral scaling rate of 20% (the equivalent of a 20% decrease in the size of each lateral image pixel).

The lateral sampling rate was derived from Figure 5-1, by dividing the size of one line pair by the number of pixels it occupied. Line pair 5:1 (Figure 5-1) corresponds to 32 line pairs per mm, giving a total distance covered by 2 line pairs of 62.5µm. These two lines occupy 46 pixels giving a lateral sampling rate of 1.36µm per pixel. However, as the Photonfocus camera had a different pixel pitch to the Silicon Imaging camera (8µm compared to 9.9µm), the lateral sampling rate was also different. The lateral sampling rate for the Silicon Imaging camera was calculated from Figure 5-2; line pair 4:1 corresponds to a total distance covered by 2 line pairs of 125µm. These two lines occupy 82 pixels giving a lateral sampling rate of 1.52µm per pixel. Therefore, images taken with the Photonfocus camera had a sampling rate of 1.36µm per pixel and images taken with the Silicon Imaging camera had a lateral scaling of 1.52µm per pixel.

In both cases, the sampling rate is more than twice that of the measured optical resolution. Therefore, the system with either camera was sufficiently oversampled and there was no loss of lateral information.

5.4.3 Axial resolution

The axial resolution of all OCT systems is determined by the coherence length of the optical source used. The coherence length of an optical source can be determined from its relationship to the range of wavelengths that the light source outputs i.e., its bandwidth.

This relationship is derived from the addition of all wavelengths present on a detector, the greater the number of wavelengths, the narrower the coherence length becomes.

$$\Delta z = L_c = \frac{2log_e(2)}{\pi n}\frac{{\lambda_0}^2}{\Delta\lambda} \qquad \text{Eqn. 20}$$

The coherence length of a light source (L_c) and hence, the theoretical axial resolution of the OCT system are inversely proportional to both the tuning bandwidth of the light source ($\Delta\lambda$) and the refractive index of the sample medium, *n*. Note here that the tuning band width is equal to the range of wavelengths the light source can produce (50.8nm) and not the instantaneous bandwidth which is equal to the line width of the light source (0.045nm). The dependence on the refractive index of the sample on the coherence length is due to the reduction in the speed of light in the higher refractive index medium, resulting in a reduction of the wavelength of the light source and therefore, its coherence length[3,13,22].

For the FFSSOCT system, the central wavelength was 850nm and the bandwidth was 50.8nm giving a theoretical axial resolution of 6.3µm in air. To obtain an accurate measurement of the working axial resolution of the FFSSOCT system, an image of a planar reflecting surface was collected. By examining the axial 'edge' profile of the planar reflecting surface, the spatial broadening due to the limited axial resolution could be measured. A mirror was used since the axial edge profile is equivalent to a step function rising from zero to near 100% reflectance; therefore, the measured broadening of the step function will give the axial resolution of the system.

Additionally, as the bandwidth of the light source and the microscope objective were never changed, the resolution of the FFSSOCT system stayed constant throughout the project.

5.4.4 Axial Sampling

Sampling in the axial direction via the number of frequency steps is one limiting factor determining the maximum imaging depth (section 5.3). However, the only variable in Equation 18 is the number of frequency steps (Ns) and the maximum image depth changes linearly with this variable resulting in a constant value for the axial sampling.

$$Axial\ sampling\ = \frac{d}{N_s} = \frac{{\lambda_0}^2}{4\Delta\lambda} \qquad \text{Eqn. 21}$$

As the axial resolution for a swept source system (Equation 20) scales by the same variables as Equation 21, the ratio between the axial resolution and the axial sampling does not change regardless of the light source used. Substituting the axial resolution Equation 20 into Equation 21 gives:

$$Axial\ sampling\ = \frac{1}{4}\left(\frac{{\lambda_0}^2}{\Delta\lambda}\right) = \frac{1}{4}\left(\frac{\pi\delta z}{2log_e(2)}\right) = \left(\frac{\pi}{8log_e(2)}\right)\delta z = 0.567\delta z \qquad \text{Eqn. 22}$$

From Equation 22, it can be seen that the axial sampling size is not less than half the axial resolution (the axial sampling rate should be two samples per resolution size in order to satisfy the Nyquist criteria). Therefore, one important consideration when using a swept source system is the fixed axial undersampling rate. To compensate for this, the zero padding operation should be used when processing the spectral data (section 4.7).

5.5 Signal to noise ratio (SNR)

The SNR is the most commonly used method in comparing the sensitivity of different OCT systems since it can be used as a measure of the minimum signal the system can detect[13,77].

The SNR is defined as:

$$SNR_{db} = 20log_{10}\left(\frac{S_{max}-N_{floor}}{SD_{Noise}}\right) \quad \text{Eqn. 23}$$

Where S_{max} is the amplitude of the peak signal, N_{floor} is the amplitude of the average noise around the signal peak and SD_{Noise} is the standard deviation of the noise around the peak. By taking into account the noise floor of the signal, the overall amplitude of the measurement becomes normalised. The advantage of this is that the SNR of different measurements and images can be directly compared even when the images have been subject to brightness or contrast modifications:

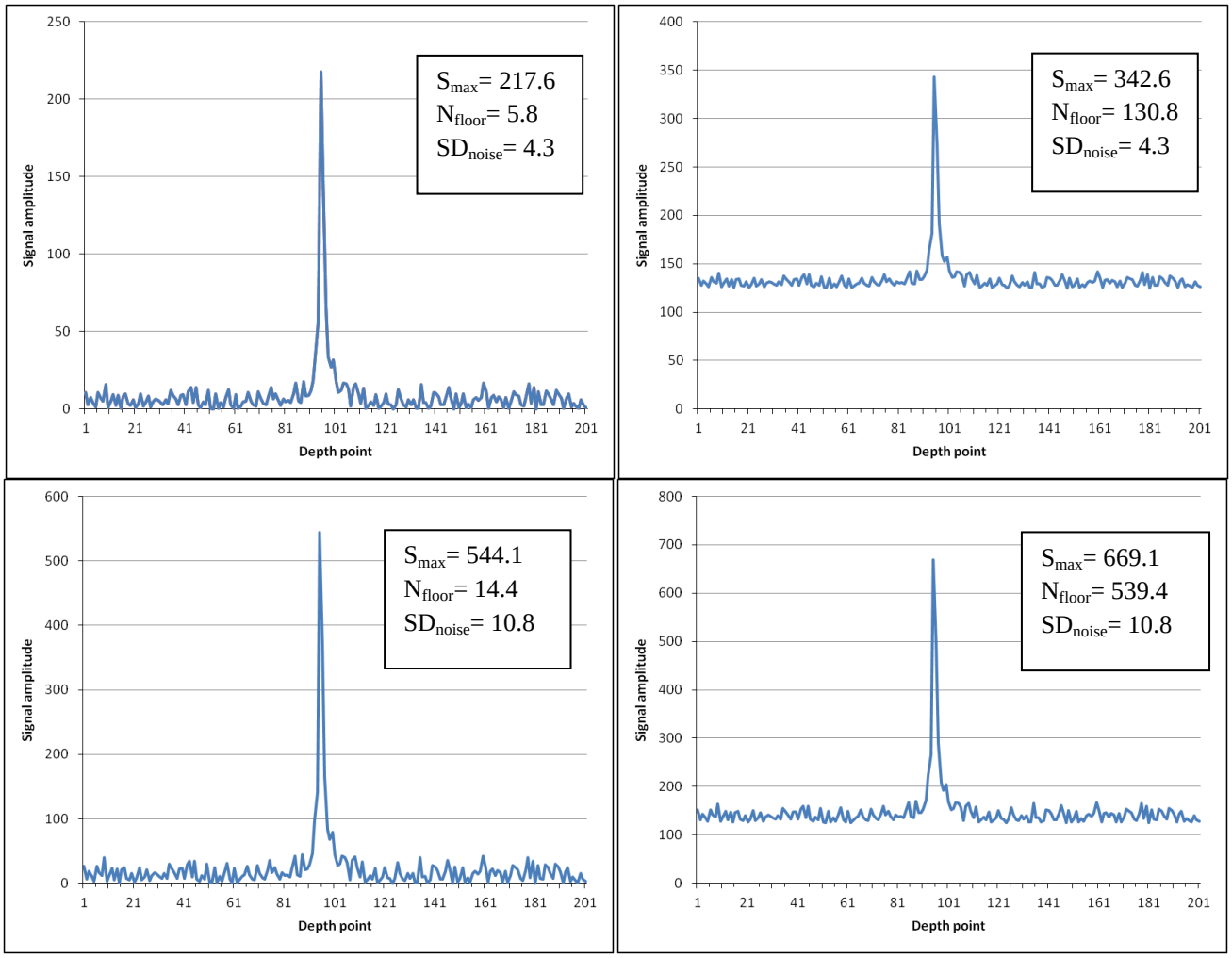

Figure 5-3: Four sample spectra generated by a Fourier transform of a noisy sine wave signal. The sine wave source signal has a frequency of 100hz and an amplitude of 1 with random noise between -0.5 and 0.5 added to it. Top left: the absolute real part of the FFT of the data (cropped from 1000 to 200 samples). Top right: the FFT of the data with 125 added to it. Bottom left: the FFT multiplied by 2.5. Bottom right: the FFT multiplied by 2.5 with 125 added to it.

Figure 5-3 shows typical A-line data which was generated for a mirror. A different adjustment was applied to each frequency spectrum thereby simulating typical brightness and/ or contrast alterations that might be made to an image. The top right spectrum shows a typical background adjustment, adding or subtracting an arbitrary amount in order to decrease the apparent noise. The bottom left spectrum shows a scaling modification, an operation used to redistribute intensity values into a different dynamic range. The bottom right spectrum shows a combination of the two. Despite these differences, each case has the same SNR value of 33.78dB, indicating that using the SNR is a valid method of comparing two OCT systems despite modifications made to the final images.

5.5.1 Problems with measuring real SNR

When dealing with OCT data, there were multiple factors that affected the overall signal shape and characteristics including, sensitivity roll-off, signal broadening and multiple reflectance spikes. These made measurements of the SNR somewhat arbitrary if, for example, the signal contained multiple frequencies with less noise compared to the rest of the spectrum. Such a situation arose with OCT due to the sensitivity roll-off phenomenon, based on finite linewidth frequency detection.

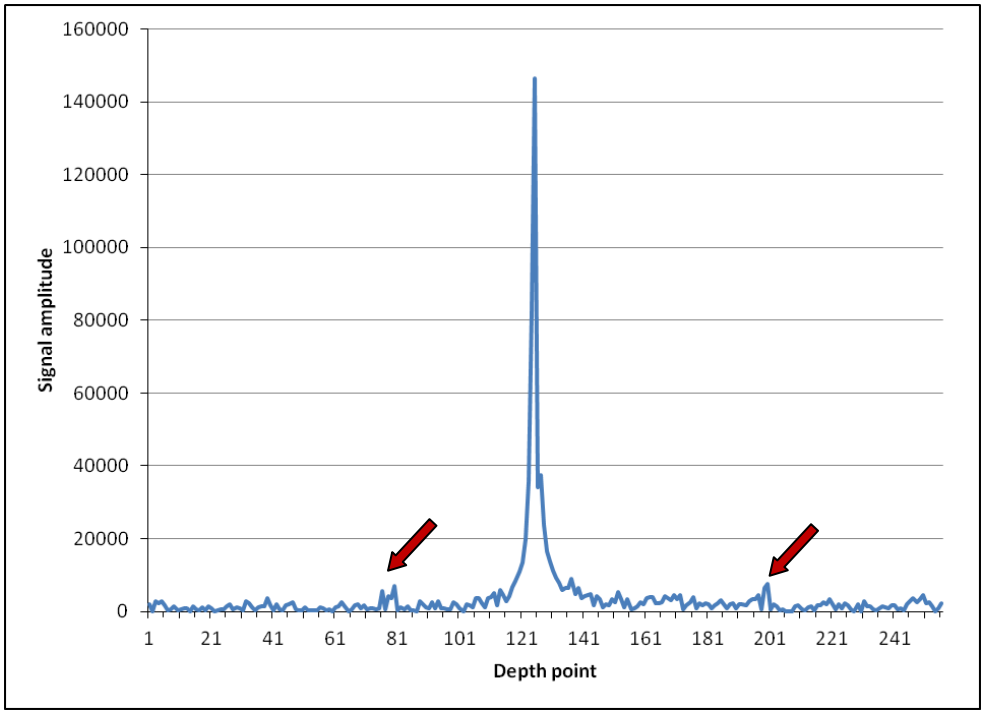

Figure 5-4: An A-line of FFSSOCT data taken from an image of a mirror. The red arrows indicate signal from surfaces within the system. The only processing applied to the data was the removal of the DC offset.

With non-linear noise artefacts, the SNR could be artificially boosted by taking the N_{floor} measurement where the noise is lowest. To avoid this, the best method would be to measure the N_{floor} directly surrounding the signal of interest.

As the spectral data in Figure 5-4 shows, the peak of the signal resulting from the mirror was broadened around the base. This broadening is the result of a combination of different effects; the axial resolution of the system, phase instabilities and finite spectral resolution. The effect of finite spectral resolution can also been seen in the broadening of the signal peaks in Figure 5-3. Additionally, while the axial and spectral resolutions are fixed by the system design, the phase instability, resulting from micro-vibrations during the image acquisition time were random and could have caused more, or less, broadening in subsequent images. The challenge was therefore, to determine where to define the N_{floor} for a particular SNR measurement. The region selected must be sufficiently far away from the peak that the wide base has negligible effect on the noise level in that area.

An alternative method, which was not used, would have been to acquire a second image without the mirror in the sample arm, thereby allowing the N_{floor} to be measured at exactly the same position as the signal. After an image was obtained with the mirror in place, it would be removed and another image obtained. This would allow for a more precise measure of the noise but would not account for any time variations in the SNR or contributions from the signal to the local noise (i.e. the broadening).

To compound this problem of measuring the N_{floor}, the spectrum also contained many other signal peaks originating from other reflecting surfaces within the coherence length of the SLD source. The largest of these was removed by tilting the components with the FFSSOCT system (such as the objective lenses) but many other peaks remained (red arrows, Figure 5-4 and Figure 5-5). As these additional peaks were caused by static internal components of the FFSSOCT system, they could be reduced by background subtraction; however, the peaks were also subject to the same random broadening due to phase instabilities as the main signal peak. As a result, it was impossible to completely remove them. Though these peaks can be regarded as noise, due to their static location in the A-line, it is possible to discern the sample signal around them, making the sensitivity of these small regions higher. For example, in Figure 5-5 a signal with amplitude of 3500

could be detected at a depth of 57 but not at 78 where one of the static artificial signal peaks lies. This will remain true as the artificial signal peaks do not appear at other positions giving the FFSSOCT system a variable sensitivity profile with depth.

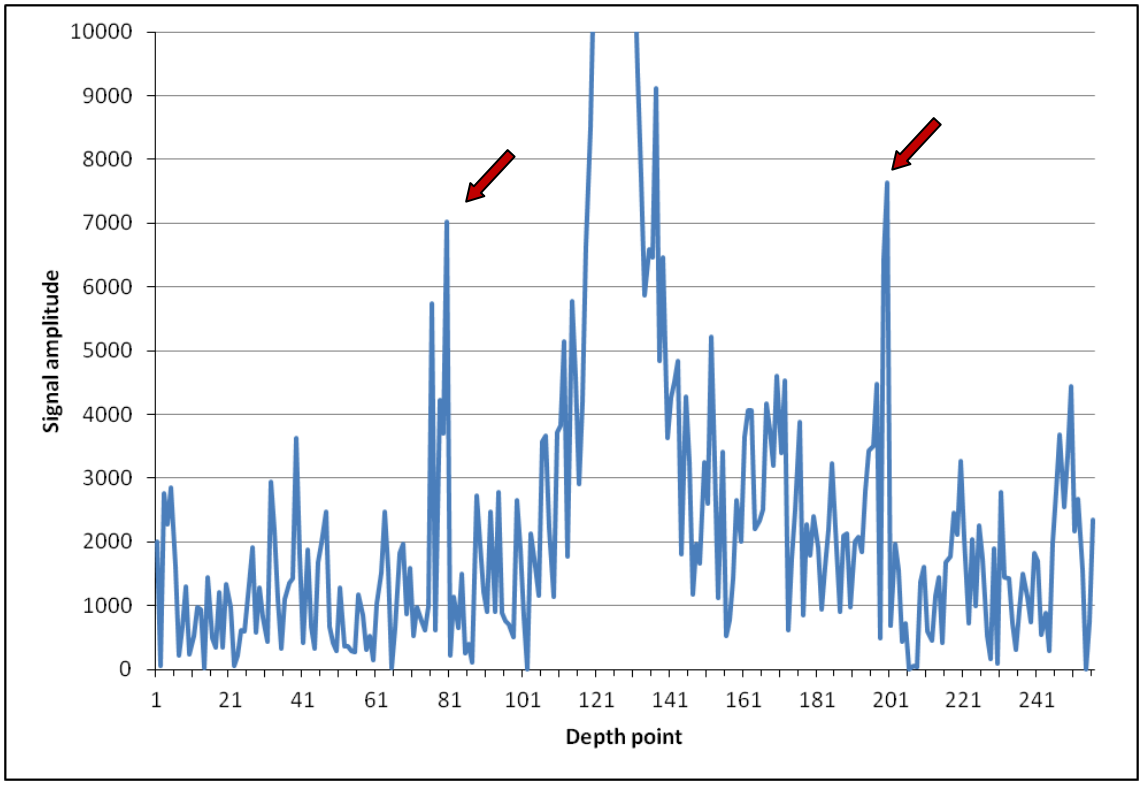

Figure 5-5: An A-line of FFSSOCT data with the amplitude cropped.

The red arrows indicate signal from surfaces within the system. The data from Figure 5-4 has been cropped to a signal amplitude of 10,000.

Therefore, the SNR of the FFSSOCT system was measured by processing the data as normal, subtracting the background in order to minimise the artefact peaks and, finally, taking the N_{floor} from as close to the peak as possible without including any of the signal from the broad base. By this method, both the uneven noise distribution due to sensitivity roll-off and the artefact peaks created by unwanted reflections from within the FFSSOCT system were addressed.

5.6 Sensitivity fall-off

FDOCT captures information on the sample in the frequency domain and converts to the time domain by a Fourier transform. The benefit of this is a very fast acquisition time compared to TDOCT but there is also a disadvantage to this method of acquisition. The

problem lies with the sampling of the analogue frequency signal and its corresponding digital transform to the time domain. When sampling an analogue signal, the user decides the amount of sampling required in order to accurately sample the highest frequency of interest. For OCT, this would be the 'deepest' signal i.e., furthest from the zero delay for a particular application. Depending upon the light source used, only a few mm of depth penetration can be achieved in weakly scattering tissue before the signal is scattered beyond the sensitivity limits of the system[18]. The required imaging depth can be calculated from the equations in section 5.3.

5.6.1 Theory of OCT sensitivity fall-off

Using a broad bandwidth light source in FDOCT (in order to achieve a high resolution) distributes the optical power into each wavelength of the spectral continuum. Therefore, each wavelength must be detected in order to utilise the full power of the light source. However, the spectrometer has only a limited number of pixels on its detector and bins multiple wavelengths into the same pixel[75,78]. This has an averaging effect on the spectral waveform that degrades the detected waveform amplitude and sensitivity. As FFSSOCT (and SSOCT) use a light source that outputs a single frequency per unit time, this averaging effect is less significant and therefore, the sensitivity of the system is not degraded as much as FDOCT systems. However, the averaging effect does still occur due to the finite linewidth of the output frequency.

In addition to the pixel sampling of the spectrometer in and FDOCT system, the point spread function of the focussing optics also contribute to the sensitivity decay. Due to the finite resolution limit of the optics in the spectrometer, the focussed spot has a limited resolution, resulting in a Gaussian distribution of the intensity of each wavelength on the detector. The Gaussian distribution for each wavelength will overlap, creating an additional spectral averaging that will further degrade the sensitivity roll off. For FFSSOCT, each optical wavelength is separated in time and therefore, this effect is not an issue[79,80].

Further factors that affect the sensitivity roll off of both FDOCT and FFSSOCT include the coherence length of the light source and the depth of field of the objective optics. The

coherence length of a light source has a Gaussian distribution with time . As the optical path length difference (and therefore time difference) between the reference and sample arms increases, the amount of overlap between their respective Gaussian functions decreases. This results in a decrease in sensitivity as the imaging depth increases. As described in section 1.3, the depth of field affects the lateral resolution of the optics and hence, as the sample moves further out of the focal plane, the amount of light detected by the system decreases, reducing the sensitivity.

Figure 5-6 illustrates how a low frequency signal (16hz) would be detected by both FDOCT (green) and FFSSOCT (red) considering only the spectral properties of their respective detection systems; pixel sampling for FDOCT and optical linewidth for FFSSOCT .

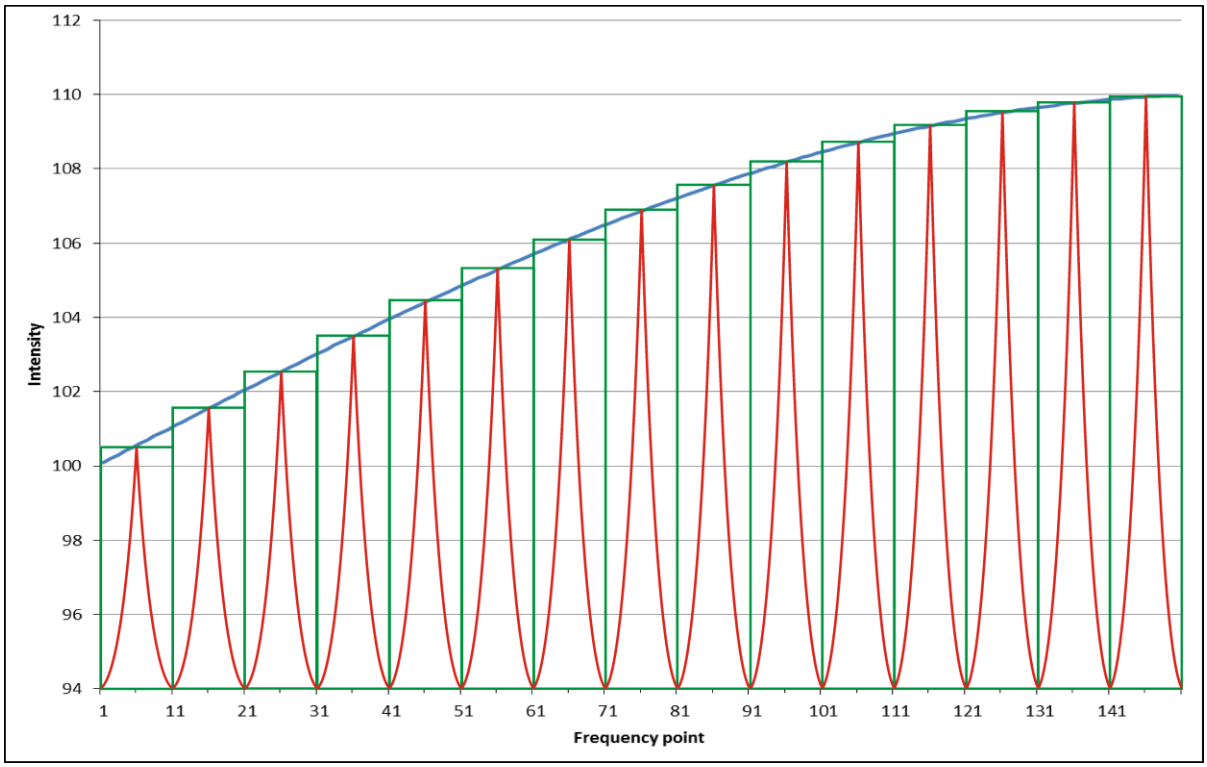

Figure 5-6: Sampling a 16hz waveform with FDOCT and FFSSOCT.

Blue line - A 16hz signal sampled 10,000 times (150 points shown). The green boxes represent the sampling of the frequency by the pixels on the spectrometer in an FDOCT system. The red lines represent the Gaussian spectra of a single frequency used in FFSSOCT where the FWHM of the Gaussian would be equal to the linewidth of the light source and the x-axis would be acquisition time.

The linewidth of the SS based OCT systems is shown as approximately half the width of the FDOCT spectral bins, representing a typical difference in spectral resolution between the techniques[26]. The binning of the signal by the pixels of the spectrometer in FDOCT results in an average of the detected frequency domain signal across each sample. The resulting outcome is not apparent with a low frequency signal (the blue, green and red signals appear at the same point at the centre of each sample bin). Therefore, after Fourier transform (Figure 5-7), the amplitude of both the FDOCT and FFSSOCT (green and red - Figure 5-6) close to the zero delay is near identical (<0.1%) to the highly sampled data (blue line - Figure 5-6).

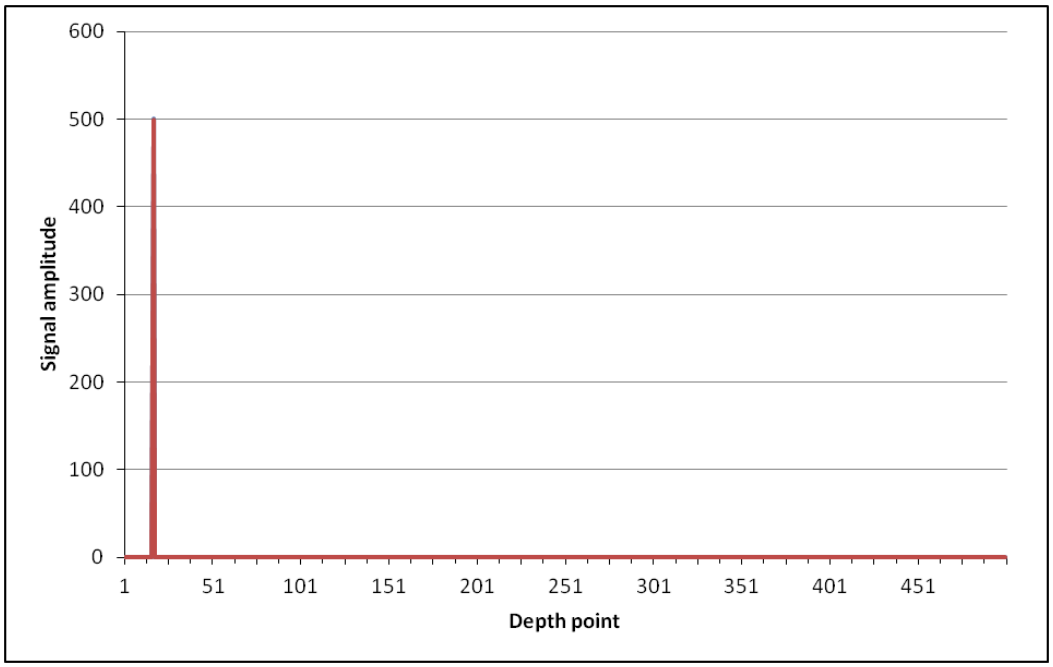

Figure 5-7: The real part of the Fourier transform of the sampled data shown in Figure 5-6. The data has been cropped to remove the duplicate signal and DC component. The amplitudes shown are overlaid on one another: blue: 500.0 (highly sampled data), red: 500.0 (FFSSOCT sampled data) and green: 499.8 (FDOCT sampled data) corresponding to the colours in Figure 5-6.

Figure 5-8 and Figure 5-9 show how the limited sampling affects a high frequency signal. As the green boxes illustrate, the effect of sampling multiple spectral points with the spectrometer based FDOCT approach has produced a data point with a different amplitude to the original data. This is particularly apparent where the gradient change of the sinusoid is greatest, which has the effect of decreasing the amplitude of the reconstructed waveform (Figure 5-9) and, therefore, the post FFT time domain signal. Sampling in time with the

narrow line width swept source approach has resulted in greater sampling accuracy of the waveform and hence, the time domain signal is not reduced as greatly. As Figure 5-10 illustrates, sampling a higher frequency waveform with a spectrometer based sampling (green line) results in a greater loss of sensitivity than a swept source based OCT (red line). As the frequency of the sampled waveform increases further, the amount of sensitivity decay becomes greater. As the frequency increases, the degree of sinusoidal gradient change covered by a single pixel becomes greater and the overall amplitude of the reconstructed waveform becomes correspondingly smaller.

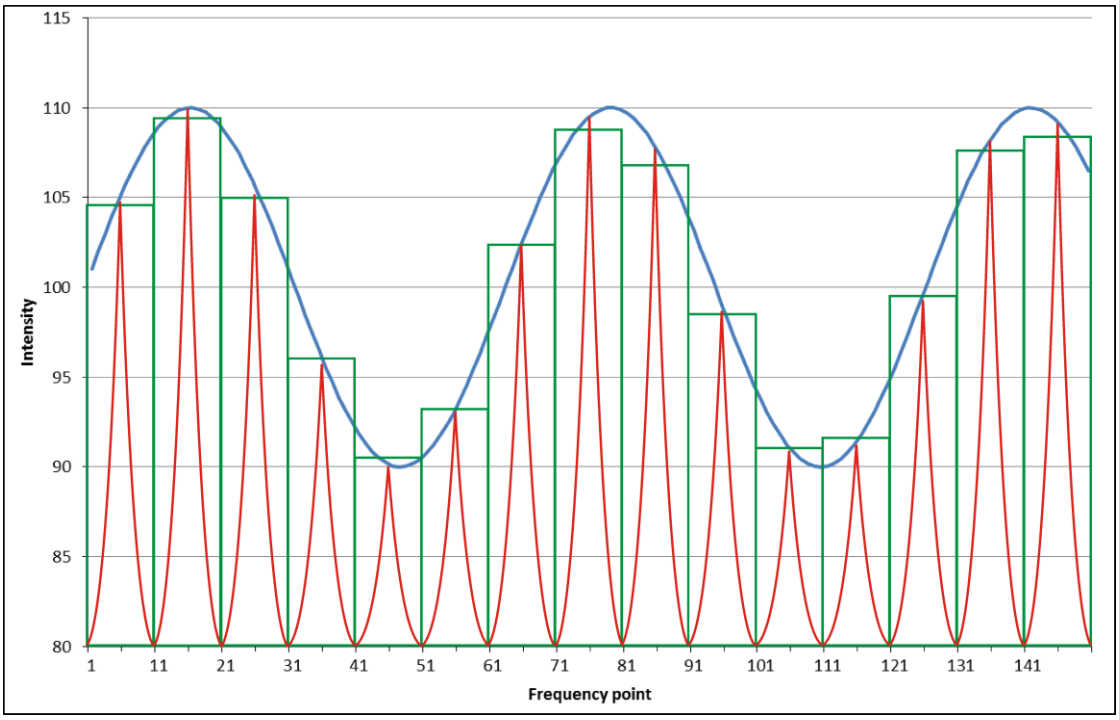

Figure 5-8: Sampling a 159Hz waveform with FDOCT and FFSSOCT.

Blue line - A 159hz signal sampled 10,000 times (150 points shown). The green boxes represent the sampling of the frequency by the pixels on the spectrometer in an FDOCT system. The red lines represent the Gaussian spectra of a single frequency used in FFSSOCT where the FWHM of the Gaussian would be equal to the line width of the light source and the x-axis would be acquisition time.

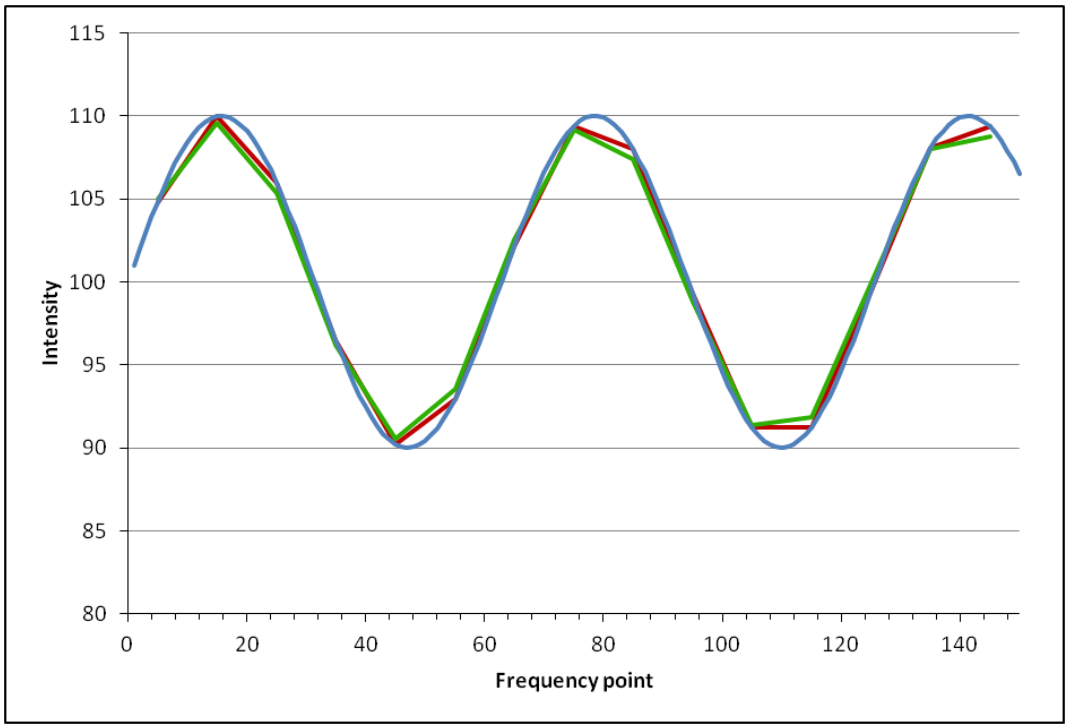

Figure 5-9: The reconstructed waveform from the data sampled by FDOCT and FFSSOCT.

The coloured lines correspond to the colours in Figure 5-8. Blue: highly sampled data. Red: data sampled by FFSSOCT. Green: data sampled by FDOCT.

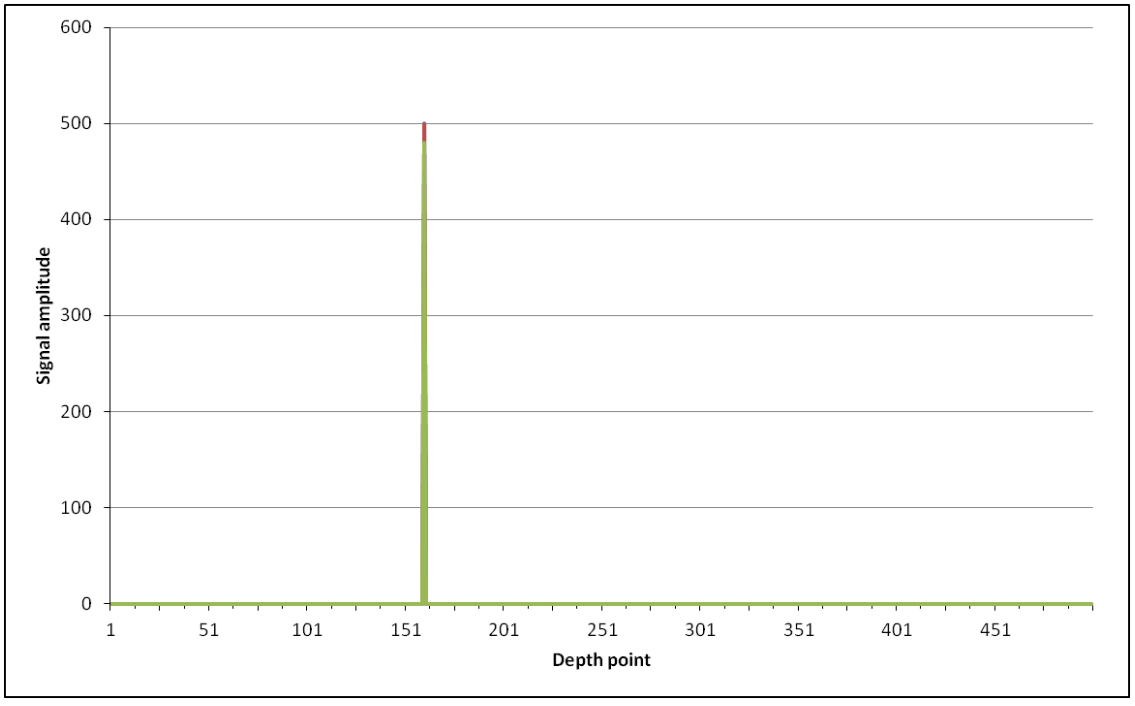

Figure 5-10: The FFT of the data sampled by FDOCT and FFSSOCT.

The data has been cropped to remove the duplicate signal and DC component. The amplitudes shown are: blue: 500.0, red: 498.6 and green: 479.7 corresponding to the colours in Figure 5-9.

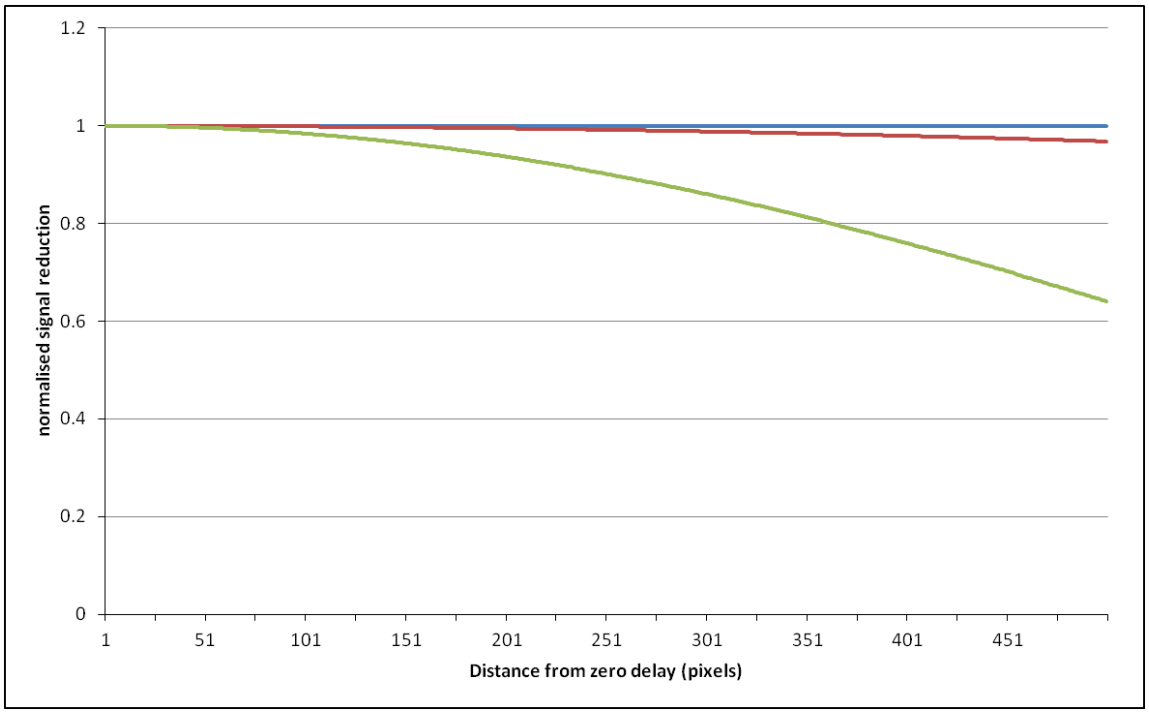

Figure 5-11: The sensitivity decrease of OCT.

Blue line – highly sampled data. Green line – data sampled by FDOCT. Red line – data sampled by FFSSOCT. The data has been normalised.

Figure 5-11 shows the time domain decrease in sensitivity over all frequencies. As the frequency increases, the sampling becomes less accurate and the time domain signal amplitude decreases. The rate of decrease is greater for FDOCT (green line) due to the reduced accuracy of its sampling method compared to FFSSOCT (red line). As the sensitivity is highest at the low interferometric signal frequencies (close to the zero delay), the highest image quality is achieved when the sample of interest is as close to the zero delay as possible. In the case of retinal imaging, this may involve adjusting the reference arm length in order to invert the image, thereby increasing the captured signal from the deeper layers, e.g. the choroid or the optical nerve head[15,25,56].

The advantage of the decreased sensitivity fall-off achieved with SSOCT then becomes apparent as the image can remain uninverted without loss of signal from the deeper layers. Therefore, shallow and deep sample structures can be acquired with homogenous detection sensitivity in a single image, eliminating the need for multiple images to be taken. Additionally, the resulting image gives a true representation of the actual scattering properties of the sample without the need to account for the sensitivity fall-off beforehand, something that may not be known to those analysing the image.

The fall-off function for FDOCT can be described mathematically as the Fourier transform of the spectral window function (a single pixel) multiplied by the Gaussian form of the point spread function resulting from focussing optics of the spectrometer. The pixel can be described as a top hat function with length, *x*, equal to the number of pixels on the detector and amplitude 0 with a single pixel having an amplitude of 1. The positive real values of this Fourier transform are identical to the values of the green line shown in Figure 5-11[3,13,19,22]. The fall-off function for FDOCT can be shown to be:

$$F_{decay}(z) = \left(\frac{sin(d_{norm})}{d_{norm}}\right)^2 . exp^{\left(-\frac{w^2}{2log_e(2)}{d_{norm}}^2\right)} \quad \text{where} \quad d_{norm} = \frac{z}{d}, \quad w = \frac{N_s}{\Delta\lambda} \quad \text{Eqn. 24}$$

where z is the depth within the imaging range, d is the maximum image depth (Equation 18), and N_s is the number of pixels[75,79,80]. It can also be seen that a doubling of the available number of pixels (N_s) does not change the shape of the overall fall-off function (as it is normalised) but does reduce the amount of sensitivity loss at a given pixel. For example, the sensitivity loss at pixel 250 (N_s=500) is 10% whereas for pixel 250 (N_s=1000) the loss is only 2.25%.

5.6.2 Sensitivity fall-off in FFSSOCT

The FFSSOCT fall-off data can also be modelled by a Fourier transform of the spectral window function, however this now takes the form of a Gaussian rather than a top hat function. The Gaussian function is a result of the instantaneous spectral output of the light source (linewidth). The sensitivity roll-off, as described as the Fourier transform of the spectral window (Equation 24) for FDOCT, does not equal the sinc function for FFSSOCT, but rather another Gaussian function (as the Fourier transform of a Gaussian function is a Gaussian).

The Gaussian form shown in Figure 5-6 has a base equal to one pixel from an FDOCT system; this was shown for illustration as the linewidth of the light source used in FFSSOCT systems is much smaller. For example, if the FDOCT system had 1000 pixels on its spectrometer and a light source with a bandwidth of 100nm, the spectral resolution would be 0.1nm, equal to the spectrum covered by a single pixel. The spectral resolution (linewidth) of the FFSSOCT system was 0.045nm and, therefore, the interferometric

waveform can be more accurately reproduced; consequently, the fall-off function is less severe. It should be noted that even with an infinitely narrow linewidth, there will always be a sensitivity fall-off due to noise; shot noise and camera noise (dark current, thermal noise) will decrease the definition of each frequency in the spectral interferogram. The decreased definition effect is greater at higher frequencies due to the reduced sampling (see Figure 5-8) and hence, the loss of sensitivity is correspondingly greater.

The theoretical fall-off rate due to the spectral sampling for FFSSOCT can be calculated from the linewidth, bandwidth, centre wavelength and number of frequency samples used. The majority of the images captured with the FFSSOCT system used 512 frequency samples and 50.8nm bandwidth. The linewidth and centre wavelength were 0.045nm and 849.3nm, respectively. This gave a maximum theoretical depth range of 1.82mm in air (Equation 18). The theoretical sensitivity fall-off rate for FFSSOCT can then be calculated by sampling each of the 512 frequency points with the Gaussian frequency distribution of the light source.

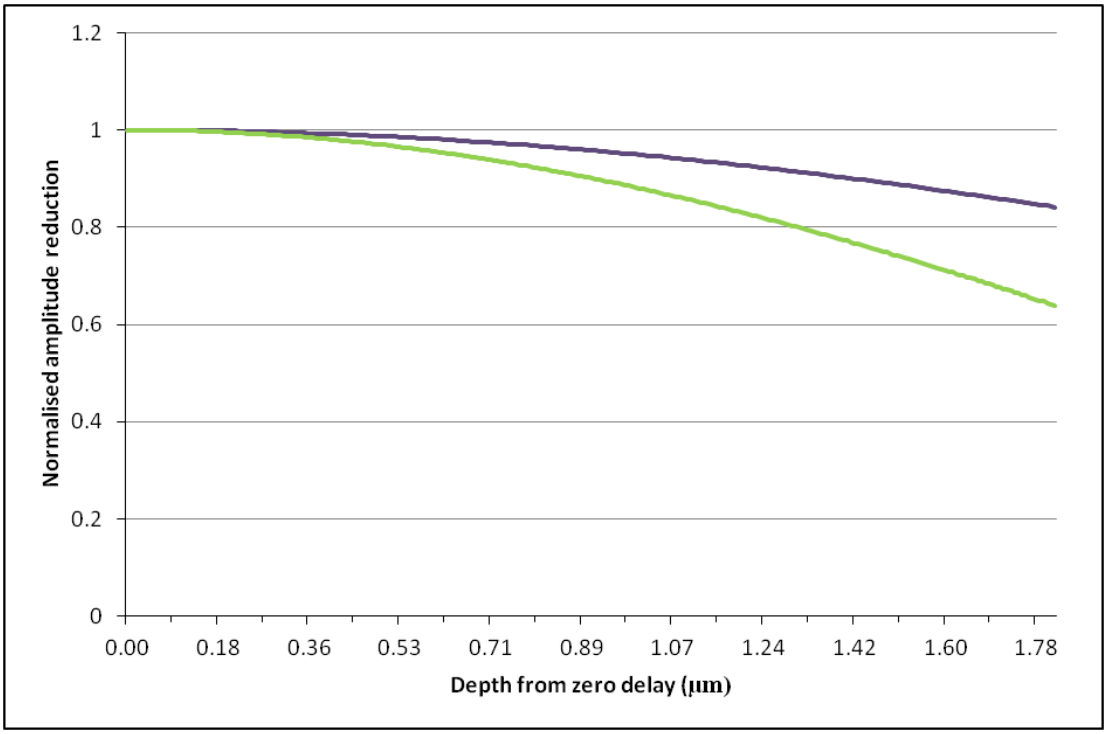

Figure 5-12: The theoretical sensitivity decrease of FFSSOCT and FDOCT due to spectral sampling.

The acquisition parameters of both theoretical systems are the same. Green line – data sampled by FDOCT. Purple line – data sampled by FFSSOCT. The data has been normalised.

Figure 5-12 shows the FFSSOCT fall-off data. The FFSSOCT data has been sampled with a Gaussian distribution (FWHM = 0.045nm) and the FDOCT has been sampled by a top hat function representing the pixels on the spectrometer (spectral resolution = 0.1nm). As expected, Figure 5-12 demonstrates that the theoretical sensitivity decrease due to spectral sampling for FFSSOCT is ~50% less than FDOCT (as the spectral resolution is approximately half).

5.6.3 Measurement of the sensitivity fall-off of the FFSSOCT instrument

The theoretical calculated FDOCT data assumes that the full spectral bandwidth is distributed linearly across the spectrometer. In reality, this will never be true as the frequency distribution across the spectrometer is chirped (non-linear) resulting from the different phase shifts experienced by each wavelength for each depth position (section 4.6). This non-linearity affects both FD and FFSSOCT systems and can be corrected by interpolation and resampling of the data, however these operations has a slight negative effect on the slope of the fall-off function. Also, whilst the FFSSOCT light source will optimise each frequency generated to the same power level (by the inbuilt APC unit), a typical broad bandwidth light source used in FDOCT will have a non-linear power output, i.e. each output wavelength has a different optical power . Therefore, the bandwidth distribution across the spectrometer may be clipped at the edges in order to reduce the number of pixels illuminated by very low optical power. Again, this will negatively affect the performance of the FDOCT system; however, the FFSSOCT system will not suffer from this effect due to its constant power output.

Unfortunately, there is another property of FFSSOCT that has a far more detrimental effect on the fall-off function then those listed above. This is a fundamental problem resulting from the long frame acquisition time required for this instrument. As described in section 1.6, a single A-line from the spectral interferogram is only complete when all the image data has been acquired, currently taking several seconds. As a result, the acquired data is very susceptible to corruption through any movement experienced by the sample and any large movement of the sample during the acquisition will destroy the image. Movement on the order of the wavelength of the light source (850nm) will blur the frequency information in the spectral domain. The effect is similar to the FDOCT spectral sampling

detailed above and the result is a sharp deterioration of the fall-off function of FFSSOCT. A typical FDOCT or SSOCT will also experience this effect but as the acquisition time is several orders of magnitude shorter, the effect of sample movement on the sensitivity of the instrument is less severe.

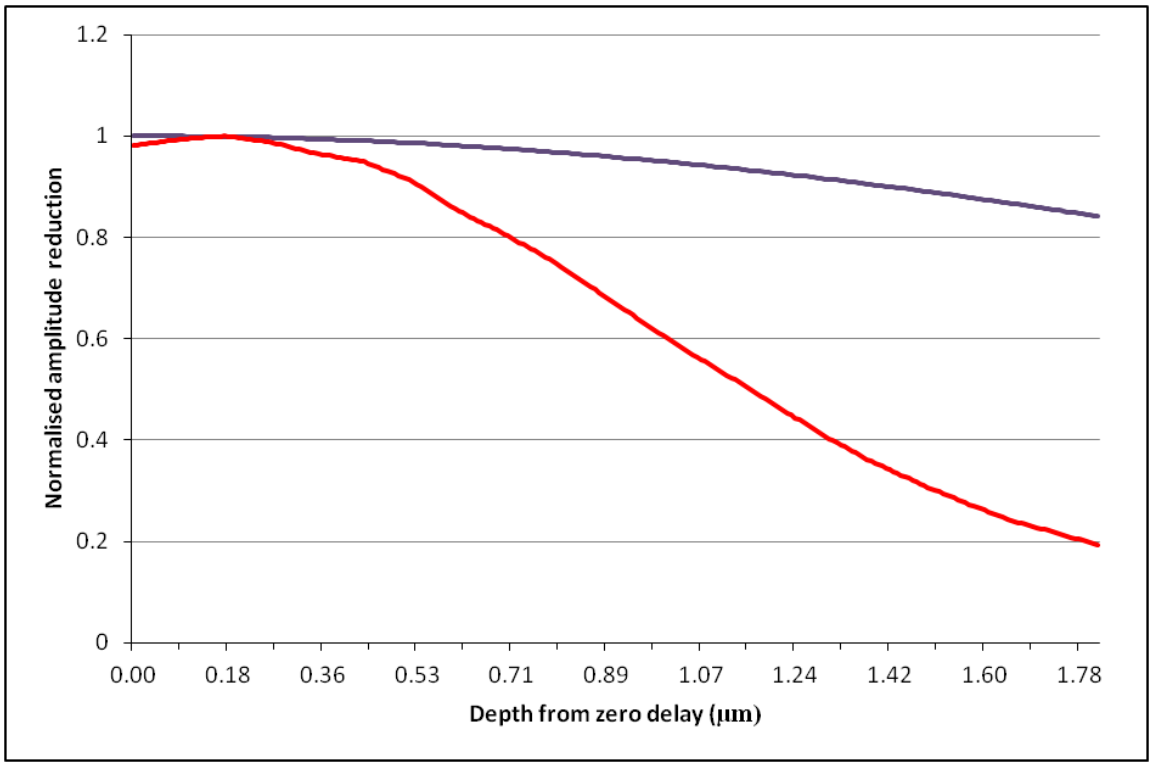

Figure 5-13: The theoretical and measured fall-off functions of FFSSOCT.
Purple line – theoretical FFSSOCT data (Figure 5-12). Red line – measured FFSSOCT data. The reduced signal at the 0.00 depth is caused by the background subtraction.

As shown in Figure 5-13, the fall-off function of the measured FFSSOCT data is substantially greater than that of the theoretical data. The data was acquired by taking repeated measurements of a mirror at equally spaced depth positions and subjecting the data to the processing steps detailed in Chapter 4, with the exception of intensity rescaling (the rescaling $20\log_{10}$ step was omitted).

The measured roll off data (Figure 5-13) is consistent with the theory of the origin of the sensitivity fall-off function. At greater depths, the averaging of the recorded frequency information causes a decrease in the amplitude of the generated spectral interferogram. However, the increase in the observed fall-off function compared to the theoretical data is

due to the added effect of phase instabilities within the system during the image acquisition time. At deeper axial positions (higher frequency on the spectral interferogram), a small change in the axial position of the sample causes a large change in the phase of the light in the sample arm relative to the reference arm. As a result, the amplitude of the interference fringe becomes very noisy and the average measured intensity over the frame acquisition time decreases (the phase noise cannot increase the amplitude above that of complete constructive interference). The overall result is a decrease in the amplitude of the waveform in the spectral interferogram and, consequently, less well defined peaks after the inverse Fourier transform is applied. At depths close to the zero delay, the frequency of the spectral interferogram is lower and the phase change due to small axial position changes is smaller. Therefore, the amplitude of the spectral interferogram waveform and the post iFFT signal is not reduced as severely as at deeper axial positions.

As the phase data in Figure 5-14 shows, the higher the frequency of the spectral interferogram waveform, the smaller the amplitude of the waveform resulting in a smaller signal at deep axial positions. In addition to this, the highly unstable phase of the deepest axial positions results in the distribution of signal amplitude being distributed to neighbouring data points resulting in a further decrease of the measured signal at these depths.

As the spectral interferogram ‘noise’ is a result of the unstable phase of FFSSOCT, it is commonly known as phase instability or phase jitter. Although the data shown in Figure 5-14 was acquired from a rigid sample on a vibration dampening bench, the micro vibrations of the instrument have enough of an effect to cause the large observed increase in the fall-off of the sensitivity function. This highlights the inherent extreme phase sensitivity of FFSSOCT at long frame acquisition times. For FFSSOCT to have a comparable sensitivity fall-off function of FDOCT, the image acquisition time needs to be dramatically reduced, far beyond what is capable with the Photonfocus camera used in the instrument design[28].

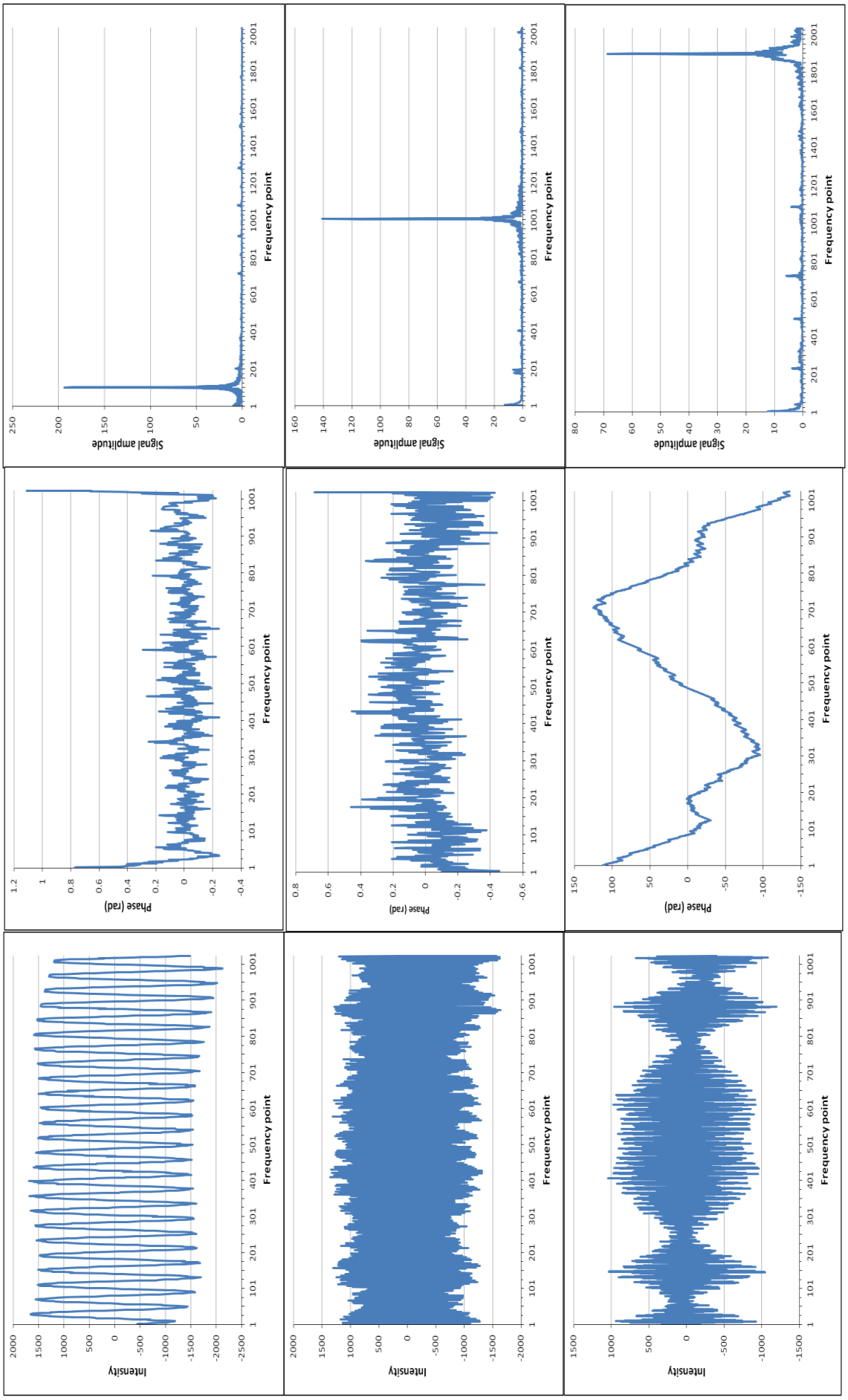

Figure 5-14: The spectral interferogram, phase and iFFT data for three axial positions.
Left: Spectral interferogram. Middle: phase information. Right: Inverse Fourier Transform.

Attempting to decrease the acquisition time introduces other problems. Decreasing the acquisition time requires that the power on the sample is proportionally increased, thereby increasing the cost of the instrument. Also, as described in section 4.5, increasing the power, increases the unwanted signal from the other reflecting surfaces within the instrument (objective lens etc.) which become increasingly difficult to remove from the acquired image.

In theory, FDOCT and SSOCT designs are also susceptible to phase jitter; however, due to the very fast acquisition rate of the spectral interferogram, the small movements of the sample do not have a noticeable effect on the sensitivity fall-off function. Large scale movements (such as the saccades of the eye) do have a negative effect on the image, but manifest as ‘tearing’ where consecutive B-scans are misaligned, but the axial information remains unaffected.

In addition to the phase jitter, several other factors may contribute to the increased sensitivity fall-off. Any optical element in the design that broadens the initial line width of the camera will have the effect of worsening the spectral resolution and decreasing the high frequency amplitude of the spectral interferogram (as described above). The spinning diffuser elements designed to reduce the crosstalk noise may have had an effect on the linewidth. The ground glass diffusing plate is designed to scatter light and, as different wavelengths will scatter by different amounts, it is possible that this resulted in an unwanted broadening of the linewidth. However, this is only speculation since the necessary equipment to measure the spectral output from the instrument was not available.

From the point of view of sample imaging, the poor sensitivity roll-off of the FFSSOCT instrument would limit the amount of axial depth with which to image the sample. From Figure 5-13, beyond 0.36mm the sensitivity begins to fall-off very rapidly, creating an unwanted reduction in image quality of any sample larger than this distance. This represents a critical problem that would need to be overcome in order to make FFSSOCT a viable alternative to FDOCT or SSOCT.

5.7 Summary

This Chapter explores the different parameters of the FFSSOCT system and determines the effect that they have on the images acquired with the system. The axial and lateral resolution of the system was determined theoretically and by measurement and a small loss in both the lateral and axial resolution measurements compared to the theoretical minimum resolution. The cause of the loss in resolution was discussed. The relationship between the resolution and critical sampling rate for FFSSOCT was investigated, and it was found that the axial sampling rate will always be undersampling (0.567 times the resolution), necessitating the use of zero padding to reach the critical sampling limit (Nyquist sampling). This was derived by calculating the maximum depth range of the FFSSOCT system.

The optimum approach to measuring the SNR was investigated. The problems measuring the SNR due to the presence of the pseudo static background noise signal were also discussed. The background signal obscured the image signal but did not prevent the image signal from being detected, making the definition of the background noise less definable. The optimum solution, though not always available, was to subtract consecutive background images, leaving only the random noise. In the cases where this was not achievable, a single image was used and an area of background with no fixed pattern noise was selected.

The sensitivity roll-off of the FFSSOCT system was theoretically derived and compared to the measured roll-off performance. The measured performance of the system showed a significantly larger roll-off in the sensitivity than was theoretically expected and was attributed to the phase instabilities within the system.

Chapter Six: FFSSOCT in comparison to FDOCT

6.1 Comparing FFSSOCT to FDOCT

The final part of the project comprised an image quality comparison between the FFSSOCT system and an FDOCT microscope system. The FDOCT system was a research FDOCT system owned by the Cardiff Biomedical Imaging Group and, located in the same room as the FFSSOCT system, thereby facilitating the rapid transportation of the sample from one system to the other.

The FDOCT system was based on a traditional scanning Fourier domain set up comprising a broadband width light source split by a fibre coupler into two interferometer arms[81]. The sample arm contained two galvanometers to scan the beam across the sample. The interferometric information in the recombined beam was then recorded by a spectrometer. The light source used was a titanium sapphire laser (Femtolasers Femtosource Integral OCT Titanium Sapphire laser (Femtolasers, GmbH, Austria)) that had a bandwidth of 130nm, a central wavelength of 820nm and a power output of 40mW. The spectrometer was constructed of two lenses, a diffraction grating and a high speed linescan camera (ATMEL AViiVA M2 CL 2048 pixel CCD camera (ATMEL Corp, California, USA)). The camera had 2048 pixels and was capable of acquiring 20,000 frames per second (20k A-lines per second) and an image acquisition time (500x500 A-lines) of 12.5 seconds. The FDOCT system had a measured transverse resolution of 5µm (0.11NA telecentric lens) and a measured axial resolution of 4.5µm in air (theoretical maximum resolution was 2.28µm from Equation 2).

The optical power of the FDOCT system was reduced to avoid any potential damage to the sample being imaged. Using optical filtering, the optical power on the sample from the FDOCT system was reduced from 5mW to 1.3mW. This resulted in a signal to noise ratio of 93dB and an energy deposition per A-line of 65nJ. As described in section 4.5, the increase in the available optical power provided by the SLD booster module created problems with saturation of the camera due to reflections from within the FFSSOCT system. As a result, the image integration time had to be reduced, decreasing the 3D dataset acquisition time to 1.7 seconds. To achieve higher quality images, and to make the overall acquisition time similar to the FDOCT system, successive frames were averaged increasing the acquisition time to 8.5 seconds. By increasing the effective FFSSOCT

image acquisition time to 8.5 seconds and decreasing the FDOCT optical power, the total optical energy deposited on each pixel was significantly higher for FFSSOCT (168.85nJ) than for FDOCT (65nJ).

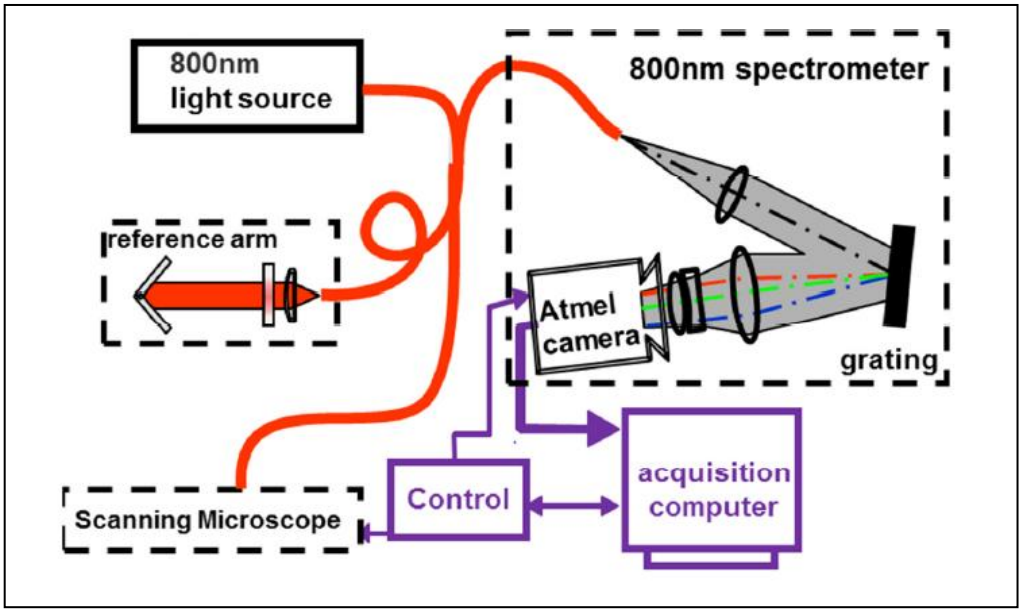

Figure 6-1: Schematic of the FDOCT instrument.
The box marked 'Control' represents an input/output device (field programmable grid array - FPGA) that controls the timing of the galvanometers and the frame acquisition[81].

It can be seen that if the acquisition times and optical powers of both systems were the same (5 sec and 2mW each), then the total optical power deposited on each pixel by both systems will be the same (40nJ). However, the optical power deposited per pixel *per second* would be only 8nJ for the FFSSOCT system, potentially allowing for more optical power to be applied to the sample without damaging it. The wavelength used for OCT (850nm) heats the sample and can potentially damage it if the optical power levels were too high (photo chemical damage is negligible at this wavelength)[23]. The heat from the incident irradiation is dissipated through the sample over time, resulting in an upper limit to the amount of power that can be applied per second depending on the properties of the sample. For example, if a sample has a damage threshold of 40nJ per pixel per second, the FFSSOCT approach could deposit 5 times more energy onto the sample then the FDOCT approach (given the acquisition parameters mentioned above), increasing the potential SNR by 14dB. The actual value will be less than this due to the way energy is dissipated through the sample, in FFSSOCT the neighbouring pixels will also be illuminated by the

same optical power, reducing the rate of cooling by approximately two thirds (considering each voxel to be a regular cube).

The potential to be able to use more optical power is an important factor since the limiting factor in increasing the sensitivity of FDOCT systems is the maximum optical power that the sample can be irradiated with (~2mW incident on the cornea for a human eye[42]). A small increase in SNR maybe also be achieved by using a more biased splitting ratio in the fibre coupler (more power in the reference arm), better transfer optics or a more sensitive camera.

The following table lists the key comparative features of the two OCT systems.

Parameter	FFSSOCT (5 frame average)	FDOCT
SNR	~93dB (86dB without averaging)	93dB
Volume acquisition time	8.5 seconds (504x500x512 pixels)	12.5 seconds (500x500x2048 pixels)
Equivalent A-line rate	30,000 A-lines per second	20,000 A-lines per second
Camera data format	12 bit	12 bit
Bandwidth	50nm	130nm
Axial resolution (in air)	8.5µm measured, 6.27µm theoretical	4.5µm measured, 2.28µm theoretical
Axial sampling (after zero padding)	1.8µm per pixel	0.7µm per pixel
Lateral resolution	7.8µm measured, 4.7µm theoretical	5µm measured, 2.8µm theoretical
Lateral sampling	1.52µm/pixel (Silicon Imaging camera), 1.36µm/pixel (PhotonFocus camera)	2µm per pixel
Volume size	Lateral dimension: 670x685µm. Axial dimension: 870µm	Lateral dimension: 1x1mm. Axial dimension: 1.4mm
Optical power on sample	5.5mW	1.3mW
Energy deposition per pixel per tomogram	168.85nJ	65nJ
Energy deposition per pixel per second	19.85nJ	65nJ

Table 6-1: Comparison of FFSSOCT and FDOCT system parameters

6.2 Retinal imaging comparison

To assess the imaging performance of the FFSSOCT system compared to the FDOCT system, images were acquired of the same *ex vivo* retinal tree shrew sample. The tree shrew sample was prepared by the same method as described in section 3.6. The half cup of the retina was filled with preserving fluid (phosphate buffered saline) and a cover slip was used to prevent back reflections into the system from the surface of the liquid.

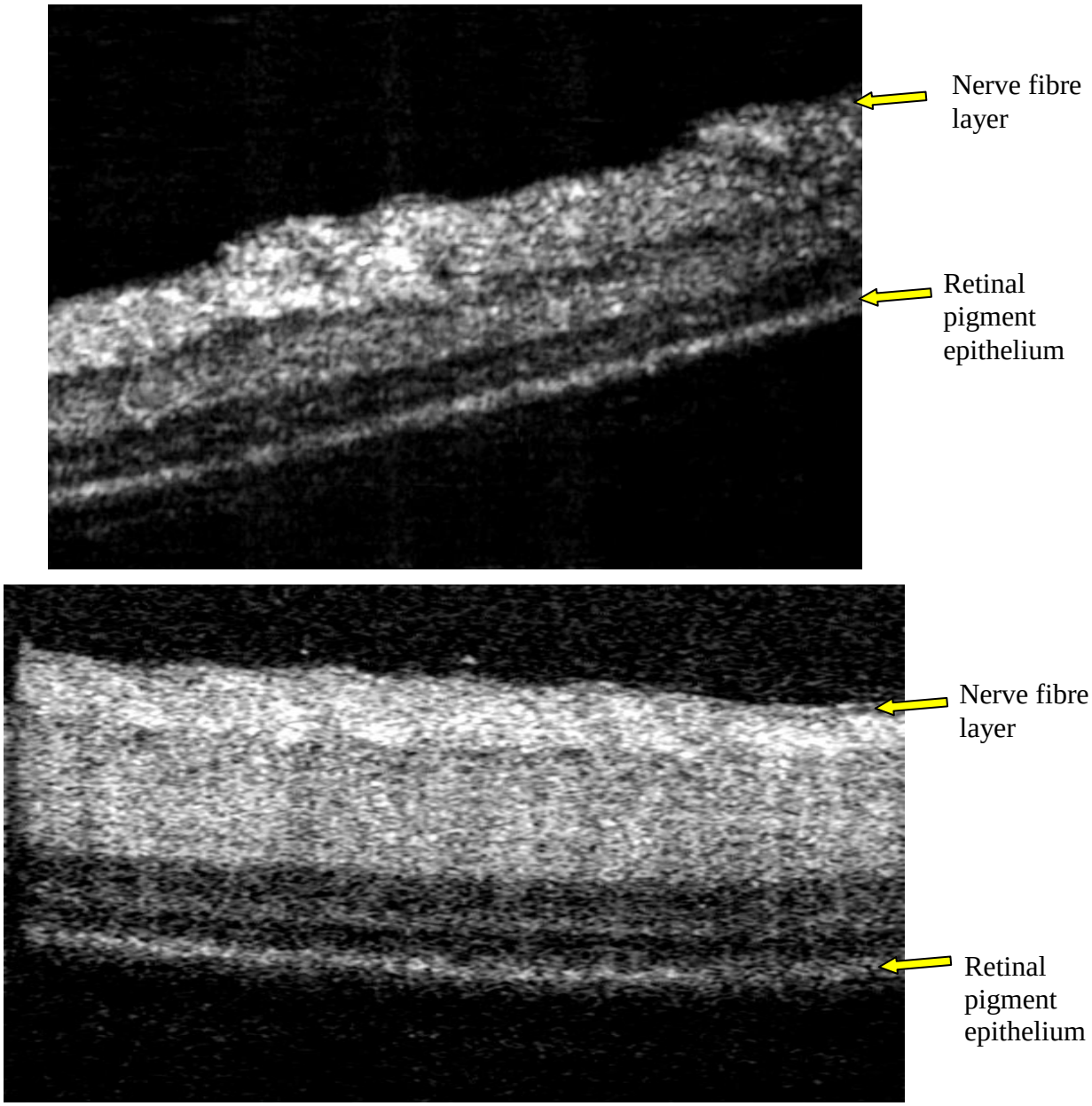

Figure 6-2: *Ex vivo* tree shrew retina imaged by FFSSOCT (top) and FDOCT (bottom).

The FFSSOCT image (Top - centre slice of a 5 image average) is 500x576 pixels (670x485µm), each image was acquired in 1.7 seconds. The FDOCT image (Bottom - centre slice) is 500x848 pixels (1mmx595µm) and was acquired in 12.5 seconds.

Both the FFSSOCT and FDOCT retinal images (Figure 6-2: top and bottom respectively) show the most prominent layers of the tree shrew retina down to the RPE. The superior axial resolution of the FDOCT system can be seen in the nerve fibre, which cannot be seen in the FFSSOCT image. The overall contrast in the two images is very similar indicating that the FFSSOCT system is capable of generating images with comparable quality to the FDOCT system. The retinal thickness as measured by the two systems was 378µm (FFSSOCT) and 365µm (FDOCT).

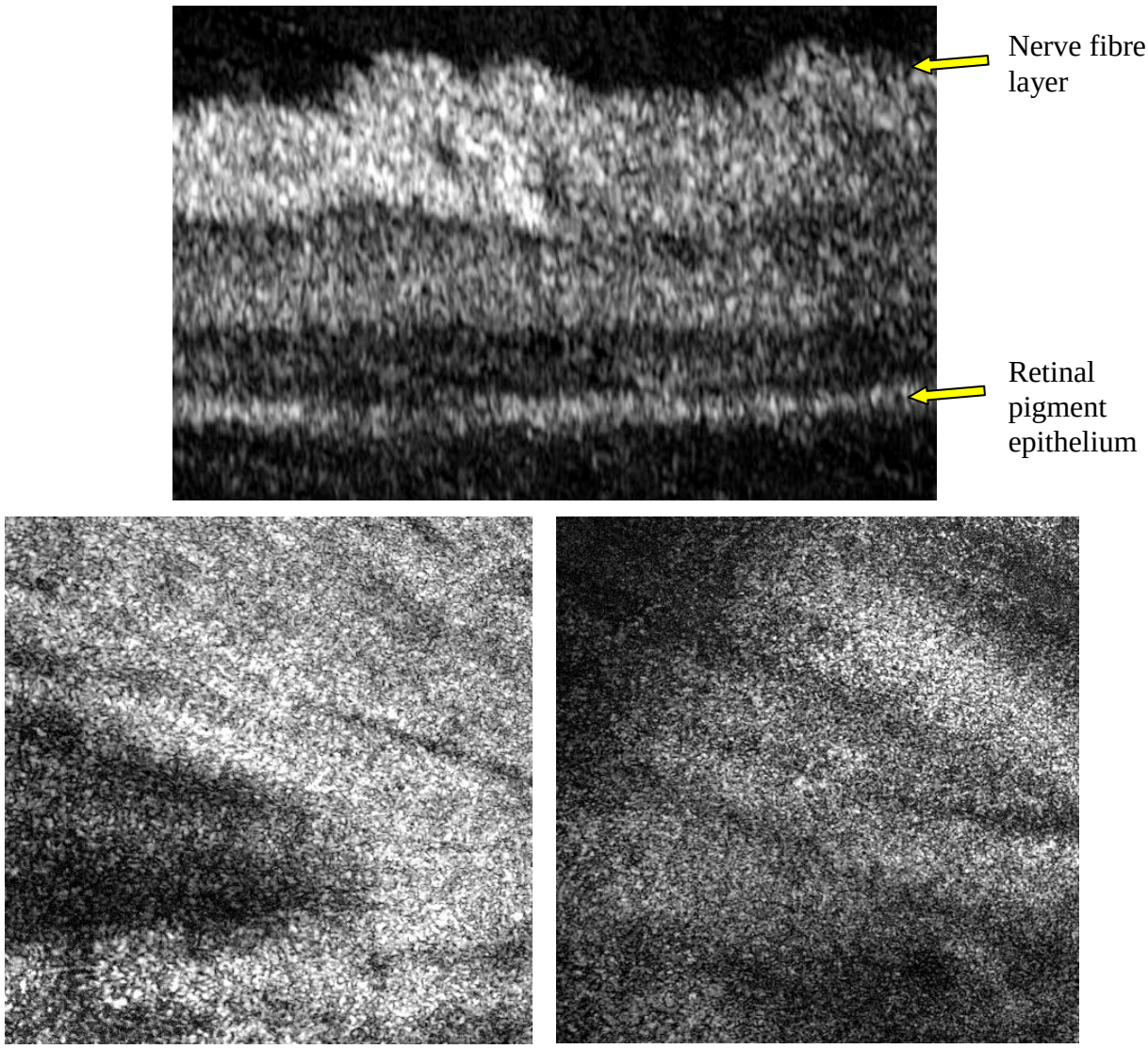

Figure 6-3: *Ex vivo* tree shrew retina imaged with FFSSOCT.

The volumetric image dimensions were 504x500 lateral pixels (670x685µm) and 512 axial pixels (870µm) acquired in 8.5 seconds (5 averages). Top: a B-scan from the volume (central slice). The image is 504x200 pixels (670x340µm). Bottom left: En face image of the nerve fibre layer, resliced from the volume at axial pixel 50, of 504x500 pixels (685x670µm). Bottom right: En face image of the RPE, resliced from the volume at axial pixel 165, of 504x500 pixels (685x670µm).

Figure 6-3 and Figure 6-4 show the comparative en face quality of the two imaging systems. Despite the relatively similar transverse resolution of the two systems, the combination of the speckle and residual crosstalk has significantly reduced the apparent en face image quality of the FFSSOCT system.

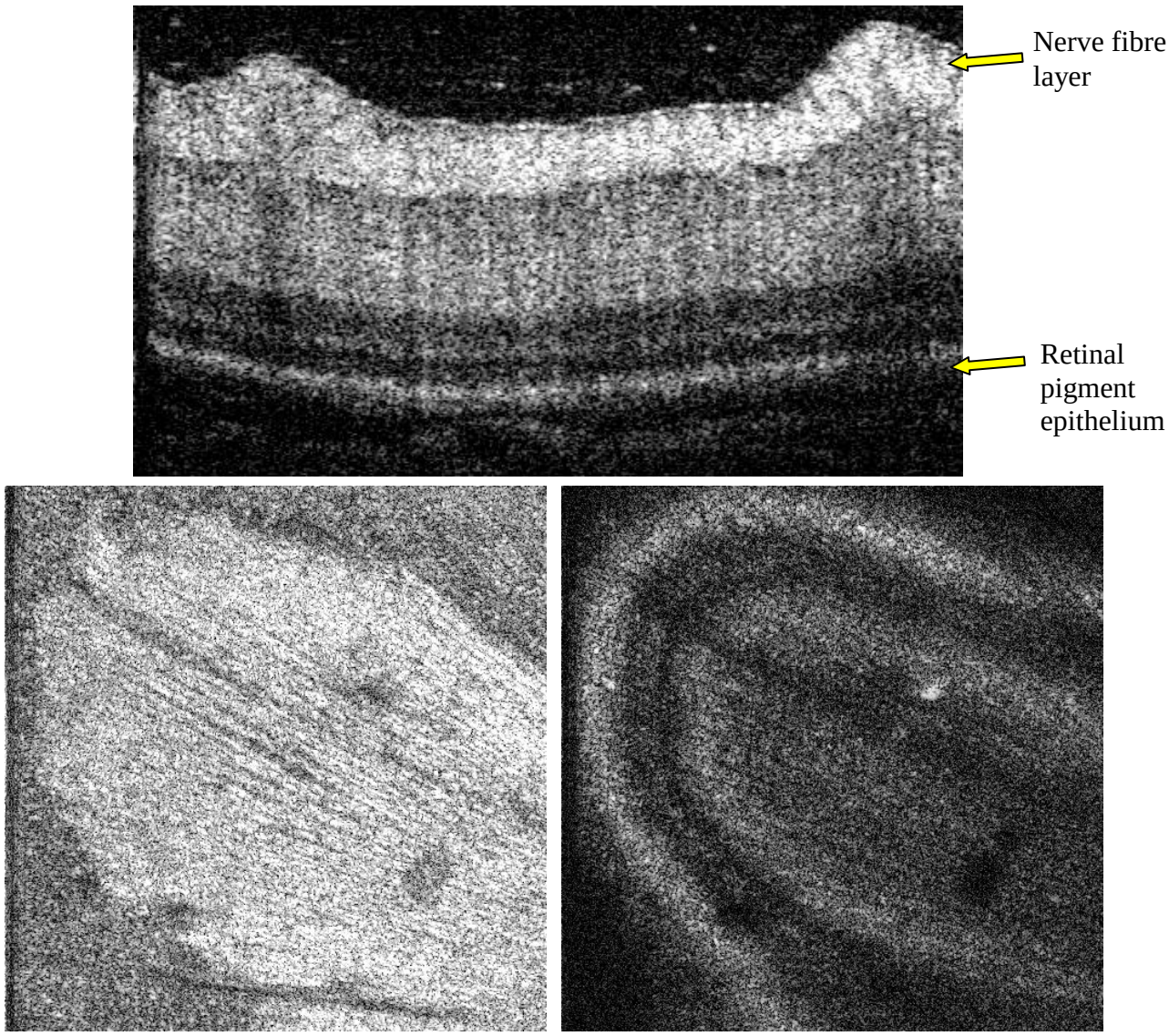

Figure 6-4: *Ex vivo* tree shrew retina imaged with FDOCT.

The volumetric image dimensions were 500x500 lateral pixels (1x1mm) and 2048 axial pixels (1.4mm) acquired in 12.5 seconds. Top: a B-scan from the volume (central slice). The image is 500x585 pixels (1mmx400μm). Bottom left: En face image of the nerve fibre layer, resliced from the volume at axial pixel 90, of 500x500 pixels (1x1mm^2). Bottom right: En face image of the RPE, resliced from the volume at axial pixel 485, of 500x500 pixels (1x1mm^2).

The effect would only be noticed when imaging a scattering sample; the highly directional reflectivity of the USAF resolution target would not induce any crosstalk in the FFSSOCT images.

6.3 Mirror sample comparison

To examine spectral differences between the FFSSOCT and FDOCT systems, images of a mirror were acquired with both systems. As both systems were set up for acquiring images of weakly scattering retinal tissue, the optical power levels of both systems were attenuated in order to avoid saturating their respective cameras. The FFSSOCT system was attenuated with an ND filter in the illumination path and the FDOCT system had the reference arm power reduced by a variable ND filter wheel.

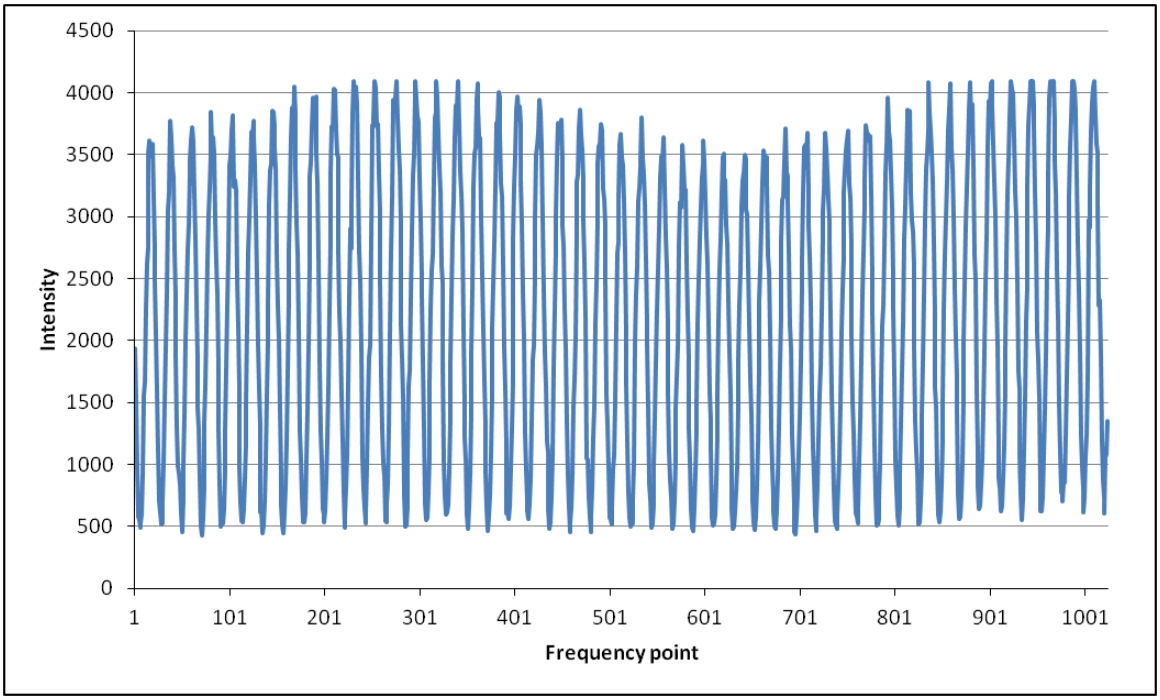

Figure 6-5: Spectral waveform of a mirror recorded with FFSSOCT.

The 1024 frequency steps were recorded in 3.5 seconds. The A-line was taken from the centre of a tomogram with dimensions of 504x500 pixels.

Several obvious differences present themselves when comparing the spectral data from the two OCT systems (Figure 6-5and Figure 6-6). The first is the shape difference. The FFSSOCT demonstrates the constant optical power output generated by the feedback

circuits in the Broadsweeper, while the FDOCT has rapidly diminishing intensities at the edges of the spectrum. The second is the greater modulation amplitude of the FFSSOCT system (~3000 peak to peak) compared to the FDOCT system (~1750). This difference is most likely due to the unbalanced splitting ratio of the fibre coupler in the FDOCT system, reducing the interference fringe visibility. The third is the high degree of chirp in the FDOCT signal; the periodicity of the spectral waveform increases considerably from left to right resulting from the spectrometer based acquisition.

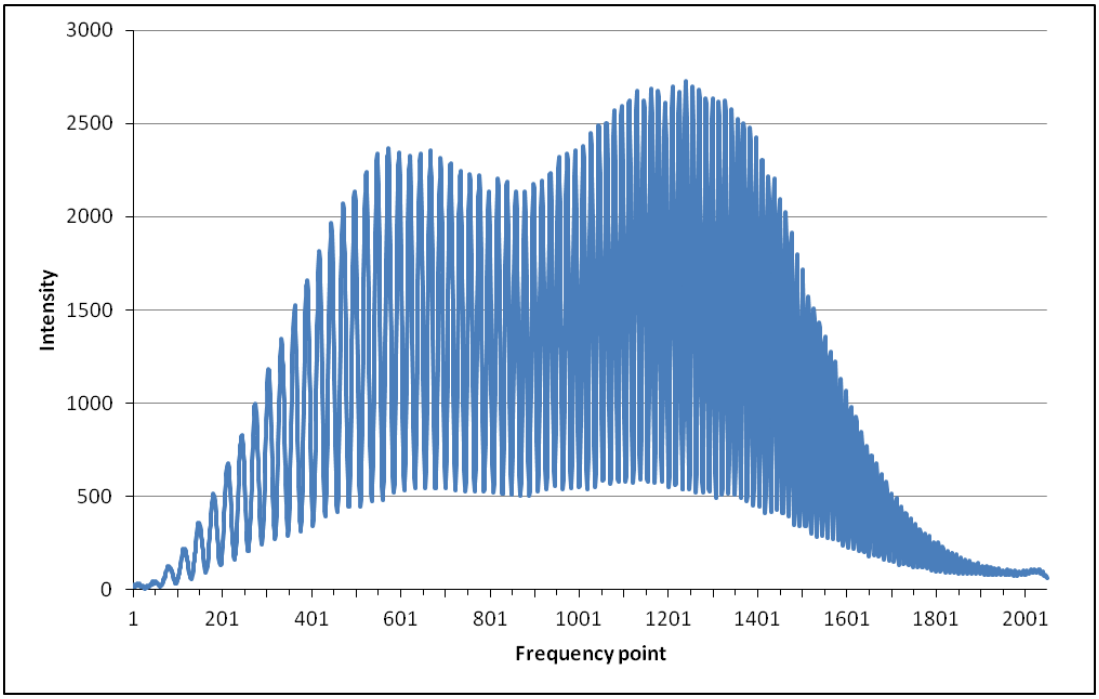

Figure 6-6: Spectral waveform of a mirror recorded with FDOCT.

The 2048 frequency steps were recorded in 50µs. The A-line was taken from the centre of a tomogram with dimensions of 500x500 pixels recorded in 12.5 seconds.

Each of these observations highlights the potential benefits of using the FFSS approach: the consistent level of the amplitude of the spectral modulations will result in a higher time domain signal peak and a spectral waveform that can be more readily manipulated with spectral shaping (section 4.4). The interpolation algorithm required to de-chirp the signal is a processor-intensive task and may slow down the real time B-scan viewer in the acquisition software if the processing computer is insufficiently powerful. The amount of chirp in the FFSSOCT spectrum is almost negligible and the real time B-scan viewer can be used without it. By performing the phase analysis program described in section 4.6, the phase of the signal from the two systems can be examined. In each case, the phase

information was unwrapped and then flattened by subtracting a 2nd order polynomial from the data.

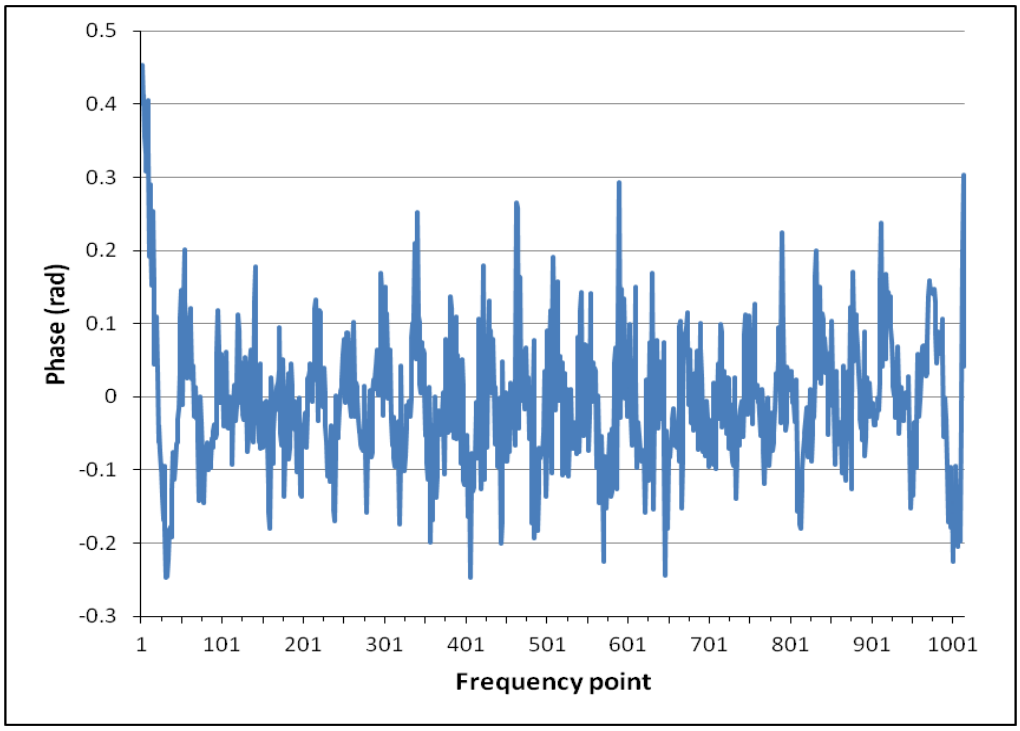

Figure 6-7: The phase signal generated from the FFSSOCT spectral waveform.

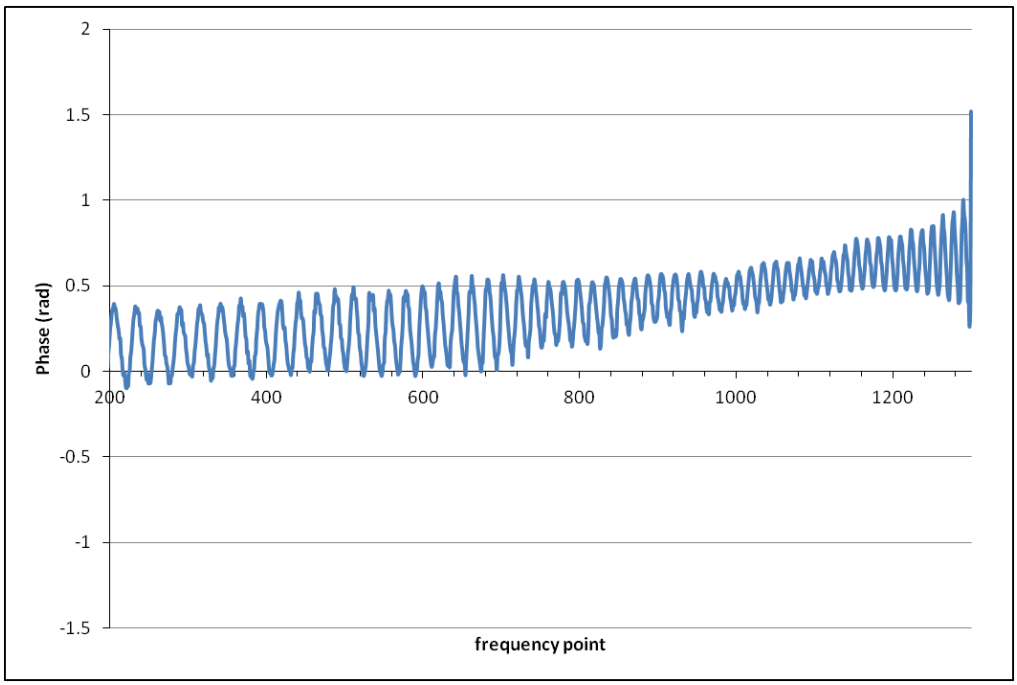

Figure 6-8: Cropped section of the phase signal generated from the FDOCT spectral waveform.

The full phase data has 2048 frequency points and was cropped to remove large phase jumps. The high frequency phase noise is caused by background signal.

After removing the phase data associated with the signal from the mirror, the remaining phase signal contains only background noise information. Analysis of this phase noise gives an indication of the level of noise that will be present in the final TD signal. As can be seen in Figure 6-8, the noise in the FDOCT phase signal has a strongly oscillating pattern which is a result of some residual interference within the instrument. Consecutive A-lines have a similar noise pattern and by averaging multiple A-lines together, the consistent noise pattern can be separated and removed from each individual A-line. While this technique will work for retinal tissue samples where the time domain data is very different between individual A-line, it will not work on a spatially invariant sample such as a mirror (when placed horizontally). Therefore, the background subtracted FDOCT data cannot be shown.

The FFSSOCT data (Figure 6-7), however, does not have a strong pattern to it, indicating that there are many factors contributing to the phase noise. Furthermore, the phase noise from consecutive A-lines do not show any similarities to this data suggesting that the phase noise originates from a random source rather, than from a combination of multiple static background signals (section 4.5 has more details on this). The origin of the phase noise is most likely to be a combination of intensity fluctuations in the optical power on the sample, micro vibrations of the sample during the tomogram acquisition and unwanted signal from back reflections within the FFSSOCT system. Intensity fluctuations in the optical power could be traced to the spinning diffuser, spinning too slowly to properly average the diffusing pattern over the shortened acquisition time. The combination of the first two ‘random’ noise factors makes background subtraction much more difficult in FFSSOCT then FDOCT and, as a result, the noise in the TD signal is higher (Figure 6-9 through Figure 6-12).

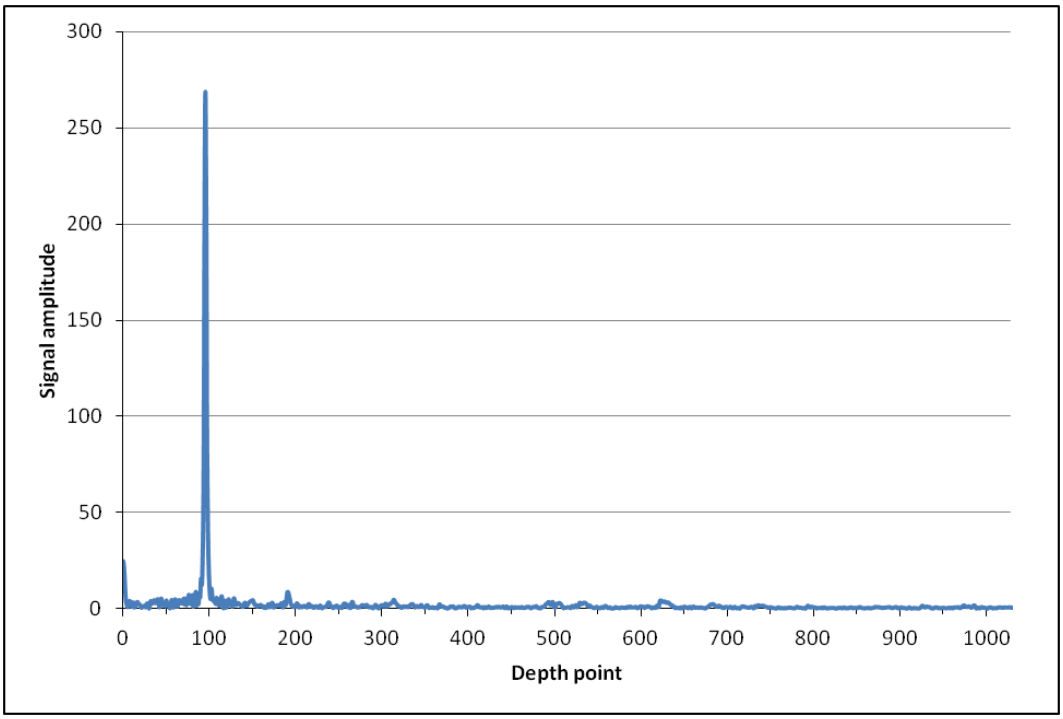

Figure 6-9: Fourier transform of the FFSSOCT spectral waveform.

The signal was processed using the standard FFSSOCT processing (Chapter 4). The signal peak from the mirror has an amplitude of 268.5 and an axial FWHM of 4.5 pixels (8.1µm).

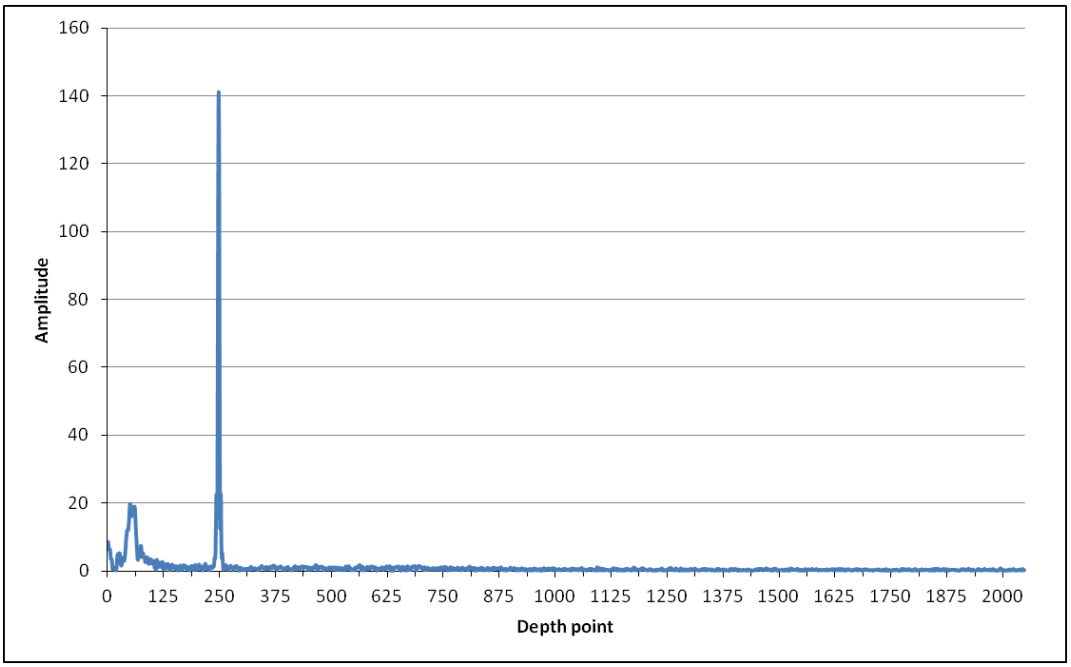

Figure 6-10: Fourier transform of the FDOCT spectral waveform.

The signal was processed using an adapted version of FFSSOCT processing (Chapter 4). The signal peak from the mirror has an amplitude of 141.1 and an axial FWHM of 5 pixels (3.5µm).

Comparing the TD data from the FFSSOCT and FDOCT systems (Figure 6-9 and Figure 6-10), some of the features identified in the spectral waveform data and discussed above (Figure 6-5 to Figure 6-8) can be seen. The larger amplitude of the spectral waveform data from the FFSSOCT system has resulted in a larger TD signal peak (268.5 compared to 141.1), indicating that the FFSSOCT system had a greater dynamic range than the FDOCT instrument. The oscillating pattern identified in the phase noise of the FDOCT signal (Figure 6-8) can be seen as a broad TD signal at depth point 60 in Figure 6-10. The large amounts of random phase noise shown in Figure 6-7 have manifested as background noise at all the depth points in Figure 6-10, though there are some small peaks at depth positions 194, 315, 494, 534 and 624. These peaks are the pseudo-fixed pattern noise (section 4.5) resulting from back reflections within the FFSSOCT system and, although their amplitude is relatively small, when the ND filter in the illumination is removed and a weakly scattering sample is imaged, they dominate the signal from the sample.

By examining a small section of the TD background signal from both systems, the effect of the greater FFSSOCT phase noise can be seen. The background noise in the TD signal from the FFSSOCT system (Figure 6-11) has a higher average amplitude (1.33 compared to 0.83) and a higher standard deviation (0.732 compared to 0.321) than that from the FDOCT system (Figure 6-12). As a result, any image details from a weakly reflecting sample (amplitude of 1) would not be detectable with the FFSSOCT even if the images were averaged indefinitely. Also, image details up to an amplitude of 3 would be interspersed with random noise. In comparison, the FDOCT system would be able to detect a signal amplitude of 1 and would acquire noise free images above an amplitude of 2. This refers to background noise only; signal related shot noise would still create some variation in the detected signal. In addition to the higher background noise, the data from the FFSSOCT system is punctuated with signal peaks from back reflections within the system (as discussed above); these have been omitted from the background calculation as they are not true random noise (a sample can still be imaged around them).

Although the noise in the TD data recorded by the FFSSOCT system was greater than that of the FDOCT system, the amplitude of the signal from the mirror was also higher. As a result, the SNR of both systems was approximately equal (51.29dB for FFSSOCT and 52.86dB for FDOCT calculated using Equation 23). However, the FDOCT was attenuated

more than the FFSSOCT system; therefore, the overall sensitivity of the FDOCT system was higher.

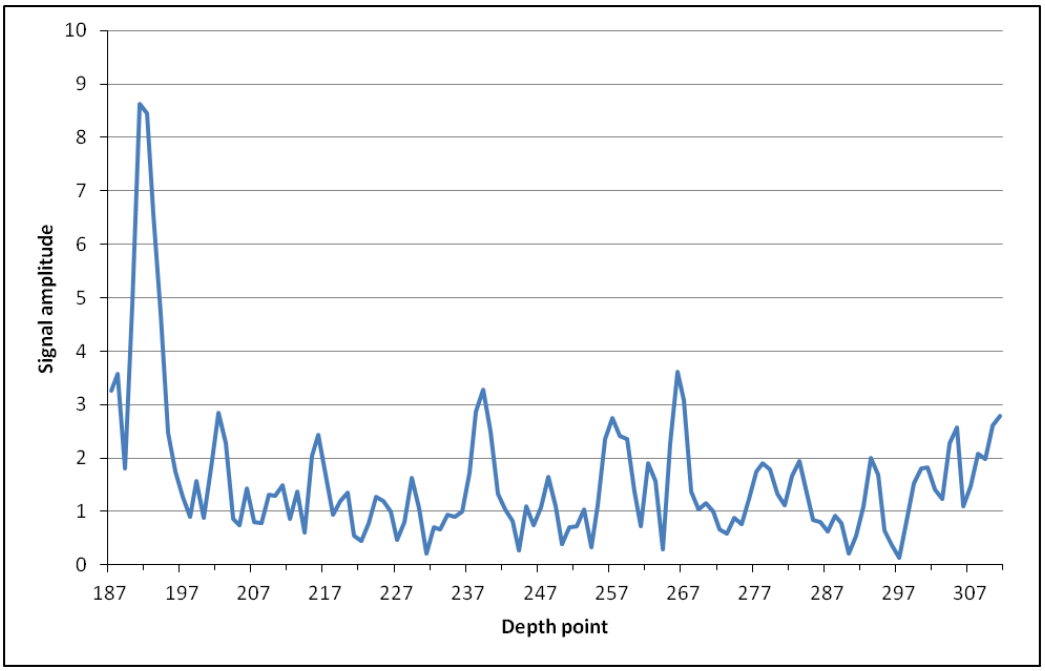

Figure 6-11: Section of the background noise taken from the FFSSOCT mirror signal.

The section was between depth points 187 and 312 of Figure 6-9. The signal spike at depth point 192 is fixed pattern noise caused by back reflections with the FFSSOCT system. The noise has an average of 1.33 and a standard deviation of 0.732 (excluding the fixed pattern noise – first 20 pixels omitted).

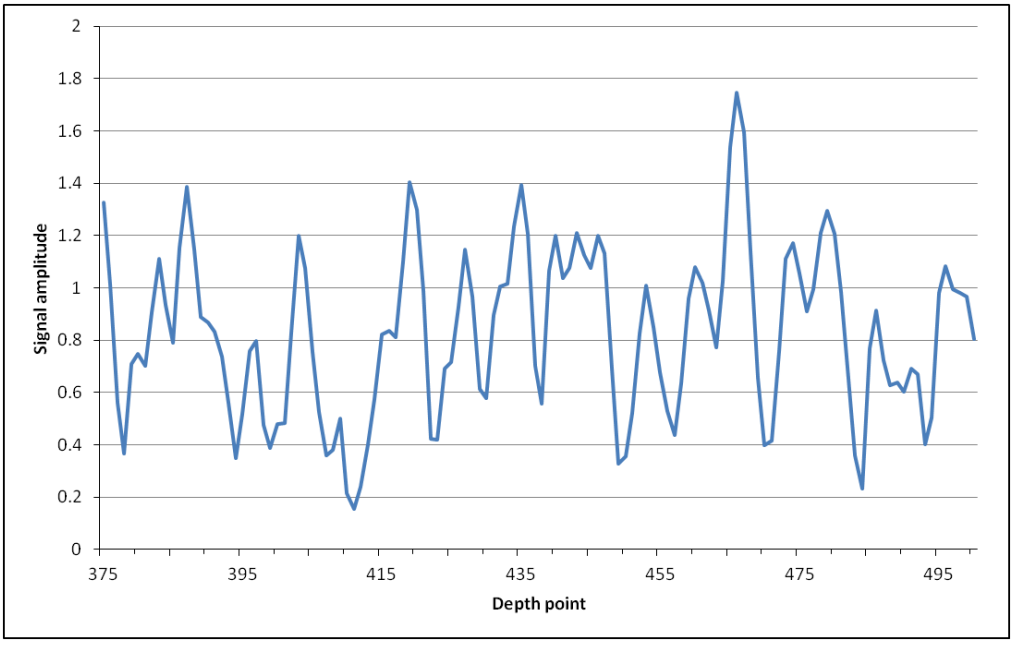

Figure 6-12: Section of the background noise taken from the FDOCT mirror signal.

The section used was between depth points 375-500 of Figure 6-10. The noise has an average amplitude of 0.83 and a standard deviation of 0.321.

6.4 *In vivo* imaging

In vivo imaging of unrestrained human skin was attempted with the FFSSOCT system; however, the movement of the sample was too great, destroying the phase relationship between each A-line. It may be possible to achieve *in vivo* imaging in a restrained sample. In order to image an unrestrained sample, the acquisition speed of the system would need to be greatly increased, something that was not possible with the limited rotation speed of the spinning diffuser and acquisition camera.

6.5 Summary

The work presented in this Chapter is a comparison of the operating parameters and image quality between the FFSSOCT system and an FDOCT system with similar specifications. Tomographic images were acquired of the same sample with both systems, showing comparable image quality and contrast. The retinal layers within the sample could be identified with both systems although the higher axial resolution of the FDOCT system enabled clearer visualisation of the nerve fibre layer. The *en face* images acquired also showed comparable quality between the systems though the FFSSOCT appeared to have more noise in the image, due to the inferior lateral resolution and additional crosstalk factors.

The energy deposition for both OCT systems was also examined, revealing that more optical power could be utilised with the FFSS approach as the energy deposited per second was lower than that of the FDOCT system. This occurred from the constant illumination experienced by each pixel of the FFSSOCT system.

A comparison of the two systems was performed by analysing the signal from a mirror. By using a constant highly reflecting sample for each system, the maximum signal peak and noise levels could be compared. The FFSSOCT was able to achieve a higher amplitude spectral waveform than the FDOCT system resulting in a greater potential dynamic range of the TD images. The phase noise and the resulting TD noise were higher in the FFSSOCT system and, as a result, both systems produced approximately the same SNR.

Chapter Seven: Conclusions

7.1 Aim and accomplishments

The aim of the work undertaken during this project was to create and evaluate an optical coherence domain imaging system using a FFSS approach and to determine its advantages and disadvantages over established OCT modalities.

This was successfully achieved and a FFSS optical coherence microscope was created with custom written software, ultimately acquiring volumetric images with 86dB of SNR in <2 seconds. Hardware solutions unique to the project were employed to resolve the problem of crosstalk inherent to the full field approach to OCT. The software needed to acquire and to process the unique interferometric data from the FFSSOCT system was written in Labview.

7.2 Advantages and disadvantages of using a FFSS approach to OCT

By analysing the system performance, several distinct advantages and disadvantages of the FFSSOCT design were discovered.

The parallel acquisition of FFSSOCT provides some advantages over the scanning OCT modalities. The lack of galvanometer-based scanning reduces the complexity and the cost of the overall OCT design, potentially resulting in a more affordable clinical instrument with greater long-term reliability. By acquiring the spectral data in parallel, the sample can be monitored at the same time, a feat that requires a separate camera and optical path in scanning OCT systems. This greatly improves the localisation of the tomographic data whilst simultaneously reducing the complexity of the optical design that would otherwise be required to capture en face images. In a clinical instrument, this would provide immediate feedback on the position of the OCT scan. By distributing the optical power over the entire sample, the amount of energy deposited per unit area is much less than that of a typical scanning OCT, improving the potential sensitivity of the OCT system.

In addition to the advantages of parallel acquisition, the swept source aspect of the system has all the inherent advantages that swept source OCT offers. As the spectral data is acquired by scanning through the bandwidth of the light source in time, there is no need for a spectrometer, thereby further reducing the complexity of the design. Also there is a

potential for better sensitivity performance due to the slower roll off of swept source based OCT systems compared to FDOCT systems.

There are also several disadvantages to using a parallel acquisition modality. Firstly, the increased image noise occurs due to crosstalk interference between pixels. This manifests as additional speckle in the images, although it can be reduced by destroying the spatial coherence of the light and averaging spatially separated images together. The transverse resolution of the FFSSOCT system will typically be lower than that of a scanning OCT system due to the loss of the confocal gating effect offered by the optical fibres used in the scanning systems. The fixed size of the detector chip restricts the possible imaging configurations as opposed to a scanning OCT system that has almost limitless flexibility in the possible size of the scan area and lateral sampling rate. Phase noise and back reflections from optical components in the FFSSOCT system posed the greatest problem to achieving the same levels of sensitivity as the established OCT systems. If left unchecked, the back reflections would saturate the FFSSOCT camera even when reduced, interference would occur between different optical surfaces, creating pseudo-static noise patterns across any acquired B-scan. It may be possible to reduce the back reflections by removing any optics from the reference arm and using a beamsplitter with a different splitting ratio to reduce the optical power on the objective lens in the sample arm. Phase noise occurs because of movements in the sample between successive frames during an acquisition and not only degrades the image quality but also increases the sensitivity roll-off rate, reducing the usable image size. This may be overcome by acquiring the phase of the signal from a strongly reflecting surface simultaneously along with the sample. The phase shifts due to movement in the sample may then be numerically corrected for. However, achieving this in a clinical ophthalmic situation is not practical. A more straightforward method for reducing the phase noise would be to image fast enough to acquire a tomographic image without the sample moving. Although the imaging speeds required to perform this were not achieved during the project, it has subsequently been shown to be possible by another group working on FFSSOCT[23].

In addition to these disadvantages, FFSSOCT was also susceptible to the same limitations as SSOCT and FDOCT namely, the presence of the mirror image, sensitivity roll off and limited depth of focus. It was shown that the sensitivity roll off was theoretically better

that a typical FDOCT system however the presence of micro vibrations during the acquisition increased the rate of sensitivity decay significantly.

7.3 Applications of FFSSOCT

Considering the extremely high acquisition speed and therefore, cost, required for *in vivo* imaging using FFSSOCT, the disadvantages of using FFSSOCT outweigh the advantages at this time. However, using FFSSOCT does appear as a possible option for an optical coherence microscope, where the sample is static. The integrated en face imaging and possibility for greater SNR may be of more use in the field of microscopy than the scanning size flexibility provided by scanning OCT systems.

7.4 Future work

The most straightforward way of improving the specifications of the FFSSOCT system would be to invest in the instrument's hardware, specifically: replacing the camera with a faster, more sensitive model and the light source with higher optical power. In addition to this, the optical path should be redesigned to reduce the back reflections from the optical components within the system. This could be achieved by removing the objective lens in the reference arm and by using a beam splitter with an uneven splitting ratio. Using beam shaping optics would distribute the optical power more evenly across the sample and reduce the optical power loss when filling the back plane of the objective lenses. The phase instabilities could be reduced by increasing the acquisition speed of the camera but these could also be overcome by acquiring the phase information. The latter could be achieved by including a reflective target in the same field of view as the sample, giving a relatively easy way to access the phase information and improve the quality of the image.

References

1. Huang, D., Swanson, E.A., Lin, C.P., Schuman, J.S., Stinson, W.G., Chang, W., Hee, M.R., Flotte, T., Gregory, K., Puliafito, C.A. & et, a. Optical coherence tomography. *Science* **254**, 1178-1181 (1991).

2. Yun, S., Tearney, G., de Boer, J., Iftimia, N. & Bouma, B. High-speed optical frequency-domain imaging. *Opt. Express* **11**, 2953-2963 (2003).

3. Drexler, W. & Fujimoto, J.G. *Optical coherence tomography - technology and applications*, (Springer, New York, 2008).

4. Swanson, E.A., Izatt, J.A., Hee, M.R., Huang, D., Lin, C.P., Schuman, J.S., Puliafito, C.A. & Fujimoto, J.G. In vivo retinal imaging by optical coherence tomography. *Opt. Lett.* **18**, 1864-1866 (1993).

5. Drexler, W. Ultrahigh-resolution optical coherence tomography. *J. Biomed. Opt.* **9**, 47-74 (2004).

6. Huang, S.-W., Aguirre, A.D., Huber, R.A., Adler, D.C. & Fujimoto, J.G. Swept source optical coherence microscopy using a Fourier domain mode-locked laser. *Opt. Express* **15**, 6210-6217 (2007).

7. Huber, R., Adler, D.C. & Fujimoto, J.G. Buffered Fourier domain mode locking: unidirectional swept laser sources for optical coherence tomography imaging at 370,000 lines/s. *Opt. Lett.* **31**, 2975-2977 (2006).

8. Huber, R., Adler, D.C., Srinivasan, V.J. & Fujimoto, J.G. Fourier domain mode locking at 1050 nm for ultra-high-speed optical coherence tomography of the human retina at 236,000 axial scans per second. *Opt. Lett.* **32**, 2049-2051 (2007).

9. Klein, T., Wieser, W., Eigenwillig, C.M., Biedermann, B.R. & Huber, R. Megahertz OCT for ultrawide-field retinal imaging with a 1050nm Fourier domain mode-locked laser. *Opt. Express* **19**, 3044-3062 (2011).

10. Akiba, M. & Chan, K.P. In vivo video-rate cellular-level full-field optical coherence tomography. *J. Biomed. Opt.* **12**, 064024-064027 (2007).

11. Dubois, A., Vabre, L., Boccara, A.C. & Beaurepaire, E. High-resolution full-field optical coherence tomography with a Linnik microscope. *Appl. Opt.* **41**, 7 (2002).

12. Grieve, K., Paques, M., Dubois, A., Sahel, J., Boccara, C. & Le Gargasson, J.-F. Ocular tissue imaging using ultrahigh-resolution, full-field optical coherence tomography. *Invest. Ophth. Vis. Sci.* **45**, 4126-4131 (2004).

13. Bouma, B.E. & Tearney, G.J. *Handbook of optical coherence tomography*, (Marcel Dekker, inc., New York, 2001).

14. Bohren, C.F. & R., H.D. *Absorption and scattering of light by small particles*, (Wiley, 1983).

15. Brezinski, M.E., Tearney, G.J., Bouma, B.E., Izatt, J.A., Hee, M.R., Swanson, E.A., Southern, J.F. & Fujimoto, J.G. Optical coherence tomography for optical biopsy : properties and demonstration of vascular pathology. *Circulation* **93**, 1206-1213 (1996).

16. Choma, M.A., Hsu, K. & Izatt, J.A. Swept source optical coherence tomography using an all-fiber 1300-nm ring laser source. *J. Biomed. Opt.* **10**, 044009-044006 (2005).

17. Považay, B., Hermann, B., Unterhuber, A., Hofer, B., Sattmann, H., Zeiler, F., Morgan, J.E., Falkner-Radler, C., Glittenberg, C., Blinder, S. & Drexler, W. Three-dimensional optical coherence tomography at 1050 nm versus 800 nm in retinal pathologies: enhanced performance and choroidal penetration in cataract patients. *J. Biomed. Opt.* **12**, 041211-041217 (2007).

18. Unterhuber, A., Povazay, B., Hermann, B., Sattmann, H., Chavez-Pirson, A. & Drexler, W. In vivo retinal optical coherence tomography at 1040 nm - enhanced penetration into the choroid. *Opt. Express* **13**, 3252-3258 (2005).

19. Schmitt, J.M. Optical coherence tomography (OCT): a review. *IEEE J. Sel. Top. Quant. Electron.* **5**, 1205-1215 (1999).

20. Watanabe, Y. & Sato, M. Three-dimensional wide-field optical coherence tomography using an ultrahigh-speed CMOS camera. *Opt. Commun.* **281**, 1889-1895 (2008).

21. Fercher, A.F., Hitzenberger, C.K., Kamp, G. & El-Zaiat, S.Y. Measurement of intraocular distances by backscattering spectral interferometry. *Opt. Commun.* **117**, 43-48 (1995).

22. Fercher, A.F., Drexler, W., Hitzenberger, C.K. & Lasser, T. Optical coherence tomography - principles and applications. *Rep. Prog. Phys.* **66**, 239-303 (2003).

23. Bonin, T., Franke, G., Hagen-Eggert, M., Koch, P. & Hüttmann, G. In vivo Fourier-domain full-field OCT of the human retina with 1.5 million A-lines/s. *Opt. Lett.* **35**, 3432-3434 (2010).

24. Cense, B., Nassif, N., Chen, T., Pierce, M., Yun, S.-H., Park, B., Bouma, B., Tearney, G. & de Boer, J. Ultrahigh-resolution high-speed retinal imaging using spectral-domain optical coherence tomography. *Opt. Express* **12**, 2435-2447 (2004).

25. Lee, E.C., de Boer, J.F., Mujat, M., Lim, H. & Yun, S.H. In vivo optical frequency domain imaging of human retina and choroid. *Opt. Express* **14**, 4403-4411 (2006).

26. Leitgeb, R., Hitzenberger, C. & Fercher, A. Performance of fourier domain vs. time domain optical coherence tomography. *Opt. Express* **11**, 889-894 (2003).

27. Wang, R.K. In vivo full range complex Fourier domain optical coherence tomography. *Appl. Phys. Lett.* **90**, 054103-054103 (2007).

28. Wojtkowski, M., Kowalczyk, A., Leitgeb, R. & Fercher, A.F. Full range complex spectral optical coherence tomography technique in eye imaging. *Opt. Lett.* **27**, 1415-1417 (2002).

29. Zhang, J., Nelson, J.S. & Chen, Z. Removal of a mirror image and enhancement of the signal-to-noise ratioin Fourier-domain optical coherence tomography using an electro-optic phasemodulator. *Opt. Lett.* **30**, 147-149 (2005).

30. Hughes, M. & Podoleanu, A.G. Simplified dynamic focus method for time domain OCT. *Electron. Lett.* **45**, 623-624 (2009).

31. Qi, B., Phillip Himmer, A., Maggie Gordon, L., Victor Yang, X.D., David Dickensheets, L. & Alex Vitkin, I. Dynamic focus control in high-speed optical coherence tomography based on a microelectromechanical mirror. *Opt. Commun.* **232**, 123-128 (2004).

32. Zhang, K. & Kang, J.U. Real-time 4D signal processing and visualization using graphics processing unit on a regular nonlinear-k Fourier-domain OCT system. *Opt. Express* **18**, 11772-11784 (2010).

33. Chinn, S.R., Swanson, E.A. & Fujimoto, J.G. Optical coherence tomography using a frequency-tunable optical source. *Opt. Lett.* **22**, 3 (1997).

34. Huber, R., Taira, K., Wojtkowski, M., Ko, T.H., Fujimoto, J.G. & Hsu, K. High-speed frequency swept light source for Fourier domain OCT at 20 kHz A-scan rate. in *SPIE 5690*, Vol. 5690 (Eds. Tuchin, V.V., Izatt, J.A. & Fujimoto, J.G.) 96-100 (SPIE, San Jose, CA, USA, 2005).

35. Yasuno, Y., Madjarova, V.D., Makita, S., Akiba, M., Morosawa, A., Chong, C., Sakai, T., Chan, K.-P., Itoh, M. & Yatagai, T. Three-dimensional and high-speed swept-source optical coherence tomography for in vivo investigation of human anterior eye segments. *Opt. Express* **13**, 10652-10664 (2005).

36. Lim, H., de Boer, J.F., Park, B.H., Lee, E.C., Yelin, R. & Yun, S.H. Optical frequency domain imaging with a rapidly swept laser in the 815-870 nm range. *Opt. Express* **14**, 5937-5944 (2006).

37. Lim, H., Mujat, M., Kerbage, C., Lee, E.C., Chen, Y., Chen, T.C. & de Boer, J.F. High-speed imaging of human retina in vivo with swept-source optical coherence tomography. *Opt. Express* **14**, 12902-12908 (2006).

38. Potsaid, B., Baumann, B., Huang, D., Barry, S., Cable, A.E., Schuman, J.S., Duker, J.S. & Fujimoto, J.G. Ultrahigh speed 1050nm swept source / Fourier domain OCT retinal and anterior segment imaging at 100,000 to 400,000 axial scans per second. *Opt. Express* **18**, 20029-20048 (2010).

39. Srinivasan, V.J., Huber, R., Gorczynska, I., Fujimoto, J.G., Jiang, J.Y., Reisen, P. & Cable, A.E. High-speed, high-resolution optical coherence tomography retinal imaging with a frequency-swept laser at 850 nm. *Opt. Lett.* **32**, 361-363 (2007).

40. Wieser, W., Biedermann, B.R., Klein, T., Eigenwillig, C.M. & Huber, R. Multi-megahertz OCT: High quality 3D imaging at 20 million A-scans and 4.5 Gvoxels per second. *Opt. Express* **18**, 14685-14704 (2010).

41. Choma, M., Sarunic, M., Yang, C. & Izatt, J. Sensitivity advantage of swept source and Fourier domain optical coherence tomography. *Opt. Express* **11**, 2183-2189 (2003).

42. ICNIRP. Revision of guidelines on limits of exposure to laser radiation of wavelengths between 400nm and 1.4um. Vol. 79 431-440 (Walters Kluwer, Health Physics, 2000).

43. Karamata, B., Leutenegger, M., Laubscher, M., Bourquin, S., Lasser, T. & Lambelet, P. Multiple scattering in optical coherence tomography. II. Experimental and theoretical investigation of cross talk in wide-field optical coherence tomography. *J. Opt. Soc. Am. A* **22**, 1380-1388 (2005).

44. Anna, T., Shakher, C. & Mehta, D.S. Simultaneous tomography and topography of silicon integrated circuits using full-field swept-source optical coherence tomography. *J. Opt. A-pure Appl. Op.* **11**, 045501 (2009).

45. Dubey, S.K., Anna, T., Shakher, C. & Mehta, D.S. Fingerprint detection using full-field swept-source optical coherence tomography. *Appl. Phys. Lett.* **91**, 181106-181103 (2007).

46. Podoleanu, A.G. Optical coherence tomography. *J. Microsc* **247**, 209-219 (2012).

47. Yu, L. & Chen, Z. Digital holographic tomography based on spectral interferometry. *Opt. Lett.* **32**, 3005-3007 (2007).

48. Silverman, R.H. High-resolution ultrasound imaging of the eye – a review. *Clin. Exp. Ophthalmol.* **37**, 54-67 (2009).

49. Muir, E.R. & Duong, T.Q. Layer-specific functional and anatomical MRI of the retina with passband balanced SSFP. *Magn. Reson. Med.* **66**, 1416-1421 (2011).

50. Obel. Introduction to optical coherence tomography. 2008 (Ed. Research, O.) A short report on optical coherence tomography (University of Western Australia - School of electrical, electronic and computer engineering, Western Australia) (Accessed on 31/01/13).

51. Tan, P.E., Yu, P.K., Balaratnasingam, C., Cringle, S.J., Morgan, W.H., McAllister, I.L. & Yu, D.Y. Quantitative confocal imaging of the retinal microvasculature in the human retina. *Invest. Ophth. Vis. Sci.* **53**, 5728-5736 (2012).

52. Inoue, S. Foundations of confocal scanned imaging in light microscopy. in *Handbook of Biological Confocal Microscopy,* Vol. 1 (ed. Pawley, J.B.) 19 (Springer, New York, 2006).

53. Goldsmith, J.A., Li, Y., Chalita, M.R., Westphal, V., Patil, C.A., Rollins, A.M., Izatt, J.A. & Huang, D. Anterior chamber width measurement by high-speed optical coherence tomography. *Ophthalmology* **112**, 238-244 (2005).

54. Nassif, N., Cense, B., Park, B., Pierce, M., Yun, S., Bouma, B., Tearney, G., Chen, T. & de Boer, J. In vivo high-resolution video-rate spectral-domain optical coherence tomography of the human retina and optic nerve. *Opt. Express* **12**, 367-376 (2004).

55. Schmidt-Erfurth, U., Leitgeb, R.A., Michels, S., Povazay, B., Sacu, S., Hermann, B., Ahlers, C., Sattmann, H., Scholda, C., Fercher, A.F. & Drexler, W. Three-dimensional ultrahigh-resolution optical coherence tomography of macular diseases. *Invest. Ophth. Vis. Sci.* **46**, 3393-3402 (2005).

56. Wojtkowski, M., Leitgeb, R., Kowalczyk, A., Bajraszewski, T. & Fercher, A.F. In vivo human retinal imaging by Fourier domain optical coherence tomography. *J. Biomed. Opt.* **7**, 457-463 (2002).

57. Považay, B., Unterhuber, A., Hermann, B., Sattmann, H., Arthaber, H. & Drexler, W. Full-field time-encoded frequency-domain optical coherence tomography. *Opt. Express* **14**, 7661-7669 (2006).

58. Alonso-Caneiro, D., Read, S.A. & Collins, M.J. Speckle reduction in optical coherence tomography imaging by affine-motion image registration. *J. Biomed. Opt.* **16**, 116027-116027 (2011).

59. Schmitt, J.M., Xiang, S.H. & Yung, K.M. Speckle in optical coherence tomography. *J. Biomed. Opt.* **4**, 95-105 (1999).

60. Library, T.S.P. Wasp Foot (SEM). 2010 (Ed. Images, G.) (Gallo Images, www.galloimages.co.az) (Accessed on 31/01/13).

61. Krebs, C. Wasp eye and antenna. 2010 (Barcroft media, The Telegraph) (Accessed on 31/01/13).

62. Wagstaff, C., Clarkson, G.J., Zhang, F., Rothwell, S.D., Fry, S.C., Taylor, G. & Dixon, M.S. Modification of cell wall properties in lettuce improves shelf life. *J. Exp. Bot* **61**, 1239-1248 (2010).

63. Wriedt, T. Mie Theory: A Review. in *The Mie Theory*, Vol. 169 (Eds. Hergert, W. & Wriedt, T.) 53-71 (Springer Berlin Heidelberg, 2012).

64. Fergusson, J., Považay, B., Hofer, B. & Drexler, W. In vitro retinal imaging with full field swept source optical coherence tomography. in *SPIE 7554* (Eds. Izatt, J.A., Fujimoto, J.G. & Tuchin, V.V.) 75540I-75540I (San Francisco, CA, USA, 2010).

65. Lim, Y., Yamanari, M., Fukuda, S., Kaji, Y., Kiuchi, T., Miura, M., Oshika, T. & Yasuno, Y. Birefringence measurement of cornea and anterior segment by office-based polarization-sensitive optical coherence tomography. *Biomed. Opt. Express* **2**, 2392-2402 (2011).

66. Ruggeri, M., Wehbe, H., Jiao, S., Gregori, G., Jockovich, M.E., Hackam, A., Duan, Y. & Puliafito, C.A. In Vivo Three-Dimensional High-Resolution Imaging of Rodent Retina with Spectral-Domain Optical Coherence Tomography. *Invest. Ophth. Vis. Sci.* **48**, 1808-1814 (2007).

67. Harris, F.J. On the use of windows for harmonic analysis with the discrete Fourier transform. in *Proceedings of the IEEE*, Vol. 66 51-83 (Naval Ocean Systems Center, San Diego, CA, 1978).

68. Rollins, A.M. & Izatt, J.A. Optimal interferometer designs for optical coherence tomography. *Opt. Lett.* **24**, 1484-1486 (1999).

69. Nicolas, K.F., Ryan, P.S., Linjie, Z., Francisco, M.S., Heritage, J.P. & Yoo, S.J.B. Real-time full-field arbitrary optical waveform measurement. *Nat. Photonics* **4**, 248-254 (2010).

70. Eigenwillig, C.M., Biedermann, B.R., Palte, G. & Huber, R. K-space linear Fourier domain mode locked laser and applications for optical coherence tomography. *Opt. Express* **16**, 8916-8937 (2008).

71. Hayes, J. Dynamic interferometry handles vibration. in *Laser Focus World*, Vol. 38 6 (Pennwell corporation, Tulsa, OK, 2002).

72. Akcay, A.C., Lee, K. & Rolland, J.P. Dispersion manipulation in optical coherence tomography with Fourier-domain optical delay line. in *SPIE 5690* (Eds. Tuchin, V.V., Izatt, J.A. & fujimoto, J.G.) 512-522 (San Jose, CA, USA, 2005).

73. Hofer, B., Považay, B., Hermann, B., Unterhuber, A., Matz, G. & Drexler, W. Dispersion encoded full range frequency domain optical coherence tomography. *Opt. Express* **17**, 7-24 (2009).

74. Marks, D.L., Oldenburg, A.L., Reynolds, J.J. & Boppart, S.A. Digital algorithm for dispersion correction in optical coherence tomography for homogeneous and stratified media. *Appl. Opt.* **42**, 204-217 (2003).

75. Lee, S.-W., Jeong, H.-W., Kim, B.-M., Ahn, Y.-C., Jung, W. & Chen, Z. Opitmization for axial resolution, depth range and sensitivity of spectral domain optical coherence tomography at 1.3um *J. Korean Phys. Soc.* **55**, 2354-2360 (2009).

76. Luke, H.D. The origins of the sampling theorem. *IEEE Communications Magazine* **37**, 106-108 (1999).

77. Firbank, M.J., Coulthard, A., Harrison, R.M. & Williams, E.D. A comparison of two methods for measuring the signal to noise ratio on MR images. *Phys. Med. Biol.* **44**, N261 (1999).

78. Akca, B.I., Nguyen, V., Kalkman, J., Ismail, N., Sengo, G., Fei, S., Driessen, A., van Leeuwen, T.G., Pollnau, M., Wo, x, rhoff, K. & de Ridder, R.M. Toward spectral-domain optical coherence tomography on a chip. *IEEE J. Sel. Top. Quant. Electron.* **18**, 1223-1233 (2012).

79. Hu, Z., Pan, Y. & Rollins, A.M. Analytical model of spectrometer-based two-beam spectral interferometry. *Appl. Opt.* **46**, 8499-8505 (2007).

80. Yun, S., Tearney, G., Bouma, B., Park, B. & de Boer, J. High-speed spectral-domain optical coherence tomography at 1.3 um wavelength. *Opt. Express* **11**, 3598-3604 (2003).

81. Rey, S.M., Považay, B., Hofer, B., Unterhuber, A., Hermann, B., Harwood, A. & Drexler, W. Three- and four-dimensional visualization of cell migration using optical coherence tomography. *J. Biophotonics* **2**, 370-379 (2009).

Appendix A: Labview Diagrams

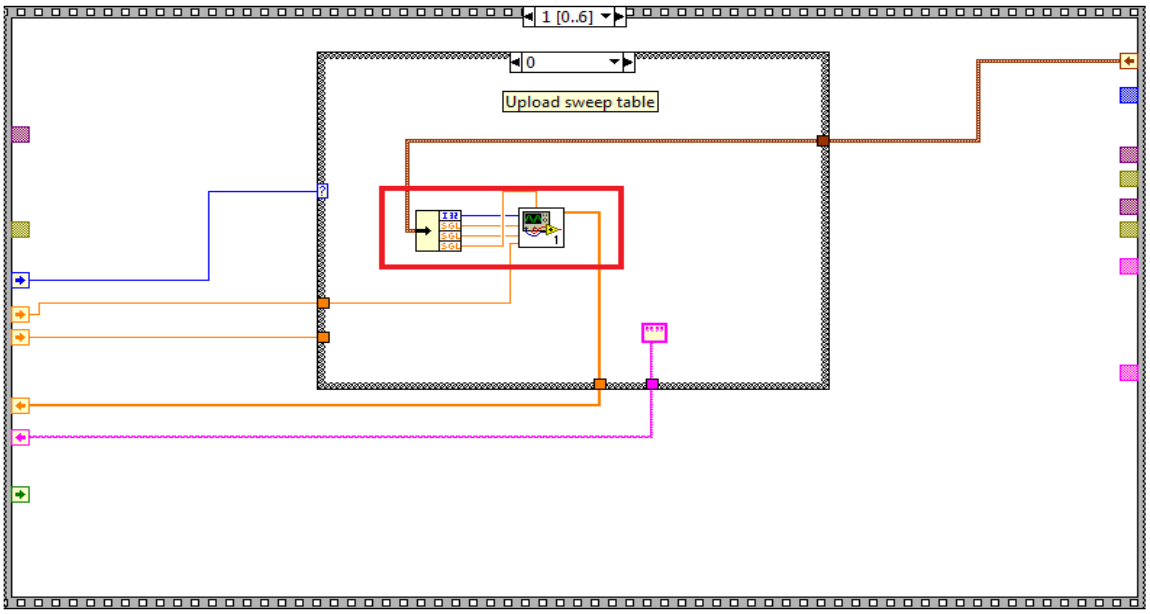

Figure A-1: The first frame of the frequency sweeper control Labview VI.

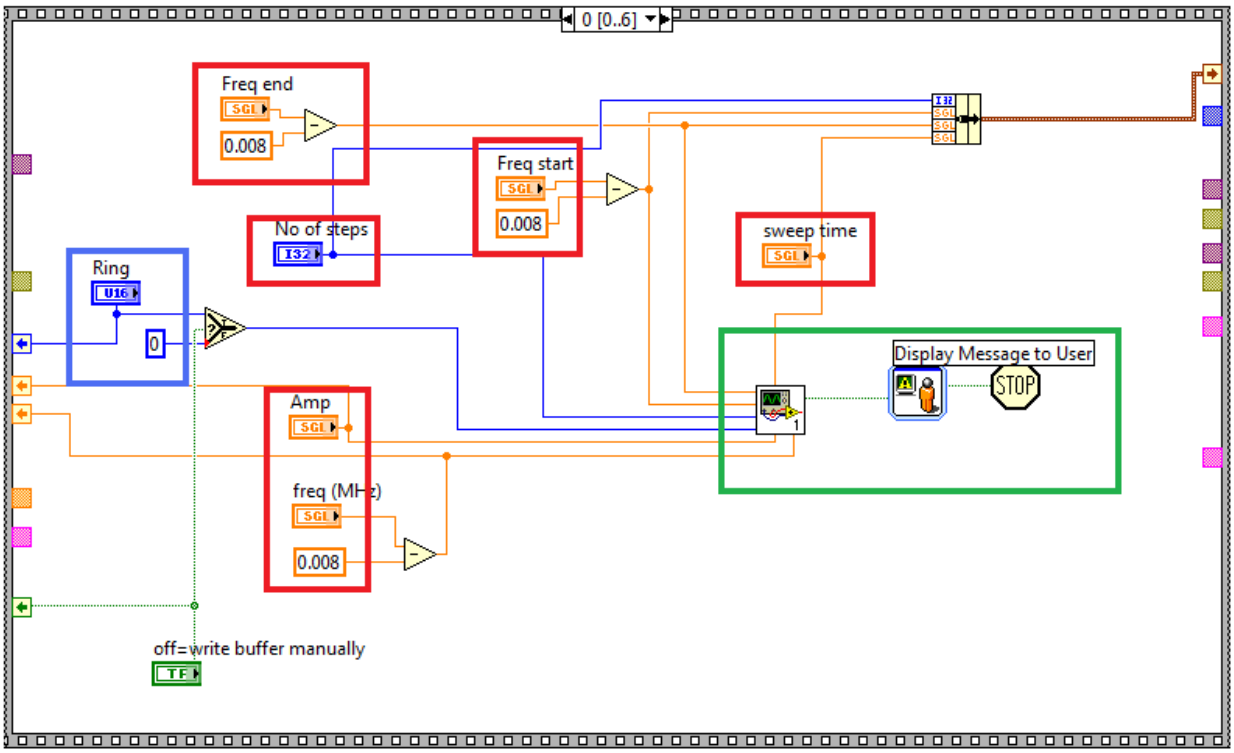

Figure A-2: The second frame of the frequency sweeper control Labview VI.

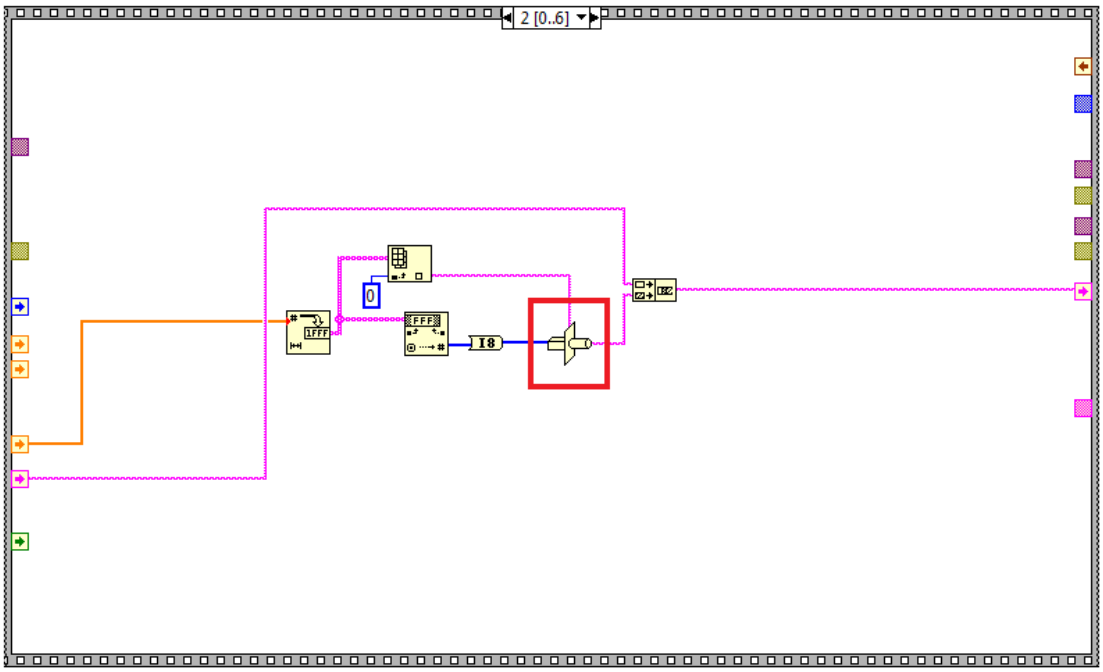

Figure A-3: The third frame of the frequency sweeper control Labview VI.

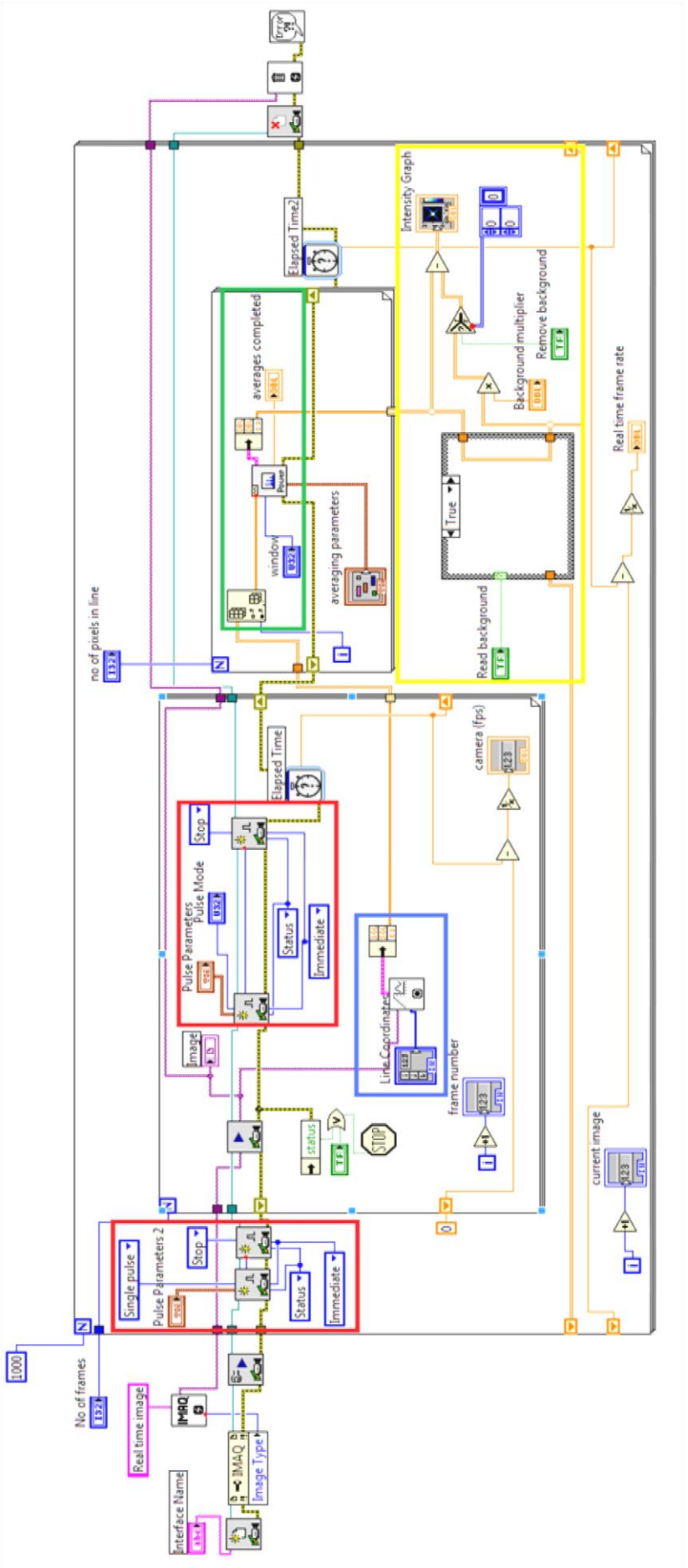

Figure A-4: The Labview VI for the real time 2D imager.

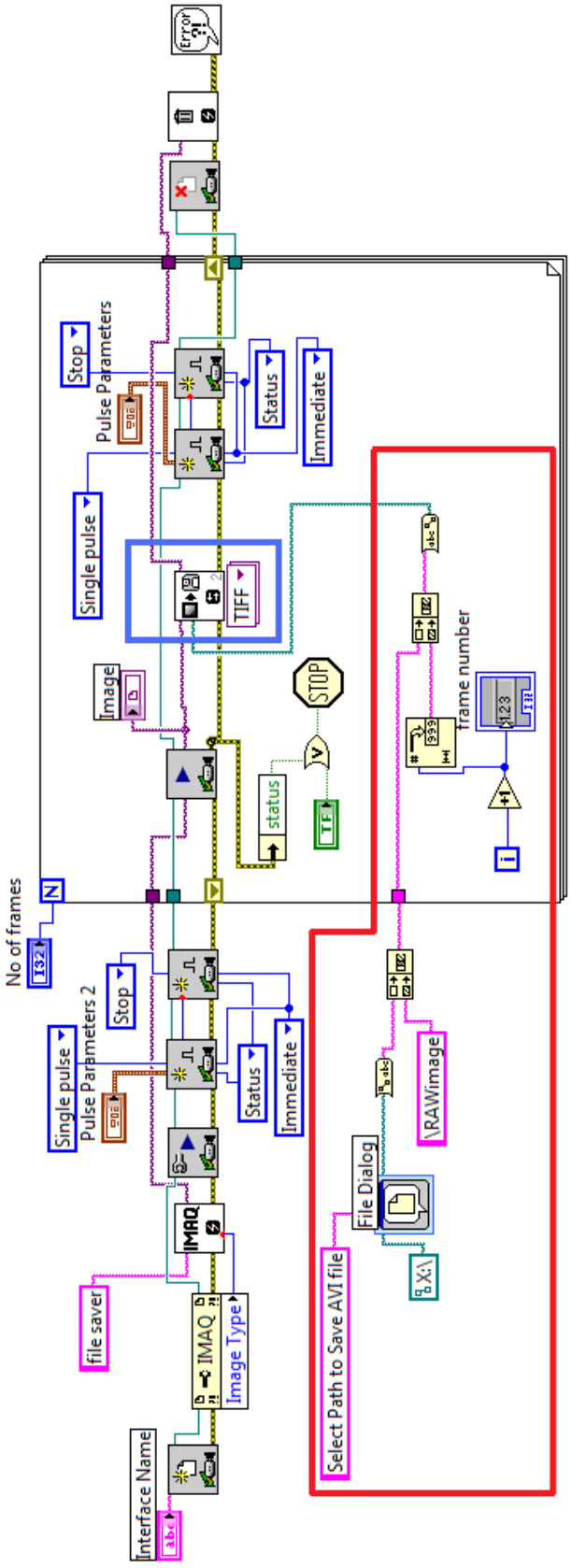

Figure A-5: FFSSOCT acquisition software.

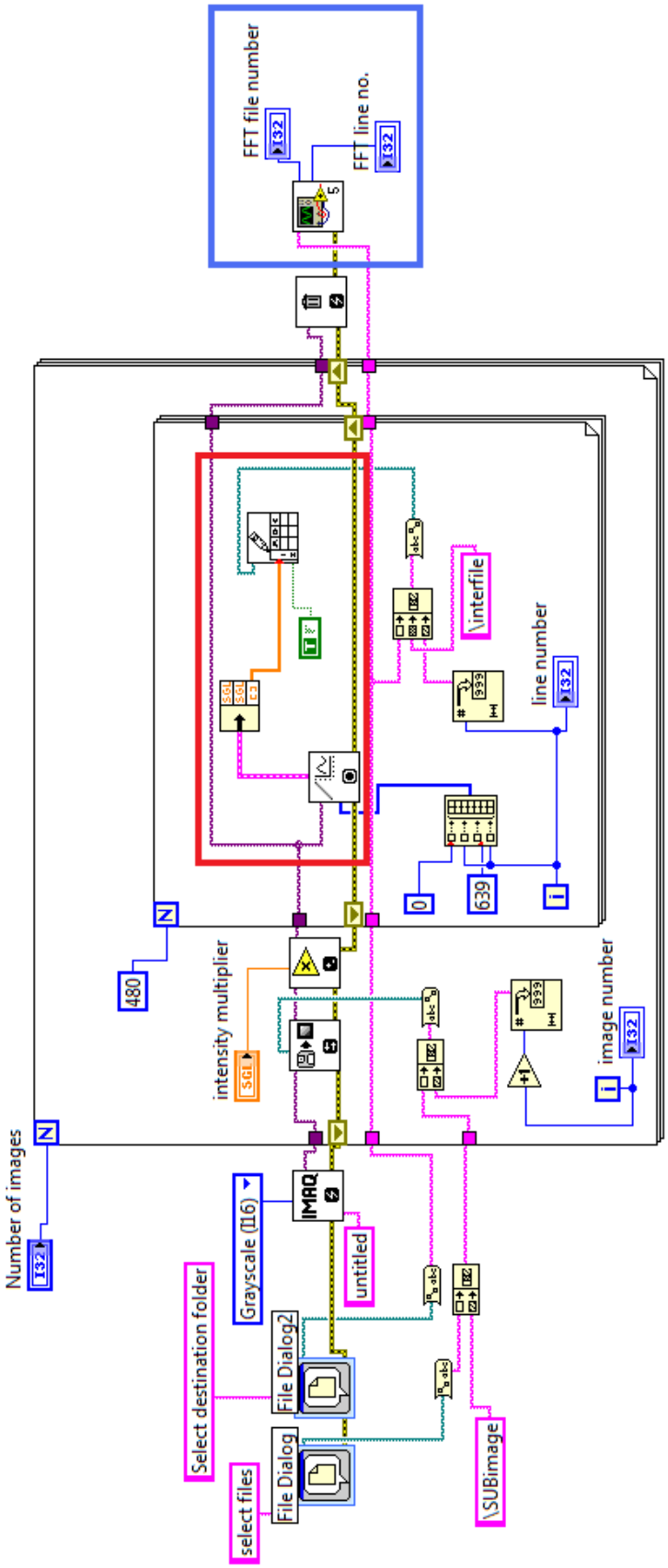

Figure A-6: The first part of the Labview VI for processing the acquired data

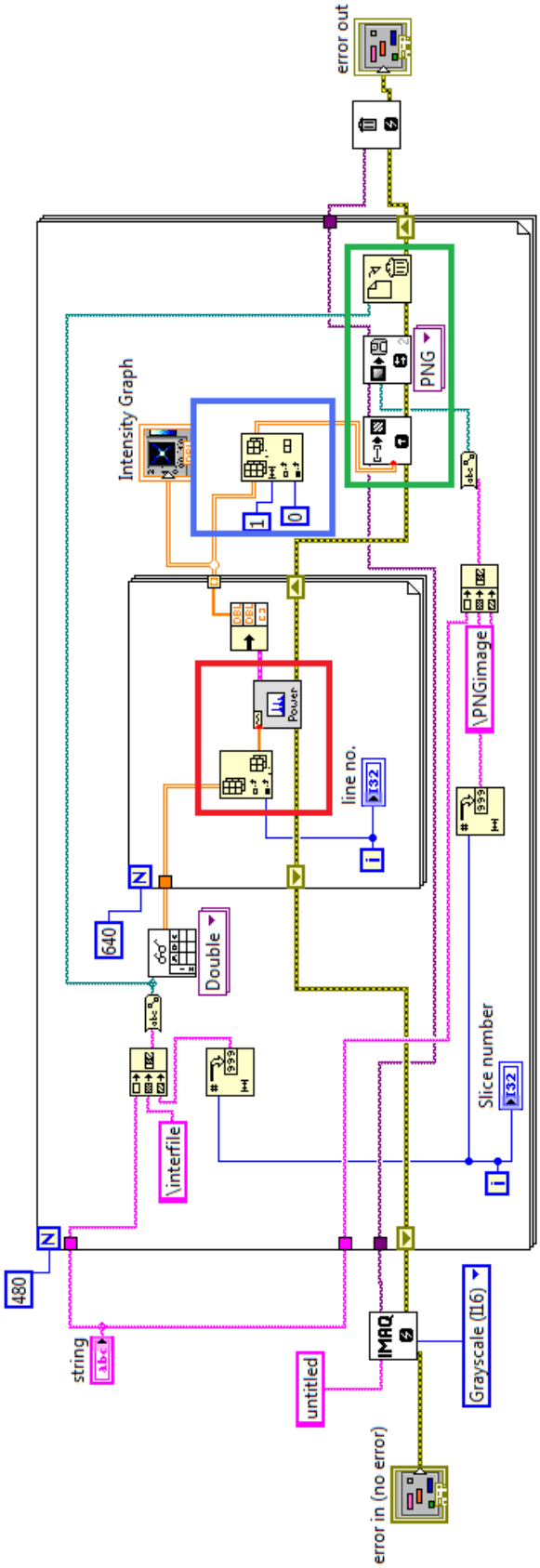

Figure A-7: The second part of the Labview VI for processing the acquired data.

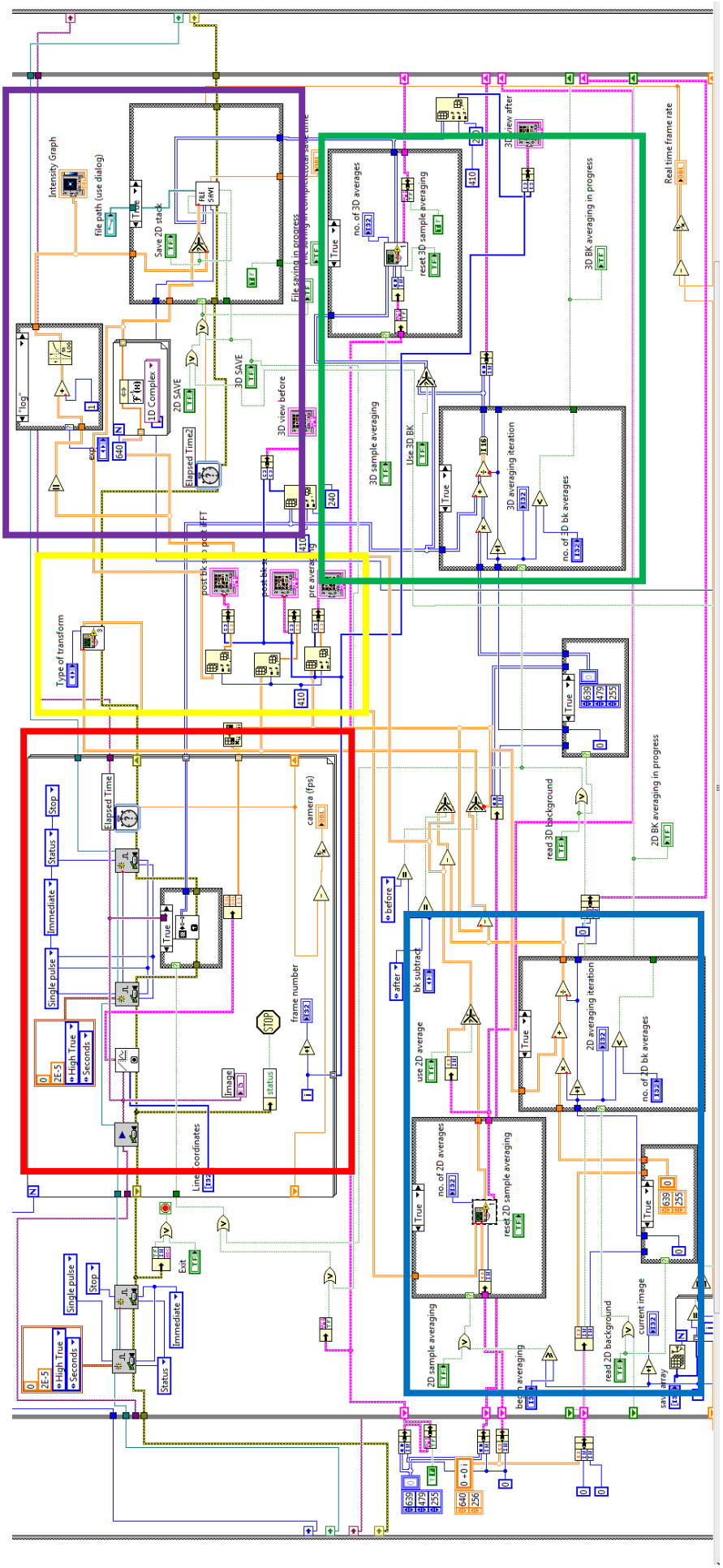

Figure A-8: The final version of the acquisition software (v2.1) for the FFSOCT instrument.

The program incorporates the frequency generator control program (Figure A-2), initialising it in the first frame (not shown) of the stacked architecture. The functions of the highlighted areas are explained on pages 67-69 and relate to the input controls shown on Figure 3-20.

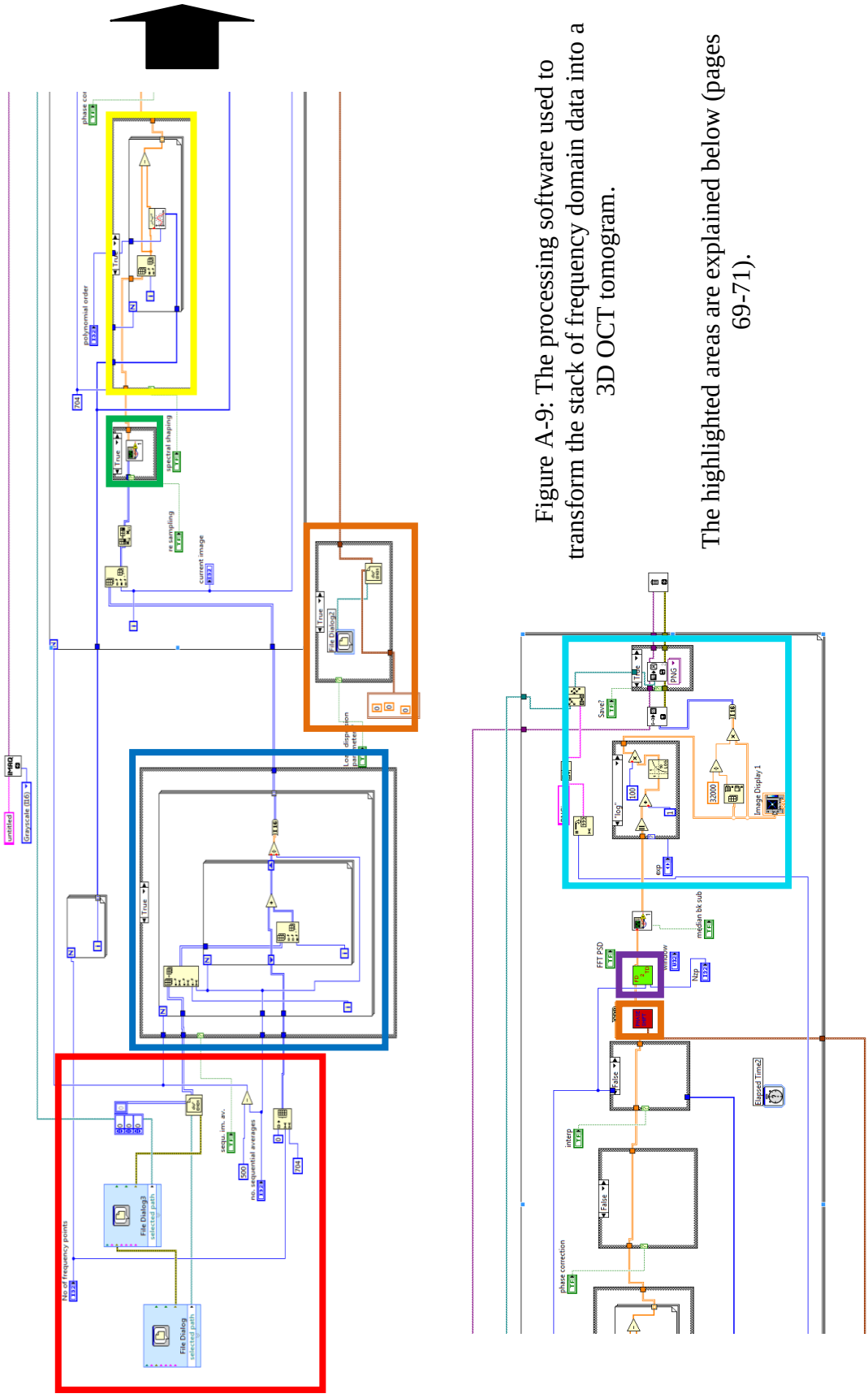

Figure A-9: The processing software used to transform the stack of frequency domain data into a 3D OCT tomogram.

The highlighted areas are explained below (pages 69-71).